GFZ
Helmholtz-Zentrum
POTSDAM

HELMHOLTZ-ZENTRUM POTSDAM
DEUTSCHES
GEOFORSCHUNGSZENTRUM

Oliver Heidbach

Spatial and temporal variability of the contemporary crustal stress pattern of the Earth

Scientific Technical Report STR11/05

www.gfz-potsdam.de

HELMHOLTZ
GEMEINSCHAFT

Impressum

Helmholtz-Zentrum Potsdam
Deutsches
GeoForschungsZentrum

D-14473 Potsdam

Gedruckt in Potsdam
Februar 2011

ISSN 1610-0956

Die vorliegende Arbeit
in der Schriftenreihe
Scientific Technical Report (STR) des GFZ
ist in elektronischer Form erhältlich unter
www.gfz-potsdam.de - Neuestes - Neue
Publikationen des GFZ

Oliver Heidbach

Spatial and temporal variability of the contemporary crustal stress pattern of the Earth

Kumulative Habilitationsschrift
zur Erlangung der venia legendi

der Fakultät für Physik
der Universität Karlsruhe (TH)

2009

Scientific Technical Report STR11/05

Spatial and temporal variability of the contemporary crustal stress pattern of the Earth

Kumulative Habilitationsschrift
zur Erlangung der venia legendi
der Fakultät für Physik
der Universität Karlsruhe (TH)

vorgelegt von
Dr. Oliver Heidbach

Karlsruhe 2009

Scientific Techncial Report STR 11/05
DOI: 10.2312/GFZ.b103-11055

Deutsches GeoForschungsZentrum GFZ

Contents

Heidbach, O., Fuchs, K., Müller, B., Reinecker, J., Sperner, B., Tingay, M., Wenzel, F., (2007). The World Stress Map - Release 2005, 1:46,000,000. *Commission of the Geological Map of the World*, Paris.

Heidbach, O., Höhne, J., (2008). CASMI - a tool for the visualization of the World Stress Map data base. *Computers and Geosciences*, 34 (7), 783-791, doi:1016/j.cageo.2007.06.004.

Heidbach, O., Reinecker, J., Tingay, M., Müller, B., Sperner, B., Fuchs, K., Wenzel, F., (2007). Plate boundary forces are not enough: Second- and third-order stress patterns highlighted in the World Stress Map database. *Tectonics*, 26, TC6014 doi:10.1029/2007TC002133.

Heidbach, O., Iaffaldano, G., Bunge, H.-P., (2008). Topography growth drives stress rotations in the Central Andes - observations and models. *Geophys. Res. Lett.*, 35, L08301, doi:10.1029/2007GL032782.

Heidbach, O., Ben-Avraham, Z., (2007). Stress evolution and seismic hazard of the Dead Sea fault system. *Earth Planet. Sci. Lett.*, 257, 299-312.

Hergert, T., Heidbach, O., (2006). New insights in the mechanism of post-seismic stress relaxation exemplified by the June 23rd 2001 $M_w = 8.4$ earthquake in southern Peru. *Geophys. Res. Lett.*, 33, L02307, doi:1029/2005GL024585.

Summary

In the 1950s and 1960s it became evident that the driving mechanisms of tectonic plate motion are the plate boundary forces. Based on this fact it was hypothesized that these forces also control the crustal stress field pattern. This was confirmed with the first release of the World Stress Map (WSM) in 1992 based on ~7300 data records providing the orientation of maximum horizontal compressional stress S_H. The qualitative analysis of this dataset revealed that large areas with first-order plate-wide scale stress patterns exist and that S_H orientations are for some plates sub-parallel to the absolute plate motion trajectories. Given this result it was concluded that the sources of the first-order stress pattern are the plate-boundary forces. Beside fundamental questions related to global plate tectonics the knowledge of the crustal stress is also important for a number of issues with high societal relevance such as stability assessment of all kinds of underground openings (mines, boreholes, tunnels etc.), management of hydrocarbon and geothermal reservoirs, and to assess catastrophic stress release e.g. during earthquakes.

This thesis summarizes the results of the WSM project's second phase (1996-2008). In particular it presents the major achievements that have been accomplished with the WSM 2008 database release that has been compiled under the guidance of the author. Furthermore, the thesis briefly presents three of the author's numerical models that aim at quantification the temporal changes of the crustal stress field.

In the second phase of the WSM project (1996-2008) the objective was to accomplish a better global coverage of stress information and to establish local data densifications to investigate in greater detail the impact of regional and local stress sources on the stress pattern. With the current WSM 2008 database release the number of data records was almost tripled to 21,750 with respect to the database from the project's first phase. This substantially enlarged WSM database now allows a global statistical analysis that quantifies the spatial variability of the stress pattern. The results of this new analysis confirm the existence of very long wave-length, i.e. plate-wide scale stress pattern (> 2000 km, e.g. in North America). However, the higher density of stress data records also reveals that there are large areas with shorter wavelengths of the stress pattern (< 400 km, e.g. whole Western Europe). Regional studies of the stress pattern in the Alpine foreland and the North German Basin confirm this. In both examples the mean S_H orientation rotates clockwise within a few hundred kilometres by 30°-50°. Zooming further into the North German Basin rotations of the mean S_H orientation by up to 90° are detected within a few kilometres. It is shown that this is due to mechanical decoupling by means of a low shear strength salt layer that prevents the transition of the far-field stress pattern from the basement to the layers above salt. Thus, local structural and strength conditions determine the stress pattern and not the plate boundary forces. Even though plate-boundary forces are probably the most significant stress source, the contribution of regional and local stress sources from topography, large crustal density and strength contrasts, as well as active tectonics can reach similar or larger stress magnitudes. The superposition of these with the far-field stress source can lead to large rotations of the S_H orientation with respect to

the expected first-order S_H orientation. The amount of the rotation depends on their relative magnitude and their relative orientation.

Based on this results it is obvious that stress information from WSM database has to be used with caution for the characterization of an area in particular when (1) only few data records represent the stress state, (2) the mean S_H orientation in the area of interest has a high standard deviation, (3) when heterogeneous density distributions, large strength contrasts or active faults are present, or (4) when the area of interest is mechanically decoupled from the far-field stress. Because the geological structure is heterogeneous in most regions of academic or industrial interest (seismically active zones, hydrocarbon and geothermal reservoirs, CO_2 sequestration sites etc.) a prediction of S_H orientations from linear interpolation using the nearest stress data records can be inappropriate. Furthermore, the time-dependence of the stress state is not reflected in the WSM database even though we know from the advent of GPS and InSAR techniques that e.g. inter-, co- and post-seismic deformations have a significant local impact on the stress state. Thus, in order to quantify the stress state and its temporal changes, geomechanical modelling is an essential tool.

The three examples of numerical models presented in this thesis simulate geodynamic processes that act on different spatial and temporal scales. The first experiment shows a model that couples global mantel circulation with lithosphere dynamics. The results show that the growth of the Andean topography controls the temporal evolution of the stress pattern on geological time scales. In the other two examples the stress changes on time-scales of the seismic cycle is investigated. The second numerical experiment calculates the changes in Coulomb failure stress due to interseismic loading along the Dead Sea fault system and co-seismic stress transfer from 14 historical earthquakes. The analysis of the current stress state from this loading and deloading history reveals that a 90 km long segment of the Jordan fault north of the Dead Sea accumulated significant stresses that could lead to a M_S 7.4 earthquake. The third experiment investigates the cause of an unexpected post-seismic deformation signal observed at the continuous GPS station in Arequipa after the June 2001 M_w 8.4 earthquake in Southern Peru. Published interpretations of this post-seismic GPS signal assume that it results from after slip or down dip creep on the earthquake rupture plane. In contrast to this the model results reveal that non-linear visco-elastic relaxation of co-seismically induced extensional stresses can also explain the observed co- and post-seismic GPS signals.

These numerical models as well as the quantitative statistical stress pattern analysis of the WSM 2008 database release indicate that the various processes and structural conditions that contribute to the crustal stress state act on a wide range of spatial and temporal scales. In order to describe and quantify the crustal stress state and its temporal changes in greater detail both is needed: more stress data and in particular stress magnitude measurements as well as an integrated 4D geomechanical model concept for the absolute stress state that is consistent with observed 3D kinematics.

1 Introduction

The identification and quantification of the geodynamic processes like seafloor spreading and subduction in the 1950s and 60s proved the theory of plate tectonics by *Alfred Wegener* [1915]. This gave way to the idea that the associated plate boundary forces such as ridge push and slab pull are also the key control of the lithospheric stress pattern. *Sykes and Sbar* [1973] addressed the question between the relation of plate motion, plate boundary forces and the lithospheric stress field, but the data available at that time was rather sparse. To prove the relation between plate boundary forces and crustal stress pattern on a global scale the International Lithosphere Program (ILP) established the World Stress Map (WSM) Project in 1985. After the project's first phase (1986-1992) the global database contained ~7300 data records that amongst other information give the orientation of maximum horizontal compressional stress S_H [*Zoback*, 1992]. The qualitative analysis of this dataset revealed that large areas with first-order, plate-wide scale stress patterns exist and that S_H orientations are for some plates sub-parallel to the absolute plate motion trajectories [*Richardson*, 1992; *Zoback et al.*, 1989; *Zoback*, 1992]. From this finding it was concluded that the sources of the first-order stress pattern are plate-boundary forces. Second-order stress patterns with shorter wave-length were assigned to regional and local sources such as lithospheric flexure and density and strength contrasts [*Zoback*, 1992].

Beside fundamental questions related to global plate tectonics the knowledge of the crustal stress state is also important for a number of issues with societal relevance such as stability assessment of all kinds of underground openings (mines, boreholes, tunnels etc.), management of hydrocarbon and geothermal reservoirs, and to assess catastrophic stress release e.g. during earthquakes [e.g. *Fuchs and Müller*, 2001; *Parsons*, 2005; *Steacy et al.*, 2005]. For instance stress-induced failure of boreholes is a known cause of wellbore instability and related drilling problems such as 'stuck pipe' [*Aadnoy*, 2003; *Bradley*, 1979]. The crustal stress state is also known to be a major control on the hydraulic conductivity of structures and, thus, on fluid flow in the subsurface. Fractures that strike within 30° of the maximum principal stress orientation or which are parallel to that orientation are expected to yield in tensile or shear failure. Consequently they are observed to transport the largest volumes of fluids [*Barton et al.*, 1995; *Sibson*, 1996]. For earthquake hazard assessment the interseismic stress accumulation and in particular the co-seismic stress transfer is of great importance. *Stein et al.* [1997] successfully predicted the location of the 1999 Izmit event from numerical simulation of the change of Coulomb Failure Stress due to the westward migrating sequence of 11 large earthquakes along the North Anatolian fault.

In the second phase of the WSM project (1996-2008) as a research project of the Heidelberg Academy of Sciences and Humanities the vision was to accomplish a better global coverage of stress information to quantify the spatial variability of the wave-length of the stress pattern, but also to compile local data densifications to investigate in greater detail the impact of regional and local stress sources on the stress pattern. With the current WSM database release 2008 the number of data records was almost tripled to 21,750.

This habilitation thesis gives a summary of six publications from the last three years (reprints are provided in the appendix). In the following second chapter I first give an overview of the WSM database release 2008, the refined and restructured quality ranking scheme, the procedure and results of a quantitative analysis of the spatial variability of the wave-length of the stress patterns as well examples of stress patterns at different spatial scales [*Heidbach et al.*, 2007a; *Heidbach et al.*, 2007b; *Heidbach et al.*, 2007c; *Heidbach et al.*, 2008b; *Heidbach et al.*, subm.].

In the third chapter I focus on the temporal changes of the stress pattern on geological and earthquake cycle time scales. These changes are investigated by means of three numerical experiments taken from three publications. The first paper addresses the impact of plate-boundaries that interact with the mountain-building process of the Andes on time-scales of several million years [*Heidbach et al.*, 2008a]. The second and the third paper investigate the inter-, co-, and post-seismic stress changes in seismically active regions of the Dead Sea fault system and at the subduction zone in southern Peru [*Heidbach and Ben-Avraham*, 2007; *Hergert and Heidbach*, 2006].

However, before proceeding with these two chapters on spatial and temporal variability of the stress pattern, I define the stress terms as they are used throughout this thesis (Section 1.1). Furthermore, an overview of the history, objectives, and compilation strategy of the WSM project is given in section 1.2.

1.1 Stress definitions and terms

The stress state is described with a second-order tensor σ_{ij} that is symmetrical with six independent components [e.g. *Jaeger et al.*, 2007]. After its transformation into the principal axis system the off-diagonal shear components vanish and the three principal stresses S_1, S_2, and S_3 remain. In the Earth's crust it is assumed that one of the principal stresses is oriented vertically (S_v) corresponding to the vertical load of the overburden [*Engelder*, 1992; *Zoback and Zoback*, 1989]. In this case the other two principal stresses are horizontally oriented. They are called maximum and minimum horizontal principal compressional stress S_H and S_h, respectively. Strictly speaking this assumption is only true at the shear stress free Earth's surface. However, it has been observed that this assumption is still a good approximation at depth [*Zoback and Zoback*, 1989].

The relative magnitudes of these principal stresses were used by *Anderson* [1951] to classify the three main tectonic regimes (Figure 1). In a normal faulting regime (NF) S_v exceeds the horizontal principal stresses ($S_v > S_H > S_h$), in a strike slip regime (SS) S_v is the intermediate principal stress ($S_H > S_v > S_h$), and in a thrust faulting regime (TF) S_v is the smallest principal stress ($S_H > S_h > S_v$) (Figure 1).

Besides the term *tectonic regime*, the term *tectonic stress* is frequently used in the geosciences literature [*Engelder*, 1992; *Greiner and Illies*, 1977; *Jaeger et al.*, 2007; *Richardson et al.*, 1979;

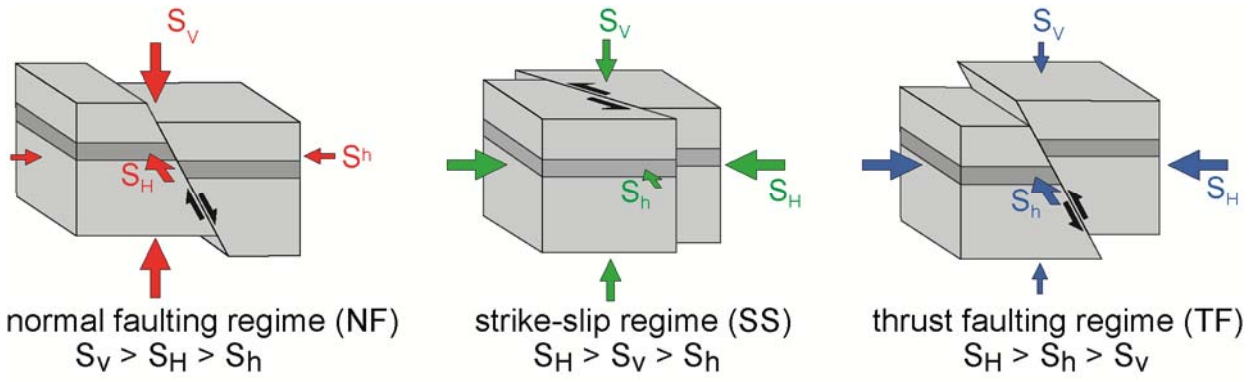

Figure 1. According to *Anderson* [1951] the relative magnitudes can be used to distinguish the three main tectonic regimes. Note that the colour codes and the abbreviations for the tectonic regimes given here are used in the World Stress Map project.

Solomon et al., 1980; *Zoback and Zoback*, 1989]. Following the definition of *Engelder* [1992] "tectonic stresses are usually horizontal components of the stress field which are a deviation from a reference stress state as a consequence of natural processes on all scales from plate-wide to local". A very commonly used reference stress state is the lithostatic stress state. In this case all three principal stresses have the same magnitude

$$S_1 = S_2 = S_3 \Rightarrow S_H = S_h = S_v = p = \rho \cdot g \cdot z$$

with pressure p, rock density ρ, depth z, and the gravitational acceleration g [*Engelder*, 1992]. A material which has a lithostatic stress state is for example magma. It has no shear strength and thus behaves like a fluid. The deviation from the reference stress state is a consequence of natural sources including (1) tectonic stresses (i.e. stresses that origin from tectonic plate motion such as plate boundary forces, earthquakes, flexural forces), (2) residual stresses (e.g. folding, topography induced, thermal stresses), and (3) near surface stresses (e.g. annual thermal stresses, moon attraction). Furthermore there are also man-made sources that contribute to the deviation from the reference stress state. These sources are e.g. tunnelling, drilling, mining, excavations, building and filling of dams, fluid injection (CO_2 sequestration, hydro-fracturing for reservoir stimulation), and reservoir production [*Engelder*, 1992]. Traditionally, tectonic stresses are often associated with a stress state that is generated from the large-scale natural sources such as plate-boundary forces [*Hickman*, 1991; *Zoback and Zoback*, 1989]. Stresses from regional sources such as topography (excess of gravitational potential energy) as well as massive deglaciation after ice ages, and local stresses from unloading due to erosion and sedimentation are often considered non-tectonic [*Engelder*, 1992].
However, the distinction between tectonic, i.e. plate-wide, regional, and local stresses can only be made when the absolute or relative contribution of the various stress sources of the stress state is quantified. Thus, the definition of *tectonic stress* is simplified if most constraints concerning scale and source are removed from the definition. *Tectonic stresses* are usually horizontal components of the stress field which are a deviation from a reference state as a consequence of natural processes on all scales from plate-wide to local. In order to avoid misunder-

standing the term *tectonic stress* is not used in this thesis. Instead the more general term *stress state* is applied in order to indicate that the stress state this thesis refers to is always a superposition from all natural stress sources (tectonic, plate-wide, regional, local etc.).

1.2 World Stress Map Project

The first regional comprehensive stress data compilations were available for Europe [*Ahorner*, 1967; 1975; *Greiner and Illies*, 1977; *Illies and Greiner*, 1976; 1978; *Stephansson et al.*, 1987] and North America [*Sykes and Sbar*, 1973; 1974; *Zoback and Zoback*, 1981; *Zoback and Zoback*, 1980]. A key problem of these regional stress data compilations was that they combined a variety of stress indicators (e.g. overcoring, hydrofrac in boreholes, borehole breakouts, geological indicators, earthquake focal mechanisms) in one data set. Since the different stress indicators represent very different rock volumes [*Ljunggren et al.*, 2003] an evaluation scheme was needed. Therefore, in 1985 the International Lithosphere Programme formed a task group to develop a general quality ranking scheme for the different stress indicators in order to establish a World Stress Map (WSM) by unifying the existing regional stress maps in Europe, Canada and the United States. From this initiative the WSM database developed into one of the fundamental global geo databases. The WSM project and its database became internationally accepted by academia and industry likewise to be the standard reference for contemporary crustal stress information. The key scientific objective of the project's first phase (1986-1992) was to investigate the hypothesis whether plate-wide stress pattern in intra-plate areas exist or not.

Zoback et al. [1989], *Richardson* [1992], and *Zoback* [1992] demonstrated in their qualitative analysis of the WSM database that the S_H orientation in North America, South America and Europe are, at the plate-scale, predominately oriented sub-parallel to absolute plate motions. The correlation of S_H orientations and plate motion directions suggests that the first-order intra-plate stress field is the result of forces generated at plate boundaries, primarily mid-ocean ridge 'push', subducting slab 'pull', trench 'suction' and traction at the base of the lithosphere (Figure 2). Examinations of more complex plates (such as the Indo-Australian Plate) and of stresses proximal to mountain ranges and subduction zones has revealed that continental collision and large intra-plate forces, e.g. isostatic compensation and lithospheric flexure have an additional major impact on the large-scale lithospheric stress field [*Hillis and Reynolds*, 2000; *Zoback*, 1992].

In the course of further compilation of stress information a paradigm change took place in the WSM project's second phase (1996-2008). Instead of compiling the stress information hypothesis-driven the compilation is now data-driven. I.e. all stress information that meet the WSM requirements is subjected to the quality assessment according to the WSM quality ranking scheme regardless of its spatial representation. Nevertheless, this does not imply that near surface overcoring stress indicators are included, as these are very likely to be affected by local surface topography.

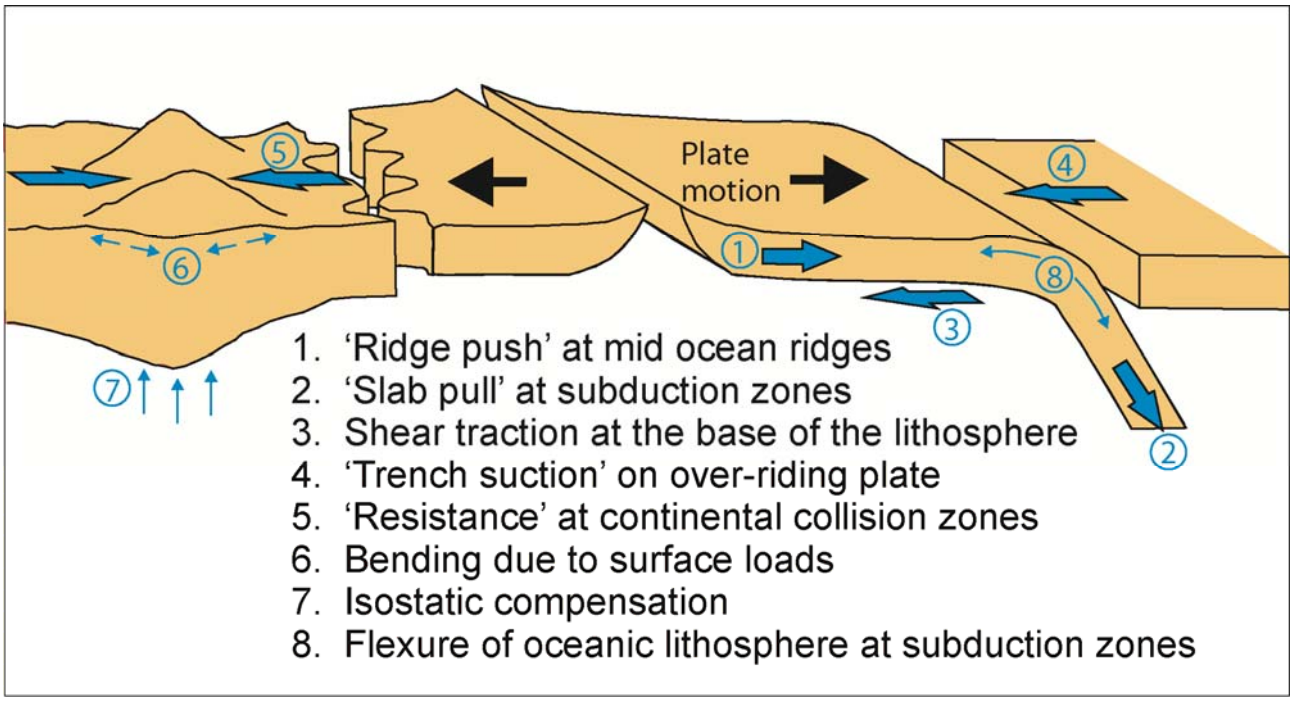

Figure 2. Forces controlling the present-day stress field at the 'primary' plate-scale (large blue arrows) and 'secondary' broad regional scales (small blue arrows; adapted and modified from *Zoback et al.* [1989]).

Due to this change of compilation philosophy the number of stress data records increased in particular in areas that are probably not representative for the large intra-plate areas. The majority of new data records are from areas with seismic activity (focal mechanism solutions) or sedimentary basins (borehole breakouts, drilling induced fractures, hydrofracs). Provided that a plate-wide stress pattern exists the result of further data acquisition that are necessarily not representative for the large spatial scales can become over-represented in the WSM database. However, the advantage of this procedure is that in some areas the density of data records is now sufficiently high to detect small scale changes of S_H orientations that were not visible before [*Heidbach et al.*, 2007c].

As a consequence, stress information from WSM database has to be used with caution and appropriate subsets must be defined in dependence of the question that is addressed. Areas with only a few stress data records might suggest a large-scale stress pattern, but obviously local deviations cannot be ruled out. Vice versa, areas with high data record density have presumably a larger scatter in S_H orientation, but this must not imply that at greater depth in the basement a large-scale stress pattern exists that is decoupled from the one observed in the boreholes of the sedimentary basins [*Heidbach et al.*, 2007c; *Tingay et al.*, 2005a; *Tingay et al.*, 2005b]. Furthermore, the entries in the WSM database are static, i.e. they do not document the temporal change in S_H orientation. In order to understand the geodynamic processes and to predict the temporal and spatial changes of the stress field due to plate-boundary forces, earthquakes, magma ascent, surface processes (erosion and sedimentation), fluid injection in geothermal reservoirs, CO_2 sequestration, and depletion in hydrocarbon reservoirs, 3D geomechanical models of the absolute stress state are essential.

2 Stress observations and spatial stress pattern

In the following I present a brief review of the status of the WSM project. In particular I will summarize the WSM project's major achievements of the last three years that are published and submitted respectively, in the following four publications:

Heidbach, O., Fuchs, K., Müller, B., Reinecker, J., Sperner, B., Tingay, M., Wenzel, F., (2007). The World Stress Map - Release 2005, 1:46,000,000. Commission of the Geological Map of the World, Paris.

Heidbach, O., Höhne, J., (2008). CASMI - a tool for the visualization of the World Stress Map data base. Computers and Geosciences, 34 (7), 783-791, doi:1016/j.cageo.2007.06.004.

Heidbach, O., Reinecker, J., Tingay, M., Müller, B., Sperner, B., Fuchs, K., Wenzel, F., (2007). Plate boundary forces are not enough: Second- and third-order stress patterns highlighted in the World Stress Map database. Tectonics, 26, TC6014, doi:10.1029/2007TC002133.

Heidbach, O., M. Tingay, A. Barth, J. Reinecker, D. Kurfeß, and B. Müller, Statistical analysis of global spatial wave-length stress pattern, Tectonophysics, subm.

Reprints of the three published papers can be found in the appendix of this thesis whereas the key aspects of the submitted paper of *Heidbach et al.* [subm. to Tectonophysics] are presented in sections 2.1 and 2.2.

2.1 World Stress Map database

The WSM 2008 database release has 21,750 stress data records world-wide [*Heidbach et al.*, 2008c; subm.]. The WSM database is visualised by mapping the maximum horizontal compressional stress S_H as the best known component of the stress tensor [*Heidbach et al.*, 2004; *Heidbach and Höhne*, 2008]. In addition it shows the tectonic regimes (i.e. relative magnitudes of the three principal stresses), the type of stress indicator and the quality ranking [*Heidbach et al.*, subm.; *Sperner et al.*, 2003; *Zoback and Zoback*, 1991; *Zoback and Zoback*, 1989] for each stress data record (Figure 3). Data coverage is relatively dense in North America and Europe, parts of Asia, the Indo-Australian plate and western South America due to hydrocarbon exploration and seismic activity. Other places such as Africa or Siberia are nearly as sparsely covered as the oceans either due to technically limited accessibility (deep oceans), very low seismicity (cratons and intra-plate oceanic crust) or simply due to lack of cooperation (e.g. Russia, China, Middle East). In the following three sections I briefly describe the major changes and recent achievements of the WSM project, particularly the updated and refined quality-ranking scheme for the S_H orientation that has been released with and applied to the WSM 2008 database release.

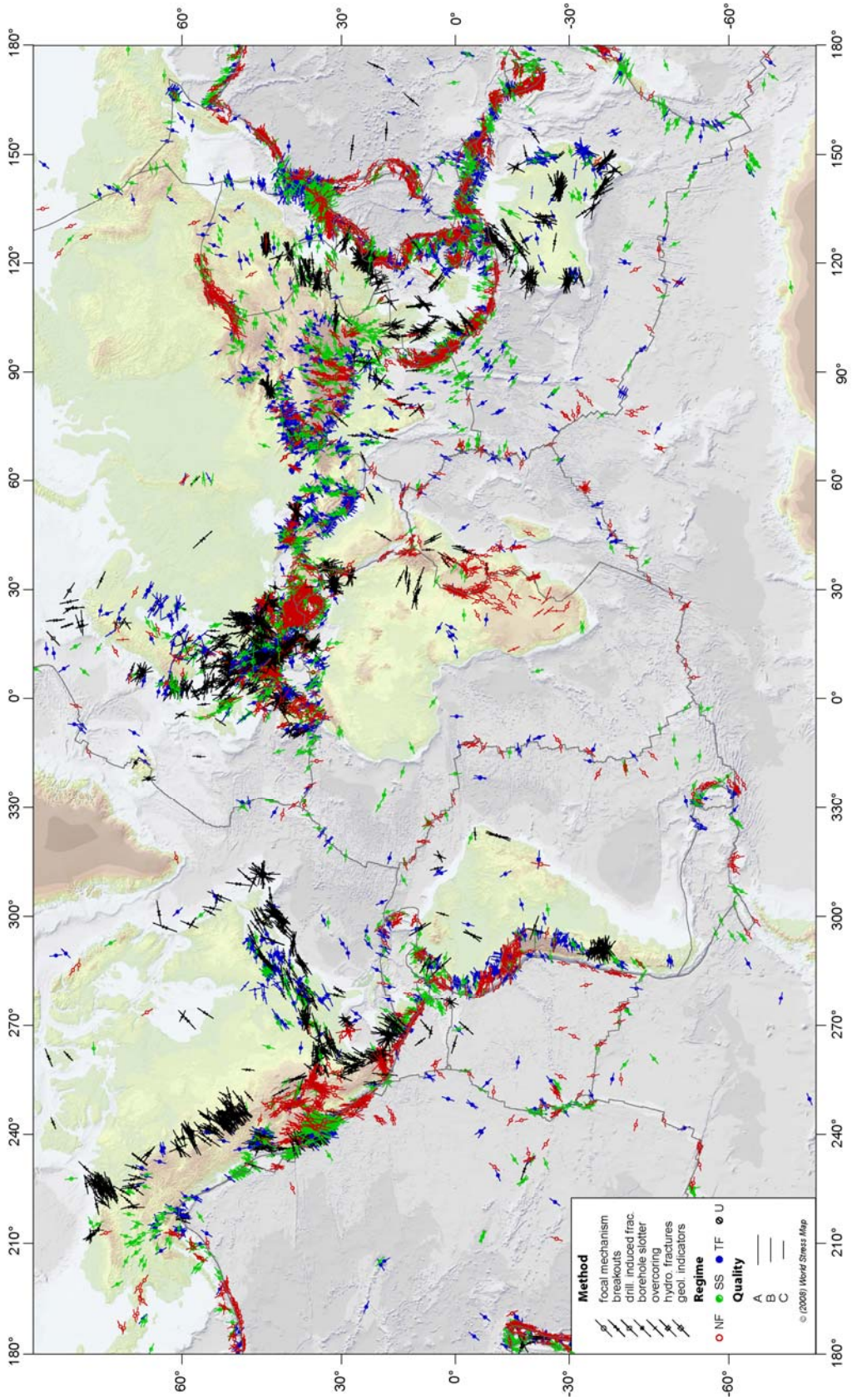

Figure 3. Global stress map based on the WSM 2008 database release with 11,346 A-C quality data records excluding Possible plate Boundary Events (PBE). Lines represent orientation of maximum horizontal compressional stress (S_H), line length is proportional to quality. Colours indicate stress regimes. Red is normal faulting (NF), green strike-slip faulting (SS), blue thrust faulting (TF), and black unknown regime (U). Plate boundaries are taken from *Bird* [2003]. Topography is based on the ETOPO1 data from the National Geophysical Data Center (NGDC) including bathymetry data from *Smith and Sandwell* [1997].

The WSM 2008 database release contains 21,750 data records determined from a wide variety of stress indicators (Table 1). The present-day S_H orientation is primarily estimated from earthquake focal mechanism solutions, borehole breakouts and drilling-induced fractures (from borehole images or caliper log data), in-situ measurements (overcoring, hydraulic fracturing) and geological indicators (fault slip data, volcanic vent alignments). The stress information from the different stress indicators represent various crustal rock volumes ranging from 10^{-3} to 10^{9} m^3 [*Ljunggren et al.*, 2003] and depths ranging from near the surface down to 40 km. Within the upper 6 km of the Earth's crust the stress field is mapped by all different stress indicators with borehole breakouts as the major contributor. Below ~6 km depth earthquake focal mechanisms are the only stress indicators available, except from a few scientific drilling projects such as the KTB site that reached 9101 m [*Brudy et al.*, 1997]. For further details on data analysis for the different stress indicators the WSM website provides easy to use guidelines for earthquake focal mechanism solutions, borehole breakouts, drilling-induced tensile fractures and overcoring tests (http://www.world-stress-map.org).

Table 1. Stress indicator and data quality in the WSM 2008 database release [*Heidbach et al.*, 2007c; *Heidbach et al.*, 2008c].

Stress indicator (abbreviation)	**WSM 2008 A-E quality**	**WSM 2008 A-C quality**
Focal mechanisms (FMF, FMS, FMA)	15,689[a]	13,959[b]
Borehole breakouts (BO, BOC, BOT)	4125	2168
Drilling-induced fractures (DIF)	278	82
Geological: fault-slip (GFI, GFM, GFS)	434	331
Hydraulic fracturing (HF, HFG, HFP, HFM)	349	228
Borehole slotter (BS)	33	0
Overcoring (OC)	611	94
Geological: Volcanic alignment (GVA)	220	98
Petal centreline fractures (PC)	9	9
Shear wave splitting (SW)	2	0
Total	21,750	16,969

[a] This number includes 5669 data records from single focal mechanism solutions (FMS) located close to a plate boundary and flagged as Possible plate Boundary Events (PBE) indicating that they have a larger potential for a large offset between the principal strain axis and the principal stress orientations.
[b] This number includes 5623 data records from single mechanism solutions (FMS) that are flagged as PBE (further details are given on the website and in *Heidbach et al.* [subm. to Tectonophysics])

WSM quality-ranking scheme

A key aspect of the compilation of stress data from different stress indicator is the quality-ranking scheme that has been developed for the different methods [*Heidbach et al.*, subm.; *Sperner et al.*, 2003; *Zoback and Zoback*, 1991; *Zoback and Zoback*, 1989; *Zoback*, 1992]. This scheme provides an assessment of the reliability of each individual stress indicator and allows the comparison between S_H orientations deduced from different stress indicators. Each stress data record is assigned a quality between A and E, with A being the highest quality and E the

lowest. A-quality indicates that the S_H orientation is accurate to within ±15°, B-quality to within ±20°, C-quality to within ±25°, and D-quality to within ±40°. E-quality marks data records with insufficient or widely scattered stress information. Data records assigned to A-, B-, or C-quality are typically considered reliable for use in stress analysis and the interpretation of geodynamic processes. The quality-ranking scheme has been refined and extended as existing techniques were further developed for borehole breakouts and focal mechanism solutions. These changes are described in the following subsections.

Updated quality-ranking scheme for borehole breakouts

The original 1992 WSM quality-ranking scheme for stress data from borehole breakouts required only four breakouts or a total of at least 30 m of breakouts (often in multiple nearby wells) with a standard deviation of < 25° to be rated as C-quality. However, at this time borehole breakouts were primarily interpreted from four-arm caliper logs, on which non-stress related features can easily be misinterpreted as breakouts (a problem that is particularly common with automatic breakout interpretation software). Furthermore, four breakouts or ≥ 30 m of breakout can encompass a very small volume of rock and the use of wells in 'close proximity' was ambiguous (sometimes interpreted to be all wells within the same basin). Hence, this quality-ranking scheme overestimated the reliability of many stress indicators for assessing the regional stress pattern. Because of these flaws, *Sperner et al.* [2003] introduced a refined quality-ranking system for stress data from borehole breakouts in which both four breakouts and a combined length of ≥ 30 m must be met in a single well to obtain a C-quality. Furthermore, all breakouts interpreted using automatic software (i.e. not manually picked and identified) were disallowed and removed from the database.

The last decade has also witnessed the more prevalent use of resistivity and acoustic image logs that allow borehole breakouts to be directly visualized and thus remove much of the possibility for misinterpretation. Image logs also allow the interpretation of much smaller breakouts (e.g. tens of cm rather than > 1 m for caliper logs) and of drilling-induced fractures, that were too small to be interpreted on caliper logs. Hence, image logs enable a much more accurate and improved interpretation of stress orientation over four-arm caliper logs.

However, the greater reliability of stress orientations interpreted from image log data was underestimated under the *Sperner et al.* [2003] quality-ranking scheme. For example, the common image log observation of numerous small consistently-oriented breakouts over a long image log interval (e.g. 25 one meter log breakouts over several hundred meters of log) would only receive a D-quality under the quality-ranking scheme described in *Sperner et al.* [2003], despite reliably reflecting the S_H orientation in a significant volume of rock. Hence, the WSM 2008 database release now includes different quality-ranking schemes for breakouts interpreted on four-arm caliper logs and for breakouts interpreted on image logs and a quality-ranking scheme for drilling-induced fractures that better reflects the ability for different log types to reliably estimate the contemporary S_H orientation (Table 2).

Table 2. 2008 World Stress Map quality-ranking system.

Stress indicator		**A** S_H believed to be within ± 15°	**B** S_H believed to be within ± 15-20°	**C** S_H believed to be within ± 20-25°	**D** Questionable S_H orientation (± 25-40°)	**E** no reliable information (> ± 40°)
Focal Mechanism (FM)	**Formal Inversion (FMF)**	• Formal inversion of ≥ 15 well constrained single event solutions in close geographic proximity and s.d. or misfit angle ≤ 12°	• Formal inversion of ≥ 8 well constrained single event solutions in close geographic proximity and s.d. or misfit angle ≤ 20°	-	-	-
	Single (FMS)	-	-	• Well constrained single event solution, $M \geq 2.5$ (e.g. CMT solutions)	• Well constrained single event solution, $M < 2.5$	• Mechanism with P,B,T axes all plunging 25°-40° • Mechanism with P and T axes both plunging 40°-50°
	Average (FMA)	-	-	-	• Average of P-axis trends or circular statistics of P-axis trends Composite solutions	
Borehole Breakout (BO)	from caliper logs	• ≥ 10 distinct breakouts and combined length ≥ 300 m in a single well with s.d. ≤ 12°	• ≥ 6 distinct breakouts and combined length > 100 m in a single well with s.d. ≤ 20°	• ≥ 4 distinct breakouts and combined length ≥ 30 m with s.d. ≤ 25°	• < 4 distinct breakouts or < 30 m combined length in a single well with s.d. ≤40°	• Wells without reliable breakouts or s.d. > 40°
	from image logs	• ≥ 10 distinct breakouts and combined length ≥ 100 m in a single well with s.d. ≤ 12°	• ≥ 6 distinct breakouts and combined length > 40 m in a single well with s.d. ≤ 20°	• ≥ 4 distinct breakouts and combined length ≥ 20 m with s.d. ≤ 25°	• < 4 distinct breakouts or < 20 m combined length in a single well with s.d. ≤40°	
Drilling Induced Fractures (DIF)		• ≥ 10 distinct fractures in a single well with a combined length ≥ 100 m and s.d. ≤ 12°	• ≥ 6 distinct fractures in a single well with a combined length ≥ 40 m and s.d. ≤ 20°	• ≥ 4 distinct fractures in a single well with a combined length ≥ 20 m and s.d. ≤ 25°	• < 4 distinct fractures in a single well or a combined length < 20 m and s.d. ≤ 40°	• Wells without fracture zones or s.d. > 40°
Hydraulic Fracture (HF)		• ≥ 5 hydrofrac orientations in a single well with s.d. ≤ 12° • depth ≥ 300 m, and distributed over a depth range ≥ 300 m	• ≥ 4 hydrofrac orientations in a single well with s.d. ≤ 20° • depth ≥ 100 m, and distributed over a depth range ≥ 200 m	• ≥ 3 hydrofrac orientations in a single well with s.d. ≤ 25° • depth ≥ 30 m, and distributed over a depth range ≥ 100 m	• Single hydrofrac orientation	• Wells in which only stress magnitudes are measured, without information on orientations
Overcoring (OC) and Borehole Slotter (BS)		• ≥ 11 measurements with depth ≥ 300 m and s.d. ≤ 12°	• ≥ 8 measurements with depth ≥ 100 m and s.d. ≤ 20°	• ≥ 5 measurements with depth ≥ 30 m and s.d. ≤ 25°	• ≥ 2 measurements with depth ≥ 10 m and s.d. ≤ 40°	• < 2 measurements or depth < 10 m or s.d. > 40° • Measurements in boreholes extending less than two excavation radii from the excavation wall • Distance to topographic features less than three times the height of the topographic feature
Fault Slip (GF)		• Inversion of ≥ 25 fault-slip data with a fluctuation ≤ 9° for ≥ 60% of the whole dataset	• Inversion of ≥ 15 fault-slip data with a fluctuation ≤ 12° for ≥ 45% of the whole dataset	• Inversion of ≥ 10 fault-slip data with a fluctuation ≤ 15° for ≥ 30% of the whole dataset • Attitude of fault and primary sense of slip known, no actual slip vector	• Inversion of ≥ 6 fault-slip data with a fluctuation ≤ 18° for ≥ 15% of the whole dataset • Offset core holes or quarry popups • Postglacial surface fault offsets	-
Volcanic Vent Alignment (GVA)		• ≥ 5 Quaternary vent alignments or "parallel" dikes with s.d. ≤ 12°	• ≥ 3 Quaternary vent alignments or "parallel" dikes with s.d. ≤ 20°	• Single well-exposed Quaternary dike • Single alignment with ≥ 5 vents	• Volcanic alignment inferred from < 5 vents	-
Petal Centerline Fractures (PC)		-	-	• Mean orientation of fractures in a single well with s.d. ≤ 20°	-	-

Updated quality-ranking scheme for focal mechanism solutions

The majority of earthquake focal mechanism solutions in the WSM database are derived from single seismic events (denoted as FMS). Due to the expansion of the global seismic network and regional broadband networks the number and quality of earthquake focal mechanism solutions increased significantly in the last decade. Furthermore, new techniques have been developed that allow to determining focal mechanism solutions for earthquakes with smaller magnitudes [e.g. *Barth et al.*, 2007]. This significant increase of earthquake focal mechanism solutions allows the application of formal stress inversion techniques in which a large number of single event solutions are used to better estimate the principal stress orientations and relative stress magnitudes [e.g. *Hardebeck*, 2004; *Kastrup et al.*, 2004; *Toussaint et al.*, 2004]. The most common inversion techniques were developed by *Angelier* [1979], *Gephart and Forsyth* [*Gephart and Forsyth*, 1984; *Michael*, 1984], *Forsyth and Gephart* [*Gephart and Forsyth*, 1984; *Michael*, 1984], and *Rivera and Cisternas* [1990].

In order to account for this development, the WSM team refined and restructured the WSM quality-ranking scheme for focal mechanism solutions (FM*) and added the new subtype FMF for stress data records from formal stress inversions. Since formal inversions minimize the difference between earthquake slip direction and maximum shear stress the result of the inversion gives a standard deviation or average misfit angle from the minimization procedure. These and the number of focal mechanisms are used for the inversion to quality-rank the resulting stress orientation (Table 2).

The quality of a formal inversion cannot be inferior than B-quality (± 20°). A higher average misfit angle or standard deviation would be in conflict with the C-quality (± 25°) that is per default assigned to all data records from FMS data (Table 2). If the result of a formal inversion is not better than the quality resulting from single focal mechanism solutions one has to assume that either the binning is not appropriate (i.e. the assumption made for the formal inversion that all events in a bin are driven by the same stress tensor is violated) or that the quality of the incorporated focal mechanism solutions is poor.

Furthermore, the original average focal mechanism solution (FMA) data type that formerly included formal inversions is restructured. This FMA data type now consists of stress data records from averaged or composite focal mechanisms only. Since these two methods do not take into account the conceptual difference between the stress tensor and the moment tensor they might be even less precise in fault plane orientations than FMS and thus are assigned to D-quality (reliable within ± 40°).

2.2 Spatial variability of stress pattern

Since the first WSM database release in 1992, there has been an increase from ~7700 to 21,750 stress data records in 2008. Almost 17,000 of these data records have A-C quality and are considered to record the S_H orientation to within ± 25°. The last ten years has also witnessed a ma-

jor increase in the amount of closely spaced data records from numerous sedimentary basins that allows a more detailed examination of 'third-order' stress patterns of 1-100 km spatial wave-length [*Heidbach et al.*, 2007c; *Tingay et al.*, 2005b]. These third-order stress patterns can be generated by local density and strength contrasts, basal detachment, basin geometry, topography and active faulting [e.g. *Bell*, 1996a; *Müller et al.*, 1997; *Heidbach et al.*, 2007c].

In the substantially smaller WSM dataset available in 1992 third-order stress patterns were either not observed or smoothed out and ignored [*Heidbach et al.*, 2007c]. For example, *Müller et al.* [subm.] discuss the detailed stress pattern and its sources in Romania. They note that earlier stress analysis in Romania overly smoothed this stress data [*Bada et al.*, 1998] using a smoothing radius of > 200 km to estimate a regional stress pattern. However, the smoothed stress field has a mean deviation of > 40° from the observed S_H orientation. The resulting mean S_H orientation in Romania is N70° with a standard deviation of 59.5° clearly indicating that a smoothing radius > 50 km is not justified [*Müller et al.*, subm.]. The results show that there is even no regional trend in the observed S_H orientation in Romania, but that the stress pattern has short spatial wave-lengths in the order of 70 km. This indicates that the crustal stress state is probably close to lithostatic and even small local stress sources contributions can have a major impact on the local S_H orientation [*Heidbach et al.*, 2007c; *Müller et al.*, subm.].

The first quantitative statistical analysis of the global stress pattern using the standard deviation as a measure for the wave-length was conducted by *Coblentz and Richardson* [1995]. Their study investigated the spatial wave-length of the stress pattern by estimating the mean S_H orientation for 5° × 5° bins using a subset with 4527 A-C quality stress data records from the WSM 1992 database release. In their statistical analysis *Coblentz and Richardson* [1995] rejected the null hypothesis that a stress pattern exists in the bins when the standard deviation of the mean S_H orientation exceeds 25°. As a result, they found that only half of the 382 bins that contained two or more stress data records pass the null hypothesis. This indicates that in the remaining bins the stress pattern is probably controlled by regional and local stress sources. However, their work did not quantify the varying spatial wave-length of the stress pattern, but provides only an estimate whether the mean S_H orientation within a bin is random or not. The fixed bin size of 5° × 5° is equivalent to a constant smoothing radius of approximately 250 km.

Aim of the following analysis is to estimate the wave-length on a global 0.5° grid. In contrast to the work of *Coblentz and Richardson* [1995] variable smoothing radii are used. This allows determining the appropriate smoothing radius for the global grid. As a result, we obtain a global stress map that displays both, the mean S_H orientation on a 0.5° grid and a contour map illustrating the spatial wave-length of the stress pattern.

Spatial wave-length analysis procedure

For the analysis I use a subset of with 11,347 A-C quality data records from the WSM 2008 database release (Figure 3). This data set is two and a half times the number of S_H orienta-

tions used in the analysis of *Coblentz and Richardson* [1995] and the purely qualitative analysis of *Zoback* [1992]. Using this dataset I calculate for a global 0.5° grid the mean S_H orientation that is weighted by quality of the stress data record and its distance to the grid point as well as the circular variance of the mean S_H orientation. I start with a smoothing radius of 1000 km that is then decreased in steps of 100 km until the maximum smoothing radius r_{max} for which the circular variance is < 25° is determined. However, I only plot the mean S_H orientation when at least five data records are within r_{max}. The resulting smoothed global stress map displays both the mean S_H orientation and colour coded the smoothing radius r_{max}.

Stress data are weighted by their quality (w_Q = 1/15 for A-, w_Q = 1/20 for B-, and w_Q = 1/25 for C-quality data) and their inverse distance to the grid point (w_D = min(1/D, 1/20) km, where D is the distance between the data location and the grid point) for the computation of average S_H orientation and r_{max}. The minimum value of w_D = 20 km that is allowed for the distance weight is necessary in order to avoid an over-representation of data records that are located close to the grid point during calculation of the mean S_H orientation. Following *Mardia* [1972] the mean S_H direction θ_G results from the single azimuths θ_i of the N data records located within the search radius by the following relations ($\theta_i \in [0°,180°]$):

$$w_i = w_Q w_D \tag{2.1}$$

$$Z = \sum_{i=1}^{N} w_i \tag{2.2}$$

$$\bar{C} = \frac{1}{Z}\sum_{i=1}^{N} w_i \cos 2\theta_i \tag{2.3}$$

$$\bar{S} = \frac{1}{Z}\sum_{i=1}^{N} w_i \sin 2\theta_i \tag{2.4}$$

$$\theta_G = \frac{\arctan 2(\bar{S}, \bar{C})}{2} \mathrm{mod} 180° \tag{2.5}$$

The circular variance is

$$s_G = \frac{\sqrt{-2\log_e \sqrt{\bar{C}^2 + \bar{S}^2}}}{2} \cdot \frac{180°}{\pi} \tag{2.6}$$

Using $\bar{R} = \sqrt{\bar{C}^2 + S^2}$, the circular variance is

$$s_G = \frac{\sqrt{-2\log_e \bar{R}}}{2} \cdot \frac{180°}{\pi} \tag{2.7}$$

A circular variance of $s_G = 25°$ corresponds to $\bar{R} = 0.7$ which is the value used by *Coblentz and Richardson* [1995] to discriminate between small and large dispersion of the stress orientations within each one of their 5° × 5° bins.

In my analysis for each grid point the spatial wave-length is defined as the maximum search radius for which the circular variance $s_G < 25°$ and when the number of data records is N within the search radius is ≥ 5. If for a grid point the search radius of 100 km still results in $s_G > 25°$ the search radius is not further decreased, but "< 100 km" is defined to be the spatial wave-length provided that there are still minimum five data records within the 100 km search radius.

Results

The results of this statistical analysis is presented with stress maps that display both, the mean S_H orientation that results from the maximum smoothing radius r_{max} for which the standard deviation is < 25° and the colour-coded r_{max} (Figure 4 and 5). Blue colours indicate that the stress pattern is of regional to local spatial wave-length (second- to third-order; $\leq$ 400 km); yellow to red colours indicates regional to plate-wide spatial wave-length of > 400 km (first- to second-order). Qualitatively the results are very similar to the principal findings of *Coblentz and Richardson* [1995]. Large areas show long spatial wave-length of the stress patterns, such as in North America and NE Asia (Figures 4 and 5). Short spatial wave-length stress patterns prevail in a wide variety of areas, particularly in the Basin and Range area, central South America, Western Europe, the Caucasus region, Himalaya region, and SE Asia (Figure 4). Also the mean S_H orientations presented on a 2.5° global grid in Figure 4 shows very similar stress pattern to the ones presented in *Coblentz and Richardson* [1995] and qualitatively discussed by *Zoback* [1992] and *Zoback and Zoback* [1991; *Zoback and Zoback*, 1980; *Zoback and Zoback*, 1989].

Short spatial wave-lengths correlate well with topography (Alps, Andes, Basin and Range, Caucasus, and Himalaya) and with plate boundary zones where along strike the style of the plate boundary type varies significantly (Central America, Mediterranean, and SE Asia). There is often a correlation between data density and short spatial wave-lengths, with many regions that have high resolution stress datasets exhibiting scattered stress orientations (Figure 4a). However, there are also areas with long spatial wave-length stress pattern where data density is high (California, NW and SE of North America, NE Asia). The degree of correlation between data density and short spatial wave-lengths is probably due to the higher disposability of

Figure 4 (next two pages). Global map of the stress pattern wave-length. (A) Points indicate the location of the used data set with 11,346 stress data records from the WSM database release 2008. (B) Grey lines represent the mean orientation of the maximum horizontal compressional stress (S_H) calculated quality and inverse distance weighted and averaged over the search radius indicated by the colour code.

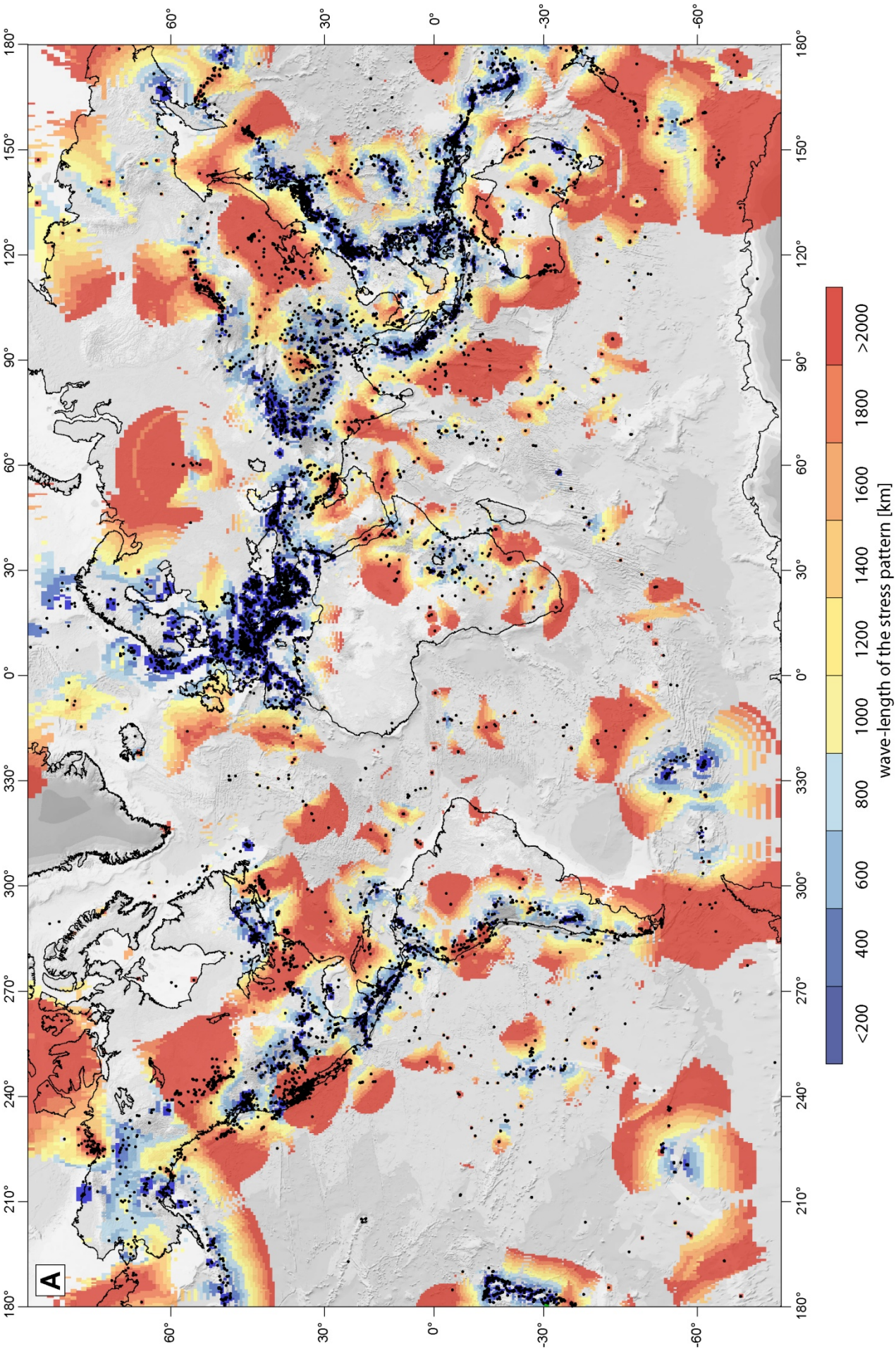
60°
30°
0°
-30°
-60°
180°
150°
120°
90°
60°
30°
0°
330°
300°
270°
240°
210°
A
<200
400
600
800
1000
1200
1400
1600
1800
>2000
wave-length of the stress pattern [km]

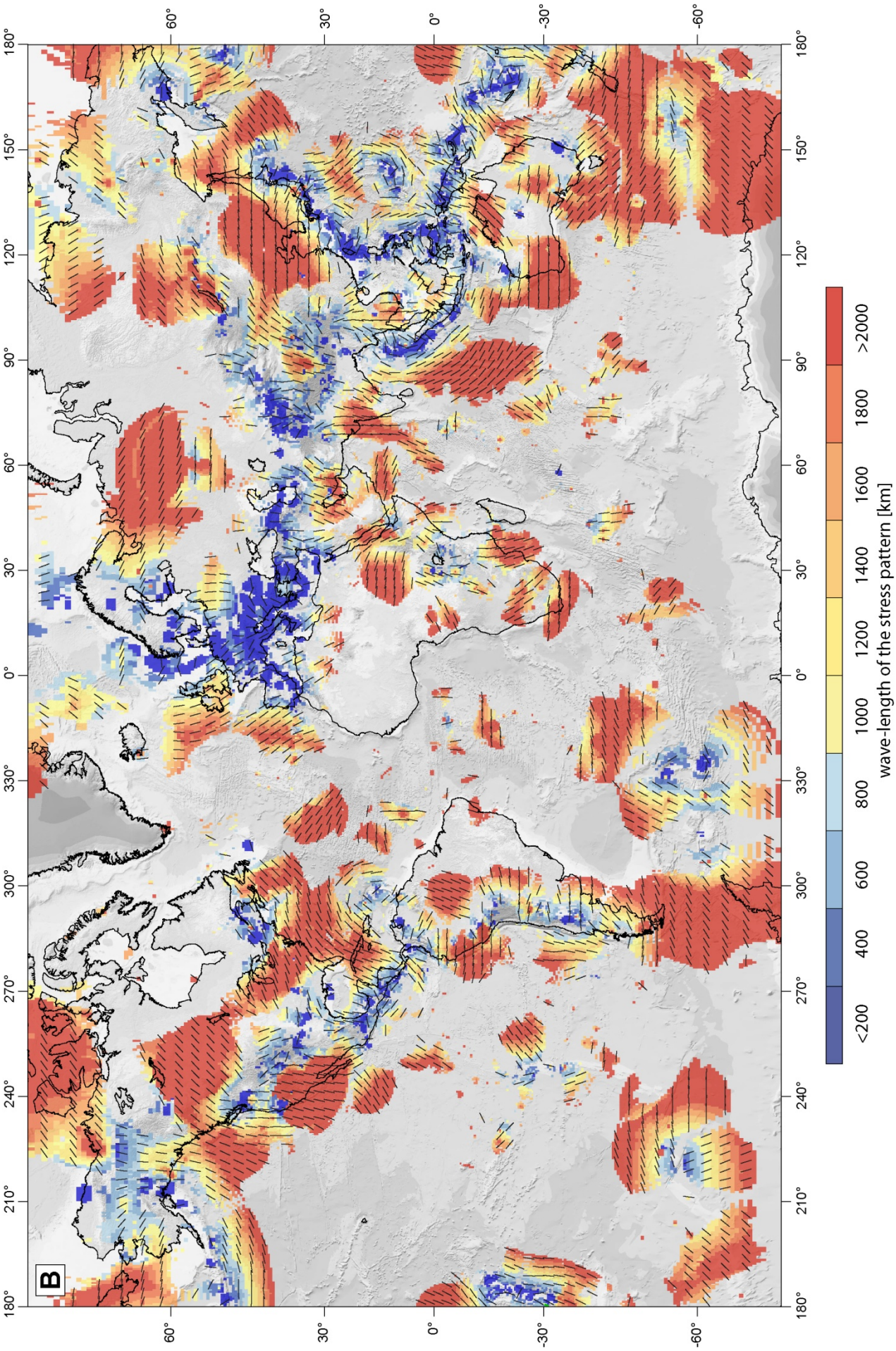
B
60°
30°
0°
-30°
-60°
180°
150°
120°
90°
60°
30°
0°
330°
300°
270°
240°
210°
wave-length of the stress pattern [km]
<200
400
600
800
1000
1200
1400
1600
1800
>2000

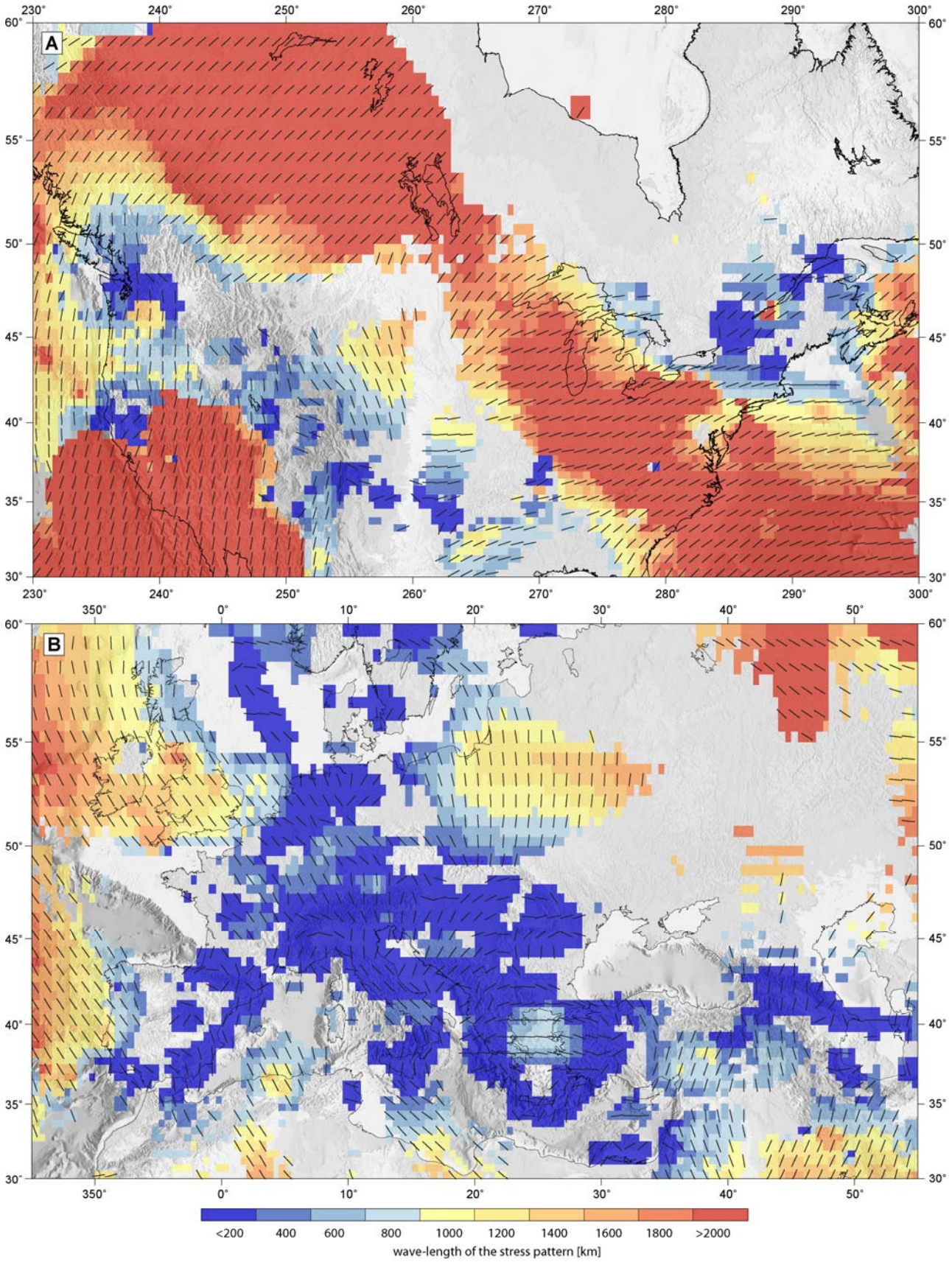

Figure 5. Maps of the wave-length of the stress pattern; same legend as in Figure 4. (A) North America: Note the large areas with long spatial wave-length stress pattern except the areas of the Basin and Range. (B) Western Europe: Note that only offshore in the west and east of the Tornquist-Teissyre Zone that marks the border to the East European carton the stress pattern has long wave-length. In central Europe and the Mediterranean the prevailing stress pattern shows short wave-length indicating that regional to local stress sources contribute significantly to the mean S_H orientation.

stress data in tectonically active regions and, at the same time, that these areas have intra-plate stress sources due to topography, density contrasts, and strength anisotropies. The widespread occurrence of mean S_H rotations on short spatial scales indicate that second- and third-order sources of stress have a major impact on the stress pattern.

Figure 5 displays a more detailed stress map for North America and Western Europe. As previously mentioned, the stress pattern in North America exhibits a long spatial wave-length except in the Basin and Range and NE America (Figure 5a). In contrast to this Western Europe exhibits very short spatial wave-lengths (< 100 km) except for England, Wales, Ireland and in the area east of the Tornquist-Teissyre Zone that separates Western Europe from the East European Craton (Figure 5b). The widespread prevalence of low smoothing radii and highly variable mean S_H orientations in Western Europe emphasizes that the stress pattern can be controlled by both complex plate boundary forces and more localized sources of intra-plate stress (particularly from regions that have been recently tectonically active). For example, in western Europe the Moho depth has large variations [*Tesauro et al.*, 2008] and the southern plate boundary in Europe is extremely complex, consisting of continental collision, subduction, back-arc and young spreading and major strike-slip faults [*Dewey et al.*, 1989; *Heidbach and Drewes*, 2003; *Malinverno and Ryan*, 1986; *McKenzie*, 1972; *Westaway*, 1990; *Ziegler*, 1988]. Furthermore, the intra-plate region of Europe has been significantly affected during the Cenozoic by the development the Alps, Rhine Graben and glacial rebound.

Discussion and conclusions

In comparison to *Coblentz and Richardson* [1995] I used in for my quantitative statistical analysis of the wave-length of the stress pattern two and a half times the data records and a different binning scheme, i.e. variable smoothing radii instead of a fixed 5° × 5° bin. Surprisingly, the mean S_H orientations that resulted from the work of *Coblentz and Richardson* [1995] are remarkably similar to those of the analysis presented here. However, due to the greater spatial coverage this analysis also provides mean S_H orientations in places offshore Western Europe, Northern Africa, SE Asia, the western Pacific plate and Siberia. I use for the analysis the same threshold value for the standard deviation (25°) as was used in the study by *Coblentz and Richardson* [1995]. However, the 5° × 5° bins used in the *Coblentz and Richardson* [1995] study are quite large (approximately 550 km N-S) and, as such, are much bigger than the adequate smoothing radius observed in many regions herein. Indeed, our analysis of the stress patterns of western Europe, Alaska and the Aleutians, the southern Rocky Mountains, Scandinavia, most of the Himalayas, and Indonesia reveal shorter wave-length stress patterns, in the order of less than 100 km, that could not be detected with the analysis of *Coblentz and Richardson* [1995].

The earlier visual and statistical analyses and interpretations of *Müller et al.* [1992], *Zoback* [1992], and *Coblentz and Richardson* [1995] led to the conclusion that consistent S_H orientations exist across broad regions of plate-wide dimensions and that the S_H orientations are the

result from far-field plate boundary forces that are transmitted throughout the intra-plate region. From the shorter spatial wave-lengths of the stress pattern resulting from this study I conclude that the forces that are transmitted across the plates either act over shorter distances and/or that local stress sources are in the order of the magnitudes of the long spatial wave-length stress sources.

2.3 Examples of stress pattern and stress sources

From the global statistical analysis presented in the previous section it became clear that spatial scales play a critical role in understanding the crustal stress state. Stress indicator provide information on the stress over a specific volume of rock ranging from cubic kilometres for earthquakes, to cubic centimetres or metres for breakouts, hydraulic fracturing and overcoring [*Ljunggren et al.*, 2003].

As the stress tensor is truly defined as the stresses acting upon a point in a continuum and hence, when examining the origin of stress orientations, it is critical to note that the observed stress orientations and stress magnitudes is a superposition of forces that act at spatial scales ranging from very large (e.g. tectonic plate) to very small (e.g. stress concentration at fracture tips) (Table 3).

Table 3. Sources of crustal stresses on different spatial scales

Source	Examples	Effect on stress field	Length scale
plate boundary forces	ridge push, collision, subduction, mantle drag	*1st-order control*	100s-1000s of km
large volume forces	mountain ranges, isostatic compensation, continent-ocean transition, Moho, lithosphere thickness variations, large basins	*2nd-second-order control* rotation of stress field due to mechanical and density contrasts between units	100s of km
flexural forces	deglaciation, subduction zones	*2nd-order control*	100s of km
detachment zones	evaporites, overpressured shales, low angle faults	*2nd- to 3rd-order control* changes mechanically overlying rocks from 1st- or 2nd-order stress field	10s-100s of km
strong earthquakes	plate boundaries, major intra-plate faults	*2nd- to 3rd-order control* temporal changes linked to the seismic cycle	10s-100s of km
geological structures	faults, fractures, diapirs, folds	*3rd-order control* change due to mechanical and density contrasts between units	0.001-10 km

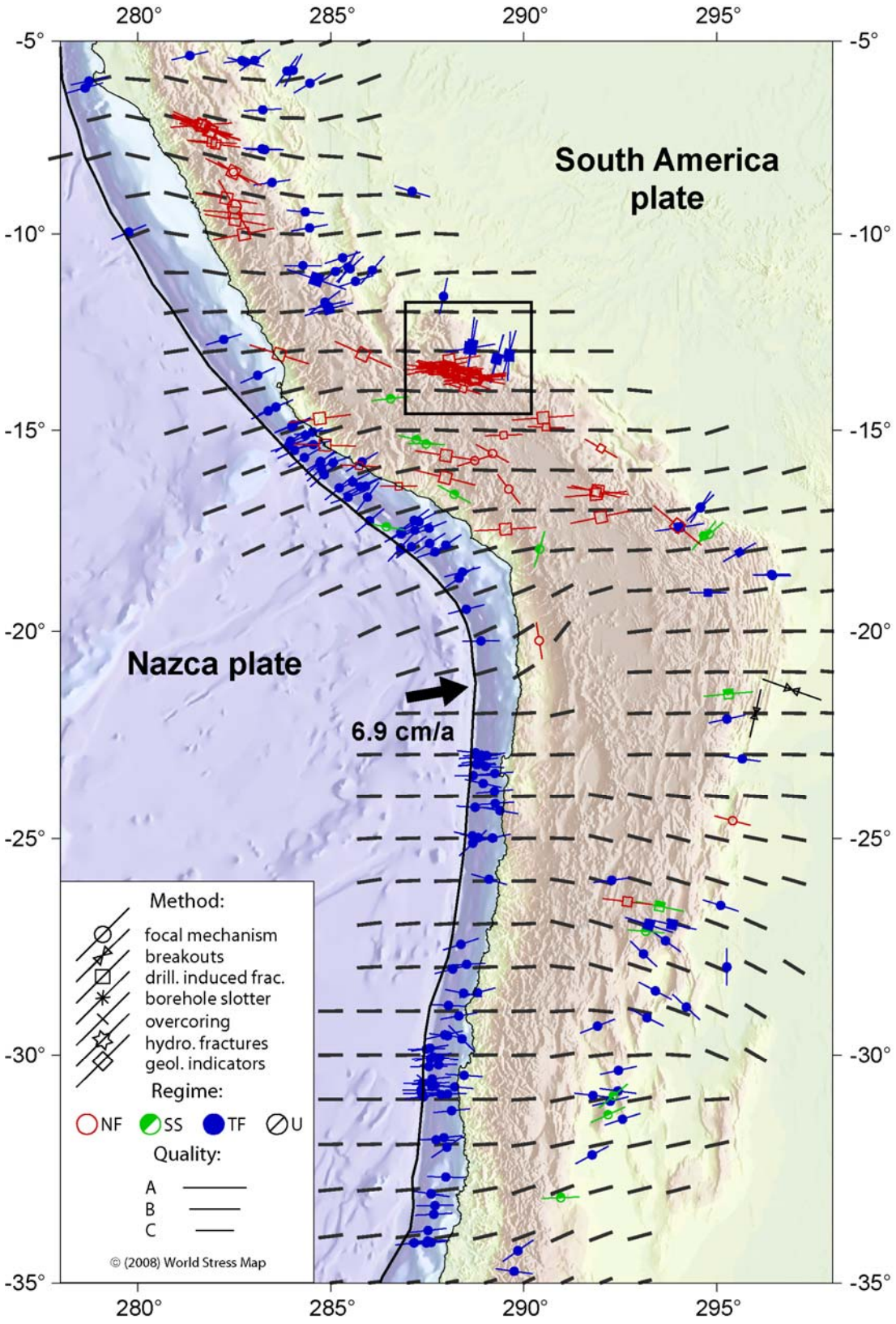

Figure 6. Stress Map of western South America using stress WSM data records with of A-C quality excluding Possible plate Boundary Events (PBE) and normal faulting regime events due to down-bending of the subducting Nazca plate. Lines represent orientation of maximum horizontal compression stress (S_H), line length is proportional to quality. Colours indicate stress regimes; red is normal faulting (NF), green is strike-slip faulting (SS), blue is thrust faulting (TF), black is unknown regime (U). Black lines on a 1° grid represent the mean S_H orientations estimated with a smoothing radius of 300 km using a smoothing algorithm described in *Müller et al.* [2003] and that is implemented in the software CASMI [*Heidbach and Höhne*, 2008; *Heidbach et al.*, 2008b]. Note the deviation between the smoothed S_H orientation and the WSM data records in the box up to 90° S_H rotation within 100 km.

In the following sub-sections I present four examples in order to review and summarise the main factors controlling the crustal state of stress beginning with the plate boundary forces and ranging progressively down to the smaller spatial scales and localised (yet often highly significant) impact of geological structures.

Plate-wide scale: South America

Stress fields observed over very wide regions (100s to 1000s of kilometres) and to large depths in the lithosphere (10s of kilometres) are the result of large 'far field' forces acting at the plate boundary or major intra-plate features (Figure 2) [*Sbar and Sykes*, 1973; *Zoback et al.*, 1989]. Plate boundary forces, such as mid-ocean ridge push and resistance at continental collision zones, provide the 'first-order' or 'primary' stress field in the intra-plate lithosphere [*Richardson*, 1992; *Zoback*, 1992]. Major intra-plate features, such as mountain ranges, oceanic to continental lithosphere transitions, major crustal fault zones and regions of lithospheric bending or large-scale deglaciation, give rise to major forces that cause the 'second-order' or 'secondary' stress field [*Richardson*, 1992; *Zoback*, 1992]. An example for such first- and second-order stress sources is the stress pattern of the western South America plate.

Figure 6 presents the smoothed stress field based on 257 WSM data records with A-C quality excluding the normal fault events offshore that are due to the down-bending of subducting Nazca plate. The stress data exhibit a general E-W oriented stress pattern that is controlled by the relative plate motion striking approximately N80°W of the Nazca plate with respect to South America. In the Eastern and Western Cordillera of the Altiplano-Puna plateau S_H is perpendicular to the strike of the Andes, and thrust faulting is the prevailing tectonic regime. In the central Andes the excess of gravitational potential energy due to the 4000-m-high Altiplano-Puna plateau leads to normal faulting regime with S_H oriented parallel to the strike of the Andes (Figure 6).

Regional scale: German Molasse Basin

The stress fields in sedimentary basins are commonly observed to be very similar to the large-scale stress pattern. This is in particular true when mechanical coupling between the sediment layers and the underlying basement is strong [*Tingay et al.*, 2005b; *Tingay et al.*, 2006]. Classical examples for such a strong coupling are the Alberta Basin in North America [*Bell and Gough*, 1979] and the Neuquén Basin in Southern Chile [*Guzman et al.*, 2007]. Hence, the first- and second-order stress sources typically provide the regional or 'background' stress field upon which stresses resulting from other, smaller, sources of stress are superimposed, but often too small to have a major impact on the S_H orientation.

A recent comprehensive study of new borehole data for the German Molasse Basin results in the same conclusion (Figure 7) [*Reinecker et al.*, subm.]. Cause of the stress pattern is the ap-

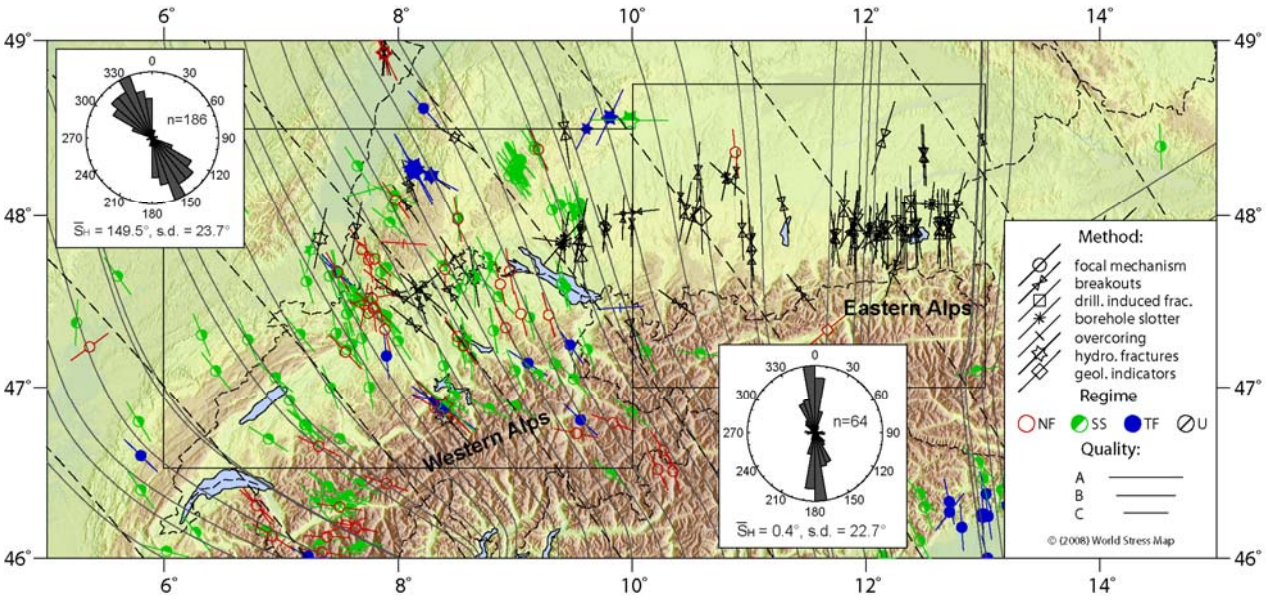

Figure 7. S_H orientations in the Molasse Basin from the WSM 2008 database release (*Heidbach et al.*, 2008c). S_H orientation rotates from N-S in the Eastern Alps (000ºN ± 23º) to NNW-SSE in the Western Alps. Note that the S_H orientation is roughly perpendicular to the topographic front throughout the basin, indicating that forces originate from the gravitational potential energy of the Alps are controlling the Molasse Basin stress field. Thin black lines are the S_H orientation trajectories using a quality and distance weighted approach with a smoothing radius of 100 km.

proximately N-S directed convergence of Africa plate with respect to the Eurasia plate, the indentation of the Adriatic block in between these two major plates and the topography of the Alps [*Jarosinski et al.*, 2006; *Regenauer-Lieb*, 1998].

The borehole breakouts and drilling induced fractures reveal that S_H orientations are highly consistent within the Molasse Basin and that they rotate from N-S in southeast Germany (002ºN ± 19º) to approximately NNW-SSE in southwest Germany and the Swiss Molasse Basin (150ºN ± 24º). The S_H orientation in the Molasse Basin is broadly perpendicular to the strike of the Alpine front, indicating that the stress pattern is probably primarily controlled by topographic body forces rather than plate boundary forces [*Reinecker et al.*, subm.].

Local scale: North German Basin salt diapirs

Mechanical coupling between sediments and basement is not the only control of intra-basin stress pattern. The impact of plate boundary forces and local, e.g. intra-basin forces on the stress field in sedimentary basins is also a function of their relative magnitudes and orientations. In general, far-field stresses have much greater magnitudes than local stresses and dominate the stress field. However, the influence of the stronger, far-field stresses (acting in the basement) can be partially or totally removed from the stresses acting in the overlying sedimentary sequences by deep mechanical detachment zones. Basins that contain some form of basal detachment zone typically exhibit complicated stress patterns due to the dominance of smaller intra-basin sources of stress, whereas basins that are mechanically attached to the basement typically display regionally con-

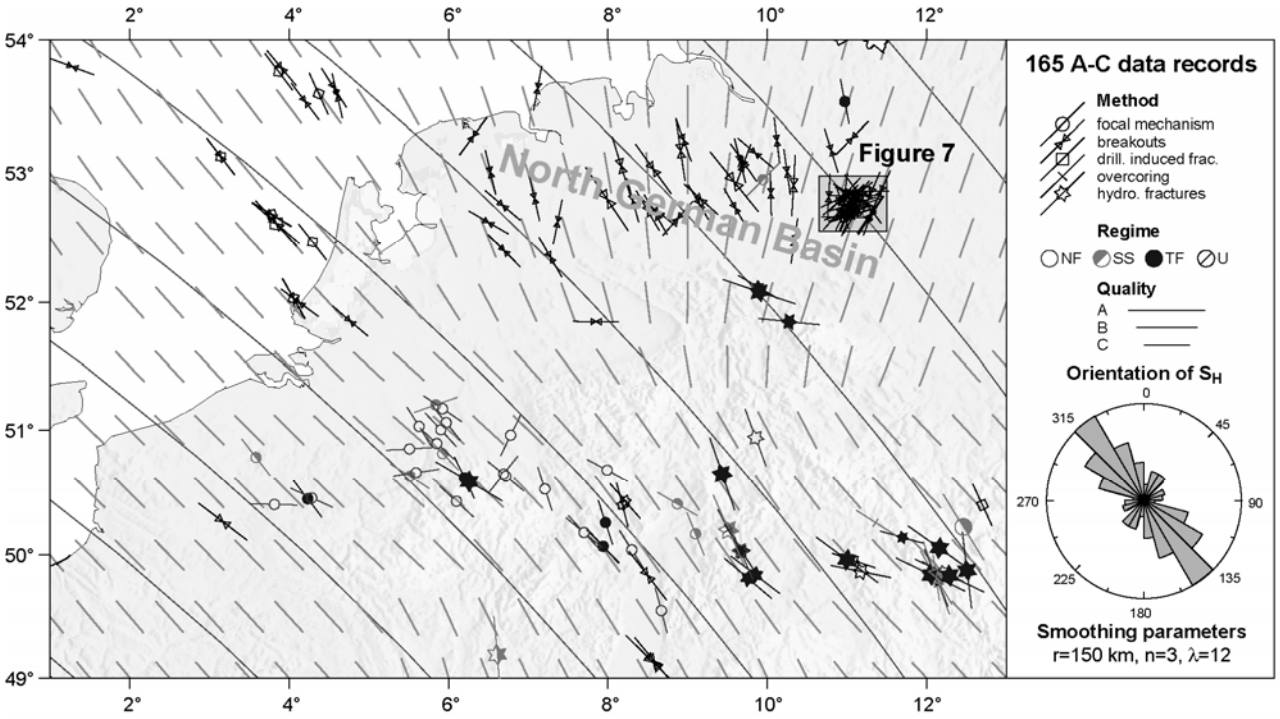

Figure 8. Stress map of northern Germany and the Netherlands. The mean S_H orientation of 144°N is in agreement with the direction of relative plate motion of approximately 137°N between the Africa Plate and the Eurasia Plate (thin lines). However, note the deviation from this trend in the eastern part of the North German Basin where a rotation to NNE is observed. Box indicates location of Figure 9.

sistent stress fields resulting from far-field forces [*Bell*, 1996b].

The North German Basin is an example where the stress pattern deviates from first-order stress source indicated in Figure 8. The stress pattern is fan-shaped rotating clock-wise from NNW is Western part of the basin to NNE [*Grünthal and Stromeyer*, 1994; *Heidbach et al.*, 2007c; *Roth and Fleckenstein*, 2001].

Roth and Fleckenstein [2001] discuss three possible reasons for this regionally differing trend in the eastern part of the North German Basin: (1) the influence of possible displacement along the Trans-European Suture Zone which separates the old East European platform from the younger western European parts of the Eurasia Plate, (2) the local dominance of stresses caused by postglacial rebound, and (3) the northward increase of lithospheric strength below the north-eastern part of the North German Basin possibly acting as a barrier. According to *Heidbach et al.* [2007c] a potential fourth source of the stress field rotation in the North German Basin is the stresses induced by lateral density and strength contrasts across the Sorgenfrei-Teisseyre and Tornquist-Teisseyre zone where crustal thickness increases sharply from about 35 km in the west to 50 km in the East European platform [*Thybo*, 2001]. This increase in crustal thickness may produce enough gravitational potential energy to create compressional stresses perpendicular to the NW-SE striking suture zone that are responsible on the regional scale rotation of the stress field.

Zooming further into the Eastern part of the North German Basin the effect of decoupling due to a salt layer is identified (Figure 9). The Zechstein salt layer with its top at 3.300 m depth

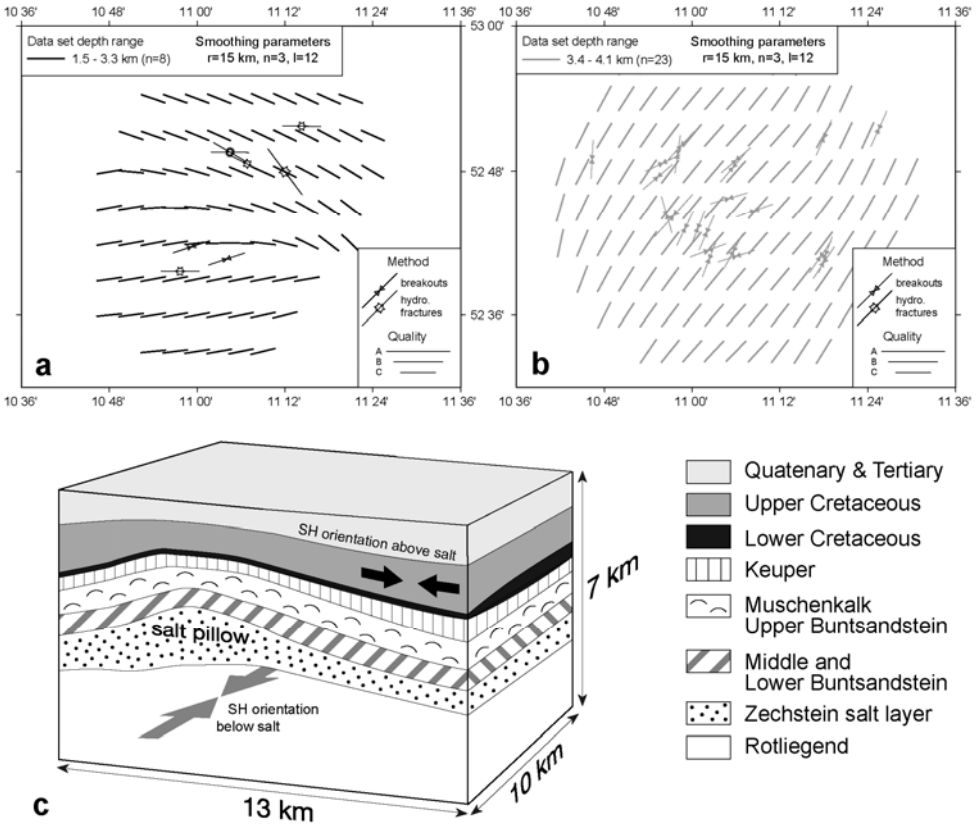

Figure 9. Stress maps at two different depth sections of the eastern part of the North German Basin. Location of stress maps as indicated in Figure 8.(a) Above salt (b) Below salt. (c) Sketch of the layering that results in lateral density contrasts controlling the S_H orientation. Note the large difference of mean S_H orientation above salt and below salt. The salt layer is not capable to transfer far-field stresses from the basement into the upper layers. Therefore, small lateral density contrast control the S_H orientation.

does not significant transfer stresses from the far-field controlled basement stress pattern into the layers above the Zechstein.

Such basal detachment zones occur due to the presence of mechanically 'weak' or ductile (e.g. having a high Poisson's ratio) material that is unable to effectively transmit shear stresses from the rocks below the detachment into overlying sequences. Basal detachment zones in sedimentary basins typically include evaporite horizons, sequences of highly overpressured shales and low angle fault zones (particularly fault zones containing high magnitude overpressures) [*Bell*, 1996b]. Thus, detachment zones may act regionally, when detachment horizons are basin-wide (e.g. overpressured prodelta shales), or only over small regions if the detachment surface is only locally present (e.g. faults, localised evaporites).

Geological Structures

The localised S_H reorientations in the North German Basin indicate that the present-day S_H orientation can be strongly influenced by existing geological structures such as faults and salt diapirs. Indeed, numerous authors have observed local stress variations, of the order of a few metres to kilometres near faults, fractures folds and diapirs [e.g. *Bell*, 1996b; *Roth and Fleck-*

enstein, 2001; *Yale*, 2003]. The change of S_H orientation near geological structures results from structures acting as a mechanical discontinuity. For example, an 'open' or very 'weak' fracture in the subsurface will act as a free surface and is unable to sustain shear stresses. As a result, the S_H orientation must be locally re-oriented in the vicinity of the fracture. Similarly, stresses will be locally deflected or 'refracted' near the boundary between mechanical contrasts [*Zhang et al.*, 1994]. It is predicted that the S_H orientation will be deflected sub-parallel to mechanically 'weak' structures (e.g. salt or overpressured shale diapirs, open fractures and weak fault zones), but be deflected perpendicular to mechanically 'stiff' structures (e.g. cemented faults and fractures or igneous intrusives [*Bell*, 1996b; *Zhang et al.*, 1994]. The scale at which structures influence the stress field will relate to the degree of the mechanical contrast, the size of the structure and the orientation of the structure relative to the far-field stresses. Greater mechanical contrasts result in bigger deflections of the principal stress axes, whereas larger structures have a broader impact on the stress field. Small fractures or faults may influence the stress field within just a few centimetres of the structure, whereas the influence of larger structures, such as folds, diapirs and major faults, may extend tens of metres to several kilometres from the structure. However, the stress orientation will only be slightly deflected if one stress orientation is approximately perpendicular to the surface of the mechanical contrast.

Conclusions

The stress patterns presented in the examples allow four major conclusions: (1) The plate-wide and regional stress pattern is controlled by the plate boundary forces confirming the findings from earlier work using the WSM database. (2) The contemporary stress pattern in the WSM database reveals also third-order effects on small spatial scales. Zooming into the western European stress map (Figures 8 and 9), where data density is high, we identified areas where regional to local effects control the stress pattern at different spatial scales. (3) Additional stress sources are necessary (i.e., forces which are not related to plate boundaries) in order to explain regional to local-scale stress patterns in regions where the contribution of plate boundary forces is small. In dependence of the stress magnitudes of the plate-wide-scale stress field regional and local stress sources can control the S_H orientation and the tectonic regime. The various stress sources and the spatial scales on which they are effective are summarized in Table 4. (4) The examples for the stress changes throughout geological times reveal that an integrated analysis of the WSM data with other information such as the geological record and the geodynamic evolution gives new insights into the relative importance of the sources of stress and their changes through geological times.

Table 4. Observed and modelled orientation of maximum horizontal compressional stress S_H.

Name	Observed S_H orientation	Depth range of measurements	Modelled S_H orientation
Halmern Z1	20°	no details, sub-salt	15°
Munster-SW Z1	126°	no details, sub-salt	20°
Wietzendorf Z3	175°	4360 - 4651 m	0°

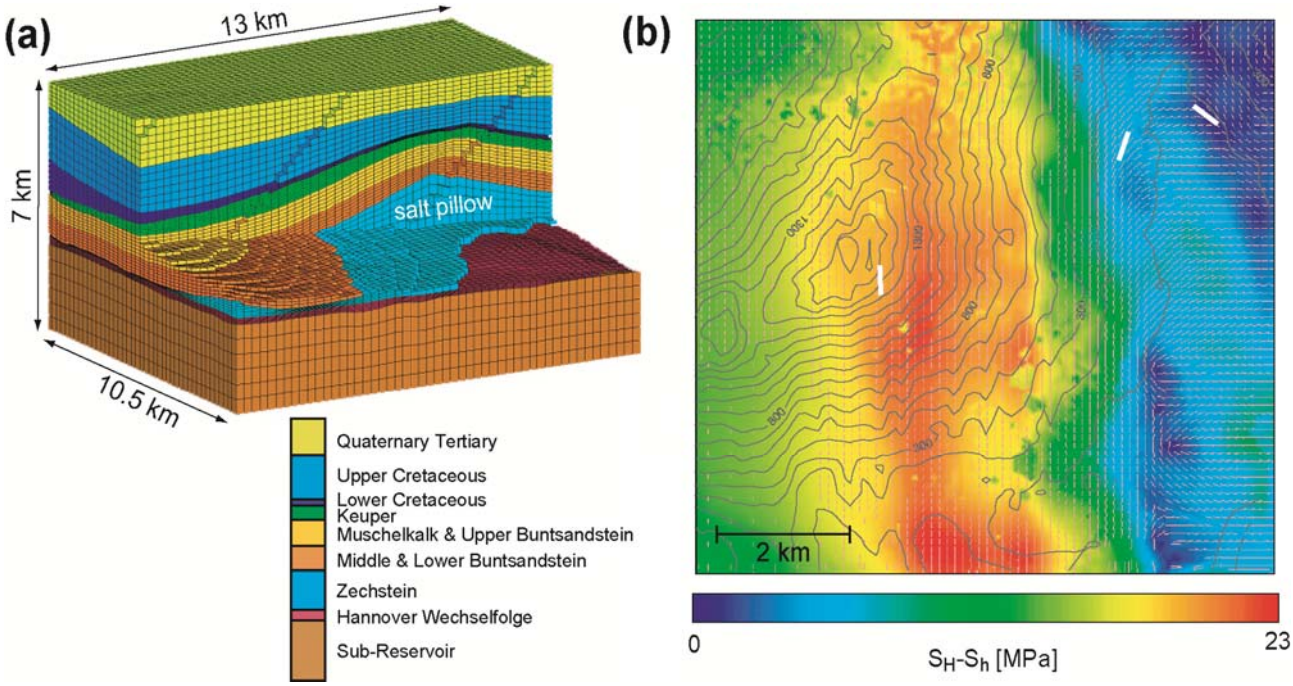

Figure 10. (a) Cutaway oblique view of the 3D Finite Element mesh with c. 125,000 hexahedral linear elements. Model rheology is linear elastic, boundary conditions are an N-S oriented regional stress field and gravity. Density and mechanical rock properties vary according to the numbers given in [*Fleckenstein et al.*, 2004]. (b) Comparison of observed (white line symbols) and modelled (short red lines) S_H orientation at 4444 m depth (intra-Rotliegend) from the northern section of the Finite Element model. Grey contours are the Zechstein isopatches in m; north is the vertical direction. Area is ~50 km south of Hamburg. White lines indicate the observed S_H orientations in the wells Wietzendorf Z3, Munster-SW Z1, and Halmern Z1 (Details are given in Table 3). Base Zechstein is between 2600 m and 4100 m. Contours lines in (b) indicate the thickness of the Zechstein layer. Results are plotted at 4444 m, i.e. below the Zechstein in the Rotliegend layer. Gravity and 2 m N-S compression of the model. Salt density is with 2220 kg/m^3 about 15% less dense than the Keuper and Muschelkalk above.

3 Temporal changes of crustal stress

As the crustal stress field is always subjected to geodynamic processes the stress pattern also changes with time. The amount and speed of change depends on the prevailing stress state and on the effectiveness of the geodynamic process. When the stress state is close to lithostatic, even small changes can have a significant impact on the S_H orientation. In general spatially large-scale stress field changes need long-term processes on geological time-scales of several hundreds of thousand to millions of year as exemplified in the following example for South America in section 3.1. On shorter spatial scales also temporally short-term processes such as inter- and co-seismic changes and post-seismic stress relaxation processes can have significant impact on the stress pattern. Section 3.2 presents the inter- an co-seismic stress changes along the Dead Sea fault system for the last 1450 yrs due to tectonic loading from plate motion and due to stress transfer of 14 large historical earthquakes. Section 3.3 focuses on even shorter time-scales of stress changes. Here the results of a numerical model that simulates the stress relaxation after the large M_w 8.4 Arequipa earthquake in Southern Peru from June 2001 are presented. The content of these three chapters is based on the following three publications that are attached as reprints in the appendix of this thesis.

Heidbach, O., Iaffaldano, G., Bunge, H.-P., (2008). Topography growth drives stress rotations in the Central Andes - observations and models. *Geophys. Res. Lett.*, 35, L08301, doi:10.1029/ 2007GL032782.

Heidbach, O., Ben-Avraham, Z., (2007). Stress evolution and seismic hazard of the Dead Sea fault system. *Earth Planet. Sci. Lett.*, 257, 299-312.

Hergert, T., Heidbach, O., (2006). New insights in the mechanism of post-seismic stress relaxation exemplified by the June 23rd 2001 $M_w = 8.4$ earthquake in southern Peru. *Geophys. Res. Lett.*, 33, L02307, doi:1029/2005GL024585.

3.1 Topography growth drives stress rotations

Observations of the convergence rate between the Nazca plate and the South America plate show that it has slowed down from 10.3 ± 0.2 cm/a 10 Ma ago [*Gordon and Jurdy*, 1986] to 6.7 ± 0.2 cm/a at present-day [*Sella et al.*, 2002]. In that time period also most of the Andean topography has developed [*Gregory-Wodzicki*, 2000]. The numerical model of *Iaffaldano et al.* [2006] that couples the global 3D spherical mantle circulation model of *Bunge et al.* [1997] with lithosphere dynamics, shows that this Andean growth is responsible for the slow-down of the convergence rate. In the following research two questions are addressed: (1) Is the model also capable to reproduce the contemporary S_H orientation of western South America and if yes, (2) what was the impact of the growth of Andean topography on the stress pattern.

The comparison of the modelled S_H orientations and the ones from the WSM database reveals that the model that fits the observed convergence rate decrease also matches the S_H orientation from the WSM database (Figure 11a). The quantitative comparison of the contemporary

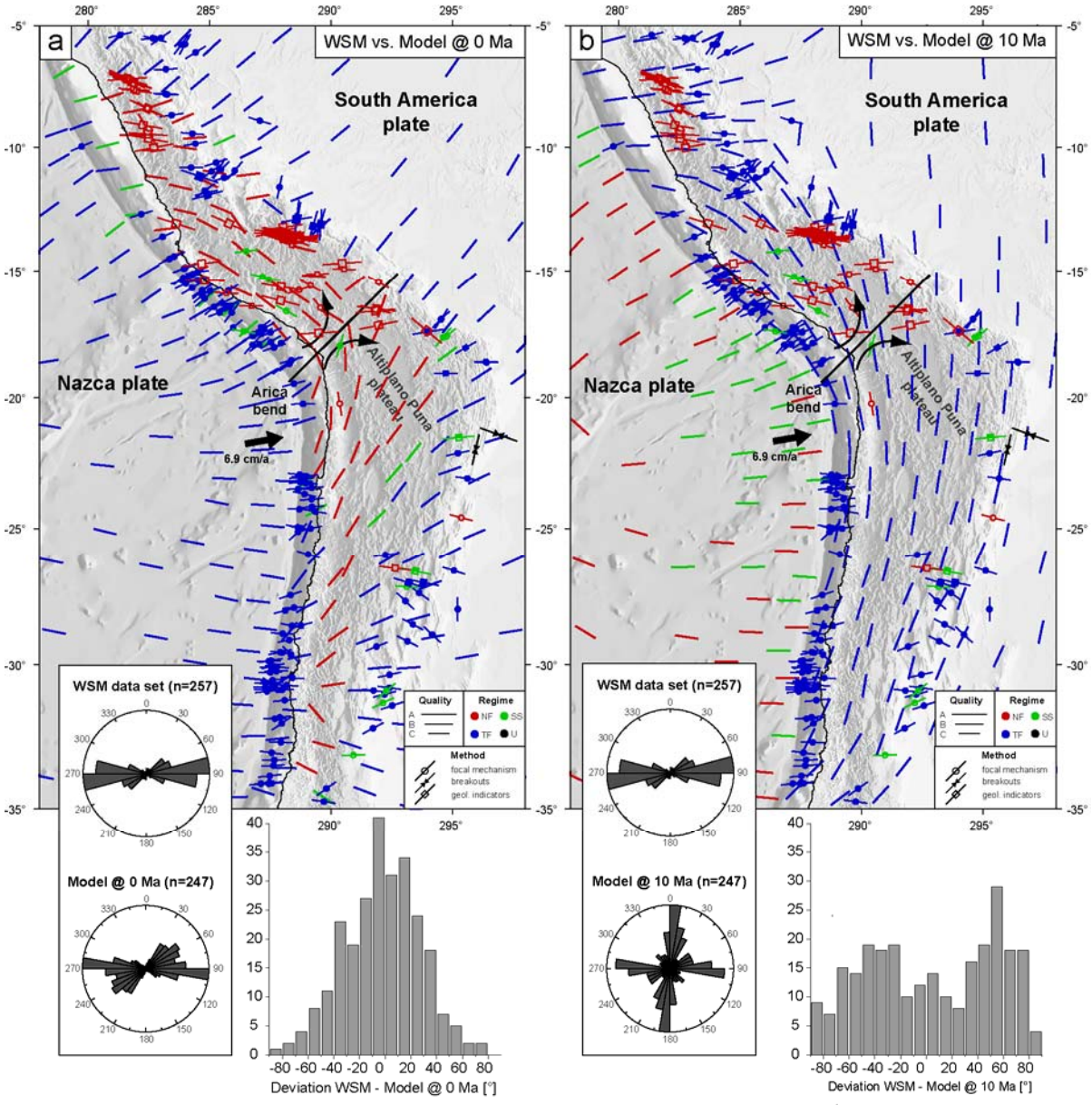

Figure 11. Comparison of model results and WSM data. Lines give the orientation of maximum horizontal compressional stress (S_H). Lines with symbols in its centre are WSM data; the ones without symbols are the numerical model results. Black arrow indicates the convergence of the Nazca Plate with respect to the South America Plate. Histograms display the deviation between the modelled and the WSM S_H orientations. Deviations are calculated at the locations of the WSM data records taking into account the three nearest model results weighted by distance. a) Comparison of WSM data and model results at 0 Ma. b) Comparison of WSM data and model results at 10 Ma. Note that most of the changes occur on the continent and that the stress pattern at 10 Ma is very different on the continents than on the oceanic lithosphere indicating that coupling at the plates interface was significant lower in contrast to today situation. Changes are clock-wise south of the SW-NE striking axis at the Arica bend (black line) and anti-clockwise north of it.

S_H orientations from the WSM with the model results at present-day result in a mean deviation of ± 23.9°. This is within the uncertainties of the A-C quality WSM data which are reliable to within ± 25°. Furthermore, the two observed general trends in S_H orientations and the prevailing tectonic regimes are also well reflected in the model (Figure 11a).

In the model that represents the scenario at 10 Ma the mean deviation between modelled and today's WSM S_H orientations is increased to ± 44.8°, i.e. larger than the uncertainties of the

WSM A-C quality data. The modelled paleostress field exhibits two first-order S_H orientations; a N-S oriented stress field in the South America plate with prevailing thrust faulting and an E-W oriented stress field in the Nazca plate with strike-slip and normal faulting regime (Figure 11b). The histogram of the deviations between observed and modelled S_H orientations at 10 Ma has no clear maximum, but exhibits homogeneous distribution of deviation (Figure 11b).

The model results indicate that the S_H orientations and the tectonic regime changed significantly during the past 10 Ma due to the growth of the Andean topography. S_H orientations rotated counter-clockwise north of an axis located in the Arica bend and a clockwise south of it (Figure 11). This axis coincides with an axis separating rotations of the same sense and similar amount that has been identified from paleomagnetic analysis [*Allmendinger et al.*, 2005, and references given therein].

Discussion and conclusion

In the numerical experiment the cause of the slow-down of the convergence velocity and the change in the stress pattern is due to an increase of resistive forces per unit length in the order of $10^{13}\ N\ m^{-1}$ at the plate interface as a result of the Andean growth. Thus, large topographic features do indeed contribute to lithosphere dynamics by as much as the far-field stresses due to mantle convection. Using the analytical approach of *Sonder* [1990] for the amount of S_H rotation θ' for extensional and compressional tectonic stress regime

$$\theta' = \frac{1}{2}\tan^{-1}\left(\frac{\sin 2\theta}{-\tau/\tau' - \cos 2\theta}\right) \tag{3.1}$$

one can estimate the relative stress increase that is needed for the observed stress rotation of $\theta' = 59°$ at 75.2°W and 15.4°S. Inserting in expression (1) $\theta = 2°$ as the angle between the orientation of the far-field stress at 10 Ma (N137°) and the regional stress anomaly, i.e. the strike of the Andes (N135°) we receive for the stress ratio $-\tau/\tau' = -0.96$. τ is the magnitude of the far-field stress and τ' the magnitude of the regional stress anomaly. Thus, the stress anomaly needed to rotate S_H by $\theta' = 59°$ is of similar magnitude as the far-field stress magnitude at 10 Ma.

It is concluded that the degree of coupling at the plate interface and its time and probably spatial variability are key controls also for the evolution of the stress pattern in the central Andes. A comparison with paleostress data from *Mercier et al.* [1992] shows for some locations good agreement with the model results, but there is also large deviations. These can be due to difficult timing of the paleostress data as well as due to the fact that the model does not take into account the lateral variations of the resistive forces. According to *Lamb* [2006] and *Lamb and Davies* [2003] the thickness of the trench sediments along strike changes significantly. Assuming that sediments have a major impact on the frictional resistance at the plate interface one

can imagine that this contributes to regional variations in the stress pattern in particular at earlier stages of the Andean growth, when the gravitational excess had less impact on the stress pattern.

3.2 Inter- and co-seismic stress changes

Even though stress changes on time-scales of the seismic cycle do not have an impact on the regional scale stress pattern they play a critical role for the earthquake hazard assessment. *Stein et al.* [1997] successfully predicted the location of 1999 Izmit event from numerical simulation of the change of Coulomb Failure Stress due to the westward migrating sequence of 11 large earthquakes along the North Anatolian fault. The change of stress on neighbouring un-ruptured fault segments has a direct impact of the probability of future events. E.g. the co-seismic stresses transfer of the August 1999 Izmit event in Turkey changed the stress field in that way that the Karadere-Düzce fault segment near-by became optimal oriented with respect to the updated stress pattern. As a result an earthquake took place in November 1999 only three month after the Izmit event [*Bohnhoff et al.*, 2006; *Parsons et al.*, 2000]. Thus, the history of the tectonic loading rate and co-seismic stress release is of great importance for time-dependent seismic hazard assessment [*Harris*, 1998; *Parsons*, 2004; *Steacy et al.*, 2005]. When stress changes shift the fault closer to failure by e.g. 0.5 MPa this is equivalent to 50 yrs of tectonic loading assuming a reasonable tectonic loading rate of 0.01 MPa. Vice versa, when stresses are dropped the future event will be delayed. In the following I will summarize the key results of the example of the loading and de-loading history of the Dead Sea fault system from the publication of *Heidbach and Ben-Avraham* [2007].

The Dead Sea fault system (DSFS) represents a continental left-lateral strike-slip fault system which separates the Arabia plate from the Africa plate (Figure 12). The relative displacement rates do not exceed 5 mm/a and are often partitioned to several parallel fault strands. Besides the instrumentally recorded earthquakes of the years 1927 and 1956 14 historical earthquakes with $M_S \geq 6.0$ using various catalogues from year 551 onwards were identified (full reference list is given in the reprint of the paper in the appendix).

The last strong earthquake with $M_S = 7.4$ took place in 1837 in the Hula basin north of the Sea of Galilee. The long recurrence intervals for strong earthquakes in the order of 10^3-10^4 yrs are due to low slip rates along the various DSFS segments. However, the dense population since historical times as well as several paleoseismological and archaeological investigations provide complete catalogues of large historical earthquakes for the last 1500 years for earthquakes with $M_S \geq 6.0$.

The numerical model for the evolution of stress along the DSFS (30.5°N-34.5°N) for the last 1450 years includes the co-seismic stress changes due to a the 14 historical $M_S \geq 6.0$ earthquakes and the tectonic loading rate from relative plate motion. With the numerical results the hypothesis is tested whether the earthquake sequence could have been triggered by the co-seismically induced static stress changes. The stress evolution until year 2005 is calculated

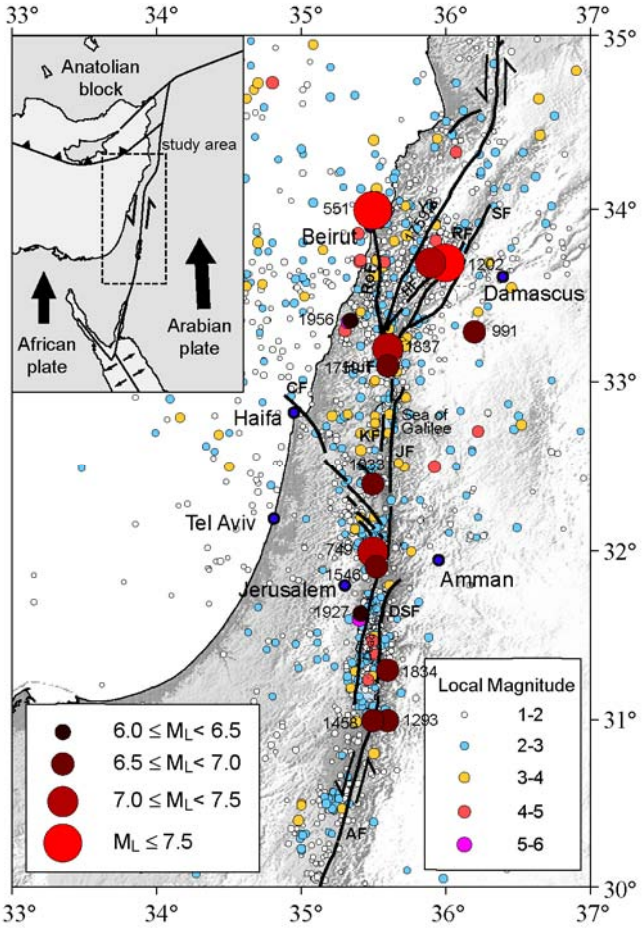

Figure 12. Recorded seismicity of the study area from 1900-2002 (Geophysical Institute of Israel, available online at http://www.gii.co.il). Black lines are the active faults. Abbreviations are: AF = Akar Fault, ArF = Arava Fault, CF = Carmel Fault, DSF = Dead Sea Fault, HF = Hasbaya Fault, HuF = Hula Fault, JF = Jordan Fault, JG = Jordan Gorge, KF = Kinnereth Fault, RoF = Roum Fault, RF = Rachaiya Fault, SF = Serghaya Fault, YF = Yammouneh Fault. Location and year of the 14 historical earthquakes ($M_S \geq 6.0$) along the Dead Sea Fault System (DSFS) of the last 1500 years.

in terms of changes of Coulomb failure stress (ΔCFS) for different time steps taking into account the varying strike of the fault segments.

In contrast to the commonly used ΔCFS representations in map view I calculate ΔCFS only at the faults in one kilometre spacing along strike taking into account the varying orientation of the rupture plane. From these calculations the stress evolution in terms of ΔCFS values at different stages of the historical earthquake sequence is displayed in profiles along the fault strike of the various DSFS segments (Figure 13 for the central segment). Assuming a threshold value of 0.01 MPa the analysis of the ΔCFS values revealed that only about half of the earthquakes could have been triggered from the accumulated stress changes from the previous earthquakes. The total accumulated stress of the 1450 yrs indicates that the present-day stress state at the Jordan segment is the highest (Figure 13). Here, the accumulated ΔCFS is > 4 MPa on a ~90 km segment. According to the empirical relations of *Wells and Coppersmith* [1994] this could result in a $M_S = 7.4$ earthquake.

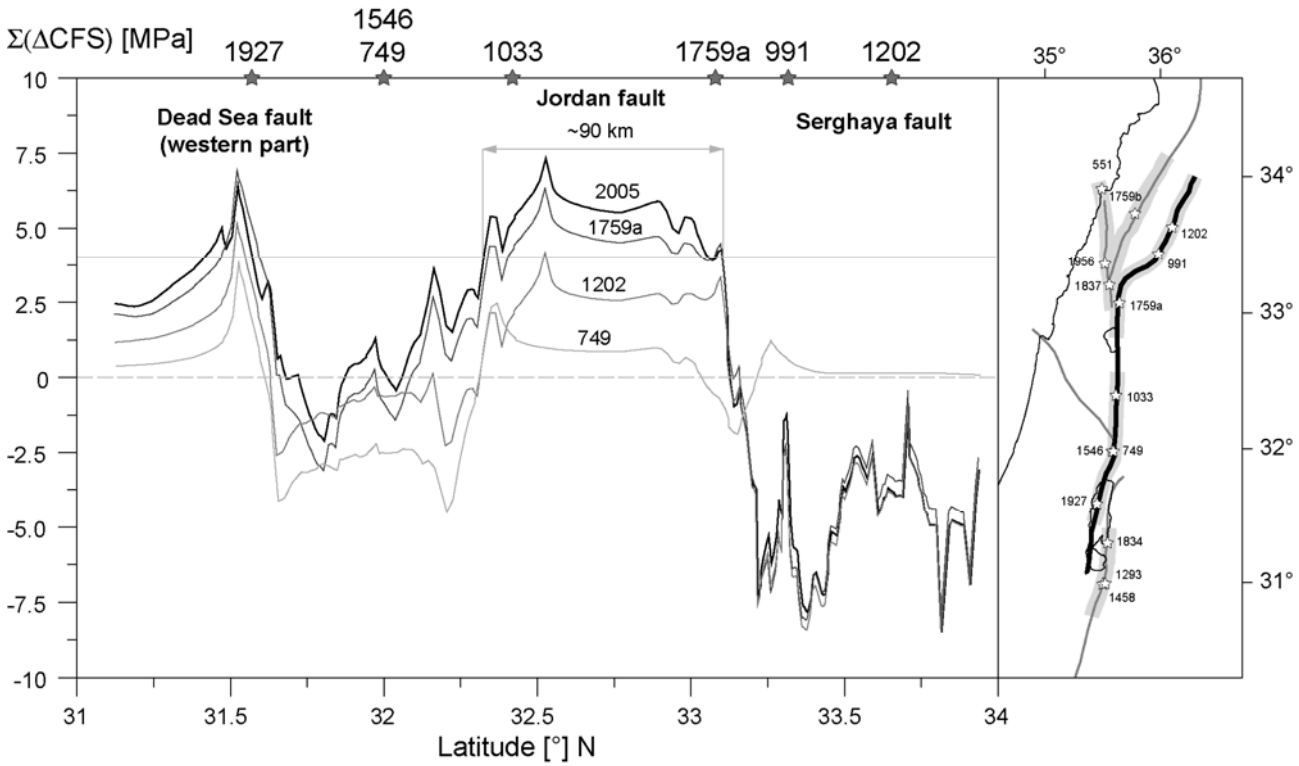

Figure 13. Evolution of ΔCFS for five fault zones along the Dead Sea Fault System (DSFS) from 551 (ΔCFS = 0) to 2005. In order to suppress unrealistic edge effects at the endings of each rupture plane, the five last points are smoothed. Plotted segments are shown on the overview maps as thick black lines. Lines with increasing grey scale represent the stress state of the given year. Stars indicate the position of the earthquake. Dashed lines are the 0 ΔCFS level and the thin grey lines in panels a and b are the 4 MPa ΔCFS level. Note the increased ΔCFS values in year 2005 for the 90-km-long section of the Jordan Fault. Applying the empirical relation between rupture length and earthquake magnitude from *Wells and Coppersmith* [1994] this segment could produce a $M_S = 7.4$ earthquake.

Discussion and conclusion

Since six major cities (Beirut, Damascus, Haifa, Tel Aviv, Amman, and Jerusalem) are in close proximity at distances between 30 and 150 km from the Jordan segment, the seismic risk is probably underestimated. Since the recurrence rates of devastating earthquakes, magnitudes, and locations of historical earthquakes are most important for the seismic hazard assessment it is crucial to receive more data in order to undertake a more detailed information on the kinematics and historical earthquakes.

To further constrain this type of numerical model, and thus the seismic hazard potential, it is essential to quantify in detail from a dense continuous GPS network the contemporary slip rates, their variation along strike, and their partitioning between the various fault segments. In order to further constrain the location and magnitude of the historical events further paleoseismological research is needed since location, rupture and slip distribution of the historical events still has high uncertainties. Thus, model results presented here are one possibility of current stress distribution, but one has to bear in mind that they are subjected to high uncertainties.

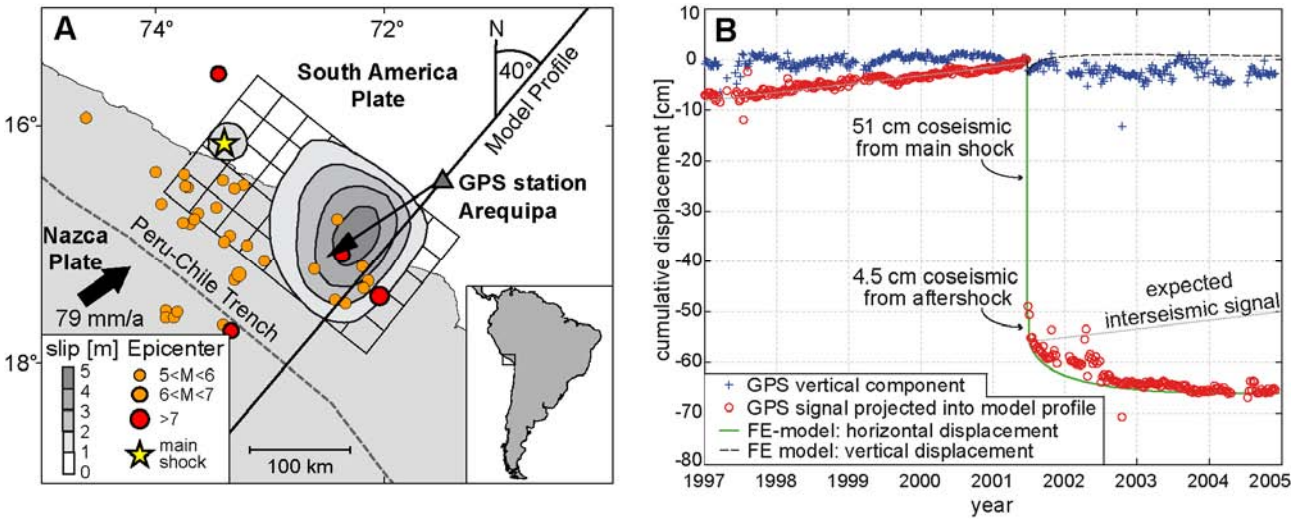

Figure 14. a) Slip distribution on the rupture plane after *Kikuchi and Yamanaka* [2001] and aftershocks locations ($M > 5$) within two weeks after the main shock. Thin black arrow indicates the coseismic slip direction, thick black arrow the movement of the Nazca Plate relative to the South America Plate. b) Modelled and observed cumulative displacements at the permanent GPS station in Arequipa (weekly solutions) relative to the position in June 2001. Modelled results are best-fit solution of the finite element model. Note the difference between the expected interseismic signal after the earthquake of 1.7 cm/a and the observed post-seismic GPS signal.

3.3 Post-seismic stress changes

With the advent of the Global Positioning System (GPS) at the end of the 1980s, first high quality time-series of deformation signals from permanent GPS stations became available during the 1990s. At some locations these signals contained unexpected transient components from post-seismic processes and demanded new concepts of internal deformation processes in the lithosphere [*Hearn*, 2003]. Different driving mechanisms have been proposed to cause these transient surface motions following earthquakes, such as after slip on the rupture plane or on its down dip extension [e.g. *Ueda et al.*, 2001], aseismic fault creep down dip of the co-seismic slip area [e.g. *Melbourne et al.*, 2002], visco-elastic relaxation of co-seismically induced stress changes [e.g. *Hu et al.*, 2004], poro-elastic rebound [e.g. *Peltzer et al.*, 1998], and transient silent slip [e.g. *Miyazaki et al.*, 2003] or combinations of these mechanisms [e.g. *Márquez-Azúa et al.*, 2002].

A prominent example is the transient post-seismic GPS signal observed after the June 23rd 2001 $M_w = 8.4$ thrust earthquake which occurred along the subduction interface of the Nazca Plate and the South America Plate in southern Peru [*Melbourne et al.*, 2002]. Figure 14 shows the location and size of the rupture plane, the co-seismic slip distribution after [*Kikuchi and Yamanaka*, 2001], and the displacement observed at the permanent GPS station in Arequipa before, during, and after the earthquake.

Melbourne et al. [2002] ascribed the transient post-seismic signal at the GPS station Arequipa to post-seismic fault creep down dip of the main shock. *Perfettini et al.* [2005] proposed a semi-analytical model referring the GPS observations to the combined effects of after slip and ductile flow along the plate interface assuming a Newtonian viscosity. In contrast to this we investigated with a numerical experiment the hypothesis that the observed transient signal

can also be explained by non-linear visco-elastic stress relaxation processes in the overriding plate.

To fit the observed co-seismic displacement at the GPS station a maximum slip of 4.87 m along the rupture plane is required in agreement with the findings of *Kikuchi and Yamanaka* [2001]. The modelled post-seismic horizontal displacement at the GPS station Arequipa presented in Figure 14b is corrected for the linear effects of the interseismic velocity observed prior to the earthquake and for the co-seismic displacement caused by the $M_w = 7.6$ aftershock. To model the transient GPS signal a wet quartzite lower crust has to be assumed.

Figure 15 displays the results of the best-fit, quartzite lower crust model in terms of the effective strain, i.e. the second invariation of the strain tensor directly after the earthquake and 3.5 yrs later. Co-seismically the effective elastic strain has its maximum at the rupture plane (Figure 15a). After 3.5 yrs a zone of high effective creep strain with maximum creep strain rates in the order of 10^{-13} s^{-1} in the lowermost part of the continental crust has evolved, whereas effective elastic strain is slightly reduced in the upper part (Figure 15b). The associated effective stress is displayed in Figure 15 with the 0.135 MPa isoline. It is reduced in the lower crust as can be seen in the shift of the 0.135 MPa isoline towards the rupture plane. In contrast, effective stress is increased in the upper crust, at least in the far field. In the upper mantle the stress magnitudes are slightly reduced after 3.5 yrs.

In Figure 15d-g the associated horizontal displacements are presented in a vertical profile through the continental crust 75 km NE of the GPS station. The co-seismic displacement decreases with depth whereas the total displacement after 3.5 yrs increases with depth reaching a maximum in approximately 40 km depth. The difference between the two lines gives the post-seismic displacement during 3.5 yrs with a maximum in 40-50 km depth.

Interpretation and conclusion

During the earthquake the fore arc moves trench-ward, so that tensional elastic stresses are induced in the crust and upper mantle of the continental plate. In the lower part of the crust a post-seismic creep process relaxes these tensional stresses. This results in a concentration of creep strain and a decrease of effective stress in the lower crust (Figure 15b) and in a trench ward directed post-seismic motion (Figure 15d). The highest deformation is found in the lower crust because of its lower effective viscosity compared to the colder upper crust and the olivine-rich upper mantle. In response to the creeping lower crust, the tensional stresses in the upper crust are relieved instantaneously due to elastic coupling leading to a concurrent trench ward directed surface motion. This can be deduced from the post-seismic decrease of effective elastic strain beneath the GPS station in the upper crust (Figure 15a,c) and from the post-seismic surface displacement (Figure 15d). A consequence of the trench ward directed surface motion is an increase of tensional stress in greater distances from the rupture plane in the upper crust, i.e. stress diffusion takes place (Figure 15a-c).

This interpretation stands in contrast to previous findings and concepts which refer to the

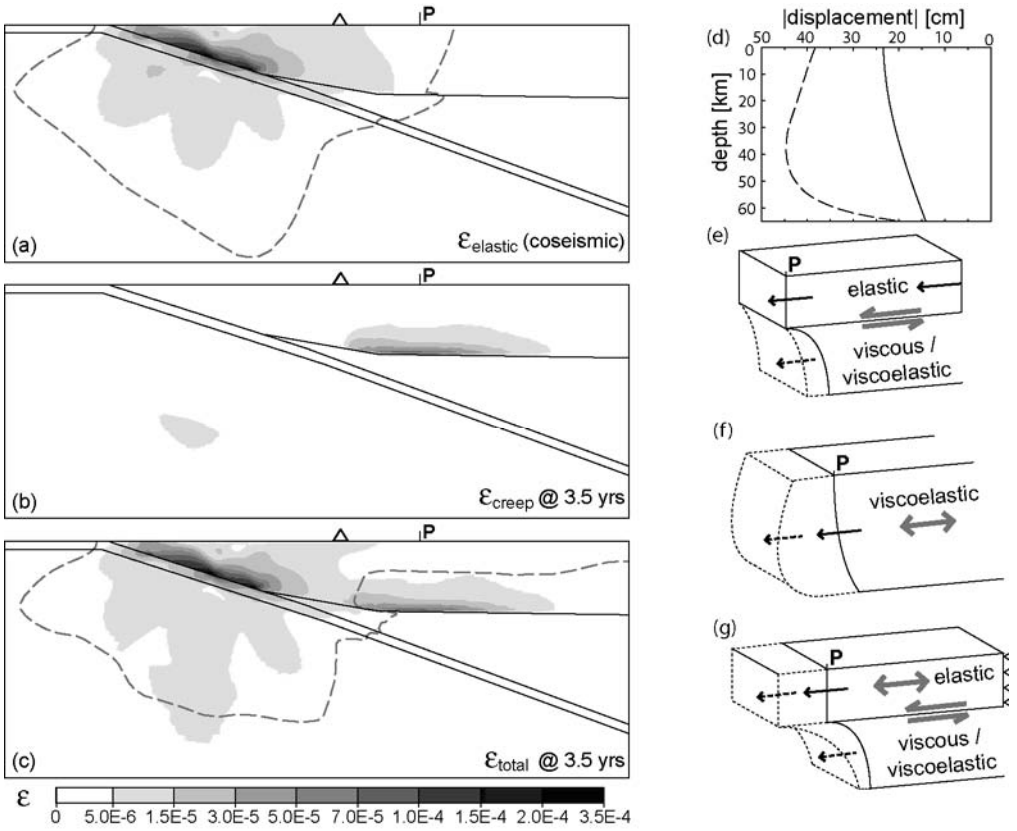

Figure 15. Eff. strain (second invariant of the strain tensor). Dashed lines indicate the 0.135 MPa isoline of eff. stress. (a) co-seismically, (b) eff. creep strain only, (c) total eff. strain (sum of eff. elastic and eff. creep strain). Note that (c) is not the sum of (a) and (b) as the eff. elastic strain has changed after 3.5 yrs. Triangle marks the position of the GPS station, 'P' the location of the vertical profile in Figure 15d-g: Conceptual models of relaxation processes. Solid lines mark coseismic displacements, dotted lines total displacements. Double arrows indicate the type of stress. (d) modelled coseismic and post-seismic horizontal displacements 3.5 yrs after the earthquake in a vertical profile 75 km northeast of the GPS station (see Figure 14); (e) mainly tensional stresses; (f) shear stresses only; (g) shear and tensional stresses.

relaxation of shear stresses. *Wernicke et al.* [2000] and *Dixon et al.* [2003] proposed an elastic crust imposing a shear traction on a viscous layer beneath. After the earthquake the viscous layer starts flowing and thereby relaxes the shear stress and imparts in turn a traction on the upper layer resulting in a post-seismic surface motion. However, relaxation of pure shear stress is not capable of producing after the earthquake any motion at the surface (Figure 15e). *Hu et al.* [2004] proposed a co-seismic tension in the crust inducing shear stresses in the upper mantle which resist the co-seismic motion. They argue that relaxation of shear stresses allows surface motion as the tensional stresses in the crust concurrently relieve (Figure 15g). This explanation is plausible but not in agreement with the results of the numerical experiment. If relaxation of shear stresses would predominate, one would not expect the sum of co- and post-seismic displacement in the lower part of the crust to be higher than in the upper part (Figure 15d).

These model results propose that the whole crust and parts of the upper mantle are co-seismically stretched rather than sheared. Thus, it is suggested that tensional stresses are the dominant driving forces in the visco-elastic stress relaxation process that controls the post-

seismic deformation measured by GPS. Assuming that a quartzite lower crust exists the visco-elastic relaxation could fully explain the observed post-seismic transient signal at the GPS station in Arequipa. Independent of the question to which extent visco-elastic relaxation contributes to the GPS signal it is emphasized that according to the numerical modelling results the general mechanism of post-seismic stress relaxation predominantly involves tensional stresses and not shear stresses.

4 Conclusions and outlook

The quantification of the stress pattern wave-length using the World Stress Map 2008 database release confirmed the existence of long wave-length stress pattern for some plates. This also underlines the finding of *Zoback* [1992] that far-field stresses imposed from the plate boundary forces are the key control of the stress pattern. *Hillis and Reynolds* [2000] show that this also holds on when the stress pattern is divided into stress provinces with very different mean S_H orientations, but still with wave-length stress patterns > 1000 km. Even though the mean S_H orientation in these provinces of the Indo-Australia plate are mostly not parallel with absolute plate motion they can be related to far-field stresses from the plate boundary forces [*Coblentz et al.*, 1998]. However, the statistical analysis also discovered that in Western Europe the spatial variability of the stress pattern wave-length is < 200 km. Some of the stress provinces correlate with plate boundary forces, but it is very much likely that internal structures have a large impact on the stress pattern. One can speculate on the reason for this difference. This different impact of regional and local stress sources can due to (1) lower magnitudes of the far-field stresses, (2) higher magnitudes of the regional and local stress sources, or (3) is a result of collecting stress data in locations that do not represent the basement stress direction as indicated in the example of North German Basin. As it is obvious that Western Europe has a long, ongoing and complex tectonic history [*Cloetingh et al.*, 2007; *Tesauro et al.*, 2008; *Ziegler*, 1988] one can imagine that internal stress sources are of great importance.

Thus, even though the WSM dataset gives insight into the sources of crustal stress, it does not provide the spatial resolution needed at reservoir scale, changes of the stress in time, and, most important, no information about the absolute stress state. In order predict the full stress tensor and its evolution in time in an area of interest geomechanical modelling is essential. The three numerical presented in this thesis are important to address specific questions of stress change, but they are not capable to address the open questions of the relative importance of stress sources and on the quantification of the absolute stress state of the Earth's crust. As the number of 3D structural information and the number of high quality model-independent observations in order to calibrate the model has increased substantially 3D geomechanical models of the absolute stress state are feasible. Critical issues of such a concept are (1) a detailed knowledge of the crustal structure (density, faults, rheology parameter), (2) definition of appropriate initial stress and boundary conditions, and (3) high number of different model-independent observations (e.g. focal mechanism solutions, GPS, InSAR, S_H orientations, tectonic regime, stress magnitudes) to calibrate the model. A very sophisticated model that takes all these aspects into account is the Ph.D. thesis by Tobias Hergert that has been prepared under my supervision [*Hergert*, 2009]. In this excellent work he presents for the Marmara Sea a 3D geomechanical model that is kinematically and dynamically consistent and it predicts absolutes stress state model and its evolution with time. With this new model concept the open question on the relative importance of stress sources can be addressed.

Acknowledgements

I would like to thank Karl Fuchs, Birgit Müller, and Friedemann Wenzel that they invited me some eight years ago to join the *World Stress Map Project* as part of the *Tectonic Stress Group* at the Geophysical Institute of the Karlsruhe Universität. Coming from the German Geodetic Research Institute it was inspiring to get to know the other fundamental tensor in geodynamics and to work on a concept to bring kinematics (strain) and dynamics (stress) into one concept. During the years there were quite a number of Diploma, Ph.D. students as well as Postdocs that I really enjoyed discussing with and all in one way or another contributed to this thesis. In particular I would like to thank Birgit Müller, John Reinecker, Blanka Sperner, Mark Tingay, Tobias Hergert, Daniel Kurfeß, Thies Buchmann, Andreas Eckert, Andreas Barth, Johannes Altmann, Gwendolyn Peters, and Peter Connolly for fruitful discussions and the open atmosphere in which we shared our often diverging thoughts.

As the World Stress Map project is a collaborative project it would have not been possible without the effort of many scientists worldwide. I am indebted to numerous individual researchers and working groups all over the world for providing stress data. As the complete list of contributors is too numerous to be given hereinit is provided on the published World Stress Map attached in the appendix of this thesis. In this context I also would like to thank the World Stress Map advisory board members Egon Althaus, John Cook, Roy Gabrielsen, Domenico Giardini, Helmut Kipphan, Onno Oncken, Chris Reigber, Markus Rothacher, and Mark Zoback for their long-term support. The work of the World Stress Map project and finally this thesis would not have been possible with the generous and long-term financial support of the Heidelberg Academy of Sciences and Humanities.

Finally I would like to thank my wife for her support and love and my two little sons for their understanding my being away for quite a number of Sunday mornings even though they still think that I am only drawing pictures of volcanoes and earthquakes the whole day with a little bit of text wrapped around it – well in a metaphoric way they are perfectly right.

References

Aadnoy, B.S., Introduction to special issue on borehole stability, *J. Pet. Sci. and Eng.*, *38*, 79-82, 2003.

Ahorner, L., Herdmechanismen rheinischer Erdbeben und der seismotektonischen Beanspruchungsplan im nordwestlichen Mittel-Europa, *Sonderveröffentlichung, Geologisches Institut, Universität Köln*, *13*, 109-130, 1967.

Ahorner, L., Present-day stress field and seismotectonic block movements along major fault zones in western Europe, *Tectonophysics*, *29*, 233-249, 1975.

Allmendinger, R., J.R. Smalley, M. Bevis, H. Caprio, and B. Brooks, Bending the Bolivian orocline in real time, *Geology*, *33*, 905-908, 2005.

Anderson, E.M., *The dynamics of faulting and dyke formation with application to Britain*, Oliver and Boyd, Edinburgh, 1951.

Angelier, J., Determination of the mean principal directions of stresses for a given fault population, *Tectonophysics*, *56*, T17-T26, 1979.

Bada, G., S. Cloetingh, P. Gerner, and F. Horváth, Sources of recent tectonic stress in the Pannonian region: inferences from finite element modelling, *Geophys. J. Int.*, *134*, 87-101, 1998.

Barth, A., F. Wenzel, and D. Giardini, Frequency sensitive moment tensor inversion for light to moderate magnitude earthquakes in eastern Africa, *Geophys. Res. Lett.*, *34*, L15302, doi:10.1029/2007GL030359, 2007.

Barton, C.A., M.D. Zoback, and D. Moos, Fluid Flow Along Potentially Active Faults in Crystalline Rock, *Geology*, *23*, 683-686, 1995.

Bell, J.S., In situ stresses in sedimentary rocks (Part 1): measurement techniques, *Geoscience Canada*, *23*, 85-100, 1996a.

Bell, J.S., In situ stresses in sedimentary rocks (Part 2): applications of stress measurements, *Geoscience Canada*, *23*, 135-153, 1996b.

Bell, J.S., and D.I. Gough, Northeast-southwest compressive stress in Alberta: Evidence from oil wells, *Earth and Planet. Sc. Lett.*, *45*, 475-482, 1979.

Bird, P., An updated digital model for plate boundaries, *Geochem. Geophys. Geosyst.*, *4* (3), 1027, doi:10.1029/2001GC000252, 2003.

Bohnhoff, M., H. Grosser, and G. Dresen, Strain partitioning and stress rotation at the North Anatolian fault zone from aftershock focal mechanisms of the 1999 Izmit M_w = 7.4 earthquake, *Geophys. J. Int.*, *166*, 373-385, doi: 10.111/j.1365-246X.2006.03027.x, 2006.

Bradley, W.B., Failure of inclinded boreholes, *J. Energy Resource Tech.*, *101*, 232-239, 1979.

Brudy, M., M.D. Zoback, F. Fuchs, F. Rummel, and J. Baumgärtner, Estimation of the complete stress tensor to 8 km depth in the KTB scientific drill holes: Implications for crustal strength, *J. Geophys. Res.*, *102*, 18453-18457, 1997.

Bunge, H.-P., M.A. Richards, and J.R. Baumgardner, A sensitivity study of 3-D spherical mantle convection at 10e8 Rayleigh number: Effects of depth dependent viscosity, heating mode and an endothermic phase change, *J. Geophys. Res.*, *102*, 11991-12007, 1997.

Cloetingh, S.A.P.L., P.A. Ziegler, P.J.F. Bogaard, P.A.M. Andriessen, I.M. Artemieva, G. Bada, R.T. van Balen, Z. Ben-Avraham, J.-P. Brun, H.-P. Bunge, E.B. Burov, R. Carbonell, C. Facenna, J. Gallart, A.G. Green, O. Heidbach, A.G. Jones, L. Matenco, J. Mosar, O. Oncken, C. Pascal, G. Peters, S. Sliaupa, A. Soesoo, W. Spakman, S. R., H. Thybo, T. Torsvik, G. de Vicente, F. Wenzel, M.J.R. Wortel, and TOPO-EUROPE Working Group, TOPO-EUROPE: the Geoscience of Coupled Deep Earth - Surface Processes, *Global and Planetary Change*, *58*, 1-118, 2007.

Coblentz, D., and R.M. Richardson, Statistical trends in the intraplate stress field, *J. Geophys. Res.*, *100*, B10, 20245-20255, 1995.

Coblentz, D., S. Zhou, R.R. Hillis, R.M. Richardson, and M. Sandiford, Topography, boundary forces, and the Indo-Australian intraplate stress field, *J. Geophys. Res.*, *103,* B1, 919-931, 1998.

Dewey, J.F., M.L. Helman, E. Turco, D.H.W. Hutton, and S.D. Knott, Kinematics of the western Mediterranean, in *Alpine Tectonics*, edited by M.P. Coward, D. Dietrich, and R.G. Park, pp. 265-283, Geological Society, London, 1989.

Dixon, T.H., E. Norabuena, and L. Hotaling, Paleoseismology and GPS: Earthquake-cycle effects and geodetic versus geologic fault slip rates in the Eastern California shear zone, *Geology*, *31* (1), 55-58, 2003.

Engelder, T., *Stress Regimes in the Lithosphere*, 457 pp., Princeton, NJ, 1992.

Fuchs, K., and B. Müller, World Stress Map of the Earth: a key to tectonic processes and technological applications, *Naturwissenschaften*, *88*, 357-371, 2001.

Gephart, J.W., and D.W. Forsyth, An Improved Method for Determining the Regional Stress Tensor Using Earthquake Focal Mechanism Data: Application to the San Fernando Earthquake Sequence, *J. Geophys. Res.*, *89,* B11, 9305-9320, 1984.

Gordon, R.G., and D.M. Jurdy, Cenozoic global plate motion, *J. Geophys. Res.*, *91*, 12389-12406, 1986.

Gregory-Wodzicki, K.M., Uplift history of the Central and Northern Andes: A review, *GSA Bulletin*, *112* (7), 1091-1105, 2000.

Greiner, G., and H. Illies, Central Europe: active or residual tectonic stress, *Pure and Appl. Geophys.*, *115*, 11-26, 1977.

Grünthal, G., and D. Stromeyer, The recent crustal stress field in Central Europe sensu lato and its quantitative modelling, *Geologie en Mijnbouw*, *73*, 173-180, 1994.

Guzman, C., E. Cristallini, and G. Bottesi, Contemporary stress orientations in the Andean retroarc between 34°S and 39°S from borehole breakout analysis, *Tectonics*, *26,* TC3016, doi:10.1029/2006TC001958, 2007.

Hardebeck, J.L., Stress triggering and earthquake probability estimates, *J. Geophys. Res.*, *109,* B4, doi:10.1029/2003JB002437, 2004.

Harris, R.A., Introduction to special section: Stress triggers, stress shadows, and implications for seismic hazard, *J. Geophys. Res.*, *103*, 24347-24358, 1998.

Hearn, E.H., What can GPS data tell us about the dynamics of post-seismic deformation? *Geophys. J. Int.*, *155*, 753-777, 2003.

Heidbach, O., A. Barth, P. Connolly, F. Fuchs, B. Müller, J. Reinecker, B. Sperner, M. Tingay, and F. Wenzel, Stress Maps in a Minute: The 2004 World Stress Map Release, *Eos Trans.*, *85* (49), 521-529, 2004.

Heidbach, O., and Z. Ben-Avraham, Stress evolution and seismic hazard of the Dead Sea fault system, *Earth Planet. Sci. Lett.*, *257*, 299-312, 2007.

Heidbach, O., and H. Drewes, 3-D Finite Element model of major tectonic processes in the Eastern Mediterranean, in *New insights in structural interpretation and modelling*, edited by D. Nieuwland, pp. 259-272, Geological Society, London, 2003.

Heidbach, O., K. Fuchs, B. Müller, J. Reinecker, B. Sperner, M. Tingay, and F. Wenzel, The World Stress Map - Release 2005, 1:46,000,000, Commission of the Geological Map of the World, Paris, 2007a.

Heidbach, O., and J. Höhne, CASMI - a tool for the visualization of the World Stress Map data base, *Computers and Geosciences*, *34* (7), 783-791, doi:1016/j.cageo.2007.06.004, 2008.

Heidbach, O., G. Iaffaldano, and H.-P. Bunge, Topography growth drives stress rotations in the Central Andes - observations and models, *Geophys. Res. Lett*, *35*, L08301, doi:10.1029/2007GL032782, 2008a.

Heidbach, O., D. Kurfeß, and J. Höhne, CASMI - An interactive software tool for stress map plotting using the 2008 release of the World Stress Map data base (available online at www.world-stress-map.org), 2008b.

Heidbach, O., B. Müller, K. Fuchs, F. Wenzel, J. Reinecker, M. Tingay, B. Sperner, J.-P. Cadet, and P. Rossi, World Stress Map Published, *Eos Trans.*, *88* (47), 504, 2007b.

Heidbach, O., J. Reinecker, M. Tingay, B. Müller, B. Sperner, K. Fuchs, and F. Wenzel, Plate boundary forces are not enough: Second- and third-order stress patterns highlighted in the World Stress Map database, *Tectonics*, *26*, TC6014, doi:10.1029/2007TC002133, 2007c.

Heidbach, O., M. Tingay, A. Barth, J. Reinecker, D. Kurfeß, and B. Müller, The 2008 release of the World Stress Map (available online at www.world-stressmap.org), doi:10.1594/GFZ.WSM.Rel2008, 2008c.

Heidbach, O., M. Tingay, A. Barth, J. Reinecker, D. Kurfeß, and B. Müller, Statistical analysis of global spatial wave-length stress pattern, *Tectonophysics*, subm.

Hergert, T., Numerical modelling of the absolute stress state in the Marmara Sea region – a contribution to seismic hazard assessment, Ph. D. thesis, 152 pp., Karlsruhe Universität, Karlsruhe, 2009.

Hergert, T., and O. Heidbach, New insights in the mechanism of post-seismic stress relaxation exemplified by the June 23rd 2001 $M_w = 8.4$ earthquake in southern Peru, *Geophys. Res. Lett.*, *33,* L02307, doi:1029/2005GL024585, 2006.

Hickman, S.H., Stress in the Lithosphere and Strength of Active Faults, *Rev. of Geophys.*, *29*, 759-775, 1991.

Hillis, R.R., and S.D. Reynolds, The Australian Stress Map, *J. Geol. Soc.*, *157*, 915-921, 2000.

Hu, Y., K. Wang, J. He, J. Klotz, and G. Khazaradze, Three-dimensional visocelastic finite element model for post-seismic deformation of the great 1960 Chile earthquake, *J. Geophys. Res.*, *109,* B12403, doi:1029/2004JB003163, 2004.

Iaffaldano, G., H.-P. Bunge, and T. Dixon, Feedback between mountain belt growth and plate convergence, *Geology*, *34* (10), 893-896, doi:10.1130/G22661.1, 2006.

Illies, H., and G. Greiner, Regionales stress-Feld und Neotektonik in Mitteleuropa, *Oberrheinische Geologische Abhandlungen*, *25*, 1-40, 1976.

Illies, H., and G. Greiner, Rhinegraben and the Alpine system, *Geol. Soc. Am. Bull.*, *89*, 770-782, 1978.

Jaeger, J.C., N.G.W. Cook, and R.W. Zimmermann, *Fundamentals of Rock Mechanics*, Blackwell Publishing, Oxford, 2007.

Jarosinski, M., F. Beekman, G. Bada, and S. Cloetingh, Redistribution of recent collision push and ridge push in Central Europe: insights from FEM modelling, *Geophys. J. Int.*, *167*, 860-880, 2006.

Kastrup, U., M.L. Zoback, N. Deichmann, K.F. Evans, D. Giardini, and A.J. Michael, Stress field variations in the Swiss Alps and northern Alpine foreland derived from inversion of fault plane solutions, *J. Geophys. Res.*, *109,* B01402, doi:10.1029/2003JB002550, 2004.

Kikuchi, M., and Y. Yamanaka, Earthquake information center seismological note no 105, *http://www.eic.eri.u-tokyo.ac.jp/EIS/EIC_News/105E.html*, 2001.

Lamb, S., Shear stresses on megathrusts: Implications for mountain building behind subduction zones, *J. Geophys. Res.*, *111,* B07401, doi:10.1029/2005JB003916, 2006.

Lamb, S., and P. Davis, Cenozoic climate change as a possible cause for the rise of the Andes, *Science*, *425*, 792-797, 2003.

Ljunggren, C., Y. Chang, T. Janson, and R. Christiansson, An overview of rock stress measurement methods, *Int. J. Rock. Mech.*, *40*, 975-989, 2003.

Malinverno, A., and W.B.F. Ryan, Extension in the Tyrrhenian Sea and Shortening in the Apennines as Result of Arc Migration Driven by Sinking of the Lithosphere, *Tectonics*, *5*, 227-245, 1986.

Mardia, K.V., *Statistics of directional data: probability and mathematical statistics*, 357 pp., Academic Press, London, 1972.

Márquez-Azúa, B., C. DeMets, and T. Masterlark, Strong interseismic coupling, fault afterslip, and viscoelastic flow before and after the Oct. 9, 1995 Colima-Jalisco earthquake: Continuous GPS measurements from Colima, Mexico, *Geophys. Res. Lett*, *29* (8)*,* 1281, doi:10.1029/2002GL014702, 2002.

McKenzie, D., Active tectonics of the Mediterranean region, *Geophys. J. R. astr. Soc.*, *30*, 109-185, 1972.

Melbourne, T.I., F.H. Webb, J.M. Stock, and C. Reigber, Rapid post-seismic transients in subduction zones from continuous GPS, *J. Geophys. Res.*, *107,* B10, doi:10.1029/2001JB000555, 2002.

Mercier, J.L., M. Sebrier, A. Lavenu, J. Cabrera, O. Bellier, J.-F. Dumont, and J. Machare, Changes in the Tectonic Regime Above a Subduction Zone of Andean Type: The Andes of Peru and Bolivia During the Pliocene-Pleistocene, *J. Geophys. Res.*, *97,* B8, 11945-11982, 1992.

Michael, J., Determination of stress from slip data: Faults and folds, *J. Geophys. Res.*, *89*, 11517-11526, 1984.

Miyazaki, S., J. McGuire, and P. Segall, A transient subduction zone slip episode in southwest Japan observed by the nationwide GPS array, *J. Geophys. Res.*, *108*, B2, 2097, doi:10.1029/2001JB000456, 2003.

Müller, B., O. Heidbach, B. Sperner, and M. Negut, Attached or not attached – how crustal stress observations contribute to interpret the intermediate depth seismicity of Vrancea, *Tectonophysics*, subm.

Müller, B., V. Wehrle, H.J. Zeyen, and K. Fuchs, Short-scale variations of tectonic regimes in the western European stress province north of the Alps and Pyrenees, *Tectonophysics*, *275*, 199-219, 1997.

Müller, B., M.L. Zoback, K. Fuchs, L. Mastin, S. Gregersen, N. Pavoni, O. Stephansson, and C. Ljunggren, Regional Patterns of Tectonic Stress in Europe, *J. Geophys. Res.*, *97*, 11783-11803, 1992.

Parsons, T., Recalculated probability of M=> 7 earthquakes beneath the Sea of Marmara, Turkey, *J. Geophys. Res.*, *109* (B05304), doi:10.1029/2003JB002667, 2004.

Parsons, T., Significance of stress transfer in time-dependent earthquake probability calculations, *J. Geophys. Res.*, *110* (B05S02), doi:10.1029/2004JB003190, 2005.

Parsons, T., S. Toda, R.S. Stein, A. Barka, and J.H. Dieterich, Heightened odds of large Earthquakes near Istanbul: An interaction-based Probability calculation, *Science*, *288*, 661-664, 2000.

Peltzer, G., P. Rosen, F. Rogez, and K. Hudnut, Poroelastic rebound along the Landers 1992 earthquake rupture, *J. Geophys. Res.*, *102,* B12, 30131-30145, 1998.

Perfettini, H., J.P. Avouac, and J.C. Ruegg, Geodetic displacements and aftershocks following the 2001 M_w=8.4 Peru earthquake: Implications for the mechanics of the earthquake cycle along subduction zones, *J. Geophys. Res.*, *110,* B09404, doi:10.1029/2004JB003522, 2005.

Regenauer-Lieb, K., Dilatant plasticity applied to Alpine collision: ductile void growth in the intraplate area beneath the Eifel volcanic field, *Geodynamics*, *27* (1), 1-21, 1998.

Reinecker, J., M. Tingay, B. Müller, and O. Heidbach, Stress variations along strike the German Molasse Basin, *Tectonophysics*, subm.

Richardson, R.M., Ridge Forces, Absolute Plate Motions, and the Intraplate Stress Field, *J. Geophys. Res.*, *97*, 11739-11748, 1992.

Richardson, R.M., S.C. Solomon, and N.H. Sleep, Tectonic Stress in Plates, *Rev. of Geophys.*, *17* (5), 981-1019, 1979.

Rivera, L., and A. Cisternas, Stress tensor and fault plane solutions for a population of earthquakes, *Bull. Seism. Soc. of Am.*, *80*, 600-614, 1990.

Roth, F., and P. Fleckenstein, Stress orientations found in north-east Germany differ from the West European trend, *Terra Nova*, *13*, 289-286, 2001.

Sbar, M.L., and L.R. Sykes, Contemporary compressive stress and seismicity in eastern North America, An example of intraplate tectonics, *Geol. Soc. Am. Bull.*, *84*, 1861-1882, 1973.

Sella, G.F., T. Dixon, and A. Mao, REVEL: A model for Recent plate velocities from space geodesy, *J. Geophys. Res.*, *107,* B4, 2081, 10.1029/2000JB00033, 2002.

Sibson, R.H., Structural permeability of fluid-driven fault-fracture meshes, *J. Struct. Geol.*, *18*, 1031-1042, 1996.

Smith, W.H.F., and D.T. Sandwell, Global Sea Floor Topography from Satellite Altimetry and Ship Depth Soundings, *Science*, *277*, 1956-1962, 1997.

Solomon, S.C., R.M. Richardson, and E.A. Bergman, Tectonic Stress: Models and Magnitudes, *J. Geophys. Res.*, *85,* B11, 6086-6092, 1980.

Sonder, L.J., Effects of density contrasts on the orientation of stresses in the lithosphere: Relation to principal stress directions in the transverse ranges, California, *Tectonics*, *9*, 761-771, 1990.

Sperner, B., B. Müller, O. Heidbach, D. Delvaux, J. Reinecker, and K. Fuchs, Tectonic stress in the Earth's crust: advances in the World Stress Map project, in *New insights in structural interpretation and*

modelling, edited by D.A. Nieuwland, pp. 101-116, Geological Society, London, 2003.

Steacy, S., J. Gomberg, and M. Cocco, Introduction to special section: Stress transfer, earthquake triggering, and time-dependent seismic hazard, *J. Geophys. Res.*, *110*, B05S01, doi:10.1029/2005JB003692, 2005.

Stein, R.S., A.A. Barka, and J.H. Dietrich, Progressive failure on the North Anatolian fault since 1939 by earthquake stress triggering, *Geophys. J. Int.*, *128*, 594-604, 1997.

Stephansson, O., L.-O. Dahlstrom, et al., Fennoscandian rock stress data base - FRSDB, *Research Report TULEA 6*, *Technical University of Lulea, Lulea, Sweden*, 1987.

Sykes, L.R., and M.L. Sbar, Intraplate earthquakes, lithospheric stresses and the driving mechanism of plate tectonics, *Nature*, *245*, 298-302, 1973.

Sykes, L.R., and M.L. Sbar, Focal mechanism solutions of intraplate earthquakes and stresses in the lithosphere, in *Geodynamics of Iceland and North Atlantic area*, edited by L. Kristjansson, pp. 207-224, Reidel, Hingham, *Massachusetts*, 1974.

Tesauro, M., M.K. Kaban, and S.A.P.L. Cloetingh, EuCRUST-07: A new reference model for the European crust, *Geophys. Res. Lett*, *35,* L05313, doi:10.1029/2007GL032244, 2008.

Thybo, H., Crustal structure along the EGT profile across the Tornquist Fan interpreted from seismic, gravity and magnetic data, *Tectonophysics*, *334* (3), 155-190, 2001.

Tingay, M., R.R. Hillis, C.K. Morley, E. Swarbrick, and S.J. Drake, Present-day stress orientation in Brunei: a snapshot of 'prograding tectonic' in a Tertiary delta, *J. Geol. Soc., London*, *162*, 39-49, 2005a.

Tingay, M., B. Müller, J. Reinecker, O. Heidbach, F. Wenzel, and Fleckenstein, P., The World Stress Map Project 'Present-day Stress in Sedimentary Basins' initiative: building a valuable public resource to understand tectonic stress in the oil patch, *The Leading Edge*, *24* (12), 1276-1282, 2005b.

Tingay, M.R.P., B. Müller, J. Reinecker, and O. Heidbach, State and Origin of the Present-day Stress Field in Sedimentary Basins: New Results from the World Stress Map Project, in *41st U.S. Symposium on Rock Mechanics (USRMS): "50 years of Rock Mechanics - Landmarks and Future Challenges*, pp. 14, Golden, Colorado, 2006.

Toussaint, G., E. Burov, and J.P. Avouac, Tectonic evolution of a continental collision zone: A thermomechanical numerical model, *Tectonics*, *23,* TC6003, doi:10.1029/2003TC001604, 2004.

Ueda, H., M. Ohtake, and H. Sato, Afterslip on the plate interface following the 1978 Miyagi-Oki, Japan, earthquake, as revealed from geodetic measurement data, *Tectonophysics*, *338*, 45-57, 2001.

Wegener, A., *Die Entstehung der Kontinente und Ozeane*, Braunschweig, 1915. Wells, D.L., and K.J. Coppersmith, New empirical relationship among magnitude, rupture length, rupture width, rupture area, and surface displacement, *Bull. Seismol. Soc. Am.*, *84* (4), 974-1002, 1994.

Wells, D.L., and K.J. Coppersmith, New empirical relationships among magnitude, rupture length, rupture width, rupture area, and surface displacement, *Bull. Seismol. Soc. Am. 84* (4), 974-1002, 1994.

Wernicke, B., A.M. Friederich, N.A. Niemi, R.A. Bennett, and J.L. Davis, Dynamics of Plate Boundary Fault Systems from Basin and Range Geodetic Network (BARGEN) and Geologic Data, *GSA Today*, *10* (11), 1-7, 2000.

Westaway, R., Present-day kinematics of the plate boundary zone between Africa and Europe, from the Azores to the Aegean, *Earth Planet. Sci. Lett.*, *96*, 393-406, 1990.

Yale, D.P., Fault and stress magnitude controls on variations in the orientation of in situ stress, in *Fracture and in-situ stress characterization of hydrocarbon reservoirs*, edited by M.S. Ameen, pp. 55-64, Geologcial Society, London, 2003.

Zhang, Y.-Z., M. Dasseault, and N. Yassir, Effects of rock anisotropy and heterogeneity on stress distributions at selected sites in North America, *Economic Geology*, *37*, 181-197, 1994.

Ziegler, P.A., *AAPG Memoir 43: Evolution of the Arctic-North Atlantic and the Western Tethys*, AAPG, Tulsa, 1988.

Zoback, M.D., and M.L. Zoback, State of Stress and Intraplate Earthquakes in the United States, *Science*, *213*, 96-104, 1981.

Zoback, M.D., and M.L. Zoback, Tectonic stress field of North America and relative plate motions, in *Neotectonics of North America*, edited by D.B. Slemmons, E.R. Engdahl, M.D. Zoback, and D.D. Blackwell, pp. 339-366, Geological Society of America, Boulder, Colorado, 1991.

Zoback, M.L., First and second order patterns of stress in the lithosphere: The World Stress Map Project, *J. Geophys. Res.*, *97*, 11703-11728, 1992.

Zoback, M.L., and M.D. Zoback, State of Stress in the Conterminous United States, *J. Geophys. Res.*, *85* (B11), 6113-6156, 1980.

Zoback, M.L., and M.D. Zoback, Tectonic stress field of the conterminous United States, in *Geophysical Framework of the Continental United States*, edited by L.C. Pakiser, and W.D. Mooney, pp. 523-539, Geol. Soc. Am. Mem., Boulder, Colorado, 1989.

Zoback, M.L., M.D. Zoback, J. Adams, M. Assumpção, S. Bell, E.A. Bergman, P. Blümling, N.R. Brereton, D. Denham, J. Ding, K. Fuchs, N. Gay, S. Gregersen, H.K. Gupta, A. Gvishiani, K. Jacob, R. Klein, P. Knoll, M. Magee, J.L. Mercier, B.C. Müller, C. Paquin, K. Rajendran, O. Stephansson, G. Suarez, M. Suter, A. Udías, Z.H. Xu, and M. Zhizhin, Global patterns of tectonic stress, *Nature*, *341*, 291-298, 1989.

Appendix

Reprints of key publications

Heidbach, O., Fuchs, K., Müller, B., Reinecker, J., Sperner, B., Tingay, M., Wenzel, F., (2007). The World Stress Map - Release 2005, 1:46,000,000. Commission of the Geological Map of the World, Paris.

Heidbach, O., Höhne, J., (2008). CASMI - a tool for the visualization of the World Stress Map data base. *Computers and Geosciences*, 34 (7), 783-791, doi:1016/j.cageo.2007.06.004.

Heidbach, O., Reinecker, J., Tingay, M., Müller, B., Sperner, B., Fuchs, K., Wenzel, F., (2007). Plate boundary forces are not enough: Second- and third-order stress patterns highlighted in the World Stress Map database. *Tectonics*, 26, TC6014, doi:10.1029/2007TC002133.

Heidbach, O., Iaffaldano, G., Bunge, H.-P., (2008). Topography growth drives stress rotations in the Central Andes - observations and models. *Geophys. Res. Lett.*, 35, L08301, doi:10.1029/2007GL032782.

Heidbach, O., Ben-Avraham, Z., (2007). Stress evolution and seismic hazard of the Dead Sea fault system. Earth Planet. *Sci. Lett.*, 257, 299-312.

Hergert, T., Heidbach, O., (2006). New insights in the mechanism of post-seismic stress relaxation exemplified by the June 23rd 2001 $M_w = 8.4$ earthquake in southern Peru. *Geophys. Res. Lett.*, 33, L02307, doi:1029/2005GL024585.

Commission de la Carte Géologique du Monde / Commission for the Geological Map of the World

WORLD STRESS MAP

2009 - 2nd edition, based on the WSM database release 2008

Helmholtz Centre Potsdam - GFZ German Research Centre for Geosciences

Authors

Oliver Heidbach, Mark Tingay, Andreas Barth, John Reinecker, Daniel Kurfeß, and Birgit Müller

Explanatory Text

The World Stress Map (WSM) is the global compilation of information on the present-day stress field in the Earth's crust. It is a collaborative project between academia, industry and government that aims to characterize the crustal stress pattern and to understand the sources of tectonic stress. The project commenced in 1986 as a part of the International Lithosphere Program, under the leadership of Mary Lou Zoback. From 1995-2008, the WSM was a project of the Heidelberg Academy of Sciences and Humanities. Since 2009 it is maintained and further developed at the Helmholtz Centre Potsdam - GFZ German Research Centre for Geosciences.

All stress information is recorded in a standardized format and quality-ranked for reliability and comparability on a global scale. The stress maps on this poster display A-C quality stress data in the upper 40 km of the Earth's crust from the WSM database release 2008. Focal mechanism solutions determined as being potentially unreliable (labelled as Possible Plate Boundary Events in the database) are not displayed. Further detailed information on the quality ranking, guidelines for various stress indicators, and software for stress map generation can be found on the WSM website at www.world-stress-map.org.

The stress maps display the maximum horizontal compressional stress S_H

Method

- focal mechanism
- breakouts
- drill. induced frac.
- overcoring
- hydro. fractures
- geol. indicators

Data depth range

0-40 km

Quality

A	——	S_H is within ±15°
B	——	S_H is within ±20°
C	——	S_H is within ±25°

Stress Regime

- Normal faulting
- Strike-slip faulting
- Thrust faulting
- Unknown regime

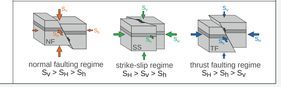

normal faulting regime $S_V > S_H > S_h$

strike-slip regime $S_H > S_V > S_h$

thrust faulting regime $S_H > S_h > S_V$

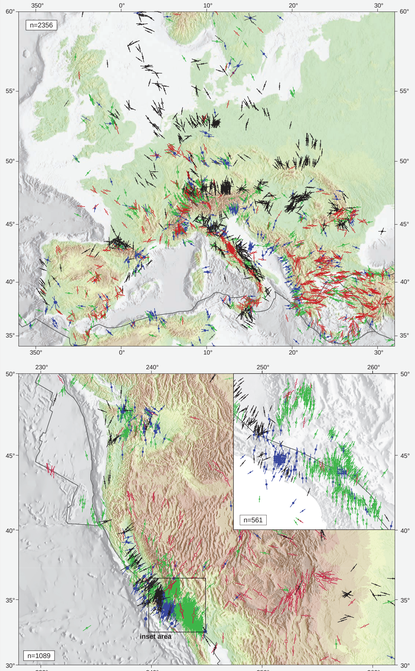

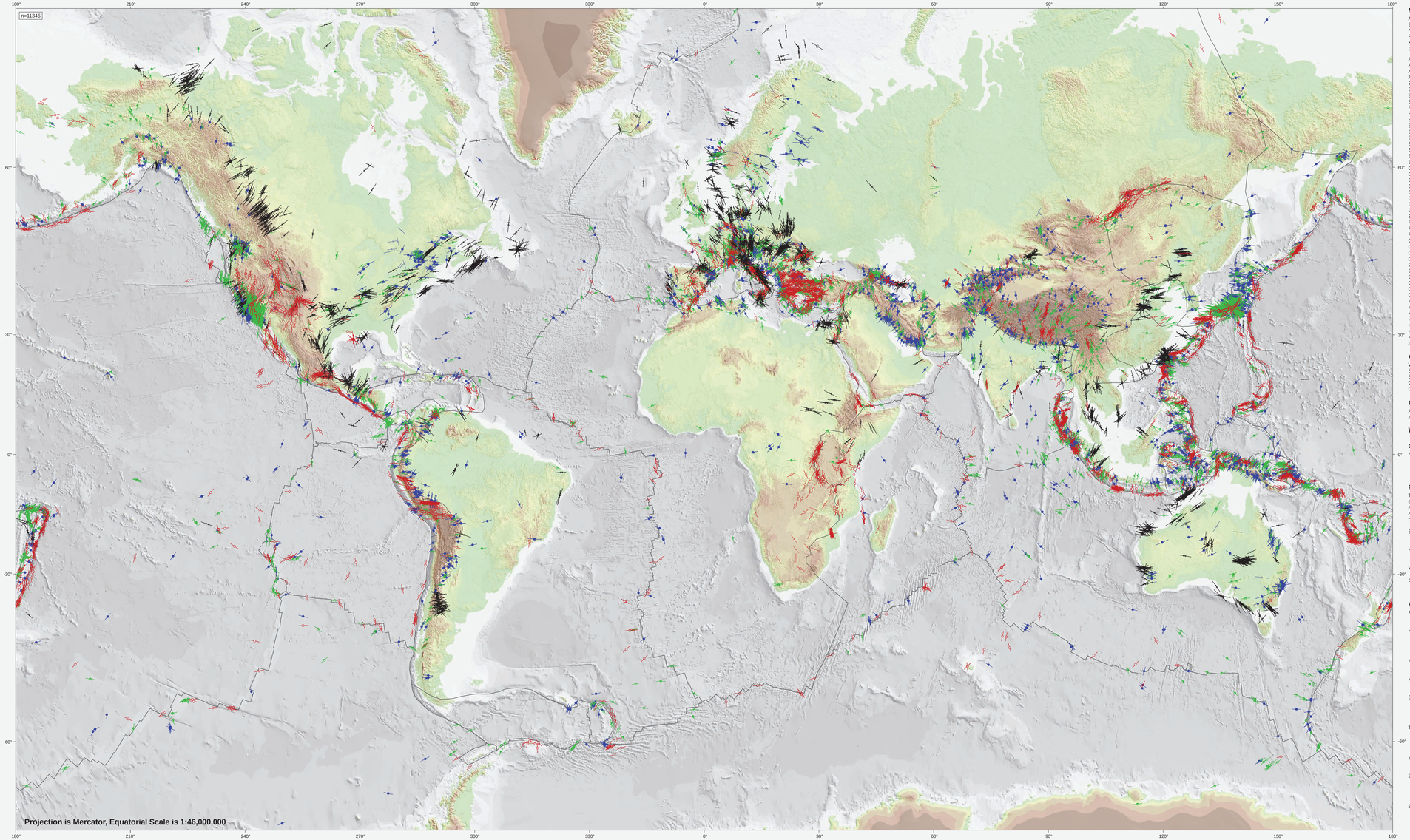

Major contributors

Australasian Stress Map Project, The Global CMT Catalogue, European-Mediterranean Regional CMT solutions, DGMK, NAGRA, PETROM, BP, Schlumberger, CHEVRON-Texaco, Fennoscandian Rock Stress Database, Wirtenshall, Shell, Karasu, PTT, Eni, RWE-Dea, Daleel Petroleum, WEG, Daleel Petroleum, Premier Oil

Adams, J.
Al-Zoubi, A.S.
Ask, M.
Assumpçaõ, M.
Babyyev, G.
Batchelor, T.
Becker, A.
Bell, S.
Bergerat, F.
Bergman, E.
Barr, M.
Bluemling, P.
Bohnhoff, M.
Bonjer, K.-P.
Bosworth, W.
Braili, R.
Brereton, R.
Brudy, M.
Chatterjee, R.
Colmenares, L.
Connolly, P.
Cornet, F.
Deichmann, N.
Delvaux, D.
Dernham, D.
Doeveny, P.
Enever, J.
Feijerskov, M.
Finkbeiner, T.
Fleckenstein, P.
Gay, N.
Gerner, P.
Gough, D.I.
Gowl, T.N.
Grasso, M.
Gregersen, S.
Grünthal, G.
Gupta, H.K.
Gvishiani, A.
Guzman, C.
Haimson, B.C.
Hanssen, T.H.
Heidbach, O.
Hergert, T.
Hickman, S.
Hillis, R.R.
Horvath, F.
Jiannin, D.
Jarosinski, M.
King, R.
Klein, R.
Kjorholt, H.
Knoll, P.
Knopoltin, P.
Larsen, R.
Lindholm, C.
Lopez, A.
Magee, M.
Mariucci, M.T.
Mastin, M.
Maury, V.
Mercier, J.
Mildren, S.
Montone, P.
Müller, B.
Negut, M.
Oncescu, M.C.
Pavoni, N.
Ragg, S.
Rajendran, K.
Reinecker, J.
Reynolds, S.D.
Roth, F.
Rummel, F.
Sebrier, M.
Sherman, S.
Stephansson, O.
Stromeyer, D.
Spenner, B.
Suarez, G.
Suter, M.
Tingay, M.
Townend, J.
Tollpanen, P.
Townend, J.
Ulitas, A.
van Dalfsen, W.
van Eijs, R.
Van-Kin, L.
Wiprut, D.
Wolter, K.
Yunga, S.
Zhonghuai, X.
Zoback, M.D.
Zoback, M.L.

Advisory board

We thank the long-term support from the members of the World Stress Map advisory board of the Heidelberger Academy of Sciences and Humanities, Egon Althaus, John Cook, Roy Gabrielsen, Domenico Giardini, Helmut Kipphan, Onno Oncken, Christoph Reigber, Markus Rothacher, and Mark Zoback.

Further information and data access

All stress data, further information and software tools are available free of charge on the project website at:

www.world-stress-map.org

Citation of this map

Heidbach, O., Tingay, M., Barth, A., Reinecker, J., Kurfeß, D., and Müller, B., The World Stress Map based on the database release 2008, equatorial scale 1:46,000,000, Commission for the Geological Map of the World, Paris, doi:10.1594/GFZ.WSM.Map2009, 2009.

References of used data and software

This map made use of a number of datasets: Plate boundaries are from the global plate model PB2002 (Bird, 2003), topography and bathymetry from Smith and Sandwell (1997). Stress maps are produced with CASMI (Heidbach and Höhne, 2008) which is based on GMT from Wessel and Smith (1998).

Bird, P., An updated digital model for plate boundaries, Geochem. Geophys. Geosyst., 4 (3), 1027, doi:10.1029/2001GC000252, 2003.

Heidbach, O., Höhne, J., CASMI - a tool for the visualization of the World Stress Map data base, Computers and Geosciences, 34, 783-791, doi:1016/j.cageo.2007.06.004, 2008.

Wessel, P., Smith, W.H.F., New, improved version of Generic Mapping Tools released, Eos Trans., 79 (47), 579, 1998.

Smith, W.H.F., and Sandwell, D.T., Global sea floor topography from satellite altimetry and ship depth soundings, Science, 277, 1956-1962, 1997.

Key references for the WSM project

Fuchs, K. & Müller, B., World Stress Map of the Earth: a key to tectonic processes and technological applications, Naturwissenschaften, 88, 357-371, 2001.

Heidbach, O., Reinecker, J., Tingay, M., Müller, B., Sperner, B., Fuchs, K. & Wenzel, F., Plate boundary forces are not enough: Second- and third-order stress patterns highlighted in the World Stress Map database, Tectonics, 26, TC6014, doi:10.1029/2007TC002133, 2007.

Heidbach, O., Tingay, M., Barth, A., Reinecker, J., Kurfeß, D. & Müller, B., The World Stress Map database release 2008 doi:10.1594/GFZ.WSM.Rel2008, 2008.

Heidbach, O., Tingay, M., Barth, A., Reinecker, J., Kurfeß, D. & Müller, B., Statistical analysis of global spatial wave-length stress pattern, Tectonophysics, in press.

Sperner, B., Müller, B., Heidbach, O., Delvaux, D., Reinecker, J. & Fuchs, K., Tectonic stress in the Earth's crust: advances in the World Stress Map project, in New insights in structural interpretation and modelling, pp. 101-116, ed. Nieuwland, D. A. Geological Society, London, 2003.

Tingay, M., Müller, B., Reinecker, J., Heidbach, O., Wenzel, F. & Fleckenstein, P., The World Stress Map Project 'Present-day Stress in Sedimentary Basins' initiative: building a valuable public resource to understand tectonic stress in the oil patch, The Leading Edge, 24, 1276-1282, 2005.

Zoback, M.L., First and second order patterns of stress in the lithosphere: The World Stress Map Project, J. Geophys. Res., 97, 11703-11728, 1992.

Zoback, M.L. & Zoback, M.D., Tectonic stress field of the conterminous United States, in Geophysical Framework of the Continental United States, pp. 523-539, eds. Pakiser, L. C. & Mooney, W. D. Geol. Soc. Am. Mem., Boulder, Colorado, 1989.

Zoback, M.D. & Zoback, M.L., Tectonic stress field of North America and relative plate motions, in Neotectonics of North America, pp. 339-366, eds. Slemmons, D. B., Engdahl, E. R., Zoback, M. D. & Blackwell, D. D. Geological Society of America, Boulder, Colorado, 1991.

Originally published as:
Computers & Geosciences 34 (2008) 783–791

CASMI - A visualization tool for the World Stress Map database✧

Oliver Heidbach[a,b,*], Jens Höhne[b]

[a] *Geophysical Institute, University of Karlsruhe, Hertzstraße 16, 76187 Karlsruhe, Germany*
[b] *Heidelberg Academy of Sciences and Humanities, Karlstraße 4, 69117 Heidelberg, Germany*

Received 6 September 2006; received in revised form 30 May 2007; accepted 4 June 2007

Abstract

The World Stress Map (WSM) project has compiled a global database of quality-ranked data records on the contemporary tectonic stresses in the Earth's crust. The WSM 2005 database release contains approximately 16 000 data records from different types of stress indicators such as earthquake focal mechanisms solutions, well bore breakouts, hydraulic fracturing and overcoring measurements, as well as quaternary fault-slip data and volcanic alignments. To provide a software tool for database visualization, analysis and interpretation of stress data as well its integration with other data records, we developed the program CASMI. This public domain software tool for Unix-like operating systems enables the selection of stress data records from the WSM database according to location, data quality, type of stress indicator, and depth. Each selected data record is visualized by a symbol that represents the type of stress indicator and the orientation of the maximum horizontal compressive stress. Symbol size is proportional to the quality of the data record, and the colour indicates different tectonic regimes. Stress maps can be produced in different geographical projections and high-quality output formats. CASMI also allows the integration of user-defined stress data sets and a wide range of other data such as topography, Harvard centroid moment tensors, polygons, text data, and plate motion trajectories. CASMI, including the WSM 2005 database release, can be requested free of charge from the project's website at http://www.world-stress-map.org/casmi. We present two stress map examples generated with CASMI ranging from plate-wide to regional scale: (1) A stress map of central Europe, that reveals the correlation of stress field orientation and relative plate motion. (2) The fan-shape stress pattern in North Germany.

Keywords: Tectonic stress; Stress indicators; Database; Stress map

1. Introduction

Knowledge of the stress field in the Earth's crust is a key issue for the understanding of geodynamic processes, seismic hazard assessment, and stability of underground openings such as waste disposals, tunnels, mines or wells, and reservoir management (*Fuchs and Müller*, 2001). The principal idea of the World Stress Map (WSM) project is to provide a global compilation of quality-ranked data about the contemporary tectonic stresses in the Earth's crust (Fig. 1). The WSM project was initiated in 1986 under the auspices of the International Lithosphere Program as a global cooperative effort. It is a collaborative project of academia, industry, and governmental organizations, which aims to understand the states and sources of tectonic stresses in the Earth's crust. In 1992 the first release of the WSM database together with major results was published (*Zoback*, 1992).

The WSM data come from a wide range of stress measurement techniques. They are provided in a database of standardized format and are quality ranked in order to be comparable on a global scale (*Heidbach et al.*, 2007a; *Reinecker et al.*, 2005; *Sperner et al.*, 2003; *Zoback*, 1992; *Zoback et al.*, 1989; *Zoback and Zoback*, 1991). The first public WSM database release in 1992 with ~7300 data records provided fundamental insights into the nature and impact of forces that drive the tectonic plates and control the large-scale crustal deformation over hundreds to thousands of kilometres. Major findings were that plate-wide stress provinces with prevailing compressive tectonic regime exist in intraplate regions and

✧ Code available at http://www.world-stress-map.org/casmi.

* Corresponding author at: Geophysical Institute, University of Karlsruhe, Hertzstraße 16, 76187 Karlsruhe, Germany.
Tel.: +49 721 4609 608; fax: +49 721 711 73.
E-mail address: oliver.heidbach@gpi.uni-karlsruhe.de (O. Heidbach).

doi: 10.1016/j.cageo.2007.06.004

that the orientation of the maximum horizontal compressive stress S_H is sub-parallel to the plate motion in North America, South America, and Europe (*Müller et al.*, 1992; *Zoback*, 1992; *Zoback et al.*, 1989). Thus, plate boundary forces are the major controls on the first-order pattern of S_H orientation in the plate interiors (*Richardson*, 1992).

Since 1996, the WSM has been a research project of the Heidelberg Academy of Sciences and Humanities with the project being located at the Geophysical Institute of Karlsruhe University in Germany. Besides the compilation and maintenance of the WSM database, the project also provides tools for the visualization of the database. The latter is a key issue for data analysis, interpretation, and integration with other geodata. From 1999 onwards the database could be visualized in terms of the so-called stress maps via CASMO (Create A Stress Map Online), a web-based database interface located at http://www.world-stress-map.org/casmo (*Heidbach et al.*, 2004). With CASMO, users can select the area of interest and data sets according to data quality, stress indicator type, and depth. The stress map will be generated within a minute and sent via e-mail to the user.

The increasing number of requests from the WSM user community on a stand-alone visualisation tool with an increased functionality and capabilities to combine the stress data with other data sets encouraged us to develop CASMI (Create A Stress Map Interactively). CASMI has a graphical user interface for choosing a wide range of appropriate parameters for the visualization of the WSM database in terms of stress maps. It also allows the combination with user stress data and other geodata.

In this paper, we present the general concept of the WSM project, the content of the WSM 2005 database release, as well as the structure and functions of CASMI. We also present two stress map examples: (1) a plate-wide scale example from central Europe where the plate motion trajectories are combined with the S_H orientations, and (2) a regional example showing the changes of S_H orientation in North Germany.

2. The WSM database

2.1. Data types

The orientation of the present-day stresses in the Earth's crust is estimated primarily from earthquake focal mechanism solutions, well bore breakouts and drilling-induced fractures (from borehole images or caliper log data), in-situ stress measurements (over-

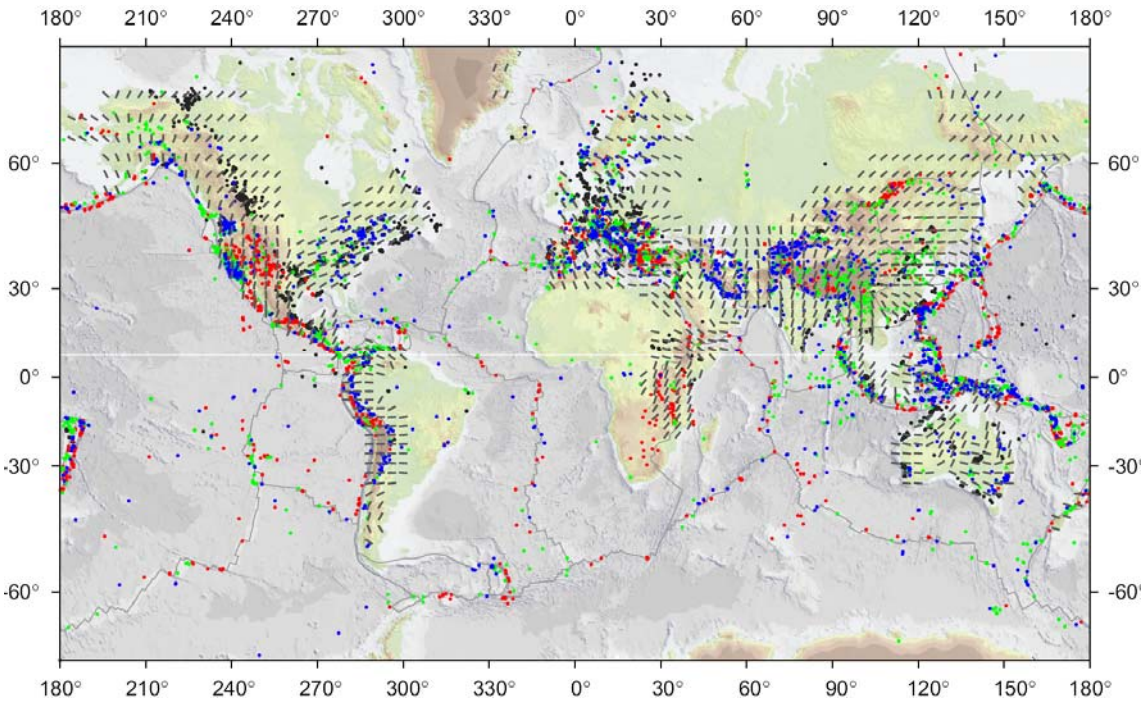

Figure 1. World Stress Map from WSM 2005 database release. Points give location of A-C quality data records from 0 to 40 km depth. Colour indicates stress regime: red = normal faulting (NF), green = strike-slip faulting (SS), blue = thrust faulting (TF), black-unknown regime (U). Short grey lines represent mean S_H orientations on a regular grid on continents calculated with smoothing algorithm of *Müller et al.* (2003). Search radius for smoothing algorithm is 750 km, data quality is weighted in smoothing procedure, and a minimum of 10 data points must be detected within this search radius for calculation of a grid value. Thin grey lines give plate boundaries from global model PB2002 of *Bird* (2003). Topography is from ETOPO2 data (National Geophysical Data Center, NGDC; http://www.ngdc.noaa.gov/), bathymetry is from *Smith and Sandwell* (1997).

coring, hydraulic fracturing), and quaternary geological indicators (fault slip, volcanic vent alignment). The stress information from these different stress measurement techniques represent various rock volumes ranging from 10^{-3} to 10^{-9} m^3 (*Ljunggren et al.*, 2003) and depths ranging from near surface down to 40 km.

2.2. Quality-ranking scheme

One of the key aspects of the WSM is on making information from different stress indicators globally comparable following a standardized quality-ranking scheme for all stress indicators. The quality-ranking scheme was introduced by *Zoback* (1991) and *Zoback and Zoback* (1989), and was refined and extended by *Sperner et al.* (2003). It guarantees reliability and global comparability of the stress data. Each data record is assigned a quality between A and E, with A being the highest quality and E the lowest. A-quality indicates that the S_H orientation is accurate to within ± 15°, B-quality to within ± 20°, C-quality to within ± 25°, and D-quality to within ± 40°. E-quality marks data records with insufficient or widely scattered (> 40°) stress information. In general, A, B, and C quality data records are considered reliable, e.g. for the use in regional stress analysis and the interpretation of geodynamic processes.

2.3. Stress information and database access

All information in the WSM database is provided in a standardized format and is available in three different file formats on the website (http://www.world-stress-map.org): ACSII, Excel spreadsheet, and dBase. The minimum information for each stress data record contains the S_H orientation, the data quality assignment, the type of stress indicator, the location, the average depth of the measurements, the tectonic stress regime, and the reference where the data are published. Additional information is compiled according to the different types of stress indicators such as stress magnitudes, number of measurements, standard deviation, rock properties, and rock age. Within the upper ~6 km of the Earth's crust the stress field is mapped by a wide range of methods with borehole breakouts being a major contributor. Below ~6 km depth, earthquakes are the only source of stress information except a few deep scientific boreholes.

2.4. WSM 2005 database release

The current WSM 2005 database was released in December 2005 and published as a Map in 2007 (*Heidbach et al.*, 2007b). It contains 15 969 data records with more than 12 000 having A-C quality (Fig. 2), i.e. they are considered to show the S_H orientation reliably to within ± 25°. Most of the stress information result from earthquake focal mechanism solutions (77%) and well bore breakouts (16%) (Fig. 2). The stress regime is unknown in 17% of the A-C quality data, since this information has not be determined or provided for most of the well bore breakouts and drilling-induced fracture data records.

3. Database visualization with CASMI

3.1. CASMI development environment

A widely used tool for plotting geodata is the Generic Mapping Tools (GMT) (*Wessel and Smith*, 1998). It is an open source collection of ~60 scripts for manipulating and plotting of geographical and Cartesian data sets as maps in encapsulated postscript format. GMT supports a wide range of map projections and transformations and comes with geographical data such as coastlines, rivers, and political boundaries. However, in order to visualize the WSM database, some additional functions are needed. The major ones are a database interface that allows to define selection criteria for the data records, a number of specific symbols for the different stress indicators and tectonic regimes, and a legend explaining the selected types and qualities of the selected stress data records.

These additional functions are provided by ~50 Unix shell and awk scripts. The scripts also execute a number of procedures needed for the automated calculation of the stress map size on the chosen plot format as well as the plate motion trajectories. In order to control both, these additional ~50 scripts as well as the options of the incorporated GMT commands for the stress map production, a so-called master script was developed. It controls all settings for the user-defined stress map production incorporating the WSM 2005 database release in combination with other data such as user stress data, plate motion trajectories, and Harvard centroid moment tensor (CMT) solutions.

For easier application of the master script, we implemented a graphical user interface based on the scripting language Perl/Tk, and gave the software tool the name CASMI (Fig. 3). It provides easy control of (a) the data record selection criteria, (b) the options of all incorporated GMT commands, and (c) the combination with a wide range of other geodata sets. CASMI contains the most recent WSM database release, the plate boundaries of the global plate model PB2002 of *Bird* (2003), the master script and

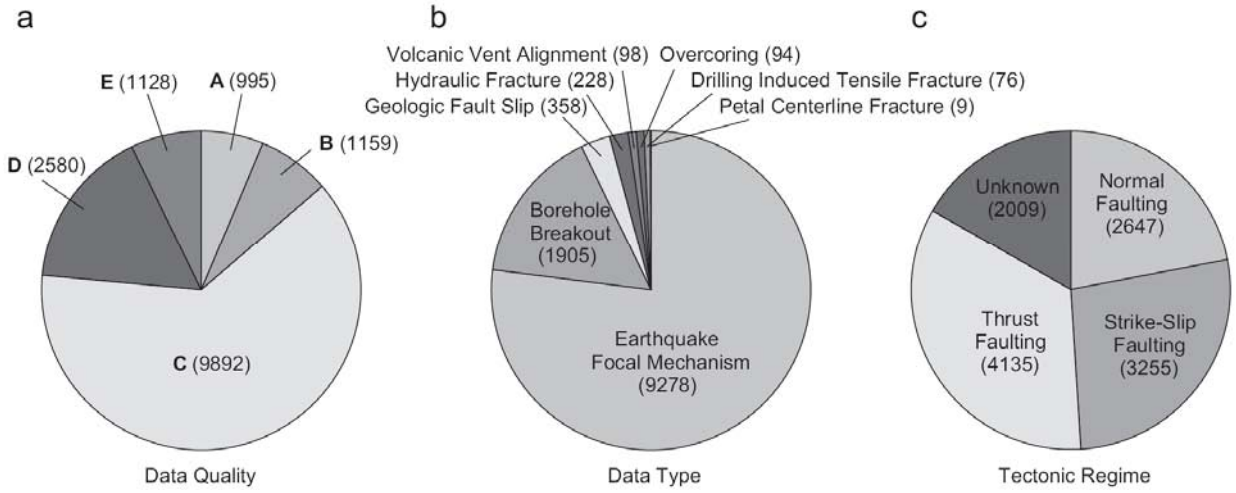

Figure 2. Statistics of WSM 2005 database release. In brackets: number of data for each subset. (a) Quality distribution of 15 976 stress data records. More than 75% have A-C quality, i.e. S_H orientation is reliable to within ±25°; (b) distribution of stress indicator type of 12 046 A-C quality stress data; (c) tectonic regime for 12 046 A-C quality stress data.

all scripts necessary to control the input and output of the used GMT commands. It is a public domain program for Unix-like operating systems. CASMI is provided free of charge via e-mail after registration on our website under http://www.world-stress-map.org/casmi. Alternatively, user-defined stress maps can be generated with the web-based database interface CASMO. The response time via e-mail is less than a minute (*Heidbach et al.*, 2004). However, compared with CASMI, its functionality is significantly lower.

3.2. Installation of CASMI

CASMI has so far been successfully tested and installed on Linux systems (SuSE, Free BSD). Since the core library is written in C and the graphical user interface in Perl/Tk, it can be installed on a wide range of Unix-like operating systems. To install and run CASMI successfully, installations of GMT (version 3.4.1 or higher), Perl (version 5.6.1 or higher), and Perl/Tk (version 800.023 or higher) must be provided.

3.3. Graphical user interface of CASMI

The graphical user interface provides control via drop down menus (Fig. 3). Each of them has a number of submenus with dialog boxes where the user can define details for the stress map production. Since GMT is the background software tool used for the stress map production, the logic for the control of the options in all dialog boxes is according to the GMT commands and options. The latter are briefly introduced in the help file of CASMI and in great detail in the GMT cookbook and the GMT manual, which are available on the GMT website (http://gmt.soest.hawaii.edu/).

The four drop down menus for the control of CASMI are

(1) The *File* menu: it controls the page setting and provides the option to produce an ASCII file of the selected stress data records, to choose the output format of the stress map (postscript, pdf, gif) and to reset, load, or save the settings for CASMI.
(2) The *Data Parameter* menu: it provides the dialog boxes for the selection criteria for the user data. It also allows the control of the symbol size and colour as well as the size and location of the stress map legend.
(3) The *Map Parameter* menu: here the setting of map attributes such as map range, projection, gridlines, topography are controlled. Topography from grid files are not included in CASMI, but can be linked in the Extras menu. The format of the grid file must be according to the definition given in the GMT manual.
(4) The *Extras* menu: in this drop down menu additional data can be added to the stress map such as topography, relative or absolute plate motion trajectories, text, polygons, symbols, and CMT solutions from Harvard (http://www.seismology.harvard.edu).

When all selections are made and confirmed in the dialog boxes, the button Make Map! generates the stress map and displays a gif-preview within the CASMI window (Fig. 3). Once the user is satisfied with the stress map, it can be saved in pdf, gif, or postscript format.

More details on the handling of CASMI and the

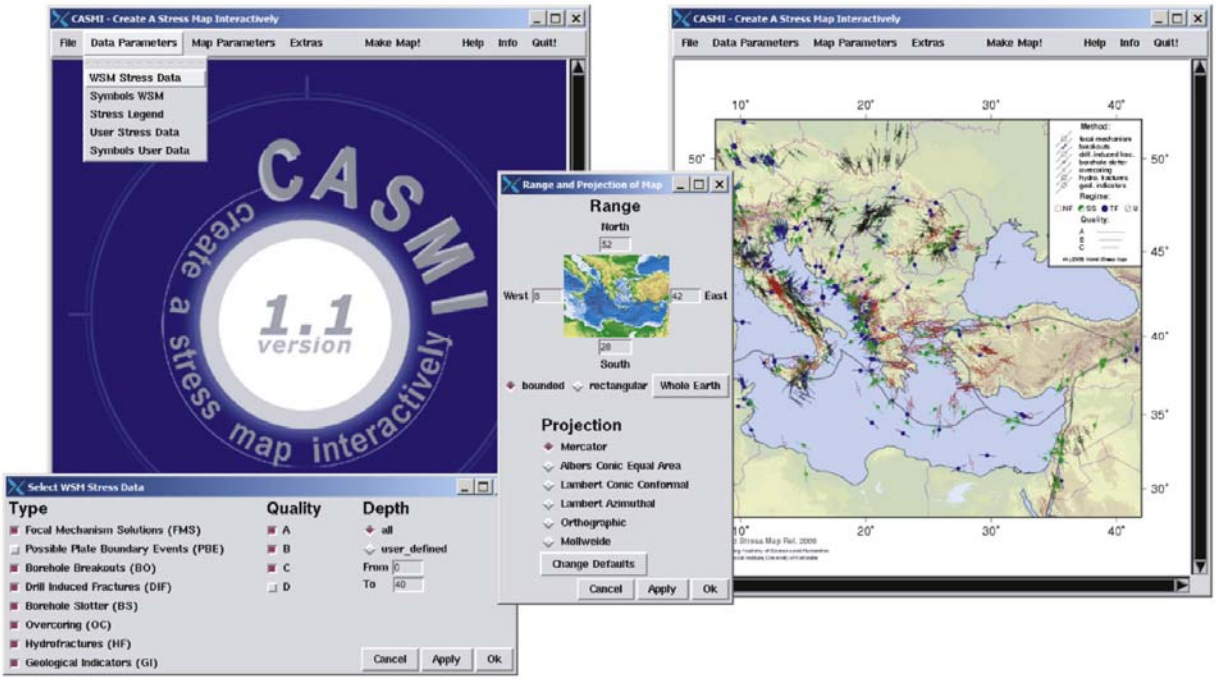

Figure 3. Graphical user interface of CASMI. Left-hand side shows starting display of CASMI and two control dialog boxes, one for stress data selection and other for range and type of projection of stress map. Right-hand side shows created stress map as a preview; it can be saved with higher resolution in postscript, pdf or gif file format.

internal structure of the program can be found in the help.pdf file. This file and the info.pdf file, which contains the GNU licence agreement, can be accessed via mouse click according to the buttons in the main menu.

4. Stress map examples

In the following sections, we present two stress maps at plate-wide and regional entirely created with CASMI. Even though the smoothed stress field on a grid was calculated externally, its visualization has been made with CASMI importing the values on the grid as user data in the Data Parameter menu. Such stress maps enable us to analyse the stress information compiled in the WSM database.

4.1. Plate-scale stress field: central Europe

For central Europe the WSM 2005 database release provides ~2700 data records with more than 1850 having A-C quality (Fig. 4). According to the principal findings of *Müller et al.*, (1992) the first-order pattern of the S_H orientation in central Europe show a NW to NNW orientation of S_H. *Müller et al.* (1992) hypothesize that this observed prevailing orientation is controlled by the plate boundary forces, i.e. by the ridge push of the Northern Atlantic and the collision of the African with the Eurasian plate. This was confirmed by several large-scale finite element models (e.g. *Jarosinski et al.*, 2006; *Gölke and Coblentz*, 1996; *Grünthal and Stromeyer*, 1992, 1994). Even though the number of data records have almost doubled since 1992 this first-order pattern can still clearly be identified in the smoothed stress field (Fig. 4). The general S_H orientation is in agreement with the convergence direction of the African plate and the Eurasian plate. Large-scale deviations from this trend occur in the Aegean and West-Anatolian region, where the slab roll-back at the Hellenic arc subduction zone produces N-S-oriented extension, and thus E-W-oriented S_H, in the back-arc (e.g. *Heidbach and Drewes*, 2003), and in the Pannonian Basin where NE-SW S_H orientation is probably due to collision in the Dinarides (*Bada et al.*, 1998). The deviations of the S_H orientation from the plate motion trajectories in the North Germany are presented in more detail in the following example.

4.2. Regional stress field changes: North Germany

In central Europe the mean S_H orientation of 144° is almost parallel to the trajectories of relative plate motion of 137° (Fig. 4). However, *Grünthal and Stromeyer* (1992) noted for the first time that there is a swing in the stress pattern towards east taking place in the North German Basin and Poland, resulting in a fan-shaped pattern of the S_H orientation (Fig. 5). Initially this observation was based on a

very small data set, but more stress data provided by *Grünthal and Stromeyer* (1994) and *Roth and Fleckenstein* (2001) supported this interpretation. These data sets and 42 additional A-C quality stress data records are now compiled in the WSM 2005 database release. They confirm the fan-shaped pattern of S_H orientation changing from NW orientation in the west over N to NE orientation in the east as seen in the smoothed stress field (Fig. 5).

Roth and Fleckenstein (2001) discuss three possible reasons for this pattern: (1) the influence of an active trans-European suture zone that separates the East European platform from the West European part of the Eurasian plate, (2) the local dominance of stresses due to postglacial rebound, and (3) that the northern boundary of the Central European Basin System has a higher lithospheric strength that acts as a mechanical barrier. Whereas the latter argument is favoured by the results of a 2D finite element model of *Marotta et al.* (2002), *Kaiser et al.* (2005) conclude from their numerical model results a combination of (1) and (2). However, the disadvantage of both models is that the eastern model boundary is close to the area of interest, and thus the rotation towards east could be to a certain extent a boundary effect of the model geometry.

A fourth source of the stress field rotation are probably the lateral density and strength contrasts across the Sorgenfrei-Teisseyre and Tornquist-Teisseyre zone where crustal thickness increases sharply from about 35 km in the west towards 50 km of the East European platform (*Thybo*, 2001). *Gölke and Coblentz* (1996) investigated in a large-scale 2D finite element model of western Europe the impact of the lateral density contrast due to topography and found that this has an impact on the stress magnitudes, but to a lesser extent on the stress orientations. *Jarosinski et al.* (2006) included in their 2D finite element model of western Europe also the effect of the varying lithospheric strength as well as the effect of the topography and received a swing of the stress field orientation towards east roughly in agreement with the stress observations. They also implemented the NW-SE striking Ham-

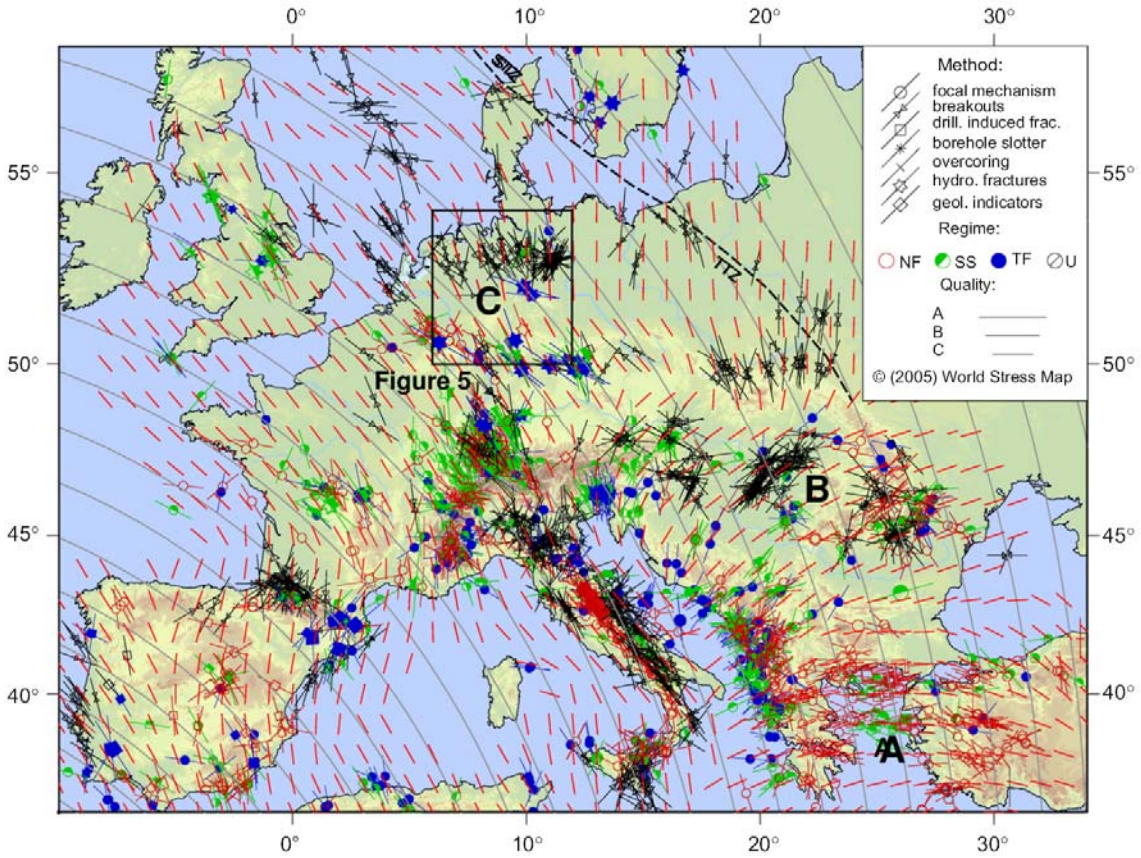

Figure 4. Stress map of central Europe. Thin grey lines show relative plate motion of Africa with respect to Eurasian plate using rotation pole from NUVEL-1A (*DeMets et al.*, 1990, 1994). Short red lines are mean S_H orientations on a regular grid calculated with smoothing algorithm of *Müller et al.* (2003). Search radius for smoothing is 300 km, data quality is weighted in smoothing procedure and a minimum of five data points must be detected within this search radius for calculation of a grid value. Regions A, B, and C are Aegean and Western Anatolian region, Pannonian basin, and North Germany where regional stress field orientation deviates from NW–SE orientation of plate-wide scale stress field. Details of region C are shown in Fig. 5. Dotted black line indicates Sorgenfrei-Teisseyre zone (STZ) and Tornquist-Teisseyre zone (TTZ), where Moho steps from about 35 to up to 50 km thickness (*Thybo*, 2001).

burg-Elbe fault zone as the southern boundary of the eastern section of the North German Basin. However, the faults display in their model results an unrealistic high displacement of 200-300 m in a predominantly aseismic area. Such a strike-slip motion releases stresses parallel to the fault, i.e. in return the remaining stresses perpendicular to the fault have a larger, but probably artificial influence on the stress orientation.

In summary, the various processes contributing to the fan-shaped stress field pattern now fully revealed in the WSM 2005 database release are still controversially discussed. So far, the existing models only reveal that strength and density contrasts, boundary conditions and geometry, as well as postglacial rebound contribute to a certain extent to the stress field re-orientations, but their relative importance is still an open question.

5. Outlook

Since data influx from the hydrocarbon industry and academia into the WSM is increasing, we will update the WSM database regularly. The new release will be announced via both the WSM and the CASMI newsletter. In the latter, we will provide the CASMI users with the new database file including a short description of how to replace the old by the new database file. A new WSM database release and a new CASMI version is planned for mid 2008. Both will be presented at the 3rd international World Stress Map conference, 15-17 October 2008 in Heidelberg, Germany (http://www.world-stress-map.org/conference).

Acknowledgements

The World Stress Map as a global collaborative project would not be possible without the effort of many scientists worldwide. We are indebted to numerous individual researchers and working groups all over the world for providing stress data, especially the WSM team members Andreas Barth, Karl Fuchs, Birgit Müller, John Reinecker, Blanka Sperner, Mark Tingay, and Friedemann Wenzel, our previous colleagues Philipp Fleckenstein and Gunda Reuschke of the Tectonic Stress Group at the Geophysical Institute of the University Karlsruhe. The complete list of WSM contributors is too numerous to be given here;

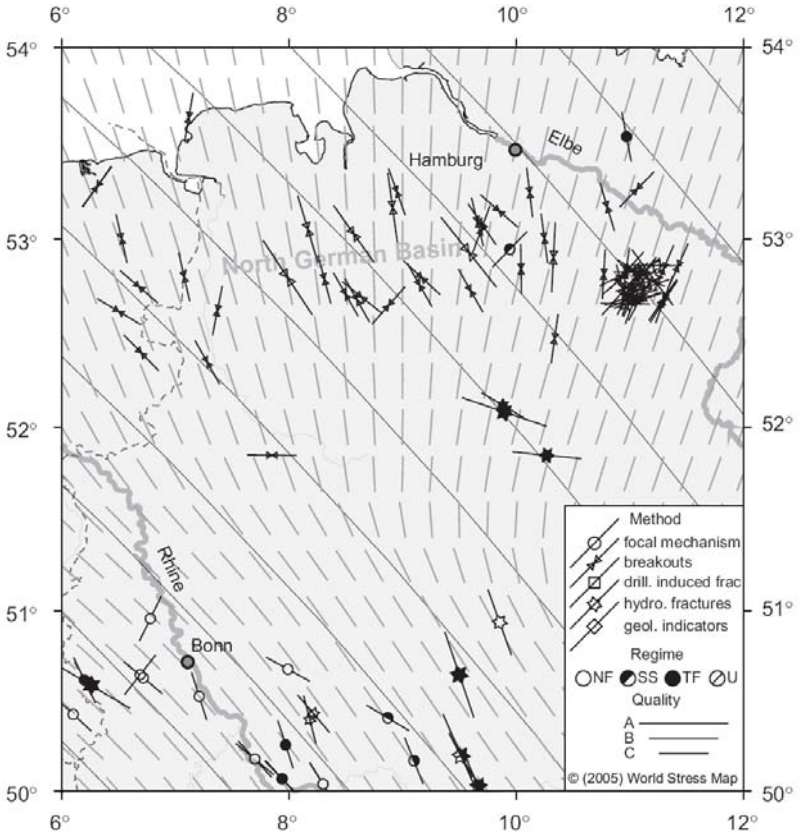

Figure 5. Stress map of northern Germany. Thin grey continuous lines mark relative plate motion of African plate relative to Eurasian plate from global plate model NUVEL-1A (*DeMets et al.*, 1990, 1994), black dotted lines are political boundaries. Short grey lines are mean S_H orientations on a regular grid calculated with smoothing algorithm of *Müller et al.* (2003). Note increase of deviation between smoothed stress field orientation to plate motion trajectories from Rhine River to Elbe River. Search radius for smoothing is 100 km, data quality is weighted in smoothing procedure and a minimum of three data points must be detected within this search radius for calculation of a grid value.

however, the authors are particularly grateful to Mark Zoback, John Townend, Richard Hillis, Philipp Fleckenstein, and Scott Reynolds for their major contributions, and to the WSM advisory board members, Egon Althaus, John Cook, Roy Gabrielsen, Domenico Giardini, Helmut Kipphan, Onno Oncken, Chris Reigber, Markus Rothacher, and Mark Zoback for their long-term support. We also want to thank Veronika Wehrle and Stefan Hettel who wrote the basic scripts to extend the functionality of GMT. We also acknowledge additional funding for Jens Höhne from the Heidelberg Academy of Sciences and Humanities, the comments and advise from Birgit Müller and Blanka Sperner on the manuscript. We explicitly thank Tom Blenkinsop and an anonymous review for very constructive comments on the paper and the software, which led to notable improvement and valuable ideas for future development of our software.

References

Bada, G., Cloetingh, S., Gerner, P., Horváth, F., 1998. Sources of recent tectonic stress in the Pannonian region: inferences from finite element modelling. Geophysical Journal International 134, 87–101.

Bird, P., 2003. An updated digital model for plate boundaries. Geochemistry, Geophysics, Geosystems 4, 1027.

DeMets, C., Gordon, R.G., Argus, D.F., Stein, S., 1990. Current plate motions. Geophysical Journal International 101, 425-478.

DeMets, C., Gordon, R.G., Argus, D.F., Stein, S., 1994. Effect of recent revisions to the geomagnetic reversal time scale on estimates of current plate motions. Geophysical Research Letters 20, 2191-2194.

Gölke, M., Coblentz, D., 1996. Origins of the European regional stress field. Tectonophysics 266, 11–24.

Grünthal, G., Stromeyer, D., 1992. The recent crustal stress field in Central Europe: trajectories and finite element modeling. Journal of Geophysical Research 97, 11805-11820.

Grünthal, G., Stromeyer, D., 1994. The recent crustal stress field in Central Europe sensu lato and its quantitative modelling. Geologie en Mijnbouw 73, 173–180.

Fuchs, K., Müller, B., 2001. World Stress Map of the Earth: a key to tectonic processes and technological applications. Naturwissenschaften 88, 357–371.

Heidbach, O., Drewes, H., 2003. 3-D Finite element model of major tectonic processes in the Eastern Mediterranean. In: Nieuwland, D. (Ed.), New Insights in Structural Interpretation and Modelling. Geological Society Special Publication 212, London, pp. 259–272.

Heidbach, O., Barth, A., Connolly, P., Fuchs, F., Müller, B., Reinecker, J., Sperner, B., Tingay, M., Wenzel, F., 2004. Stress maps in a minute: the 2004 World Stress Map Release. Eos Transactions 85, 521–529.

Heidbach, O., Reinecker, J., Tingay, M., Müller, B., Sperner, B., Fuchs, K., Wenzel, F., 2007a. Plate boundary forces are not enough: second- and third-order stress patterns highlighted in the World Stress Map database, Tectonics. doi:10.1029/2007TC002133.

Heidbach, O., Fuchs, K., Müller, B., Reinecker, J., Sperner, B., Tingay, M., Wenzel, F., 2007b. The World Stress Map-Release 2005, 1:46000000. Commission of the Geological Map of the World, Paris.

Jarosinski, M., Beekman, F., Bada, B., Cloetingh, S., 2006. Redistribution of recent collision push and ridge push in Central Europe: insights from FEM modelling. Geophysical Journal International 167, 860–880.

Kaiser, A., Reicherter, K., Hübscher, C., Gajewski, D., 2005. Variation of the present-day stress field within the North German Basin-insights from thin shell FE modeling based on residual GPS velocities. Tectonophysics 397, 55–72.

Ljunggren, C., Chang, Y., Janson, T., Christiansson, R., 2003. An overview of rock stress measurement methods. International Journal of Rock Mechanics 40, 975–989.

Marotta, A.M., Bayer, U., Thybo, H., Scheck, M., 2002. Origin of the regional stress in the North German Basin: results from numerical modelling. Tectonophysics 360, 245–264.

Müller, B., Zoback, M.L., Fuchs, K., Mastin, L., Gregersen, S., Pavoni, N., Stephansson, O., Ljunggren, C., 1992. Regional patterns of tectonic stress in Europe. Journal of Geophysical Research 97, 11783–11803.

Müller, B., Wehrle, V., Hettel, S., Sperner, B., Fuchs, F., 2003. A new method for smoothing oriented data and its application to stress data. In: Ameen, M. (Ed.), Fracture and In-Situ Stress Characterization of Hydrocarbon Reservoirs. Geological Society Special Publication 209, London, pp. 107–126.

Reinecker, J., Heidbach, O., Tingay, M., Sperner, B., Müller, B., 2005. The 2005 release of the World Stress Map, available online at http://www.world-stress-map.org.

Richardson, R.M., 1992. Ridge forces, absolute plate motions, and the intraplate stress field. Journal of Geophysical Research 97, 11739–11748.

Roth, F., Fleckenstein, P., 2001. Stress orientations found in north-east Germany differ from the West European trend. Terra Nova 13, 289–296.

Smith, W.H.F., Sandwell, D.T., 1997. Global sea floor topography from satellite altimetry and ship depth soundings. Science 277, 1956–1962.

Sperner, B., Müller, B., Heidbach, O., Delvaux, D., Reinecker, J., Fuchs, K., 2003. Tectonic stress in the Earth's Crust: advances in the World Stress Map Project. In: Nieuwland, D. (Ed.), New Insights in Structural Interpretation and Modelling. Geological Society Special Publication 212, London, pp. 101–116.

Thybo, H., 2001. Crystal structure along the EGT profile across the Tornquist Fan interpreted from seismic, gravity and magnetic data. Tectonophysics 334, 155–190.

Wessel, P., Smith, W.H.F., 1998. New, improved version of Generic Mapping Tools released. Eos Transactions 79, 579.

Zoback, M.D., Zoback, M.L., 1991. Tectonic Stress field of North America and Relative Plate Motions. In: Slemmons, D.B., Engdahl, E.R., Zoback, M.D., Blackwell, D.D. (Eds.), Neotectonics of North America Decade Map, Vol. I. Geological Society of America, Boulder, CO, pp. 339–366.

Zoback, M.L., 1992. First and second order patterns of stress in the lithosphere: the World Stress Map Project. Journal of Geophysical Research 97, 11703–11728.

Zoback, M.L., Zoback, M.D., 1989. Tectonic stress field of the conterminous United States. In: Pakiser, L.C., Mooney, W.D. (Eds.), Geophysical Framework of the Continental United States. Geological Society of America Memoirs 172, Boulder, CO, pp. 523–539.

Zoback, M.L., Zoback, M.D., Adams, J., Assumpc-a˜ o, M., Bell, S., Bergman, E.A., Blümling, P., Brereton, N.R., Denham, D., Ding, J., Fuchs, K., Gay, N., Gregersen, S., Gupta, H.K., Gvishiani, A., Jacob, K., Klein, R., Knoll, P., Magee, M., Mercier, J.L., Müller, B.C., Paquin, C., Rajendran, K., Stephansson, O., Suarez, G., Suter, M., Udi´as, A., Xu, Z.H., Zhizhin., M., 1989. Global patterns of tectonic stress. Nature 341, 291–298.

Originally published as:
TECTONICS, VOL. 26, TC6014, doi:10.1029/2007TC002133, 2007

Plate boundary forces are not enough: Second- and third-order stress patterns highlighted in the World Stress Map database

Oliver Heidbach,[1] John Reinecker,[2,3] Mark Tingay,[2,4] Birgit Müller,[2] Blanka Sperner,[2,5] Karl Fuchs,[1,2] and Friedemann Wenzel[1,2]

Received 17 March 2007; revised 3 August 2007; accepted 10 September 2007; published 29 December 2007.

[1] The World Stress Map Project compiles a global database of contemporary tectonic stress information of the Earth's crust. Early releases of the World Stress Map Project demonstrated the existence of first-order (plate-scale) stress fields controlled by plate boundary forces and second-order (regional) stress fields controlled by major intraplate stress sources such as mountain belts and zones of widespread glacial rebound. The 2005 release of the World Stress Map Project database provides, for some areas, high data density that enables us to investigate third-order (local) stress field variations, and the forces controlling them such as active faults, local inclusions, detachment horizons, and density contrasts. These forces act as major controls on the stress field orientations when the magnitudes of the horizontal stresses are close to isotropic. We present and discuss examples for Venezuela, Australia, Romania, Brunei, western Europe, and southern Italy where a substantial increase of data records demonstrates some of the additional factors controlling regional and local stress patterns. **Citation:** Heidbach, O., J. Reinecker, M. Tingay, B. Müller, B. Sperner, K. Fuchs, and F. Wenzel (2007), Plate boundary forces are not enough: Second- and third-order stress patterns highlighted in the World Stress Map database, Tectonics, 26, TC6014, doi:10.1029/2007TC002133.

1. Introduction

[2] The World Stress Map (WSM) is the global compilation of information on the present-day tectonic stress field in the Earth's crust (Figure 1a). The stress information is recorded in a standardized format and quality-ranked in order to be comparable on a global scale [*Sperner et al.*, 2003; *Zoback and Zoback*, 1991; *Zoback*, 1992; *Zoback and Zoback*, 1989]. Over the last 15 years the WSM Project has provided a global database of information on the intraplate state of stress in the Earth's crust [*Heidbach et al.*, 2007; *Sperner et al.*, 2003; *Zoback*, 1992; *Zoback et al.*, 1989]. It has revealed fundamental insights into the first- and second-order patterns of crustal stress on plate-wide and regional scales larger than 500 km as well as on the forces controlling them [*Zoback*, 1992; *Zoback et al.*, 1989] (Figure 1b). The analysis of the first WSM database release in 1992 revealed that the orientation of maximum horizontal compressional stress S_H in North America, South America and Europe are, at the plate scale, predominately subparallel to absolute or relative plate motions [*Müller et al.*, 1992; *Richardson*, 1992; *Zoback*, 1992]. This correlation of stress orientations and plate motions suggests that the first-order intraplate stress patterns are the result of the same forces that drive plate motion, in particular ridge push, slab pull, trench suction, collisional forces, and traction at the base of the lithosphere [*Gölke and Coblentz*, 1996; *Grünthal and Stromeyer*, 1992; *Richardson*, 1992; *Zoback and Zoback*, 1991; *Zoback*, 1992; *Zoback and Burke*, 1993; *Zoback et al.*, 1989]. Second-order stress patterns (100-500 km scales) show that lateral density contrasts, caused by continental rifting, isostatic compensation and topography, deglaciation effects, as well as lithospheric flexure have an additional impact on large-scale stress fields [*Bird et al.*, 2006; *Coblentz et al.*, 1998; *Coblentz and Sandiford*, 1994; *Dyksterhuis et al.*, 2005; *Hillis and Reynolds*, 2000; *Zoback*, 1992; *Zoback and Mooney*, 2003].

[3] The last 20 years have seen a major increase in the application of present-day stress information on smaller spatial scales (< 100 km) where third-order effects such as active faults, seismically induced stress changes due to large earthquakes or volcanic eruption, local density contrasts (e.g., from salt diapirs, and detachment horizons) can lead to significant deviations of the stress orientations with respect to the regional and plate-wide stress patterns [e.g., *Bell*, 1996a; *Tingay et al.*, 2006]. These local effects can be key controls for geothermal and petroleum reservoir exploration, production and management [*Fuchs and Müller*, 2001].

[4] Knowledge of the stress field is also critical for seismic hazard assessment [e.g., *Harris et al.*, 1995; *Heidbach and Ben-Avraham*, 2007; *Steacy et al.*, 2005; *Stein et al.*, 1997]. The coseismically induced changes in Coulomb failure stress can serve as indicators for the location and distribution of future earthquakes [e.g., *Harris*, 2002; *Heidbach and Ben-Avraham*, 2007; *Nalbant et al.*, 2002]. Comparison of stresses before and after strong earthquakes as well as comparison of stress orientations with strain orientations give insights into the amount of coseismic stress drop and local stress changes [*Townend and Zoback*, 2006]. This is associated with changes in the orientation of faults which are optimally oriented with respect to the prevailing regional and local stress field [e.g., *Bohnhoff et al.*, 2006; *Hardebeck and Michael*, 2004;

[1] Geophysical Institute, Universität Karlsruhe (TH), Karlsruhe, Germany.
[2] Heidelberg Academy of Sciences and Humanities, Heidelberg, Germany.
[3] Now at Institute of Geosciences, University of Tübingen, Tubingen, Germany.
[4] Now at School of Earth and Environmental Sciences, University of Adelaide, Adelaide, South Australia, Australia.
[5] Now at Geological Institute, University of Freiberg, Freiberg, Germany.

0278-7407/07/2007TC002133$12.00

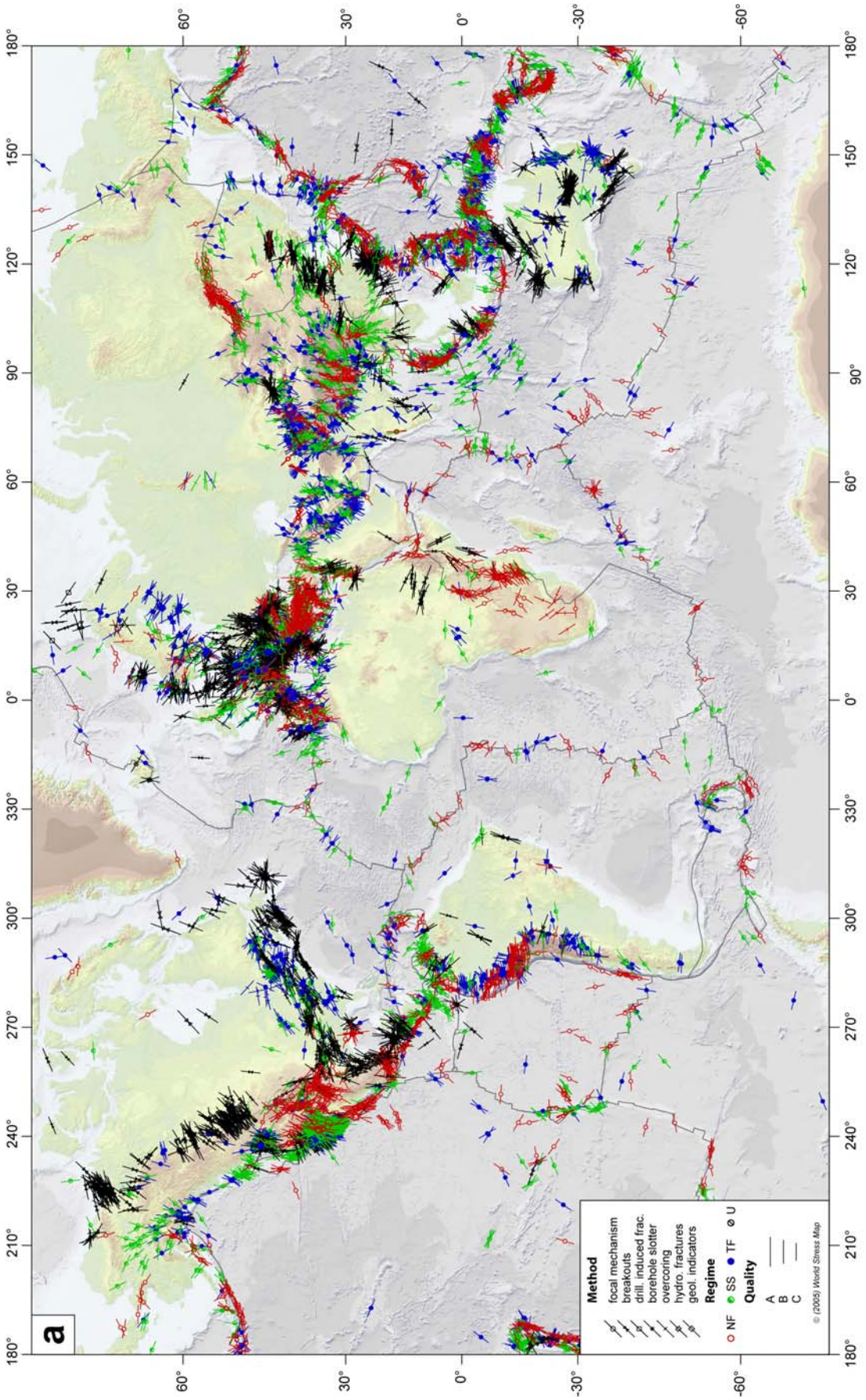

Figure 1a. Distribution of stress data records with A-C quality. Colors indicate stress regimes with red for normal faulting (NF), green for strike-slip faulting (SS), blue for thrust faulting (TF), and black for unknown regime (U). Lines represent the orientation of maximum horizontal compressional stress (S_H); line length is proportional to quality. Plate boundaries are taken from the global model PB2002 of *Bird* [2003]. Topography is based on the ETOPO2 data from the National Geophysical Data Center (NGDC) including bathymetry data of *Smith and Sandwell* [1997].

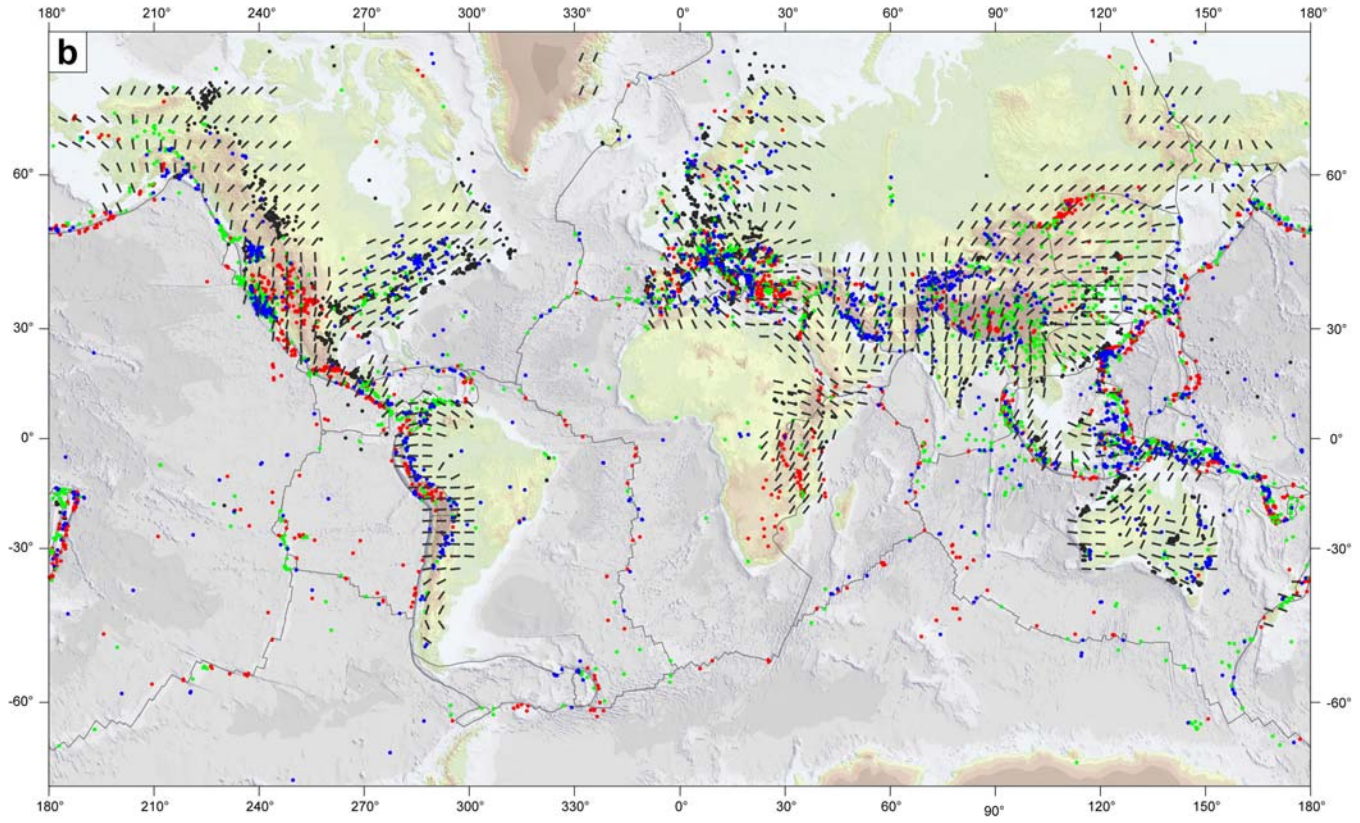

Figure 1b. Legend, stress symbols, and data as in Figure 1a. Thick grey lines represent the smoothed stress field for continental areas using a quality- and distance-weighted algorithm [*Müller et al.*, 2003]. The search radius is r = 750 km, and a minimum of 10 data records within the search radius is requested for calculating the mean stress orientation at a grid point. Note the plate-wide stress pattern and the correlation between the changes from strike-slip and thrust faulting toward normal faulting in areas with high topography.

King et al., 1994; *Provost and Houston*, 2003].

[5] For these applications, from plate-wide to regional to local scale, the WSM database provides a fundamental resource. The database itself as well as detailed descriptions for the stress indicators and other database related technical information, are available at the project's web site at http://www.world-stress-map.org. The past WSM releases gave insight into large-scale patterns of regional stress orientations, i.e., the first-order stress patterns due to plate boundary forces, and second-order patterns due to topography, large lateral density variations, and deglaciation effects. However, in addition to further defining broad-scale stress patterns, the WSM 2005 database release has developed some regions of high data density that enables us to investigate variations in stress orientations at local scales and to discuss factors controlling third-order stress patterns. With respect to the WSM 2000 release the WSM 2005 release has increased the number of data records by more than 6600 to a total of almost 16,000 (Figure 1a). The majority of the new data records are from western Europe and areas where basic knowledge on the first- and second-order stress pattern was available before (e.g., California, Australia and in the vicinity of plate boundaries). The intraplate areas of the oceans as well as the continental areas of Africa, Arabia, eastern South America and eastern Europe remain undiscovered in terms of their crustal stress state (Figure 1).

[6] This paper is organized into two sections. In the first, we present major achievements with respect to the last publication on the WSM 2000 database release [*Sperner et al.*, 2003] and give a brief overview on the data types used in the WSM, the quality ranking scheme, and the visualization software tools. Technical changes on the data records of the WSM 2005 database release, the database itself, and the visualization software are documented on the WSM website http://www.world-stress-map.org. In the second section, we illustrate the time and scale dependence of stress patterns by zooming into the stress patterns of western Europe. Furthermore, we present case studies at different spatial scales from Venezuela, Australia, Romania, and Brunei where the increase in data records gave new detailed insights into regional to local stress field properties and thus enabled new tectonic interpretations.

2. WSM Database

[7] The WSM project is a collaborative project of academia, industry and governmental organizations that aims to understand the sources of stress in the Earth's crust. It was initiated in 1986 under the auspices of the International Lithosphere Program. The results of the first WSM compilation were published in 1992 [*Zoback*, 1992]. Since 1995 the WSM is a research project of the Heidelberg Academy of Sciences and Humanities and is located at the Geophysical Institute of Universität Karlsruhe (TH) in Germany.

[8] Updates of the WSM database have been made

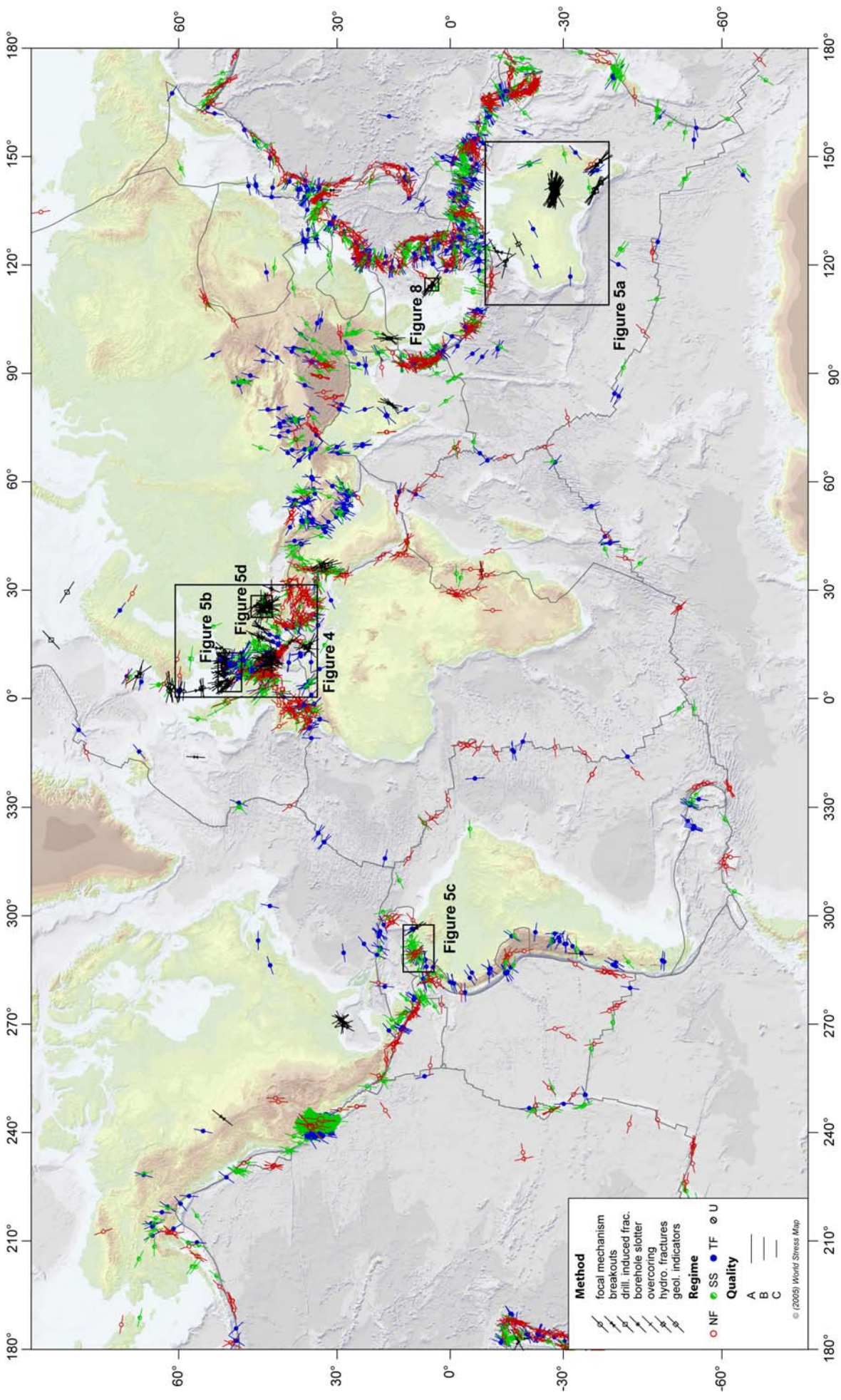

Figure 2. Global distribution of new data records with A-C quality since the WSM database release 2000. Boxes indicate location of stress map examples given in Figures 5a-5d and Figures 4 and 8. Stress symbols are as in Figure 1.

Table 1. Data Type and Quality Distribution in the WSM 2005 Database Release and Increases Since 2000

Data Type (Abbreviation)	WSM 2005 A-E Quality	WSM 2005 A-C Quality	Increase Since 2000 A-E Quality[a]	Increase Since 2000 A-C Quality[a]
Focal mechanisms (FMS, FMC, FMA)	10,619	9278	5067	4882
Borehole breakouts (BO, BOC, BOT)	3365	1905	1056	264
Drilling-induced fractures (DIF)	248	76	203	40
Geological: fault slip (GFI, GFM, GFS)	434	358	108	73
HydroFrac (HF, HFG, HFP, HFM)	349	228	89	70
Borehole slotter (BS)	33	0	33	0
Overcoring (OC)	611	94	16	4
Geological: volcanic alignment (GVA)	220	98	7	7
Petal centreline fractures (PC)	9	9	0	0
Shear wave splitting (SW)	2	0	0	0
Stress indicator not given (none)[b]	79	0	79	0
Total	15,969	12,046	6658	5340

[a] Column gives the total number of new data. However, the difference with respect to the total number given in the first column will not result in the number of data in the WSM 2000 release of *Sperner et al.* [2003] since data eliminated from the database are not taken into account.
[b] These are data records with E-quality from well bores where the data type is unknown.

available online in 1997, 2000, 2003, 2004, and in December 2005 (*B. Müller et al.*, 2000 and 1997 releases of the World Stress Map, and *J. Reinecker et al.*, 2003, 2004, and 2005 releases of the World Stress Map, available online at www.world-stress-map.org) [*Sperner et al.*, 2003]. The total number of data records increased from ~7300 in 1992 over 10,920 in 2000 to 15,969 data records in 2005.

2.1. Data Types

[9] The present-day stress orientation is deduced from focal mechanisms (FM), borehole breakouts (BO), drilling-induced fractures (DIF, from borehole images or caliper log data), in situ stress measurements (OV: overcoring, HF: hydraulic fracturing, BS: borehole slotter), and geological indicators (GF: fault slip data, GVA: volcanic vent alignments). Further details on each method are given by *Zoback and Zoback* [1989, 1991], *Zoback* [1992], *Zoback and Zoback* [2002], *Sperner et al.* [2003], *Wagner et al.* [2004], *Bell* [1996b], and references therein.

[10] The various stress indicators reflect the stress field of different rock volumes ranging from 10^{-3} to 10^{9} m^3 [*Ljunggren et al.*, 2003] and different depths ranging from near surface down to 40 km depth. Within the upper 6 km of the Earth's crust the stress field is mapped by a wide range of methods with borehole breakouts as a major contributor. Below ~6 km depth focal mechanisms are the only stress indicators available, except a few scientific drilling projects such as the KTB project in Germany which reached a depth of 9.1 km [*Brudy et al.*, 1997].

2.2. Quality Ranking Scheme

[11] The success of the WSM is based on a standardized quality ranking scheme for the individual stress indicators making them comparable on a global scale. The quality ranking scheme was introduced by *Zoback and Zoback* [1989, 1991], and refined and extended in the work of *Sperner et al.* [2003]. Details on the quality ranking scheme can be found on the project's web site at http://www.world-stress-map.org. It is internationally accepted and guarantees reliability and global comparability of the stress data. Each stress data record is assigned a quality between A and E, with A being the highest quality and E the lowest. A-quality means that the orientation of the maximum horizontal compressional stress (S_H) is accurate to within ± 15°,B-quality to within ± 20°, C-quality to within ± 25°, and D-quality to within ± 40°. For most methods these quality classes are defined through standard deviation of S_H. E-quality data records do not provide sufficient information or have standard deviations greater than 40°. These data records, mainly from well bores containing insufficient stress information, are only kept for bookkeeping purposes. In general, A-, B- and C-quality stress indicators are considered reliable for the use in analyzing stress patterns and the interpretation of geodynamic processes.

2.3. Stress Information

[12] All stress information is compiled in a database of standardized format. The minimum information for each stress data record is the orientation of S_H, the quality of the S_H orientation, the type of stress indicator, the location and depth of the measurement, the tectonic stress regime, and the source references. Additional information is compiled according to the different types of stress indicators such as stress magnitude, number of measurements, rock parameters, and rock age.

2.4. Database Access and Visualization

[13] The database can be downloaded from the WSM web site (www.world-stress-map.org) in three different data formats: ASCII, MS Excel1, and dBase1. In order to visualize the data records stress maps showing the S_H orientation, the quality, the type of stress indicator, and the stress regime can be used (Figure 1a). The project's web site provides 65 predefined stress maps for selected regions worldwide. In addition, users can generate their own custom-made stress maps either by using the Web-based database interface CASMO (Create A Stress Map Online), available at http://www.world-stress-map.org/casmo [*Heidbach et al.*, 2004] or the offline software

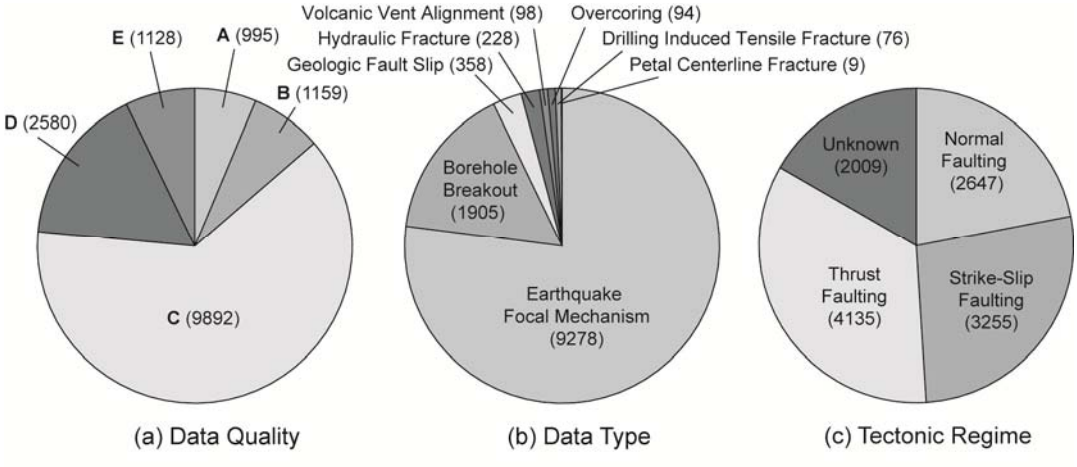

Figure 3. Distribution of data records according to (a) data quality ($\boldsymbol{n}$ = 15,969) (b) data type (only A-C, $\boldsymbol{n}$ = 12,046), and (c) tectonic stress regime (only A-C, $\boldsymbol{n}$ = 12,046). Number of data records is given in brackets.

CASMI (Create A Stress Map Interactively) [*Heidbach and Höhne*, 2007]. CASMI is a public domain program running under Unix-like operating systems. It has a graphical user interface based on the public domain software GMT (Generic Mapping Tools) [*Wessel and Smith*, 1998] and with specific features needed to visualize the WSM data. CASMI includes the WSM 2005 database release and will be sent free of charge after registration at the project's web site (http://www.world-stress-map.org/casmi).

2.5. Achievements of the WSM 2005 Database Release

[14] The WSM 2005 database release has, in comparison to the WSM 2000 release, 6658 new or revised data records, respectively (Figure 2). From the total number of 15,969 data records more than 12,000 data records are assigned to A-, B-, or C-quality (Figure 1), i.e., they are considered to show the S_H orientation to within ± 25° (Table 1 and Figure 3a). Most of the stress data records were derived from earthquake focal mechanisms (77%) and borehole breakouts (16%, Figure 3b). The majority of the new and revised data records are deduced from focal mechanism solutions (76%), borehole breakouts (16%), and drilling-induced fractures (3%). Approximately 80% of these new data records have A- to C-quality (Table 1). Most of the stress data records deduced from focal mechanisms are taken from the Global CMT Project (formally known as Harvard CMT catalogue; now available online under www.globalcmt.org), and published since 1983 in a series of reports in Physics of the Earth and Planetary Interiors [e.g., *Ekström et al.*, 2005]. The tectonic stress regime could be assigned for 83% of the A-C quality data (Figure 3c). For the remaining 17% of data records the stress regime is unknown, either because this information is in most cases not available for borehole breakouts and drilling-induced fractures, or because the principal axes are too oblique to the Earth's surface.

3. Scale-Dependent Stress Patterns

[15] The increase of present-day stress data records in the WSM 2005 database release provides a detailed stress data set in a number of regions. Zooming into local scales, i.e., regions with lateral extent in the order of the crustal thickness or smaller, we can now clearly identify stress rotations with respect to the plate-wide and regional stress orientation due to third-order sources of stress. Seven examples with stress patterns from different spatial scales are presented in the following sections. We discuss these examples in decreasing spatial scales, from plate-wide via regional to local scales.

3.1. Plate-Wide Stress Pattern: Impact of Plate Boundary Forces

3.1.1. Stress Map of Western Europe

[16] For western Europe the WSM 2005 database release provides 3188 data records with 1811 of these having A-C quality (Figure 4). According to the principal findings of *Müller et al.* [1992], the first-order pattern shows a prevailing NW to NNW orientation of S_H. *Müller et al.* [1992] conclude from their analysis that this orientation is mainly controlled by plate boundary forces, in particular by ridge push of the North Atlantic and collision of the Africa Plate with the Eurasia Plate. This has been confirmed by several large-scale finite element models [*Gölke and Coblentz*, 1996; *Grünthal and Stromeyer*, 1992, 1994; *Jarosinski et al.*, 2006]. Even though the amount of stress data for western Europe has almost doubled since 1992, this first-order pattern is still clearly visible in the smoothed stress field (Figure 4). The prevailing S_H orientation is parallel to the relative plate motion of the Africa Plate with respect to the Eurasia Plate. Large-scale deviations from this trend occur in the Aegean and the western Anatolian region, where the slab rollback at the Hellenic arc induces a E-W S_H orientation in the back-arc region [*Heidbach and Drewes*, 2003], and in the Pannonian Basin where the NE-SW orientation of S_H is probably due to collision in the Dinarides [*Bada et al.*, 1998, 2007].

[17] The smoothed S_H orientation across Italy is similar to that in western Europe (Figure 4). It shows a NW-SE trend indicating that the convergence between the Africa Plate and the Eurasia Plate is responsible for this large-

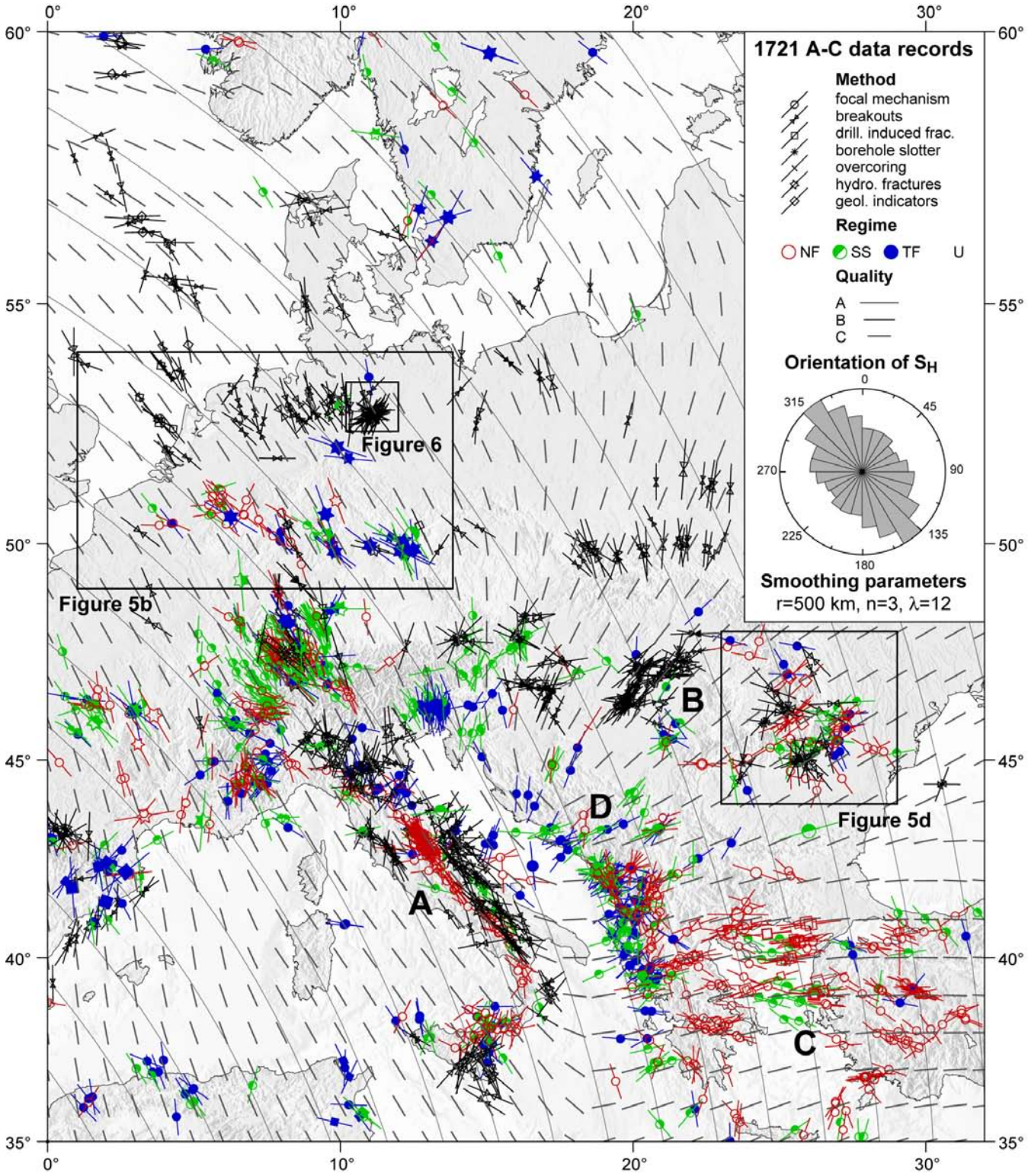

Figure 4. Stress map of western Europe. Stress symbols and smoothed stress field legend are as in Figure 1. Smoothing parameters are the search radius ($\boldsymbol{r}$), the minimum number of data ($\boldsymbol{n}$) within the search radius, and the smoothing factor ($\boldsymbol{\lambda}$). Thin gray lines represent the relative plate motion trajectories of the Africa Plate with respect to the Eurasia Plate from the global plate model NUVEL-1A [*DeMets et al.*, 1990, 1994]. Topography is based on the ETOPO2 data from the National Geophysical Data Center (NGDC) including bathymetry data from *Smith and Sandwell* [1997]. Note the rose diagram showing that the prevailing $\boldsymbol{S_H}$ orientation is approximately 145°. Letters label the areas of Italy (A), the Pannonian Basin (B), Aegean and western Anatolia (C), and the Dinarides (D).

scale stress field. Local deviations near the coast and toward the Alps and Dinarides might result from lateral density contrasts, topography, the ongoing counterclockwise rotation of the Adriatic Block relative to the Eurasia Plate, and the collisional resistance along the NW-SE striking Dinaride mountains.

[18] Plate boundary forces are clearly identified as the key control for the western European first-order plate-wide stress pattern as well as for other large tectonic plates such as the South America Plate [*Assumpção*, 1992; *Coblentz and Richardson*, 1996; *Meijer et al.*, 1997; *Meijer and Wortel*, 1992] and the North America Plate [*Humphreys and Coblentz*, 2007; *Richardson and Reding*, 1991; *Zoback and Zoback*, 1991; *Zoback*, 1992; *Zoback and Zoback*, 1989]. However, the reverse statement, i.e., that plate boundary forces do not control the stress pattern in areas not exhibiting large-scale stress patterns, is not always true, as demonstrated by the stress field across the Australian continent, shown in the next example.

3.1.2. Stress Map of Australia

[19] The data compilation for Australia and neighboring countries has been accomplished by the research team of the Australasian Stress Map (ASM) Project [*Hillis and Reynolds*, 2000] following the WSM quality assessment scheme. The ASM now contains almost 1000 A-C quality stress data records [e.g., *Hillis et al.*, 1999, 1997; *Hillis and Reynolds*, 2000; *Reynolds and Hillis*, 2000]. The Australian stress pattern is more diverse than the one from western Europe, North America or South America on the same spatial scale. Although the Australian continent is moving roughly NNW, it exhibits a number of distinct stress provinces with different mean S_H orientations [*Hillis and Reynolds*, 2000; *Reynolds et al.*, 2002]. Whereas southwestern Australia has a prevailing E-W S_H orientation, northern Australia has a NE-SW to N-S trend, and in southeastern Australia the mean S_H orientations range from NW-SE over E-W to SW-NE (Figure 5a). Thus the correlation of plate motion trajectories with S_H orientations is not visible [*Hillis and Reynolds*, 2000; *Zoback*, 1992; *Zoback et al.*, 1989]. However, despite this lack of an apparent link between the present-day stress and plate motion, the present-day stress field across Australia is still primarily controlled by far-field forces exerted at the plate boundary.

[20] In contrast to other large continental plates the Indo-Australia Plate is bordered by a complex pattern of different plate boundary types causing the diversity in the large-scale stress pattern [*Hillis and Reynolds*, 2000]. Even though the southern plate boundary exclusively consists of oceanic rifting, the northern, northwestern and eastern plate boundaries show a wide range of convergent and transform plate boundaries alternating on small scales [*Bird*, 2003]. In particular, the Indo-Australia Plate exhibits well defined stress fields, oriented normal to the plate boundary, that radiate outward from zones of continental collision, such as the Himalayas, Papua New Guinea and New Zealand (Figure 1). Furthermore, at the northern border the ongoing collision of the Ontong-Java Plateau with the Indo-Australia Plate causes a complex situation including subduction with different orientations, rollback of subduction zones which impose suction forces, back-arc spreading, and oceanic collision [*Bird*, 2003; *Mann and Taira*, 2004]. Also, farther west the distribution and orientation of different plate boundary forces is complex [*Bird*, 2003]. However, even though the stress pattern in the Indo-Australia Plate is diverse, plate boundary forces are controlling the S_H orientation [*Hillis and Reynolds*, 2000]. This is confirmed by numerical finite element studies of *Coblentz et al.* [1998], *Reynolds et al.* [2002], *Sandiford et al.* [2004], and *Dyksterhuis et al.* [2005]. These models show that the diversity of stress patterns in Australia monitors the complexities of the plate boundary geometry of the Indo-Australia Plate. The comparatively simple absolute motion-parallel plate-scale stress patterns in the Eurasia, the North America, and the South America Plate are (tectonically) bordered by rather simple boundary geometries with forces pushing and pulling the plate in broadly the same direction.

3.2. Regional-Scale Stress Patterns: Impact of Topography, Density, and Strength Contrasts

3.2.1. Stress Map of Northern Germany and Netherlands

[21] Close examination of the western European stress map (Figure 4) over northern Germany and Netherlands (Figure 5b) reveals more regional details of the stress pattern. Whilst the plate-scale stress field for this region indicates stresses to be NW-SE to NNW-SSE (Figure 4), zooming in on the same data set reveals a regional fan-shaped stress pattern with stresses ranging from NW-SE in the west to NE-SW in the east (Figure 5b). This fan-like stress pattern was noted for the first time by *Grünthal and Stromeyer* [1992]. Initially this observation was based on a very small data set, but more stress data provided by *Grünthal and Stromeyer* [1994] and *Roth and Fleckenstein* [2001] further supported the suggested fan-like stress pattern. Finally, this stress pattern was confirmed in the WSM 2005 database release owing to the addition of 298 data records in northern Germany and Netherlands, largely from borehole breakout analysis (Figure 5b). These data mainly came from WSM research projects in collaboration with the German Society for Petroleum and Coal Science and Technology, DGMK [*Fleckenstein et al.*, 2004], the Federal Office for Radiation Protection, BfS [$n = 85$, *Connolly et al.*, 2003], the Organization of Applied Natural Sciences in Holland, TNO [$n = 97$, *van Eijs and van Dalfsen*, 2004], and publications of *Grote* [1998] ($n = 42$) and *Roth and Fleckenstein* [2001] ($n = 5$).

[22] *Roth and Fleckenstein* [2001] discuss three possible reasons for this regionally differing trend in the eastern part of the North German Basin: (1) the influence of possible displacement along the Trans-European Suture Zone which separates the old East European platform from the younger western European parts of the Eurasia Plate, (2) the local dominance of stresses caused by post-glacial rebound, and (3) the northward increase of lithospheric strength below the northeastern part of the North German Basin possibly acting as a barrier. The 2.5D finite element models support either the third hypothesis [*Marotta et al.*, 2002] or a combination of the first and third hypotheses [*Kaiser et al.*, 2005]. However, in both numerical approaches, the studied sections of the North German Basin are unfortunately close to their eastern model boundary, resulting in a high likelihood for modeling arti-

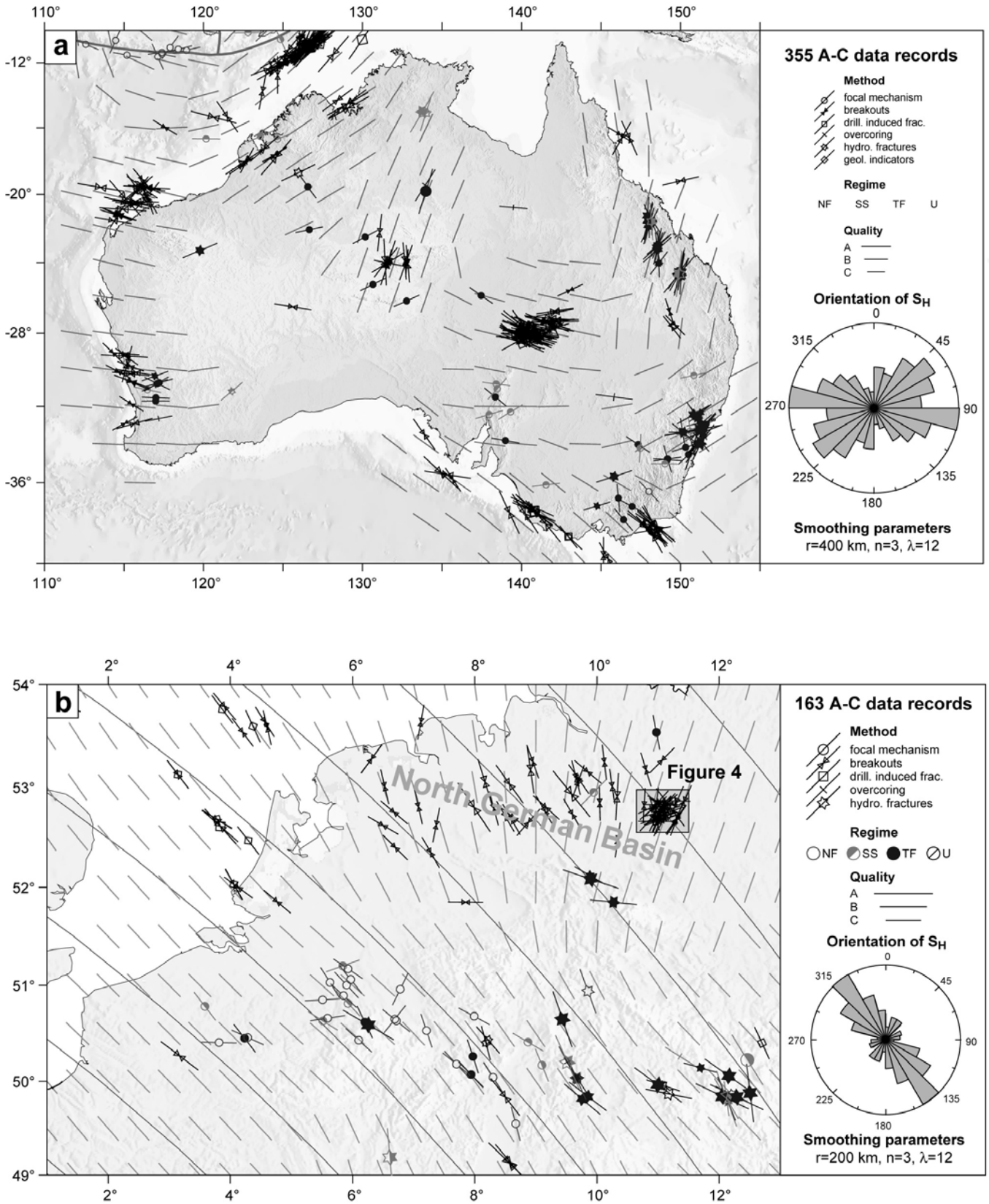

Figure 5. Legend, stress symbols and smoothed stress field legend as in Figure 1a. (a) Stress map of Australia. Note the change of the regional stress in southeastern Australia. (b) Stress map of northern Germany and Netherlands. The mean $\boldsymbol{S_H}$ orientation of 144°N is in agreement with the direction of relative plate motion of approximately 137°N between the Africa Plate and the Eurasia Plate as previously observed by *Müller et al.* [1992]. However, note the deviation from this trend in the eastern part of the North German Basin where a rotation to NE is observed. Box indicates location of Figure 6. (c) Stress map of Venezuela. Note the difference in $\boldsymbol{S_H}$ orientation and stress regime in the eastern (NW-SE, strike-slip faulting) and the western part (W-E, thrust faulting) of Venezuela. EB denotes El Pilar-Boconó fault. (d) Stress map of Romania. Grey thick line indicates the location of a high-velocity body in the upper mantle at ~120 km depths according to the tomography study by *Martin et al.* [2005]. This body, a remnant of Miocene subduction, is sinking with ~2 cm/a vertically into the mantle and is in the state of slab break-off [*Sperner et al.*, 2001; *Wenzel et al.*, 1998].

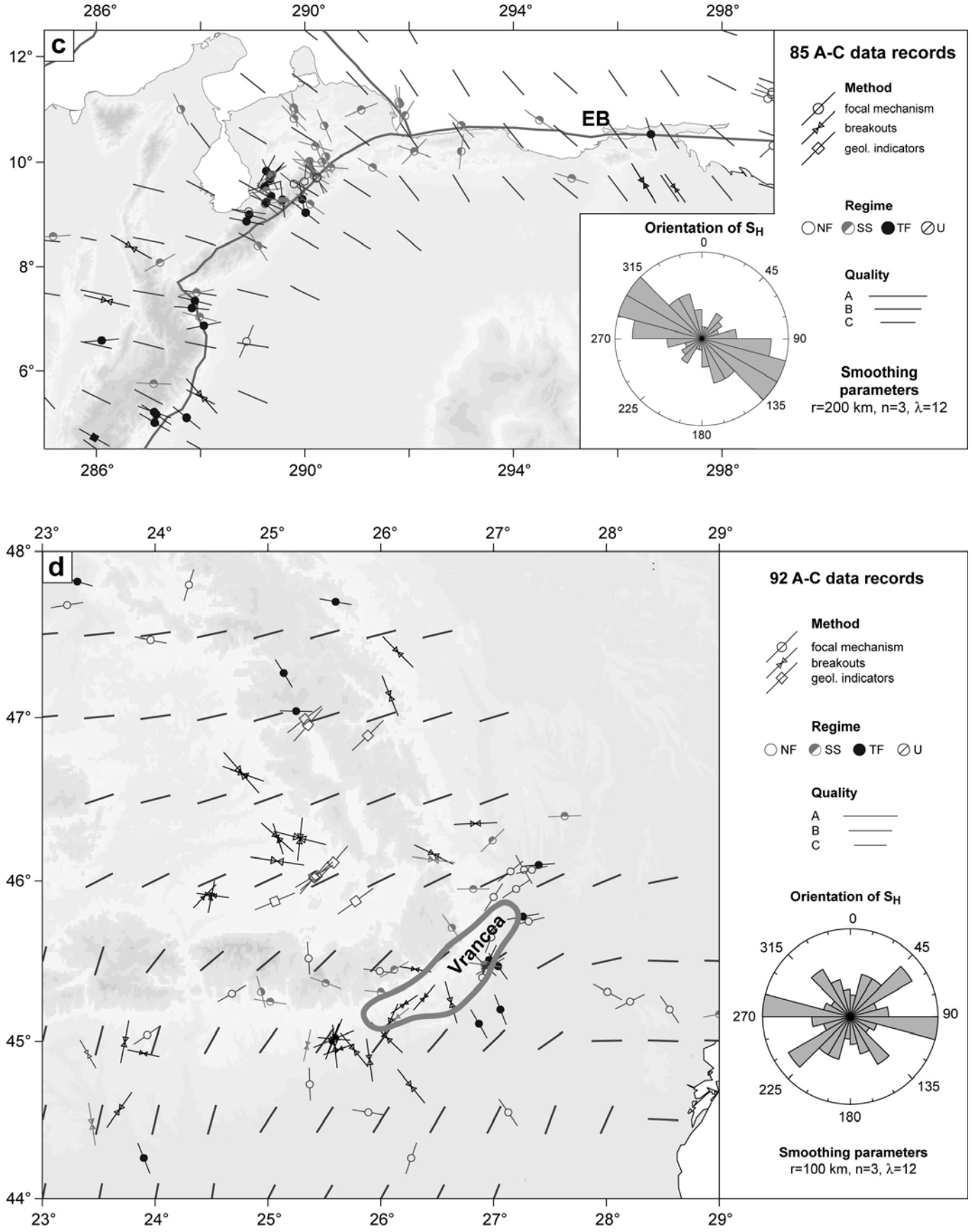

Figure 5. (Continued)

facts due to boundary effects in the easternmost parts of the basin.

[23] A potential fourth source of the stress field rotation in the North German Basin is the stresses induced by lateral density and strength contrasts across the Sorgenfrei-Teisseyre and Tornquist-Teisseyre zone where crustal thickness increases sharply from about 35 km in the west to 50 km in the East European platform [*Thybo*, 2001]. This increase in crustal thickness may produce enough gravitational potential energy to create compressional stresses perpendicular to the NW-SE striking suture zone. *Gölke and Coblentz* [1996] investigated the impact of the lateral density contrast due to topography in a large-scale 2D finite element model of western Europe and proved that these lateral density contrasts are likely to have an impact on the stress magnitudes, but only a small effect on stress orientations. *Jarosinski et al.* [2006] also included the effect of the varying lithospheric strength, as well as the effect of the topography, in their 2.5D finite element model of western Europe and reciprocated a swing of the stress field orientation in the eastern parts of the North German Basin, roughly in agreement with the observed stress. They also implemented the NW-SE striking Hamburg-Elbe fault zone as the southern boundary of the eastern section of the North German Basin. However, the faults in their model displays an unrealistic large displacement of 200-300 m in a predominantly aseismic area.

[24] In summary, the fan-shaped stress pattern in the North German Basin and farther east is now confirmed on a large, high-density stress data set, but the various processes contributing to this stress pattern are still controversial and have yet to be resolved. So far, the existing models reveal that mechanical and density contrasts, boundary conditions and geometry, as well as postglacial rebound contribute to a certain extent to the stress field reorientations across the North German Basin, but their relative importance is still questionable.

3.2.2. Stress Map of Venezuela

[25] Most of the 81 new data records come from a comprehensive compilation by *Colmenares and Zoback* [2003], and to a lesser extent, from publications of *Pérez et al.* [1997a, 1997b], *Taboada et al.* [2000], *Russo et al.* [1993], and from Harvard CMT solutions [e.g., *Ekström et al.*, 2003]. *Colmenares and Zoback* [2003] identified two distinct stress provinces in Venezuela, each with different S_H orientations. In eastern Venezuela, along the right-lateral El Pilar-Boconó transform fault, a strike-slip faulting stress regime prevails with a broadly NW-SE S_H orientation (Figure 5c). Farther west, toward the eastern Cordilleras, the tectonic regime changes toward thrust faulting and the S_H orientation rotates anticlockwise following the regional trend of topography (Figure 5c). The latter, and to a lesser extent the former, indicates that areas with high topography store enough gravitational potential energy to be a second-order, regionally dominant, control on the tectonic regime and the S_H orientation. Indeed, the global WSM database reveals numerous areas in which stresses are largely perpendicular to mountain ranges, such as the Western Canada Basin, Papua New Guinea and around the Alps (Figure 1b). A consequence of this is that stresses in foreland basins, which are sparsely sampled in the 2005 WSM release, are likely to exhibit present-day stress patterns perpendicular to the topographic front.

3.2.3. Stress Map of Romania

[26] Recently the stress information in Romania and adjacent areas have been increased by 108 data records mainly provided by M. Negut and A. Negut (unpublished work from 2002 and 2004). Thus the total number of stress data records in Romania increased to 208, 92 of which have A-C quality. In contrast, the stress pattern presented by *Bada et al.* [1998], that indicates a homogeneous WNWSES S_H orientation, the stress patterns from our new compilation do not show clear trends (Figure 5d). There are three possible explanations for this enigma: (1) The stress data set used by *Bada et al.* [1998] probably also included focal mechanism solutions from sub-crustal earthquakes within the subducting slab at 70-130 km (whereas the WSM database only includes data within the upper 40 km of the earth). (2) The smoothing parameter applied by *Bada et al.* [1998] filtered only the first-order pattern on a plate-wide scale (e.g., a large search radius of 500 km as used in Figure 4 for the Eurasia Plate). (3) The smaller number of stress data records available at that time could not reveal the complicated local stress pattern.

[27] The high variability of S_H orientations in our stress map is most likely the result of relatively isotropic and/or low far-field horizontal stress magnitudes in the area. Such low or isotropic far-field stress magnitudes allow small local stress effects to control the in situ stress and thus result in a locally perturbed stress field. According to *Sonder* [1990], the net stress field as a superposition of local and regional stresses depends on the magnitudes of the regional principal stresses, the magnitudes of the local stress component as well as the angular difference of the regional principal stress directions to the stresses caused by the local stress source. Local additional stresses that are not parallel to the regional stresses will cause the net stress field to change the orientations of the principal stresses and can also change the faulting style from for example strike-slip faulting to normal faulting on local scales. Similar localized stress perturbations, thought to be due to low and/or isotropic horizontal stresses, are observed in the central and northern North Sea and Permian Basin [*Tingay et al.*, 2006].

[28] From the diversity of S_H orientations and the changes in the tectonic regime on short spatial scales in Romania (Figure 5d) we conclude that the contribution from plate boundary forces on the magnitude of tectonic stresses is small and that the stress tensor has similar eigenvalues, i.e., a stress state that is close to isotropic. This implies that third-order sources have a large influence on both the S_H orientation and the tectonic regime. Possible local stress sources are topography, lateral density and strength contrasts (Focsani Basin with 11 km depth, foreland, Mohesian platform), basin subsidence due to slab pull of a former subduction zone, and stress rotations at fault tips. Superposition of these different stress sources leads to a complex stress field with S_H orientations changing within a few kilometers.

[29] The high variation of the local stress pattern in Romania puts upper bounds to potential regional stress

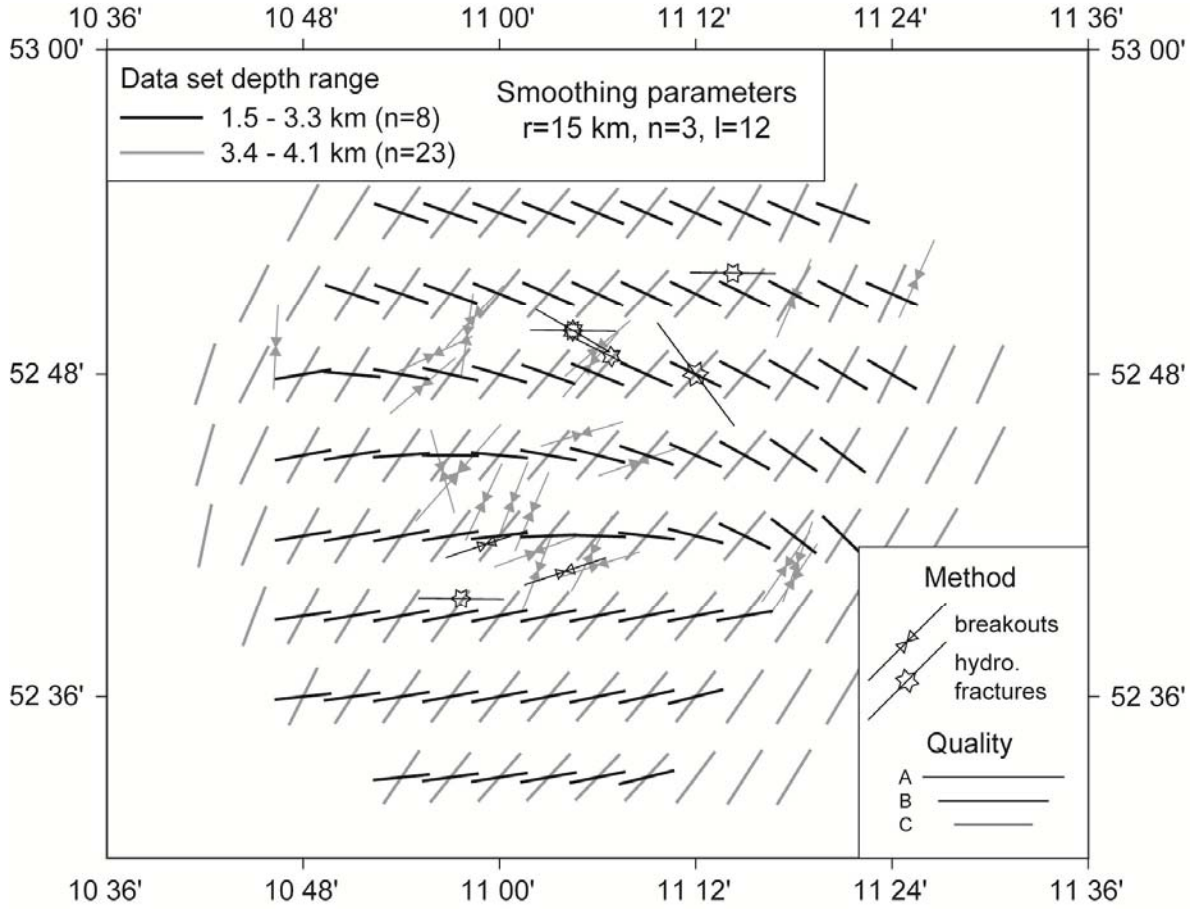

Figure 7. Stress map of the eastern part of the North German Basin. Stress symbols and smoothed stress field legend are as in Figure 1, and location is indicated in Figure 5b. The smoothed S_H orientations are calculated for two data sets from different depth ranges. Note the difference between the approximately E-W orientation in the upper layer (black symbols, 1.5-3.3 km, post-Zechstein) and the SW-NE orientation at greater depths (grey symbols, 3.4-4.1 km Zechstein) that reflects the regional stress field as displayed in Figure 5b.

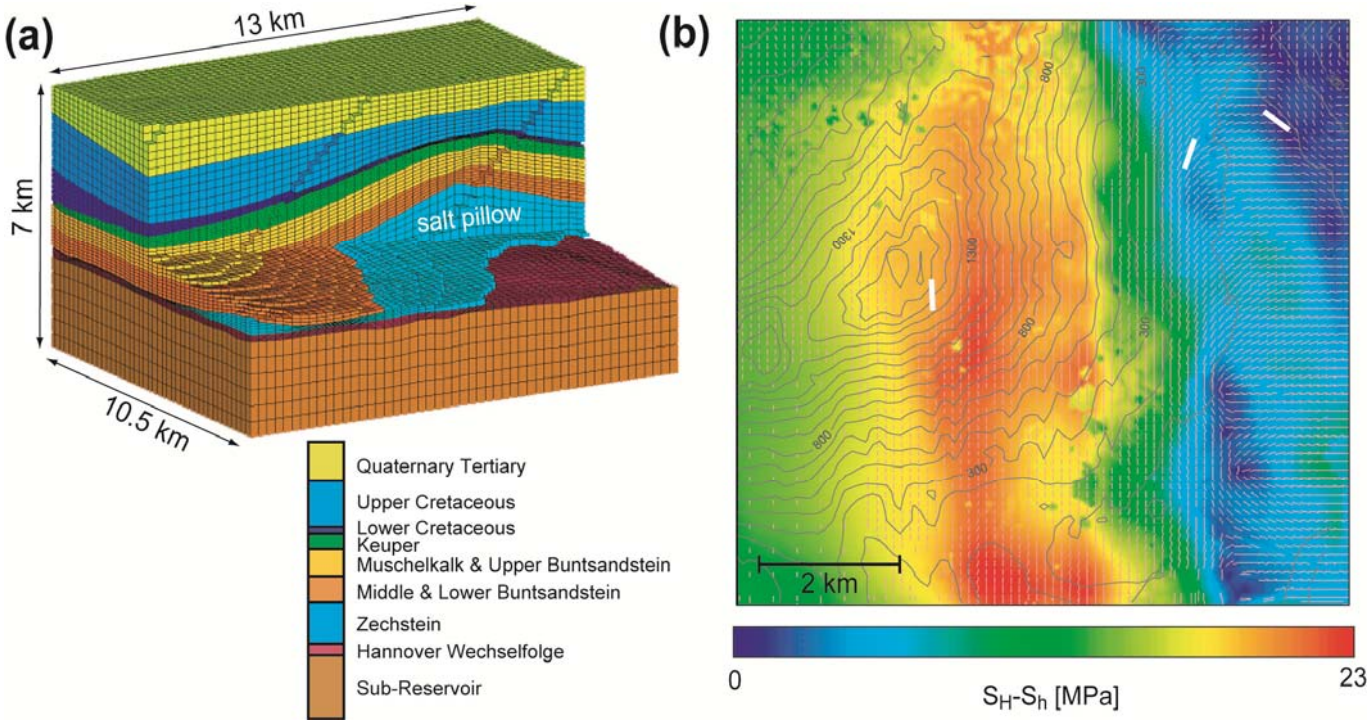

Figure 6. (a) Cutaway oblique view of the 3D finite element mesh with ~125,000 hexahedral linear elements. Model rheology is linear elastic, boundary conditions are a N-S oriented regional stress field and gravity. Density and mechanical rock properties vary according to the numbers given by *Fleckenstein et al.* [2004]. (b) Comparison of observed (white line symbols) and modeled (short red lines) S_H orientation at 4444 m depth (intra-Rotliegend) from the northern section of the finite element model. Grey contours are the Zechstein isopatches in meters; north is the vertical direction.

sources in the region such as the degree of coupling of the subducting Vrancea slab. We hypothesize that the slab beneath Vrancea does not transfer large amounts of stresses to the crust and that the coupling is probably weak. A strong coupling would produce a large regional signal in the stress pattern which cannot be identified in the stress observations. However, this hypothesis still needs to be investigated in detail with a 3D numerical model in order to compare the differential stresses produces by the local stress sources and the ones superimposed from different slab coupling scenarios.

3.3. Local-Scale Stress Patterns: Impact of Detachment Horizons

3.3.1. Eastern Part of the North German Basin

[30] High-resolution stress data sets from sedimentary basins indicate that stress orientations can locally deviate strongly from the regional stress field orientation. Detailed analysis of present-day stresses within sedimentary basins reveals significant and complex variations in the present day S_H orientation [*Tingay et al.*, 2005b; *Tingay et al.*, 2006]. The eastern section of the North German Basin gives an excellent example for such a local-scale variation. Zooming into the cluster of data records in the eastern part of the North German Basin (Figure 6) reveals that two mean S_H orientations exist: An E-W orientation from stress data at shallow depth (1500-3300 m) above the Zechstein evaporite sequences and a SW-NE orientation from stress data at greater depth (3400-4500 m) reflecting the far-field orientation with the observed regional fan-shaped pattern. This vertically decoupled stress pattern in the eastern part of the North German Basin is not visible in its western and central parts where stress data above and below the Zechstein follow roughly the same regional trend.

[31] This large change of mean S_H orientation with depth is interpreted to be primarily the result of the Zechstein evaporites acting as a mechanically weak detachment layer, and therefore not enabling transmission of the regional stress field into shallower sequences. The detachment of regional stresses results in relatively isotropic horizontal stress magnitudes above the salt and thus allows small local stress sources to have a dominant influence on the stress pattern. Most likely the cause of the localized stress perturbations in the shallow detached sequences are the large density and strength contrasts provided by the numerous salt domes in this region [*Roth and Fleckenstein*, 2001]. Such decoupling horizons are not unusual for sedimentary basins and are often visible where detailed analysis of present-day stresses reveal significant and complex variations in the present-day S_H orientation [*Tingay et al.*, 2005b]. Indeed, the Zechstein evaporite sequences are also believed to form a basal detachment and result in a similarly complex stress pattern in the central North Sea. The salt layer thickness in the North German Basin is highly variable and ranges from several hundred meters to a local thickness up to 4000 m due to halokinesis [*Scheck and Bayer*, 1999]. Measurements beside and above such salt pillows have a major impact on the stress orientations [*Brereton and Müller*, 1991].

[32] The influence of local density and mechanical contrasts in the vicinity of salt diapirs on the stress field has been demonstrated in 3D numerical experiments [*Fleckenstein et al.*, 2004]. The 3D finite element model geometry represents a existing salt pillow of up 1500 m thickness in the eastern part of the North German Basin (Figure 7a). Boundary conditions are gravitational forces and N-S compression due to the regional trend of the regional stress field. The impact of this salt layer structure is clearly seen in the model results at 4444 m depth (c. intra-Rotliegend) presented in Figure 7b. Differential stresses have magnitudes of up to 23 MPa and S_H rotates up to 80° on horizontal distances of less than one kilometer. The comparison with three data records from the WSM database (Figure 7b) shows that the model fits the large change in S_H orientation on small spatial scales very well.

[33] The eastern part of the North German Basin provides an excellent example of the local-scale third-order variations in the stress orientation that can be observed from petroleum industry data acquired in sedimentary basins. The systematic compilation of tectonic stresses from borehole data, which allows analysis of stress patterns at very small scales (0.1-100 km), reveals information that would never have been identified using seismicity data alone. The WSM 2005 database release contains information from ~70 sedimentary basins, enabling unique insights into the controls on stress changes in sedimentary basins. These changes result from the combination of various factors acting on different spatial scales, including far-field forces from the plate boundaries as well as more regional to local effects from basin geometry, geological structures, mechanical contrasts (e.g., evaporites, overpressured shales, detachment zones), topography and deglaciation [*Tingay et al.*, 2005b, 2006].

3.3.2. Stress Field of the Baram Delta Province of Brunei

[34] The Tertiary Baram Delta province of Brunei provides another excellent example of stress rotations resulting from local stress fields overprinting regional stress patterns. The early Miocene to present Baram Delta province is a series of three rapidly depositing and prograding delta sequences that were deposited adjacent to the NW Borneo active margin. The older and proximal (inboard) parts of the Baram Delta province exhibit NW-SE stress orientations that are normal to the margin and are consistent with plate motion and the most recent (Pliocene to recent) NW-SE oriented inversion of structures in the inner shelf (Figure 8) [*Tingay et al.*, 2005a, 2003]. Hence this NW-SE inner shelf stress field is believed to be the result of far-field regional stresses exerted from either the plate boundaries, ongoing convergence of the continental salient with Borneo, delamination of the proto-South China Sea subducted slab, or from topographic forces caused by the Crocker-Rajang mountain range [*Tingay et al.*, 2005a]. However, in contrast to the regional NW-SE inner shelf stress field, a NE-SW (margin-parallel) stress field is observed in the outer shelf, near the shelf edge (Figure 8) [*Tingay et al.*, 2005a]. This margin-parallel NE-SW outer shelf stress field is consistent with active margin-parallel striking growth faulting and seabed scarps observed on bathymetry and shallow seismic data in this region (Figure 8) [*Tingay et al.*, 2005a]. The margin-parallel stresses observed in the outer shelf are consistent

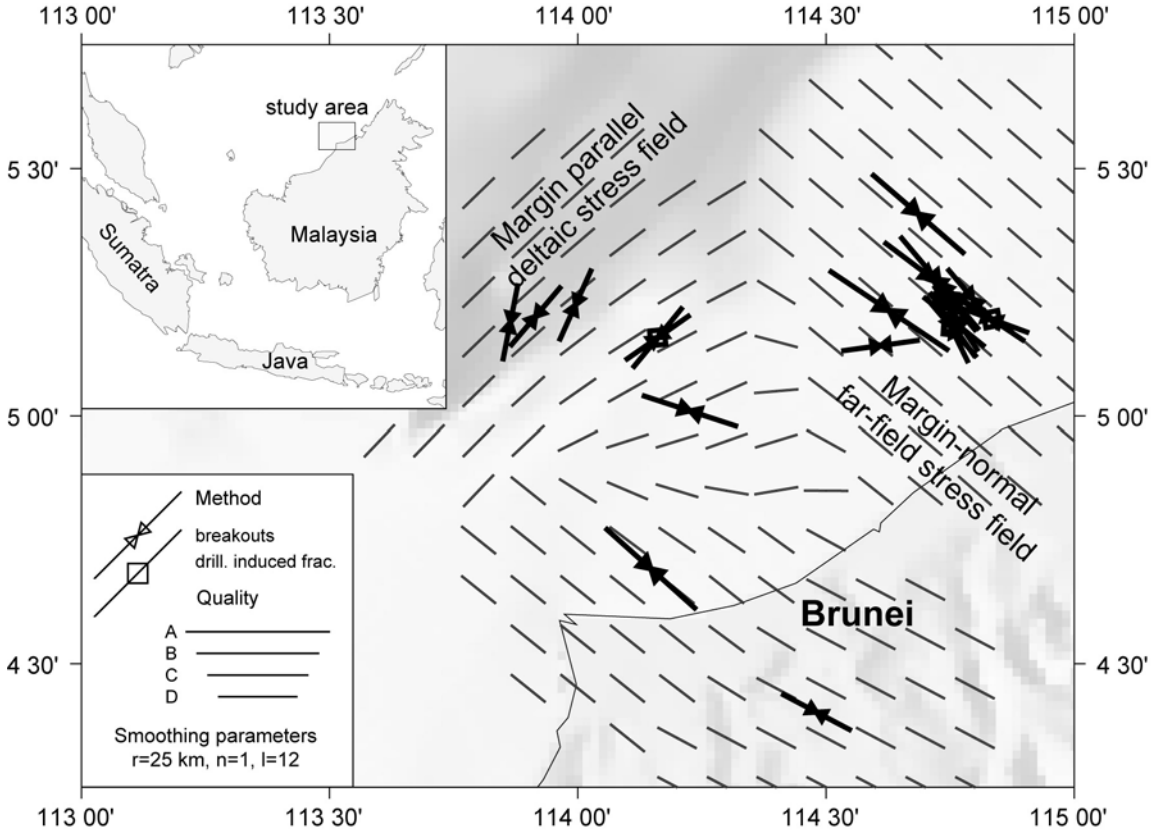

Figure 8. Stress map of the Baram Basin in Brunei. Stress symbols and smoothed stress field legend are as in Figure 1. Note the change of stress orientation offshore.

with a local "deltaic" stress field derived from gravitational instability of the convex-upward deltaic wedge. Hence the regional NW-SE S_H orientation in Brunei has been locally overprinted by a basally detached margin-parallel deltaic stress field. Furthermore, the primary original structures observed in the inner shelf are Miocene-Pliocene deltaic margin-parallel striking faults and folds that are inconsistent with the present-day margin-normal stress orientation. Hence the local spatial stress rotation observed in Brunei also reveals that stresses in the inner shelf of Brunei have rotated approximately 90° since the middle Miocene and that the region of NE-SW margin-parallel deltaic stresses has moved basinward over time (prograded), from the inner shelf to the present-day shelf edge [*Tingay et al.*, 2005a].

4. Change of Stress Pattern on Geological Timescales

[35] The examples in the previous chapter confirm that the stress pattern is mainly controlled by the superposition of tectonic forces acting along plate boundaries or arising from density contrasts including the effects of topography, mechanical rock properties, and active faults. However, the contemporary stress pattern is only the final stage of a long tectonic record that has to be taken into account to understand the geodynamic evolution of an area.

[36] Time-dependent effects on the stress pattern occur on timescales as short as earthquake cycles owing to tectonic loading, coseismic stress release, and postseismic stress relaxation [e.g., *Bohnhoff et al.*, 2006; *Freed and Lin*, 1998; *Hardebeck and Hauksson*, 2001; *Hergert and Heidbach*, 2006], but also on geological timescales on the order of millions of years, for example, as a result of changing plate boundary configurations and mountain growth [e.g., *Hippolyte et al.*, 1994; *Iaffaldano et al.*, 2006; *Lamb*, 2006; *Mercier et al.*, 1992; *Sandiford*, 2002; *Sandiford et al.*, 2004]. These time-dependent changes of the stress pattern can be studied by means of the geological record, paleostress analysis, paleomagnetic investigations or GPS and InSAR observations [*Barke et al.*, 2007; *Bertotti et al.*, 2001; *Delvaux et al.*, 1997; *Heidbach and Drewes*, 2003; *Melbourne et al.*, 2002; *Pritchard*, 2006; *Sandiford et al.*, 2004]. On the basis of these observations, it is possible to establish numerical models reflecting the geodynamic evolution and the contemporary stress pattern and tectonic regime at their final stage. In the following we present two examples to illuminate the advantage of combining stress data with geological information that enables us to investigate the geodynamic evolution and the relative importance of the forces causing the stress pattern through time.

4.1. Stress Field of Southeastern Australia

[37] *Sandiford et al.* [2004] combine stress data, numerical modeling, and the geological record in order to investigate the sources of stress manifested in the unusual stress pattern in southeastern Australia. They observe that the onset of faulting in southeastern Australia, that is still active under the present stress regime, corre-

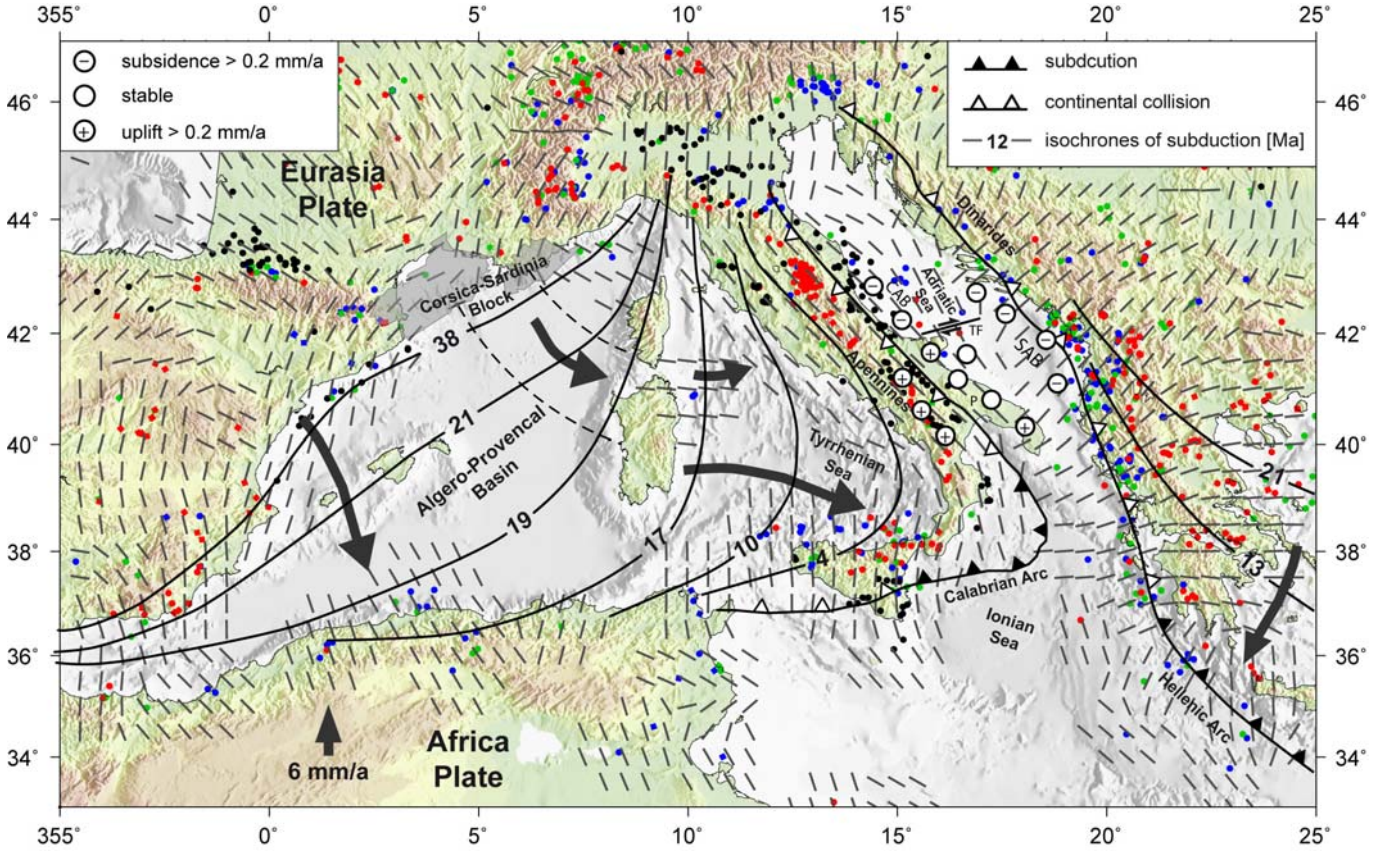

Figure 9. Geodynamic evolution and recent stress map of the western and central Mediterranean. Legend for stress symbols and smoothed stress field is as in Figure 1b. Abbreviations are: P, Puglia; CAB, Central Adriatic Basin; SAB, Southern Adriatic Basin; and TF, Tremiti Fault zone. Subsidence rates are taken from *Bertotti et al.* [2001]. Motion of the Africa Plate with respect to the Eurasia Plate is taken from NUVEL-1A [*DeMets et al.*, 1994]. Parameters for the smoothed stress field from A-C quality data are: $\boldsymbol{r}$ = 100 km, $\boldsymbol{\lambda}$ = 12, and $\boldsymbol{n}$ = 3. Isochrons display the SW migration of the subduction zone through time [*Mantovani et al.*, 1996; *Robertson and Grasso*, 1995; *Malinverno and Ryan*, 1986]. Backarc spreading formed the Algero-Provenc¸ial basin that led to a 70° counterclockwise rotation of the Sardinia-Corsica Block [*Mueller and Kahle*, 1993]. On the eastern side of the Adriatic block, continental collision had already started in early Miocene to middle Miocene that gave rise to the Dinarides [*Ziegler*, 1988]. Note the focused and small section of subduction along the Calabrian Arc.

lates with the onset of the growth of the Southern Alps (New Zealand) in the late Miocene. The growth of the Southern Alps is due to the increase of convergence rate between the Indo-Australia Plate and the Pacific plate in the late Miocene from 2 mm/a to 10 mm/a [*Batt and Braun*, 1999] that is ongoing and reflected in GPS data at the transpressional Alpine Fault [*Beavan et al.*, 2002]. From numerical experiments *Sandiford et al.* [2004] concluded that the resulting increase of resistive forces at the plate boundary on the southern island of New Zealand generates the NW-SE trend of the S_H orientation. This indicates that the oceanic crust is capable to transfer stresses over thousands of kilometers between New Zealand and Australia and that even small changes in the plate boundary configuration have a significant impact on the S_H orientation.

4.2. Stress Field of Southern Italy

[38] The growth of the Apennines in Italy is the result of subduction processes in the central Mediterranean in Miocene and early Pliocene followed by continental collision in middle Pliocene and Pleistocene (Figure 9) [*Ziegler*, 1988; *Malinverno and Ryan*, 1986; *Mantovani et al.*, 1996; *Mueller and Kahle*, 1993]. According to *Hipployte et al.* [1994] this continental collision formed the Apennines in a ENE-WSW oriented compressional tectonic regime. However, the contemporary stress pattern in southern Italy and the Adriatic Block exhibits normal and strike-slip faulting regime (Figures 4 and 9) [*Montone et al.*, 2004; *Mariucci et al.*, 1999] with NW-SE S_H orientation parallel to the strike of the Apennines. This stress pattern is prevailing throughout southern Italy including the Apenninic foreland and foredeep, as well as the adjacent offshore of the Tyrrhenian Sea and the Adriatic Sea (Figure 9). *Hipployte et al.* [1994] concluded from the analysis of paleostress data that the stress pattern in southern Italy rotated significantly in early Pleistocene to middle Pleistocene and that the tectonic regime changed from compressional to normal faulting at that time. These changes indicate that new geodynamic processes commenced in middle Pleistocene and that these are ongoing.

[39] *Hipployte et al.* [1994] hypothesize that these changes are due to slab break-off as suggested by seismic tomography [e.g., *Spakman*, 1990]. The expected vertical rebound caused by slab break-off is in agreement with the rapid uplift pattern in the Puglia region of southern Italy where Pleistocene sediments are found at 450-700 m height [*Bertotti et al.*, 2001; *Doglioni et al.*, 1994]. However, it contradicts the ongoing subsidence of the central

Table 2. Sources of Crustal Stresses on Different Spatial Scales

Source	Examples	Effect on Stress Field	Length Scale
Plate boundary forces	ridge push, collision, subduction, mantle drag	*first-order control*	100 s to 1000 s of km
Large volume forces	mountain ranges, isostatic compensation, continent-ocean transition, Moho, lithosphere thickness variations, large basins	*second-order control* rotation of stress field due to mechanical and density contrasts between units	100 s of km
Flexural forces	deglaciation, subduction zones	*second-order control*	100 s of km
Detachment zones	evaporites, overpressured shales, low-angle faults	*second- to third-order control* changes mechanically overlying rocks from first- or second-order stress field	10 s to 100 s of km
Strong earthquakes	plate boundaries, major intraplate faults	*second- to third-order control* temporal changes linked to the seismic cycle	10 s to 100 s of km
Geological structures	faults, fractures, diapirs, folds	*third-order control* change due to mechanical and density contrasts between units	0.01-10 km

Adriatic basin (Figure 9). *Doglioni et al.* [1994] explain the uplift pattern of Puglia with a steepening of the subducted lithosphere beyond Puglia leading to buckling of the lithosphere. In their model the subsidence of the central Adriatic basin decoupled to this process by the dextral Tremiti fault zone dividing the thick lithosphere (110 km) south of it from the thinner one (70 km) in the north (Figure 9). *Bertotti et al.* [2001] suggest that lithospheric folding (buckling) resulting from lateral compression is the cause of the observed uplift and subsidence pattern.

[40] Thus the contemporary stress field pattern in southern Italy is not reflecting the shortening from SW-NE compression of the Adriatic block as indicated by the tectonic record or the accretion of the Apennines, but it expresses a very recent geodynamic process of either slab break-off, slab steepening, or lithospheric folding. Even though the relative importance of these processes for the contemporary subsidence and stress pattern remains enigmatic this data integration gives new insights into geodynamic evolution of the region.

5. Conclusion and Perspectives of the WSM Database

[41] The WSM 2005 database release has developed regions of high data record density that enable us to investigate variations in stress orientations at local scales and to discuss sources controlling the third-order stress patterns. The stress patterns presented in the examples allow four major conclusions: (1) The plate-wide and regional stress pattern is controlled by the plate boundary forces confirming the findings from earlier work using the WSM database [e.g., *Hillis and Reynolds*, 2000; *Richardson*, 1992; *Coblentz and Richardson*, 1995; *Zoback*, 1992; *Zoback et al.*, 1989]. (2) The contemporary stress pattern in the WSM database reveals also third-order effects on small spatial scales. Zooming into the western European stress map (Figures 4, 5b, and 6), where data density is high, we identified areas where regional to local effects control the stress pattern at different spatial scales. (3) Additional stress sources are necessary (i.e., forces which are not related to plate boundaries) in order to explain regional- to local-scale stress patterns in regions where the contribution of plate boundary forces is small. In dependence of the stress magnitudes of the plate-wide-scale stress field regional and local stress sources can control the S_H orientation and the tectonic regime. The various stress sources and the spatial scales on which they are effective are summarized in Table 2. (4) The examples for the stress changes throughout geological times reveal that an integrated analysis of the WSM data with other information such as the geological record and the geodynamic evolution gives new insights into the relative importance of the sources of stress and their changes through geological times.

[42] This progress in understanding the contemporary stress pattern at different spatial scales has only been possible owing to the ongoing systematic compilation of stress data with international collaboration. For the forthcoming WSM database release we will focus on three issues: (1) The first issue is refinement of the quality assessments for focal mechanism solutions, borehole breakouts and hydraulic fractures. These changes are necessary owing to technical improvements and new methodologies that will be tested for their suitability as stress indicators (in comparison with the other methods). (2) The second issue is continuation of our worldwide initiative to intensify collaborations with the petroleum industry where most of the stress data in sedimentary basins are acquired. On the basis of the first results of this initiative we expect numerous new stress data records from areas with up-to-now low data coverage (e.g., Caspian Sea, SE-Asia, Nile delta). (3) The third issue is inclusion of new stress data records deduced from focal mechanism solutions using regional broadband data for waveform inversion. Focus of this work is on earthquakes with magnitudes lower than those used for the Global CMT Project (formally known as Harvard CMT catalogue) lo-

cated in intraplate areas where sparse or no stress information is currently available.

[43] In spite of the numerous improvements and upgrades reported in this publication, the future success of the WSM is nevertheless dependent on the assistance of the scientific community and the ongoing support from our partners from industry. We thus call for active participation in the development of the next WSM database release regardless of which type of support: new stress data, the analysis of the stress field of a specific region, or discussions on new stress determination methods.

[44] **Acknowledgments.** The World Stress Map project is a collaborative project that would not be possible without the effort of many scientists worldwide. We are indebted to numerous individual researchers and working groups all over the world for providing stress data. The complete list of contributors is too numerous to be given herein. However, the authors are particularly grateful for major contributions for the WSM 2005 database release by Richard Hillis and Scott Reynolds of the Australasian Stress Map project (University of Adelaide), Lourdes Colmenares (Stanford University), Philip Fleckenstein (Karlsruhe University), Mihaela Negut (PETROM, Bucarest), Paola Montone (INGV, Rome), Maria Teresa Mariucci (INGV, Rome), Mark Zoback (Stanford University), and John Townend (University of Wellington). We also thank the World Stress Map advisory board members Egon Althaus, John Cook, Roy Gabrielsen, Domenico Giardini, Helmut Kipphan, Onno Oncken, Chris Reigber, Markus Rothacher, and Mark Zoback for their long-term and ongoing support. We also thank the former members of the WSM research team Philipp Fleckenstein and Peter Connolly for providing us with the 3D FE example and very fruitful discussions on the stress pattern of the North German Basin. The manuscript has been greatly improved by encouraging and constructive reviews from Mike Sandiford, David Coblentz, and Kurt Stüwe.

References

Assumpção, M. (1992), The regional intraplate stress field in South America, *J. Geophys. Res.*, *97* (B8), 11,889-11,903.

Bada, G., S. Cloetingh, P. Gerner, and F. Horváth (1998), Sources of recent tectonic stress in the Pannonian region: Inferences from finite element modelling, *Geophys. J. Int.*, *134*, 87-101.

Bada, G., F. Horváth, P. Dövényi, P. Szafián, G. Windhoffer, and S. Cloetingh (2007), Present-day stress field and tectonic inversion in the Pannonian basin, *Global Planet. Change*, *58*, 165-180.

Barke, R., S. Lamb, and C. MacNiocaill (2007), Late Cenozoic bending of the Bolivian Andes: New paleomagnetic and kinematic constraints, *J. Geophys. Res.*, *112*, B01101, doi:10.1029/2006JB004372.

Batt, G. E., and J. Braun (1999), The tectonic evolution of the Southern Alps, New Zealand: Insights from fully thermally coupled dynamical modelling, Geophys. *J. Int.*, *136*, 403-420.

Beavan, J., P. Tregoning, M. Bevis, T. Kato, and C. Meertens (2002), Motion and rigidity of the Pacific Plate and implications for plate boundary deformation, *J. Geophys. Res.*, *107* (B10), 2261, doi:10.1029/ 2001JB000282.

Bell, J. S. (1996a), In situ stresses in sedimentary rocks (Part 2): Applications of stress measurements, *Geosci. Can.*, *23*, 135-153.

Bell, J. S. (1996b), In situ stresses in sedimentary rocks (Part 1): Measurement techniques, *Geosci. Can.*, *23*, 85-100.

Bertotti, G., V. Picotti, C. Chilovi, R. Fantoni, S. Merlini, and A. Mosconi (2001), Neogene to Quaternary sedimentary basins in the south Adriatic (Central Mediterranean): Foredeeps and lithospheric buckling, *Tectonics*, *20* (5), 771-787.

Bird, P. (2003), An updated digital model for plate boundaries, *Geochem. Geophys. Geosyst.*, *4* (3), 1027, doi:10.1029/2001GC000252.

Bird, P., Z. Ben-Avraham, G. Schubert, M. Andreoli, and G. Viola (2006), Patterns of stress and strainrate in southern Africa, *J. Geophys. Res.*, *111*, B08402, doi:10.1029/2005JB003882.

Bohnhoff, M., H. Grosser, and G. Dresen (2006), Strain partitioning and stress rotation at the North Anatolian fault zone from aftershock focal mechanisms of the 1999 Izmit $M_w = 7.4$ earthquake, *Geophys. J. Int.*, *166*, 373-385.

Brereton, N. R., and B. Müller (1991), European stress: Contributions from borehole breakouts, in *Tectonic Stress in the Lithosphere*, edited by R. B. Whitmarsh et al., pp. 165-177, R. Soc., London.

Brudy, M., M. D. Zoback, F. Fuchs, F. Rummel, and J. Baumgärtner (1997), Estimation of the complete stress tensor to 8 km depth in the KTB scientific drill holes: Implications for crustal strength, *J. Geophys. Res.*, *102* (B8), 18,453-18,457.

Coblentz, D., and R. M. Richardson (1995), Statistical trends in the intraplate stress field, *J. Geophys. Res.*, *100* (B10), 20,245-20,255.

Coblentz, D., and R. M. Richardson (1996), Analysis of the South American intraplate stress field, *J. Geophys. Res.*, *101* (B4), 8643-8657.

Coblentz, D. D., and M. Sandiford (1994), Tectonic stresses in the African plate: Constraints on the ambient lithospheric stress state, *Geology*, *22*, 831-834.

Coblentz, D., S. Zhou, R. R. Hillis, R. M. Richardson, and M. Sandiford (1998), Topography, boundary forces, and the Indo-Australian intraplate stress field, *J. Geophys. Res.*, *103* (B1), 919-931.

Colmenares, L., and M. D. Zoback (2003), Stress field and seismotectonics of northern South America, *Geology*, *31*, 721-724.

Connolly, P., M. Gölke, H. Bäßler, P. Fleckenstein, S. Hettel, M. Lindenfeld, A. Schindler, U. Theune, and F. Wenzel (2003), Finite Elemente Modellrechnungen zur Erklärung der Auffächerung der größten horizontalen Hauptspannungsrichtung in Norddeutschland, *BfS Rep. Proj. Gorleben 9G2643110000*, 163 pp., Geophys. Inst., Univ. Karlsruhe, Karlsruhe, Germany.

Delvaux, D., R. Moeys, G. Stapel, C. Petit, K. Levi, A. Miroshnichenko, and V. Ruzhich (1997), Paleostress reconstructions and geodynamics of the Baikal region, Central Asia, Part 2. Cenozoic rifting, *Tectonophysics*, *282*, 1-38.

DeMets, C., R. G. Gordon, D. F. Argus, and S. Stein (1990), Current plate motions, *Geophys. J. Int.*, *101*, 425-478.

DeMets, C., R. G. Gordon, D. F. Argus, and S. Stein (1994), Effect of recent revisions to the geomagnetic reversal time scale on estimates of current plate motions, *Geophys. Res. Lett.*, *21* (20), 2191-2194.

Doglioni, C., F. Mongelli, and P. Pieri (1994), The Puglia uplift (SE Italy): An anomaly in the foreland of the Apenninic subduction due to the buckling of a thick continental lithosphere, *Tectonics*, *13* (5), 1309-1321.

Dyksterhuis, S., R. A. Albert, and R. D. Müller (2005), Finite-element modelling of contemporary and palaeointraplate stress using ABAQUS, *Comput. Geosci.*, *31*, 297-307.

Ekström, G., A. M. Dziewonski, N. N. Maternovskaya, and M. Nettles (2003), Global seismicity of 2001: Centroid-moment tensor solutions for 961 earthquakes, *Phys. Earth Planet. Inter.*, *136*, 165-185.

Ekström, G., M. Dziewonski, N. N. Maternovskaja, and M. Nettles (2005), Global seismicity of 2003: Centroid-moment-tensor solutions for 1087 earthquakes, *Phys. Earth Planet. Inter.*, *148*, 327-351.

Fleckenstein, P., G. Reuschke, B. Müller, and P. Connolly (2004), Predicting stress reorientations associated with major geological structures in sedimentary sequences, *DGMK Rep. 593-5*, 141 pp., Dtsch. Wiss. Ges. für Erdöl, Erdgas und Kohle, Celle, Germany.

Freed, A. M., and J. Lin (1998), Time-dependent changes in failure stress following thrust earthquakes, *J. Geophys. Res.*, *103* (B10), 24,393-24,409.

Fuchs, K., and B. Müller (2001), World Stress Map of the Earth: A key to tectonic processes and technological applications, *Naturwissenschaften*, *88*, 357-371.

Gölke, M., and D. Coblentz (1996), Origins of the European regional stress field, *Tectonophysics*, *266*, 11-24.

Grote, R. (1998), Die rezente horizontale Hauptspannungsrichtung im Rotliegenden und Oberkarbon in Norddeutschland, *Erdöl Erdgas Kohle*, *114*, 478-483.

Grünthal, G., and D. Stromeyer (1992), The

recent crustal stress field in central Europe: Trajectories and finite element modeling, *J. Geophys. Res.*, *97* (B8), 11,805-11,820.

Grünthal, G., and D. Stromeyer (1994), The recent crustal stress field in central Europe sensu lato and its quantitative modelling, *Geol. Mijnbouw*, *73*, 173-180.

Hardebeck, J. L., and E. Hauksson (2001), Crustal stress field in southern California and its implications for fault mechanics, *J. Geophys. Res.*, *106* (B10), 21,859-21,882.

Hardebeck, J. L., and A. J. Michael (2004), Stress orientations at intermediate angels to the San Andreas Fault, California, *J. Geophys. Res.*, *109*, B11303, doi: 10.1029/2004JB003239.

Harris, R. A. (2002), Stress triggers, stress shadows and seismic hazard, in *International Handbook of Earthquake and Engineering Seismology, Int. Geophys. Ser.*, vol. 81B, edited by W. H. K. Lee et al., pp. 1217-1231, Academic Press, Amsterdam.

Harris, R. A., R. W. Simpson, and P. A. Reasenberg (1995), Influence of static stress changes on earthquake locations in southern California, *Nature*, *375*, 221-224.

Heidbach, O., and Z. Ben-Avraham (2007), Stress evolution and seismic hazard of the Dead Sea fault system, *Earth Planet. Sci. Lett.*, *257*, 299-312.

Heidbach, O., and H. Drewes (2003), 3-D finite element model of major tectonic processes in the Eastern Mediterranean, in *New Insights in Structural Interpretation and Modelling, Spec. Publ. Ser.*, vol. 212, edited by D. Nieuwland, pp. 259-272, Geol. Soc., London.

Heidbach, O., and J. Höhne (2007), CASMI - A tool for the visualization of the World Stress Map database, *Comput. Geosci.*, in press.

Heidbach, O., A. Barth, P. Connolly, F. Fuchs, B. Müller, J. Reinecker, B. Sperner, M. Tingay, and F. Wenzel (2004), Stress maps in a minute: The 2004 World Stress Map release, *Eos Trans. American Geophysical Union*, *85*, 521-529.

Heidbach, O., K. Fuchs, B. Müller, J. Reinecker, B. Sperner, M. Tingay, and F. Wenzel (2007), The World Stress Map-Release 2005, map, 1:46,000,000, Comm. of the Geol. Map of the World, Paris.

Hergert, T., and O. Heidbach (2006), New insights in the mechanism of postseismic stress relaxation exemplified by the June 23rd 2001 $M_w = 8.4$ earthquake in southern Peru, *Geophys. Res. Lett.*, *33*, L02307, doi:10.1029/2005GL024858.

Hillis, R. R., and S. D. Reynolds (2000), The Australian Stress Map, *J. Geol. Soc.*, *157*, 915-921.

Hillis, R. R., S. D. Mildren, C. J. Pigram, and D. R. Willoughby (1997), Rotation of horizontal stresses in the Australian North West continental shelf due to the collision of the Indo-Australian and Eurasian plates, *Tectonics*, *16* (2), 323-335.

Hillis, R. R., J. R. Enever, and S. D. Reynolds (1999), In situ stress field of eastern Australia, *Aust. J. Earth Sci.*, *46*, 813-825.

Hippolyte, J.-C., J. Anglier, and F. Roure (1994), A major geodynamic change revealed by Quaternary stress patterns in the Southern Appenines (Italy), *Tectonophysics*, *230*, 199-210.

Humphreys, E. D., and D. D. Coblentz (2007), North American dynamics and western U. S. tectonics, *Rev. Geophys.*, *45*, RG3001, doi: 10.1029/2005RG000181.

Iaffaldano, G., H.-P. Bunge, and T. Dixon (2006), Feedback between mountain belt growth and plate convergence, *Geology*, *34*, 893-896, doi: 10.1130/G22661.1.

Jarosinski, M., F. Beekman, G. Bada, and S. Cloetingh (2006), Redistribution of recent collision push and ridge push in Central Europe: Insights from FEM modelling, *Geophys. J. Int.*, *167*, 860-880.

Kaiser, A., K. Reicherter, C. Hübscher, and D. Gajewski (2005), Variation of the present-day stress field within the North German Basin - Insights from thin shell FE modeling based on residual GPS velocities, *Tectonophysics*, *397*, 55-72.

King, G. C. P., R. S. Stein, and J. Lin (1994), Static stress changes and the triggering of earthquakes, *Bull. Seismol. Soc. Am.*, *84*, 935-953.

Lamb, S. (2006), Shear stresses on megathrusts: Implications for mountain building behind subduction zones, *J. Geophys. Res.*, *111*, B07401, doi:10.1029/2005JB003916.

Ljunggren, C., Y. Chang, T. Janson, and R. Christiansson (2003), An overview of rock stress measurement methods, *Int. J. Rock Mech. Min. Sci.*, *40*, 975-989.

Malinverno, A., and W. B. F. Ryan (1986), Extension in the Tyrrhenian Sea and shortening in the Apennines as result of arc migration driven by sinking of the lithosphere, *Tectonics*, *5*, 227-245.

Mann, P., and A. Taira (2004), Global significance of the Solomon Islands and Ontong Java Plateau convergence zone, *Tectonophysics*, *389*, 137-190.

Mantovai, E., D. Albarello, C. Tamburelli, and D. Babbucci (1996), Evolution of the Tyrrhenian basin and surrounding regions as a result of the Africa-Eurasia convergence, *J. Geodyn.*, *21*, 35-72.

Mariucci, M. T., A. Amato, and P. Montone (1999), Recent tectonic evolution and present stress in the Northern Apennines (Italy), *Tectonics*, *18*, 108-118.

Marotta, A. M., U. Bayer, H. Thybo, and M. Scheck (2002), Origin of the regional stress in the North German basin: Results from numerical modelling, *Tectonophysics*, *360*, 245-264.

Martin, M., and F. Wenzel (2005), High-resolution teleseismic body wave tomography beneath SE-Romania - II. Imaging of a slab detachment scenario, *Geophys. J. Int.*, *164*, 579-595.

Meijer, P. T., and M. J. R. Wortel (1992), The dynamics of motion of the South American Plate, *J. Geophys. Res.*, *97* (B8), 11,915-11,931.

Meijer, P. T., R. Govers, and M. J. R. Wortel (1997), Forces controlling the present-day state of stress in the Andes, *Earth Planet. Sci. Lett.*, *148*, 157-170.

Melbourne, T. I., F. H. Webb, J. M. Stock, and C. Reigber (2002), Rapid postseismic transients in subduction zones from continuous GPS, *J. Geophys. Res.*, *107* (B10), 2241, doi:10.1029/2001JB000555.

Mercier, J. L., M. Sebrier, A. Lavenu, J. Cabrera, O. Bellier, J.-F. Dumont, and J. Machare (1992), Changes in the tectonic regime above a subduction zone of Andean type: The Andes of Peru and Bolivia during the Pliocene-Pleistocene, *J. Geophys. Res.*, *97* (B8), 11,945-11,982.

Montone, P., M. T. Mariucci, S. Pondrelli, and A. Amato (2004), An improved stress map for Italy and surrounding regions (central Mediterranean), *J. Geophys. Res.*, *109*, B10410, doi:10.1029/2003JB002703.

Mueller, S., and H.-G. Kahle (1993), Crust-mantle evolution, structure and dynamics of the Mediterranean-Alpine region, in *Contribution of Space Geodesy to Geodynamics: Crustal Dynamics, Geodyn. Ser.*, vol. 23, edited by D. E. Smith and D. L. Turcotte, pp. 249-298, AGU, Washington, D. C.

Müller, B., M.L. Zoback, K. Fuchs, L. Mastin, S. Gregersen, N. Pavoni, O. Stephansson, and C. Ljunggren (1992), Regional patterns of tectonic stress in Europe, *J. Geophys. Res.*, *97* (B8), 11,783-11,803.

Müller, B., V. Wehrle, S. Hettel, B. Sperner, and F. Fuchs (2003), A new method for smoothing oriented data and its application to stress data, in *Fracture and In-Situ Stress Characterization of Hydrocarbon Reservoirs, Spec. Publ. Ser.*, vol. 209, edited by M. Ameen, pp. 107-126, Geol. Soc., London.

Nalbant, S.S., J. McCloskey, S. Steacy, and A.A. Barka (2002), Stress accumulation and increased seismic risk in eastern Turkey, *Earth Planet. Sci. Lett.*, *195*, 291-298.

Pérez, O. J., M. A. Jaimes, and E. Garciacaro (1997a), Microseismicity evidence for subduction of the Caribbean Plate beneath the South American Plate in northwestern Venezuela, *J. Geophys. Res.*, *102* (B8), 17,875-17,882.

Pérez, O. J., C. Sanz, and G. Lagos (1997b), Microseismicity, tectonics and seismic potential in southern Caribbean and northern Venezuela, *J. Seismol.*, *1*, 15-28.

Pritchard, M. E. (2006), InSAR, a tool for measuring Earth's surface deformation, *Phys. Today*, *59*,68-69.

Provost, A.-S., and H. Houston (2003), Stress orientations in northern and central California: Evidence of the evolution of frictional strength along the San Andreas plate boundary system, *J. Geophys. Res.*, *108* (B3), 2175, doi:10.1029/2001JB001123.

Reynolds, S. D., and R. R. Hillis (2000), The in situ stress field of the Perth Basin, Australia, *Geophys. Res. Lett.*, *27* (20), 3421-3424.

Reynolds, S. D., D. Coblentz, and R. R. Hillis (2002), Tectonic forces controlling the regional intraplate stress field in continental Australia: Results from new finite element modelling, *J. Geophys. Res.*, *107* (B7), 2131, doi:10.1029/2001JB000408.

Richardson, R. M. (1992), Ridge forces, absolute plate motions, and the intraplate stress field, *J. Geophys. Res.*, *97* (B8), 11,739-11,748.

Richardson, R. M., and L. M. Reding (1991), North American plate dynamics, *J. Geophys. Res.*, *96* (B7), 12,201-12,223.

Robertson, A.H.F., and M. Grasso (1995), Overview of the Late Tertiary-Recent tectonic and palaeoenvironmental development of the Mediterranean region, *Terra Nova*, 7, 114-127.

Roth, F., and P. Fleckenstein (2001), Stress orientations found in north-east Germany differ from the west European trend, *Terra Nova*, *13*, 286-289.

Russo, R. M., R. C. Speed, E. A. Okal, J. B. Shepherd, and K. C. Rowley (1993), Seismicity and tectonics of the southeastern Caribbean, *J. Geophys. Res.*, *98* (B8), 14,229-14,319.

Sandiford, M. (2002). Neotectonics of southeastern Australia: Linking the Quaternary faulting record with seismicity and in situ stress, in *Evolution and Dynamics of the Australian Plate*, edited by R. R. Hillis and D. Müller, Spec. Publ. Geol. Soc. Aust., 22, 101-113.

Sandiford, M., M. Wallace, and D. Coblentz (2004), Origin of the in situ stress field in south-eastern Australia, *Basin Res.*, *16*, 325-

338, doi:10111/j.1365-2117.2004.00235.x.

Scheck, M., and U. Bayer (1999), Evolution of the Northeast German Basin - Interferences from a 3D structural model and subsidence analysis, *Tectonophysics*, *313*, 145-169.

Smith, W. H. F., and D. T. Sandwell (1997), Global sea floor topography from satellite altimetry and ship depth soundings, *Science*, *277*, 1956-1962.

Sonder, L. (1990), Effects of density contrasts on the orientation of stresses in the lithosphere: Relation to principal stress directions in the Transverse ranges, California, *Tectonics*, *9* (4), 761-771.

Spakman, W. (1990), Tomographic images of the upper mantle below central Europe and the Mediterranean, *Terra Nova*, *2*, 542-553.

Sperner, B., F. Lorenz, K. Bonjer, S. Hettel, B. Müller, and F. Wenzel (2001), Slab break-off - Abrupt cut or gradual detachment? New insights form the Vrancea Region (SE Carpathians Romania), *Terra Nova*, *13*, 172-179.

Sperner, B., B. Müller, O. Heidbach, D. Delvaux, J. Reinecker, and K. Fuchs (2003), Tectonic stress in the Earth's crust: Advances in the World Stress Map project, in *New Insights in Structural Interpretation and Modelling*, edited by D. A. Nieuwland, Geol. Soc. Spec. Publ., 212, pp. 101-116.

Steacy, S., J. Gomberg, and M. Cocco (2005), Introduction to special section: Stress transfer, earthquake triggering, and time-dependent seismic hazard, *J. Geophys. Res.*, *110*, B05S01, doi:10.1029/2005JB003692.

Stein, R.S., A.A. Barka, and J.H. Dietrich (1997), Progressive failure on the North Anatolian fault since 1939 by earthquake stress triggering, *Geophys. J. Int.*, *128*, 594-604.

Taboada, A., L.A. Rivera, A. Fuenzalida, A. Cisternas, H. Philip, H. Bijward, J. Olaya, and C. Rivera (2000), Geodynamics of the northern Andes: Subductions and intracontinental deformation (Colombia), *Tectonics*, *19* (5), 787-813.

Thybo, H. (2001), Crustal structure along the EGT profile across the Tornquist Fan interpreted from seismic, gravity and magnetic data, *Tectonophysics*, *334*, 155-190.

Tingay, M.R.P., R.R. Hillis, C.K. Morley, R.E. Swarbrick, and E. C. Okpere (2003), Variation in vertical stress in the Baram Basin, Brunei: Tectonic and geomechanical implications, *Mar. Pet. Geol.*, *20*, 1202-1212.

Tingay, M., R. R. Hillis, C. K. Morley, E. Swarbrick, and S. J. Drake (2005a), Present-day stress orientation in Brunei: A snapshot of 'prograding tectonic' in a Tertiary delta, *J. Geol. Soc.*, *162*, 39-49.

Tingay, M., B. Müller, J. Reinecker, O. Heidbach, F. Wenzel, and P. Fleckenstein (2005b), The World Stress Map Project 'Present-day Stress in Sedimentary Basins' initiative: Building a valuable public resource to understand tectonic stress in the oil patch, *Leading Edge*, *24*, 1276-1282.

Tingay, M. R. P., B. Müller, J. Reinecker, and O. Heidbach (2006), State and origin of the present-day stress field in sedimentary basins: New results from the World Stress Map Project, paper presented at Golden Rocks 2006, The 41st U. S. Symposium on Rock Mechanics (USRMS): 50 Years of Rock Mechanics - Landmarks and Future Challenges, Am. Rock Mech. Assoc., Golden, Colo.

Townend, J., and M. D. Zoback (2006), Stress, strain, and mountain-building in central Japan, *J. Geophys. Res.*, *111*, B03411, doi: 10.1029/2005JB003759.

van Eijs, R., and W. van Dalfsen (2004), Borehole observations of maximum horizontal stress orientations in the Dutch upper crust, report, Geol. Surv. of the Netherlands (TNO-NITG), Utrecht, Netherlands.

Wagner, D., B. Müller, and M. Tingay (2004), Correcting for tool decentralisation of oriented 6-arm caliper logs for determination of contemporary tectonic stress orientation, *Petrophysics*, *46*, 530-539.

Wenzel, F., U. Achauer, E. Enescu, E. Kissling, R. Russo, V. Mocanu, and G. Musacchio (1998), Detailed look at final stage of plate break-off is target of study in Romania, *Eos Trans. AGU*, *79*, 589-594.

Wessel, P., and W.H.F. Smith (1998), New, improved version of Generic Mapping Tools released, *Eos Trans. AGU*, *79*, 579.

Ziegler, P. A. (1988), Evolution of the Arctic-North Atlantic and the Western Tethys, *AAPG Mem.*, *43*, 198 pp.

Zoback, M. D., and M. L. Zoback (1991), Tectonic stress field of North America and relative plate motions, in *Neotectonics of North America, Decade Map vol. I*, edited by D. B. Slemmons et al., pp. 339-366, Geol. Soc. of Am., Boulder, Colo.

Zoback, M. D., and M. L. Zoback (2002), State of stress in the Earth's lithosphere, in *International Handbook of Earthquake and Engineering Seismology, Int. Geophys. Ser.*, edited by W. H. K. Lee, P. C. Jennings, and H. Kanamori, pp. 559-568, Academic Press, Amsterdam.

Zoback, M. L. (1992), First- and second-order patterns of stress in the lithosphere: The World Stress Map project, *J. Geophys. Res.*, *97* (B8), 11,703-11,728.

Zoback, M. L., and K. Burke (1993), Lithospheric stress patterns: A global view, *Eos Trans. AGU*, *74*, 609-618.

Zoback, M. L., and W. D. Mooney (2003), Lithospheric bouyancy and continental intraplate stresses, *Int. Geol. Rev.*, *45*, 95-118.

Zoback, M. L., and M. D. Zoback (1989), Tectonic stress field of the conterminous United States, in Geophysical Framework of the Continental United States, edited by L. C. Pakiser and W. D. Mooney, *Mem. Geol. Soc. Am.*, *172*, 523-539.

Zoback, M. L., et al. (1989), Global patterns of tectonic stress, *Nature*, *341*, 291-298.

K. Fuchs, O. Heidbach, and F. Wenzel, Geophysical Institute, Karlsruhe University, Hertzstr. 16, 76187 Karlsruhe, Germany. (oliver.heidbach@gpi. uni-karlsruhe.de)

B. Müller, Heidelberg Academy of Sciences and Humanities, Karlstraße 4, D-69117 Heidelberg, Germany.

J. Reinecker, Institute of Geosciences, University of Tübingen, Sigwartstraße 10, D-72076 Tübingen, Germany.

B. Sperner, Geological Institute, TU Bergakademie Freiberg, Bernhard-von-Cotta-Straße 2, D-09599 Freiberg, Germany.

M. Tingay, School of Earth and Environmental Sciences, DP313 Mawson Building, University of Adelaide, Adelaide, SA 5005, Australia.

Originally published as:
GEOPHYSICAL RESEARCH LETTERS, VOL. 35, L08301, doi:10.1029/2007GL032782, 2008

Topography growth drives stress rotations in the central Andes: Observations and models

Oliver Heidbach,[1] Giampiero Iaffaldano,[2,3] and Hans-Peter Bunge[2]

Received 23 November 2007; revised 3 February 2008; accepted 22 February 2008; published 16 April 2008.

[1] Recent numerical models that couple global mantel circulation with lithosphere dynamics show that growth of the central Andes controls the 30% reduction of convergence velocity between the Nazca and South America plates observed over the past 10 Ma. The increase of gravitational potential energy due to topographic growth is also a major control on the stress pattern. Here we use numerical models which reproduce the Nazca/South America convergence history to predict the change of stress pattern in the central Andes for the past 10 Ma. Comparison of the modeled stress orientations at present-day with the observed ones results in ± 23.9° mean deviation. Based on this good agreement we attempt to predict paleostress orientations 10 Ma ago. Interestingly, the modeled stress orientations 3.2 Ma ago are very similar to the present-day orientations. From this result we infer that stress rotations occurred between 10 and 3.2 Ma ago, when topography was considerably lower. **Citation:** Heidbach, O., G. Iaffaldano, and H.-P. Bunge (2008), Topography growth drives stress rotations in the central Andes: Observations and models, *Geophys. Res. Lett.*, *35*, L08301, doi:10.1029/2007GL032782.

1. Introduction

[2] Convergence rate between the Nazca and the South America plates has decreased from 10.3 ± 0.2 cm/a 10 Ma ago [*Gordon and Jurdy*, 1986] to 6.7 ± 0.2 cm/a at present-day [*Sella et al.*, 2002]. Recent models of global lithosphere dynamics [*Kong and Bird*, 1995] coupled with a global 3D spherical mantle circulation model [*Bunge et al.*, 1998] (Figure 1a) show that this c. 30% convergence rate reduction is a consequence of the growth of the Andean mountain belt [*Iaffaldano et al.*, 2006]. Using two distinct global simulations of lithosphere dynamics, one accounting for the present-day Andes topography and the other for a paleoreconstruction of the Andean relief at 10 Ma ago [*Gregory-Wodzicki*, 2000] (Figure 1b), the models predict a slow-down of Nazca/South America convergence that is in excellent agreement with the paleomagnetic and geodetic record of plate convergence over the same time (Figure 1c). The sensitivity of lithosphere dynamics to topography has received much attention lately [*Cloetingh et al.*, 2007]. In the case of the Nazca/South America plate motion history it suggests taking a step further and investigating the related stress and paleostress Fields in the lithosphere.

[3] In this paper we compute the orientation of the maximum horizontal compressional stress (S_H) in the Andean region from the aforementioned global mantle convection-lithosphere models of *Iaffaldano et al.* [2006] and compare them with the S_H orientations of central South America from the World Stress Map (WSM) database [*Reinecker et al.*, 2005]. Our comparison reveals that the model that fits the observed velocity reduction also matches the stress orientations from the WSM database. We show that the rotation of S_H orientation and the change in tectonic regime is a response to the growth of the Andean topography. We propose that our model allows us to reconstruct the first-order paleostress pattern at 10 Ma.

2. Global Mantle Convection and Lithospheric Plate Model Coupling

[4] To compute plate motions and crustal stress orientations at present-day, 3.2 Ma and 10 Ma ago, we use the global circulation models from *Bunge et al.* [1997, 1998] coupled with a global model of the lithosphere [*Bird*, 1998] as described by *Iaffaldano et al.* [2006]. The 3D spherical mantle convection model solves the conservation equations of mass, momentum and energy for a highly viscous (Stokes) fluid to compute temperature and velocity throughout the mantle [*Bunge et al.*, 1997]. The model used for the lithosphere, the SHELLS code of *Kong and Bird* [1995], is based on conservation of mass and momentum (stress-equilibrium) in the thin-sheet approximation, where the 3D force balance is vertically integrated along depth in order to reduce the 3D problem to 2D [*Bird*, 1999].

[5] Asthenosphere velocities derived from our global mantle convection model are used as a velocity boundary condition at the base of plates in SHELLS, such that realistic mantle buoyancy forces are allowed to drive plate motion (Figure 1a). Plate driving tractions are computed in SHELLS through a dislocation olivine creep rheology that depends on temperature, pressure and strain rate, where the strain rate is equal to the vertical gradient of the asthenosphere velocity pattern from our global mantle convection model. Inferences of paleo-topography at 10 Ma and 3.2 Ma as well as the present-day topography are a priori prescribed in the model. In the following we apply the model parameters used by *Iaffaldano et al.*

[1] Geophysical Institute, Universita¨t Karlsruhe, Karlsruhe, Germany.
[2] Section of Geophysics, Ludwig-Maximilian University, Munich, Germany.
[3] Now at Department of Earth and Planetary Sciences, Harvard University, Cambridge, Massachusetts, USA.

0094-8276/08/2007GL032782$05.00

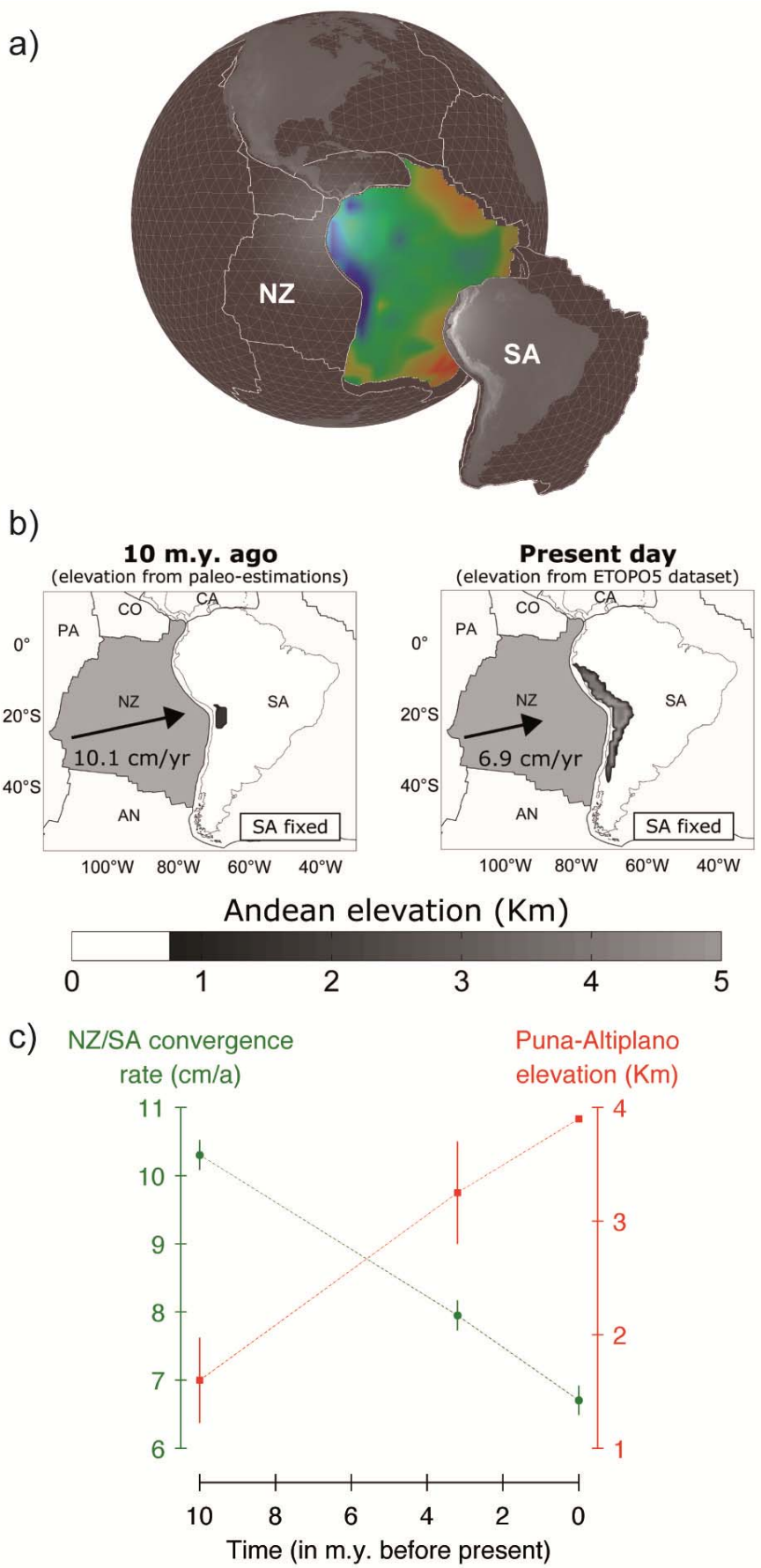

Figure 1. (a) Sketch of the global model that combines lithospheric dynamics calculated with the finite element code SHELLS (grey area) from *Bird* [1998] with a global mantle convection code (colored area) as described by *Bunge et al.* [1997]. Model rheology is non-linear, temperature and strain-rate controlled power-law rheology. (b) Map view of the change in convergence velocity of the Nazca and South America plate and change in topography. (c) Comparison of the model results (line) for three times steps at 10 Ma, 3.2 Ma and present-day with observed convergence rates (green dots with error bars) of the Nazca plate (NZ) with respect to the South America plate (SA) [*Iaffaldano et al.*, 2006]. Red graph denotes the evolution of topography. Note the inverse correlation between topography growth and decreasing convergence rate.

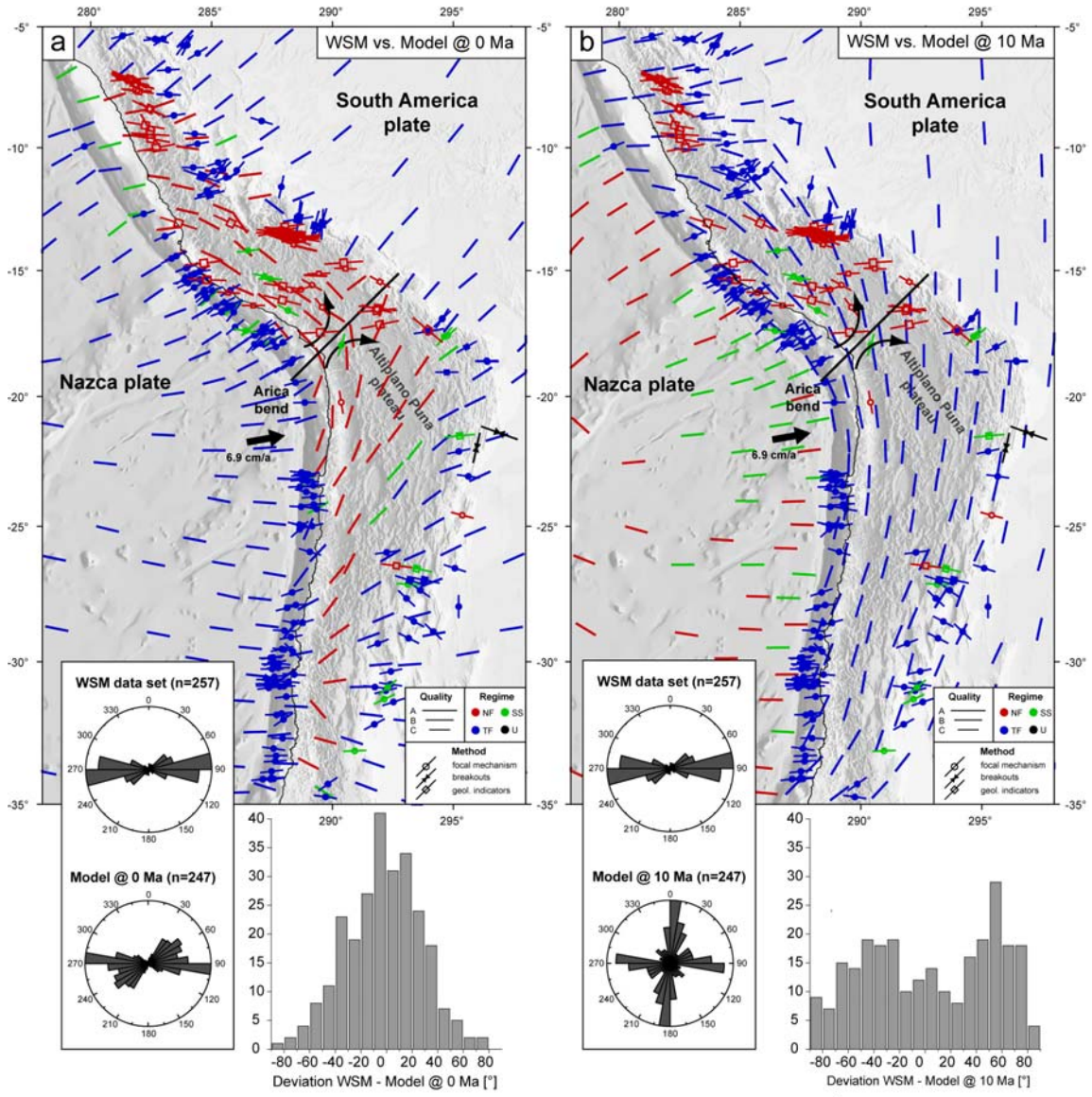

Figure 2. Comparison of model results and WSM data. Lines give the orientation of maximum horizontal compressional stress (S_H). Lines with symbols in its center are WSM data; the ones without symbols are the numerical model results. Colors indicate the tectonic regime: red is normal faulting (NF), green is strike-slip (SS), blue is thrust faulting (TF), and black is unknown tectonic regime (U). Black arrow indicates the convergence of the Nazca plate with respect to the South America plate. Histograms display the deviation distribution between the modeled data and the WSM data set. Deviations are calculated at the locations of the WSM data records taking into account the three nearest model results weighted by distance. (a) Comparison of WSM data and model results at 0 Ma. (b) Comparison of WSM data and model results at 10 Ma. Note that most of the changes occur on the continent and that the stress pattern at 10 Ma is very different on the continents than on the oceanic lithosphere indicating that coupling at the plates interface was significant lower at 10 Ma in contrast to today situation. Changes are clock-wise south of the SW-NE striking axis at the Arica bend (black line) and counter-clockwise north of it.

[2006] which successfully match the convergence between Nazca and South America plates (Figure 1c) over the past 10 Ma. To compare the S_H orientations calculated from this model we use a subset of the WSM database.

3. World Stress Map Data Versus Model Results

[6] The WSM database provides information on the S_H orientation and the tectonic regime from a wide range of stress indicators [*Heidbach et al.*, 2007; *Zoback*, 1992]. In the central Andes between 5°-35°S and 62°-82°W the database provides 257 stress data records of A-C quality data. We eliminated three data records from focal mechanism solutions that show normal faulting with N-S orientation of S_H. This orientation is due to the bending of the subducting Nazca plate in the forebulge, a process that is not represented in our modeling approach.

[7] The 257 data records exhibit a E-W oriented stress pattern that is controlled by the relative plate motion striking approximately N80°W of the Nazca plate with respect to South America. In the Eastern and Western Cordillera of the Altiplano-Puna plateau S_H is perpendicular to the strike of the Andes, and thrust faulting is the prevailing tectonic regime. In the central Andes the excess of gravitational potential energy due to the 4000-m-high Altiplano-Puna plateau leads to normal faulting regime with S_H oriented parallel to the strike of the Andes (Figure 2a).

[8] Comparison of the contemporary S_H orientations from the WSM with our modeling results at present-day

Table 1. Mean Deviation Between S_H Orientation From the WSM Data Set and the Model Results and Fit of the Tectonic Regime.

Time	Mean Deviation[a]	Tectonic Regime
0 Ma	± 23.9°	68%
3.2 Ma	± 23.2°	65%
10 Ma	± 44.8°	42%

[a] Distance weighted mean of the three nearest model values

yields a mean deviation of ± 23.9°. This is within the uncertainties of the A-C quality WSM data that are reliable to within ± 25°. Furthermore, the two observed general trends in S_H orientations and the prevailing tectonic regimes are also well reflected in our model (Figure 2a). The model shows normal faulting in the Altiplano-Puna plateau and thrust faulting in the Western and Eastern Cordilleras. The histogram of the deviation between observed and modeled S_H orientations has a distinct maximum at 0° (Figure 2a).

[9] In our tectonic model corresponding to conditions 3.2 Ma ago results are similar to the ones at present-day. However, in the model representing the scenario at 10 Ma the mean deviation between modeled and today's WSM stress S_H orientations is increased to ± 44.8°, i.e. larger than the uncertainties of the WSM A-C quality data. The modeled paleostress field exhibits two first-order stress orientations; a N-S oriented stress field in the South America plate with prevailing thrust faulting and an E-W oriented stress field in the Nazca plate with strike-slip and normal faulting regime (Figure 2b). The histogram of the deviations between observed and modeled S_H orientations at 10 Ma has no clear maximum, but exhibits homogeneous distribution of deviation (Figure 2b).

[10] The model results indicate that the S_H orientations and the tectonic regime changed significantly during the past 10 Ma (Table 1). S_H orientations rotated counter-clockwise north of an axis located in the Arica bend and a clockwise south of it (Figures 2 and 3). This axis coincides with an axis separating rotations of the same sense and similar amount that has been identified from paleomagnetic analysis [*Allmendinger et al.*, 2005, and references therein]. For the northern area of the Altiplano-Puna plateau, these findings are also confirmed by the analysis of paleostress data from Miocene faults [*Mercier et al.*, 1992], which indicate counter-clockwise rotation of 48° and 76° at two locations comparable to the 46° and 59° counter-clockwise rotation predicted from our model (Table 2). However, north of 10°S *Mercier et al.* [1992] report 33° and 52° counterclockwise rotation, whereas our model indicates 3° rotation (Table 2).

4. Discussion

[11] Qualitatively our model results at present-day are in good agreement with numerical models that use the 2D thin sheet approximation [*Coblentz and Richardson*, 1996; *Meijer and Wortel*, 1992; *Richardson*, 1992; *Richardson and Coblentz*, 1994; *Stefanik and Jurdy*, 1992]. These studies state that the major stress sources for the South America plate are topography-induced body forces, basal drag, and the portion of ridge push force from the Nazca plate transferred at the subduction interface. They also argue that the resistive forces at the interface are a key factor in the evolution of the central Andes.

[12] The buoyancy forces per unit length induced by the excess of gravitational potential energy of the Andes have been estimated to be in the order of 5×10^{12} N m^{-1} [*Froideveaux and Isacks*, 1984; *Husson and Ricard*, 2004; *Richardson*, 1992]. The ridge push force per unit length is in the range of 1.0-7.5 $\times 10^{12}$ N m^{-1} [*Richardson and Cob-*

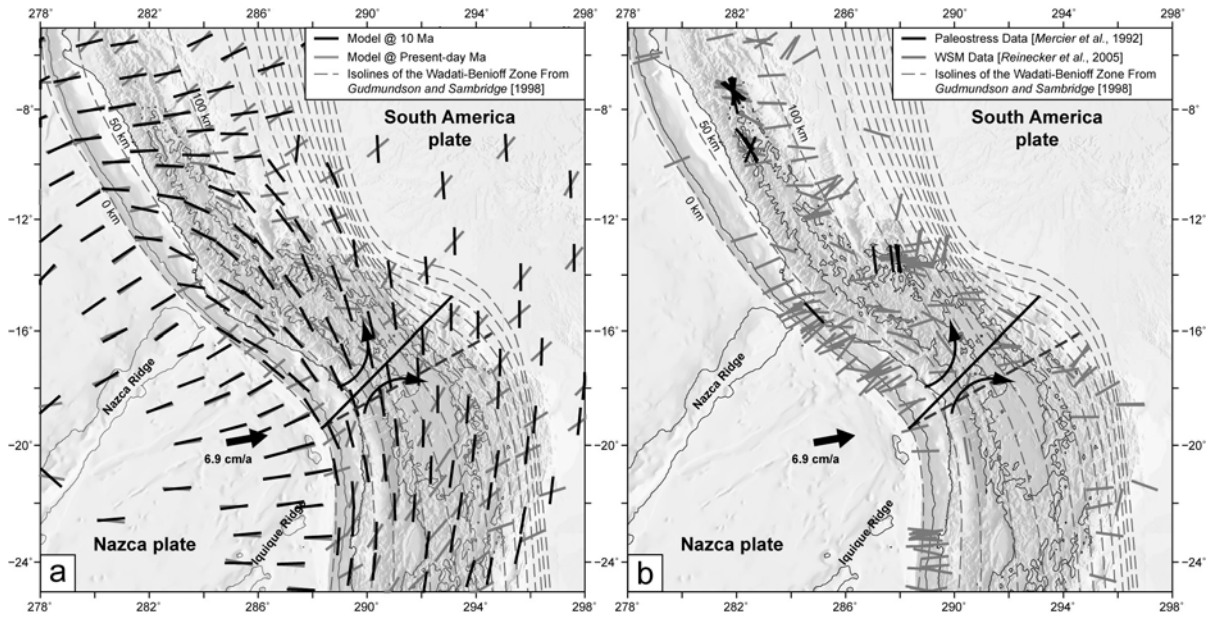

Figure 3. Comparison of observed and modeled S_H orientations in the northern section. Thin lines on the continent (ocean) are the 4000 m (-3500 m) topography (bathymetry) contour lines. SW-NE striking black line at the Arica bend separates areas with prevailing counter-clockwise rotations from areas with clockwise rotations. Black dotted line separates counter-clockwise rotations from clockwise rotations from the analysis of paleomagnetic data [*Allmendinger et al.*, 2005, and references therein]. (a) Comparison of model results at 10 Ma and present-day. Note the small rotations north of 10°S where topography is less than 4000 m. (b) Comparison of observed paleostress and present-day stress data.

Table 2. Observed and Modeled SH Orientations at 10 Ma and Present-Day.

Location[a]	10 Ma Observed[b]	10 Ma Modeled	0 Ma Observed[b]	0 Ma Modeled	Rotation[c] Observed	Rotation[c] Modeled
78.1°W 7.3°S	157° ± 23° ($n = 12$)	83°	105° ± 9° ($n = 11$)	80°	52°	3°
77.5°W 9.4°S	157° ± 25° ($n = 4$)	93°	124° ± 29° ($n = 4$)	90°	33°	3°
72.5°W 13.4°S	173° ± 3° ($n = 5$)	157°	97° ± 7° ($n = 13$)	111°	76°	46°
75.2°W 15.4°S	137° ($n = 1$)	123°	89° ± 5° ($n = 2$)	64°	48°	59°

[a] Locations are taken from sites where *Mercier et al.* [1992] provide paleostress data.
[b] Mean S_H orientation with standard deviation at 10 Ma from *Mercier et al.* [1992] and at present-day from the WSM [*Reinecker et al.*, 2005]. Numbers in brackets indicate the number of data records used for the mean value and its standard deviation.
[c] Positive values denote counter-clockwise rotation.

lentz, 1994] and *Lamb* [2006] estimates the shear forces per unit length along the plate interface in North Chile to be 9.7×10^{12} N m^{-1}. This is in agreement with our modeling results that indicate an increase of resistive forces per unit length at the plate interface due to the Andean growth in the order of 10^{13} N m^{-1}. Thus, large topographic features do indeed contribute to lithosphere dynamics by as much as the far-field stresses due to mantle convection. We also infer that the increase of resistive forces at the plates interface due to the variation in paleotopography controlled most of the stress rotations in the South America plate.

[13] Using the analytical approach of *Sonder* [1990] for the amount of S_H rotation θ' for extensional and compressional tectonic stress regime

$$\theta' = \frac{1}{2}\tan^{-1}\left(\frac{\sin 2\theta}{-\tau/\tau' - \cos 2\theta}\right) \quad (1)$$

we can also estimate the relative stress increase that is needed for the observed stress rotation of $\theta' = 59°$ at 75.2°W and 15.4°S (Table 2). Inserting in expression (1) $\theta = 2°$ as the angle between the orientation of the far-field stress at 10 Ma (N137°) and the regional stress anomaly, i.e. the strike of the Andes (N135°) we receive for the stress ratio $-\tau \,/\, \tau' = -0.96$. τ is the magnitude of the far-field stress and τ' the magnitude of the regional stress anomaly. Thus, the stress anomaly needed to rotate S_H by $\theta' = 59°$ is of similar magnitude as the far-field stress magnitude at 10 Ma.

[14] Whereas south of 10°S our modeled stress rotations match the observed ones, north of 10°S the model does not predict rotations backwards in time as indicated by paleostress data (Figure 3). Here the increase of topography in the model did not rotate S_H, but only changed the tectonic regime from prevailing thrust faulting at 10 Ma to normal faulting and strike-slip at present-day in agreement with the WSM stress data (Figure 2).

[15] This misfit in S_H rotation can result from the spatial resolution of our model. As our model is global, local to regional effects are not represented. E.g. one parameter not represented in our approach is the change of trench sediment thickness. *Lamb* [2006] concludes from his analytical modeling that trench sediment falls can act as lubricants in subduction zones and that they are probably the key control of shear force magnitudes at the plates interface. North of 10°S the sediment fall in the Nazca plate trench increases from less than 0.1 km to 0.5-2.5 km [*Lamb and Davis*, 2003]. At the same time the subduction dip angle decreases from > 30° to 10-15°. Thus, the resistive forces at the plates interface probably vary significantly along strike of the Andes.

[16] In general local to regional effects can be of great importance when the stress state is close to isotropic [*Heidbach et al.*, 2007]. Therefore, when the far-field stress has a small magnitude, even small changes in topography can induce large stress rotations. Likewise the change of other regional stress sources such as lateral tear-off of a slab after continental collision (e.g. southern Apennines, SE-Carpathians) or the far-field stresses due to reorganization of plate motion (e.g. Pacific plate at *c.* 5 Ma) can become a major control of the S_H orientation.

[17] Another source for the deviation between the modeled S_H orientation and the observed one is the uncertainty of the stress data itself. Most of the WSM stress data in South America have C-quality. This implies that the S_H orientation is reliable to within ± 25°. Furthermore, the exact timing of the paleostress data is difficult and can deviate from the chosen model time of 10 Ma.

5. Conclusions

[18] Our modeling results are in good agreement with the observations and show that growth of the central Andes controls the overall slow down of the Nazca/South America plate convergence, the change of the tectonic regime, and the rotation of S_H orientation. Furthermore, modeling results indicate that 3.2 Ma ago the stress field orientation was very similar to the present-day one. This provides independent support for the suggestion that a large part (75%) of the current topography was already in place at that time. As the fit of the S_H orientations is satisfactory for different time stages, we argue that our models reveal the relative importance of the participating stresses responsible for the evolution of the kinematics and the stress field pattern. We conclude that the degree of coupling at the plate interface and its time variability are key controls also for the evolution of the stress pattern in the central Andes.

[19] **Acknowledgments.** We thank Gwendolyn Peters, Karl Fuchs, Birgit Müller, and Zvi Ben-Avraham for constructive comments on an earlier version of this paper. We also acknowledge the reviews from Sierd Cloetingh and the editor Fabio Florindo that improved the paper. Oliver Heidbach acknowledges the financial support from the Heidelberg Academy of Sciences and Humanities and

the Task Force VII of the International Lithosphere Program. Giampiero Iaffaldano acknowledges the support by the Elitenetwork of Bavaria.

References

Allmendinger, R., J. R. Smalley, M. Bevis, H. Caprio, and B. Brooks (2005), Bending the Bolivian orocline in real time, *Geol. Soc. Am.*, *33*, 905–908.

Bird, P. (1998), Testing hypotheses on plate-driving mechanisms with global lithosphere models including topography, thermal structure, and faults, *J. Geophys. Res.*, *103*, 10,115-10,129.

Bird, P. (1999), Thin-plate and thin-shell finite element programs for forward dynamic modeling of plate deformation and faulting, *Comput. Geosci.*, *25*, 383-394.

Bunge, H.-P., M. A. Richards, and J. R. Baumgardner (1997), A sensitivity study of three-dimensional spherical mantle convection at 108 Rayleigh number: Effects of depth-dependent viscosity, heating mode, and an endothermic phase change, *J. Geophys. Res.*, *102*, 11,991-12,007.

Bunge, H.-P., M. A. Richards, C. Lithgow-Bertelloni, J. R. Baumgardner, S. P. Grand, and B. A. Romanowicz (1998), Time scales and heterogeneous structure in geodynamic Earth models, *Science*, *280*, 91-95.

Cloetingh, S.A.P.L., et al. (2007), TOPO-EUROPE: The geoscience of coupled deep Earth–surface processes, *Global Planet. Change*, *58*, 1-118.

Coblentz, D., and R. M. Richardson (1996), Analysis of the South American intraplate stress field, *J. Geophys. Res.*, 101, 8643-8657.

Froideveaux, C., and B. L. Isacks (1984), The mechanical state of stress of the Altiplano-Puna segment of the Andes, *Earth Planet. Sci. Lett.*, *71*, 305-314.

Gordon, R. G., and D. M. Jurdy (1986), Cenozoic global plate motion, *J. Geophys. Res.*, *91*, 12,389-12,406.

Gregory-Wodzicki, K. M. (2000), Uplift history of the central and northern Andes: A review, *Geol. Soc. Am. Bull.*, *112*, 1091-1105.

Heidbach, O., J. Reinecker, M. Tingay, B. Müller, B. Sperner, K. Fuchs, and F. Wenzel (2007), Plate boundary forces are not enough: Second- and third-order stress patterns highlighted in the World Stress Map database, *Tectonics*, *26*, TC6014, doi:10.1029/2007TC002133.

Husson, L., and Y. Ricard (2004), Stress balance above subduction: Application to the Andes, *Earth Planet. Sci. Lett.*, *222*, 1037-1050.

Iaffaldano, G., H.-P. Bunge, and T. Dixon (2006), Feedback between mountain belt growth and plate convergence, *Geology*, *34* (10), 893-896, doi:10.1130/G22661.1.

Kong, X., and P. Bird (1995), SHELLS: A thin-shell program for modeling neotectonics of regional or global lithosphere with faults, *J. Geophys. Res.*, *100*, 22,129-22,132.

Lamb, S. (2006), Shear stresses on megathrusts: Implications for mountain building behind subduction zones, *J. Geophys. Res.*, 111, B07401, doi:10.1029/2005JB003916.

Lamb, S., and P. Davis (2003), Cenozoic climate change as a possible cause for the rise of the Andes, *Science*, *425*, 792-797.

Meijer, P. T., and M. J. R. Wortel (1992), The dynamics of motion of the South American plate, *J. Geophys. Res.*, *97*, 11,915-11,931.

Mercier, J. L., M. Sebrier, A. Lavenu, J. Cabrera, O. Bellier, J.-F. Dumont, and J. Machare (1992), Changes in the tectonic regime above a subduction zone of Andean type: The Andes of Peru and Bolivia during the Pliocene–Pleistocene, *J. Geophys. Res.*, *97*, 11,945-11,982.

Reinecker, J., O. Heidbach, M. Tingay, B. Sperner, and B. Müller (2005), The 2005 release of the World Stress Map, www.world-stress-map.org, Res. Group of the Heidelberg Acad. of Sc. and Humanities, Heidelberg, Germany.

Richardson, R. M. (1992), Ridge forces, absolute plate motions, and the intraplate stress field, *J. Geophys. Res.*, *97*, 11,739-11,748.

Richardson, R. M., and D. Coblentz (1994), Stress modeling in the Andes: Constraints on the South American intraplate stress magnitudes, *J. Geophys. Res.*, *99*, 22,015-22,025.

Sella, G. F., T. Dixon, and A. Mao (2002), REVEL: A model for Recent plate velocities from space geodesy, *J. Geophys. Res.*, *107* (B4), 2081, doi:10.1029/2000JB000033.

Sonder, L. J. (1990), Effects of density contrasts on the orientation of stresses in the lithosphere: Relation to principal stress directions in the transverse ranges, California, *Tectonics*, *9*, 761–771.

Stefanik, M., and D. M. Jurdy (1992), Stress observations and driving force models for the South American plate, *J. Geophys. Res.*, *97*, 11,905-11,913.

Zoback, M. L. (1992), First- and second-order patterns of stress in the lithosphere: The World Stress Map Project, *J. Geophys. Res.*, *97*, 11,703-11,728.

H.-P. Bunge, Section Geophysics, Department of Earth and Environmental Sciences, Ludwig-Maximilian University, Theresienstr. 41, D-80333 München, Germany. (bunge@lmu.de)

O. Heidbach, Geophysical Institute, Department of Physics, Universität Karlsruhe (TH), Hertzstr. 16, D-76187 Karlsruhe, Germany. (oliver.heidbach@gpi.uni-karlsruhe.de)

G. Iaffaldano, Department of Earth and Planetary Sciences, Harvard University, 20 Oxford Street, Cambridge, MA 02138, USA. (iaffaldano@eps.harvard.edu)

Originally published as:
Earth and Planetary Science Letters 257 (2007) 299-312

Stress evolution and seismic hazard of the Dead Sea Fault System

Oliver Heidbach[a,*], Zvi Ben-Avraham[b]

[a] Geophysical Institute, Karlsruhe University, Hertzstr. 16, 76187 Karlsruhe Germany
[b] Department of Geophysics and Planetary Science, Tel Aviv University, P.O.B. 39040, Ramat Aviv, Tel Aviv, 69978, Israel

Received 5 January 2006; received in revised form 26 February 2007; accepted 26 February 2007
Available online 6 March 2007
Editor: R.D. van der Hilst

Abstract

We calculated the stress evolution for the central part of the Dead Sea Fault System (30.5°N-34.5°N) from 551 to 2005 through modelling the static stress changes due to 14 historical earthquakes with $M_S > 6.0$ superimposed by tectonic loading from relative plate motion. From the results of our numerical models, we identified two segments with high positive changes in Coulomb failure stress (ΔCFS) exceeding 4 MPa, a ~90-km-long segment of the Jordan Fault south of the Sea of Galilee and a ~30-km-long segment east of the Dead Sea. These segments could result in $M_S = 7.4$ and $M_S = 6.8$ earthquakes, respectively. In contrast to similar stress evolution models of other continental transform faults, our results support only partly the hypothesis that coseismically induced static stress changes control the spatial succession of earthquakes. We calculated on each rupture plane the mean of ΔCFS and the maximum ΔCFS due to the stress changes of all preceding earthquakes. The results of the calculated mean ΔCFS values reveal that only 6 out of 13 earthquakes could have been triggered the subsequent earthquake. From the analysis of the maximum ΔCFS values, we find that 8 out of 13 earthquakes could have triggered the subsequent earthquake. Since our model results are sensitive to location and magnitude of historical earthquakes and the tectonic loading rates of the fault segments, we emphasize the need for further paleoseismological studies and current slip rate estimation from continuously observing GPS arrays and geological investigations. Taking into account that six large cities (Beirut, Damascus, Haifa, Tel Aviv, Amman, and Jerusalem) are in close proximity with distances between 30 and 150 km to the Jordan segment, the seismic risk is probably higher than accounted before.

Keywords: earthquake triggering; Dead Sea Fault; seismotectonics; Coulomb failure stress

1. Introduction

Seismic hazard and its variation in time is linked to the contemporary state of stress of seismically active fault systems. The stress evolution of a fault is mainly controlled by the tectonic loading rate due to plate motion and stress perturbations induced by co- and postseismic stress transfer [1,2]. Models incorporating coseismically induced static stress changes and tectonic loading have been successfully applied to explain earthquake sequences, e.g. along the East Anatolian Fault system [3], in western Turkey [4], along the North Anatolian Fault system [5-7] and in Southern California [8-10]. These findings contributed fundamental information for the estimation of earthquake probabilities and seismic hazard assessment, e.g. for the Marmara region south of Istanbul, where a strong earthquake is expected [5,11,12], and for Southern California [13]. In contrast to these regions, where sequences of strong earthquakes have been observed in the last century, seismic records of the same period from the central part of the Dead Sea Fault System (DSFS) between 30.5°N and 34.5°N exhibit only two earthquakes with $M_S > 6.0$: The 1927 earthquake ($M_S = 6.2$) at the north-western rim of the Dead Sea and the 1956 earthquake ($M_S = 6.0$) southwest of Beirut (Fig. 1). The last strong earthquake took place in 1837 ($M_S = 7.4$) in the Hula basin north of the Sea of Galilee. The long recurrence intervals for strong earthquakes in the order of 103-104 years [14-18] are due to low slip rates along the various DSFS segments between 1 and 7 mm/yr [19-23]. However, the dense population since historical times as well as several paleoseismological and archaeological investigations provide comprehensive catalogues of large

* Corresponding author. Tel.: +49 721 6084609; fax: +49 721 71173.
E-mail address: oliver.heidbach@gpi.uni-karlsruhe.de (O. Heidbach).

doi:10.1016/j.epsl.2007.02.042

historical earthquakes for the last 2000 years [14,15,18,19,24-32]. Taking into account that six major cities (Beirut, Damascus, Haifa, Tel Aviv, Amman, and Jerusalem) are located close to the DSFS (< 50 km), the analysis of its stress evolution provides fundamental information for the evaluation of seismic hazard and seismic risk.

Here we present a numerical model for the evolution of stress along the central DSFS (30.5°N-34.5°N) for the last 1450 years including coseismic stress changes due to a sequence of 14 $M_S > 6.0$ earthquakes and tectonic loading due to plate motion. We test the hypothesis whether the earthquake sequence could have been triggered by the coseismically induced static stress changes. We also calculate the evolution of stress in terms of changes of Coulomb failure stress (ΔCFS) for different time steps taking into account the varying strike of the fault segments. The final time step in the year 2005 (of the numerical stress evolution calculations) reveals the current state of stress and enables us to assess the seismic hazard for individual fault segments.

2. Neotectonics and historical seismicity

The DSFS represents a continental left-lateral strike-slip fault system which separates the Arabia plate from the Africa plate (Fig. 1). A displacement of 105 km occurred along this 1000-km-long boundary since the late Miocene [33]. Our study area is the central part, from 30.5°N to 34.5°N, including the Dead Sea and the Sea of Galilee connected by the Jordan Fault. At the Dead Sea, the Jordan fault splits

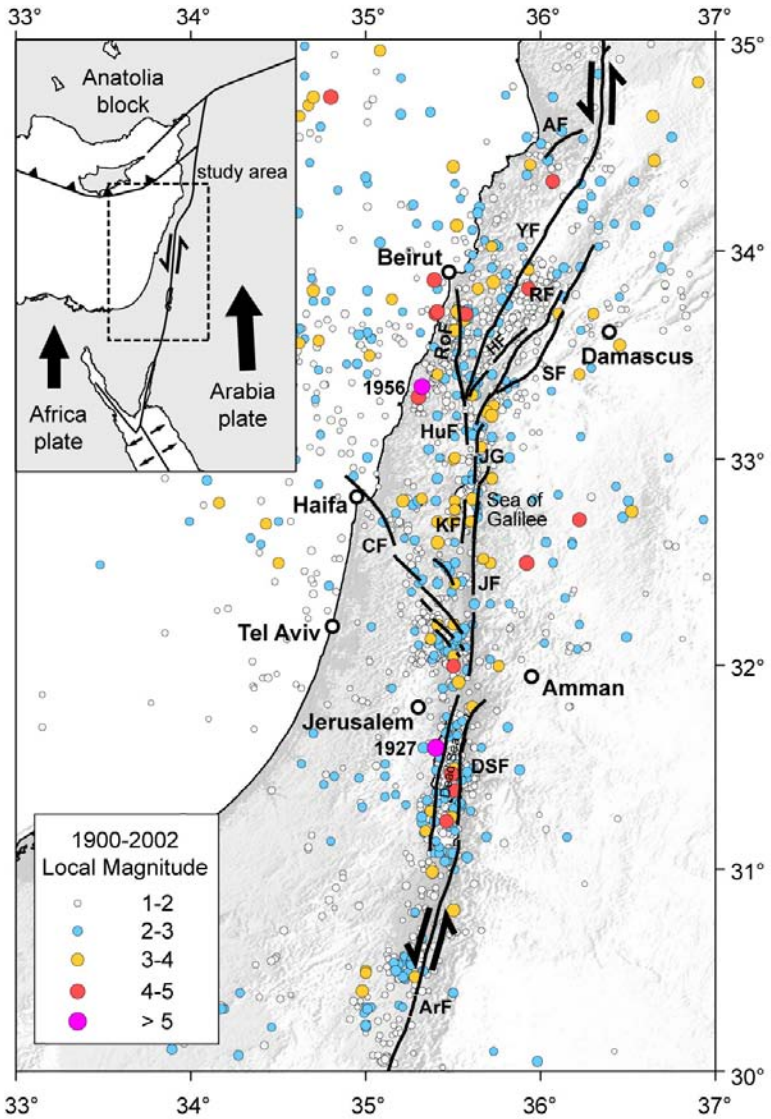

Figure 1. Recorded seismicity of the study area from 1900 to 2002 (Geophysical Institute of Israel, available online at http://www.gii.co.il). Black lines are the active faults. Abbreviations are: AF = Akar Fault, ArF = Arava Fault, CF = Carmel Fault, DSF = Dead Sea Fault, HF = Hasbaya Fault, HuF = Hula Fault, JF = Jordan Fault, JG = Jordan Gorge, KF = Kinnereth Fault, RoF = Roum Fault, RF = Rachaiya Fault, SF = Serghaya Fault, YF = Yammouneh Fault. The locations of the two $M_L \geq 6.0$ earthquakes from the 20th century are indicated by the year numbers.

into a western and a eastern segment separated by the Dead Sea pull-apart basin. Further south, the Arava Fault connects the DSFS to the Gulf of Aqaba [34]. North of the Sea of Galilee, the DSFS splits into several branches. From west to east these branches are: the Roum Fault, the Yammouneh Fault, the Hasbaya Fault, the Rachaiya Fault, and the Serghaya Fault (Fig. 1).

2.1. Fault kinematics

It has been recognized that the total left-lateral slip of ~105 km south of the Sea of Galilee is not older than 18 Ma [33,35,36]. This gives a minimum slip rate of 5.8 mm/yr. A review of the overall DSFS kinematics for the last ~5 Ma from *Westaway* [37] states that the system had an average slip rate of ~7 mm/yr. For the Late Pleistocene and Holocene *Klinger et al.* [23] estimated a slip rate of 4.0 ± 2 mm/yr for the Arava Fault between the Gulf of Aqaba and the Dead Sea. From continuous GPS observations in Israel and Jordan, *Wdowinski et al.* [20] observed a contemporary slip rate of 3.3 ± 0.4 mm/yr for the Jordan Fault.

Further north *Meghraoui et al.* [32] found a slip rate of 6.9 ± 0.1 mm/yr for the Missyaf segment in Syria north of the Yammouneh Fault from paleoseismologic and archaeological evidence. This is slightly higher than the Late Pleistocene-Holocene slip rate of 3.8-6.4 mm/yr for the Yammouneh Fault from *Daëron et al.* [38]. However, the findings of *Meghraoui et al.* [32] represent an average slip rate from ~2000 years including a succession of four strong earthquakes, and thus probably represents an upper bound.

These findings contradict the older results which assume that the Yammouneh Fault as well as the faults further east (Hasbaya Fault, Rachaiya Fault, and Serghaya Fault) are inactive [22,39]. This is also

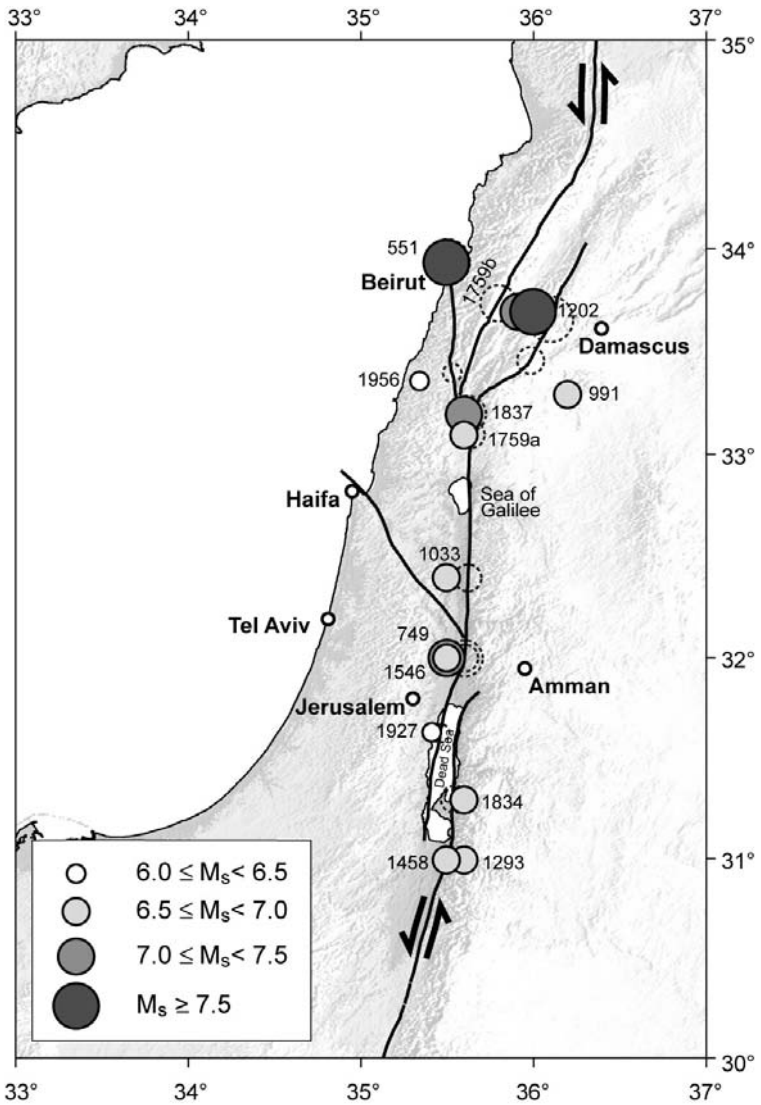

Figure 2. Location and year date of the 14 historical earthquakes ($M_S \geq 6.0$) along the Dead Sea Fault System (DSFS) of the last 1500 years (for details see Table 1). Dashed circles indicate the locations after shifting the epicentres onto the nearest major active fault.

in contrast to the findings of *Gomez et al.* [40]. They find from the analysis of Late Pleistocene and Holocene lake deposits slip rates between 1 and 2 mm/yr on the Serghaya Fault including large offsets from historical earthquakes.

Walley [41] states that the Yammouneh Fault shows, in recent geological times, small slip rates between 0.8 and 1.6 mm/yr. He proposes that the faults further east have been active in Pre-Pliocene, but that the activity shifted to the Roum Fault. The Roum Fault is the northern prolongation of the DSFS and strikes N10°W (Fig. 1). Even though its surface trace disappears south of Beirut it shows recent tectonic activity [42]. River channel displacements for the last 5 Ma reveal offsets of ~8 km in the south and smaller ones in the order of a few kilometres in the north [42,43]. This would give a maximum slip rate of 1.6 mm/ yr for the Roum Fault. Thus, the Roum Fault can take up only a minor portion of the total relative plate motion of ~5 mm/yr between the Arabia plate and the Africa plate.

We assume for our model that the Yammouneh Fault is the most active fault with slip rates of 3-4 mm/yr. The Roum Fault and the Serghaya Fault are less active and have slip rates of ~1 mm/yr, whereas the Hasbaya Fault and the Rachaiya Fault are assumed to be inactive.

South of this complex system the Jordan Gauge, the small fault segment just north of the Sea of Galilee, shows a minimum slip rates for the Holocene of 3 mm/yr [19] which fits to the geodetically observed slip rate of 3.3 ± 0.4 mm/yr [20]. Another seismically active fault is the Carmel Fault. It strikes N40°W, starts north of the Dead Sea, and continues offshore crossing Haifa Bay [44,45] (Fig. 1). Here we assume a slip rate of 1 mm/yr for our model.

2.2. Historical earthquakes

Besides the instrumentally recorded earthquakes of the years 1927 and 1956 we compiled historical earthquakes using various catalogues from year 551 onwards [14,15,18,24-27,29]. In total we identified 14 historical earthquakes with $M_S > 6.0$ (Fig. 2 and Table 1). We are aware that these compilations have limited accuracy with respect to the given epicentre location and the estimated magnitude from the observed intensities. Furthermore, the publications on historical earthquakes are not consistent since they account for different historical documents and their interpretations. Our selection of earthquake location and magnitude is not an attempt to compile a new catalogue, but a selection of historical earthquake data where the majority of publications are in agreement. The data for the historical earthquakes used for the modelling are summarized in Table 1.

Since no detailed source mechanisms are known for historical earthquakes, we made the following assumptions: (1) They occurred along the known major active faults. We projected the epicentres onto the nearest major active fault following the findings of *Garfunkel* [21] and *Ambraseys and Jackson* [46] who found a good correlation of large earthquakes with major active faults in the region (Fig. 2). The mean relocation distance of ~10 km indicates that this is a reasonable assumption. (2) The slip directions of the earthquakes follow the strike of the associated faults and are horizontal. (3) The dip of the faults is vertical which is in agreement with the available focal mechanisms solutions of recorded smaller earthquakes [47,48]. (4) The locking depth is $w = 12.5$ km and defines the vertical extension of the rupture plane for all earthquakes. This is in agreement with average focal depths of 8.7 km for earthquakes in the study area with $M_L \geq 3.0$ recorded in the period from 1982 to 2002 (Israel seismological network of the Geophysical Institute of Israel, available online at http://www.gii.co.il). (5) The slip distribution along the rupture plane is uniform and bi-directional from the epicentre for all earthquakes, except the 551 and the 1837 earthquake.

For the 551 earthquake we extend the rupture plane only in southern direction from the reported epicentre since no fault trace has been detected offshore [42,43]. For the 1837 earthquake, we extend the rupture plane only in northern direction along the Yammouneh Fault from the reported epicentre. Assuming that the Roum Fault and the Serghaya Fault are less active it is more likely that the 1837 earth-

Table 1
Model parameters for the historical earthquakes

Year (AD)	Lat. (deg N)	Lon. (deg E)	M_S	l[a] (km)	u[b] (m)
551	33.9	35.5	7.5	115	3.8
749	32.0	35.5	7.3	79	2.8
991	33.3	36.2	6.7	25	1.1
1033	32.4	35.5	6.7	25	1.1
1202	33.7	36.0	7.5	115	3.8
1293	31.0	35.6	6.8	31	1.3
1458	31.0	35.5	6.8	31	1.3
1546	32.0	35.5	7.0	45	1.7
1759a	33.1	35.6	6.8	31	1.3
1759b	33.7	35.9	7.4	95	3.2
1834	31.3	35.6	6.3	12	0.6
1837	33.2	35.6	7.1	54	2.0
1927	31.6	35.4	6.2	11	0.5
1956	33.35	35.32	6.0	7	0.4

[a] Length of the ruptured fault segment assuming that $M_L \approx M_S$ in case only M_L was given in the sources.
[b] Displacement along the fault segment assuming a locking depth w of 12.5 km.

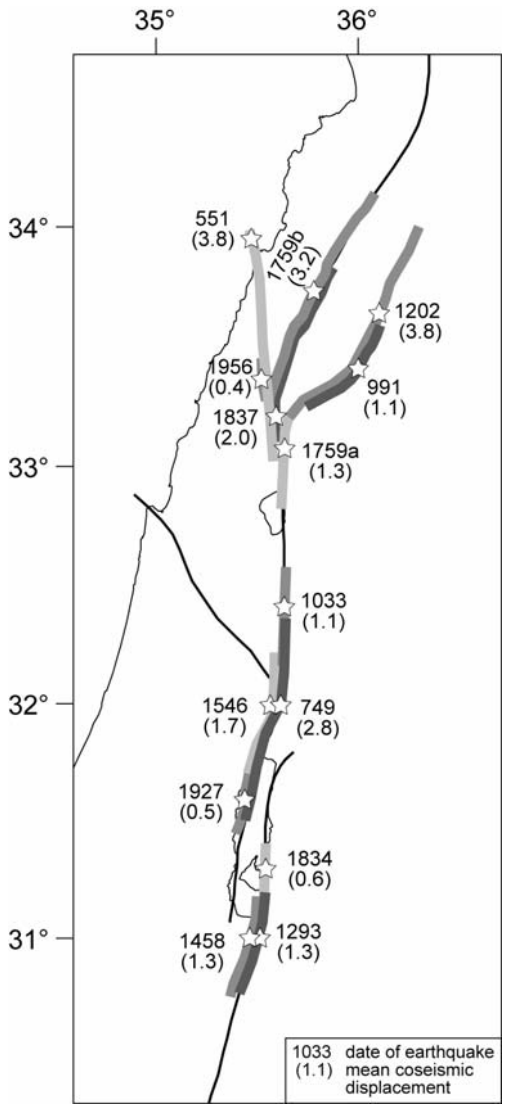

Figure 3. Epicentres (stars) and rupture lengths (grey thick lines) of the 14 historical earthquakes along the Dead Sea Fault System (thin black line). The average coseismic displacement on the rupture planes is calculated from Eqs. (1) and (2) in the text.

quake occurred on the Yammouneh Fault. An alternative fault could have been the Jordan Gauge, but this is less likely since this is not a through going structure and does not provide the needed rupture plane length of 54 km for the $M_S = 7.1$ earthquake. This assumption is in agreement with *Marco et al.* [19]. They assume that the two historical earthquakes which are seen in their paleoseismological trenches crossing the Jordan Gorge are the 1202 earthquake and the 1759a earthquake. Even though *Ambraseys* [24] states that there is no clear evidence whether the 1837 earthquake occurred on the Roum Fault or the Yammouneh Fault we decided to place it on the latter since (a) the slip rates on the Roum Fault are too small to accumulate enough strain after the 551 earthquake and (b) a major aftershocks of the 1837 occurred slightly east of the Yammouneh Fault [24].

3. Stress evolution model

To model the static stress field changes due to the sequence of the 14 historical earthquakes and the tectonic loading we applied the boundary element method for a 3D elastic half space using the software Poly3D of *Thomas* [49]. For the DSFS model geometry we implemented the major active segments and neglected smaller, presumably inactive fault branches such as the Hasbaya, Kinnereth [50], and Rachaiya Fault (Figs. 1 and 2). For the tectonic loading we assume a slip rate of 5 mm/yr between the Africa plate and the Arabia plate. Given the discussion in the previously presented fault kinematics section we assign to the Carmel Fault, the Roum Fault, and the Serghaya Fault a slip rate of 1 mm/yr. The Yammouneh Fault is given slip rates between 3 and 5 mm/yr. The Arava Fault and the Jordan Fault is given a slip rate of 5 mm/yr and, for the western and eastern fault segments along the Dead Sea, the slip rates decrease from 4 mm/yr to 0 at the ends of the faults (Fig. 4).

The second boundary condition comes from the coseismic slip on the rupture plane. The rupture plane length l is calculated with the empirical formula of *Ambraseys and Jackson* [46]

$$\log l \ [\mathrm{km}] = 0.82 M_S - 4.09 \qquad (1)$$

The coseismic displacement u along the rupture plane is given with the formula

$$u = M_0/(G \cdot A) \qquad (2)$$

where A is the area of the rupture plane ($A = lw$), G the shear modulus and M_0 the seismic moment. According to *Ambraseys and Jackson* [46], M_0 is given with the empirical formula

$$\log M_0 = 1.5 M_S + 9.0 \qquad (3)$$

The results of the calculations for the rupture plane lengths l and the coseismic displacements u for each earthquake are summarized in Table 1 and represented in Fig. 3.

In addition to the coseismic slip of the earthquakes, the ongoing relative movement between the Arabia plate and the Africa plate produces stress loading along the seismogenic part of the fault, i.e. the upper 12.5 km. We model this tectonic loading by increasing the fault slip rates in steps of 1 mm/yr from zero at 12.5 km depth (locking depth w) to the full relative displacement rate for each segment of the DSFS at 17.5 km depth. From 17.5 to 100 km depth the full slip rates are applied (Fig. 4).

From the resulting stress field of the boundary element model we calculated the change of Coulomb

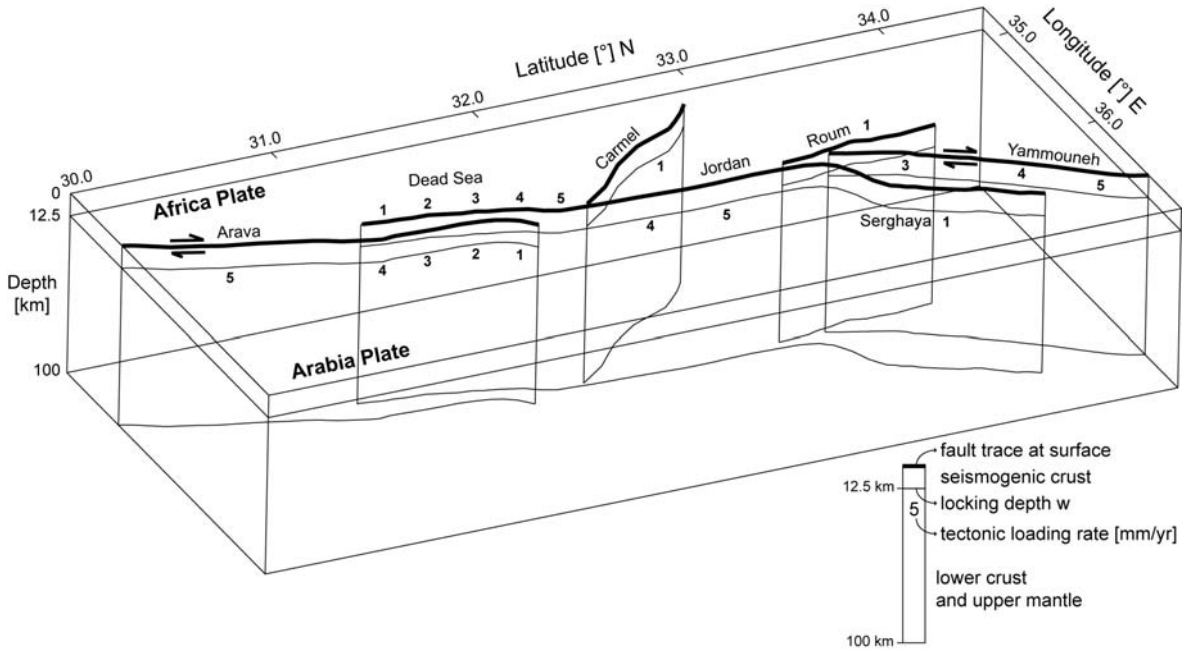

Figure 4. 3D model sketch of the study area. The numbers at the various fault segments give the applied tectonic loading rate (slip rate) in mm/yr below the locking depth w at 12.5 km.

failure stress (ΔCFS) on the rupture plane of the subsequent earthquake (Table 1). *Reasenberg and Simpson* [51] define ΔCFS as

$$\Delta\mathrm{CFS} = \Delta\tau + \mu'\Delta\sigma_n \qquad (4)$$

where $\Delta\tau$ is the change in shear stress (positive in slip direction of the subsequent earthquake), $\Delta\sigma_n$ the change of normal stress perpendicular to the rupture plane of the subsequent earthquake (negative for compression), and μ' the apparent coefficient of friction. We performed all calculations with a shear modulus of $G = 33$ GPa, a Poisson ratio of 0.25 for the 3D elastic half space, and an apparent friction coefficient of $\mu' = 0.4$.

In contrast to the commonly used ΔCFS representations in map view (e.g., [5,7,8]), we follow the concept of *Nalbant et al.* [3] displaying ΔCFS only at the faults. These ΔCFS values are calculated at a depth of 6.25 km in 1-km spacing, taking into account the varying orientation of the rupture plane. From these calculations, the stress evolution in terms of ΔCFS values at different stages of the historical earthquake sequence is displayed in profiles along the fault strike of the various DSFS segments (Fig. 5).

4. Results

We analysed the numerical model results for the evolution of stress from two different perspectives: (1) *Stress triggering:* Could the sum of the coseismically induced stress changes from the preceding earthquakes have triggered the subsequent earthquake? (2) *Present-day stress state:* We calculated for each fault segment the present-day stress state considering the stress evolution for the years 551-2005 including the tectonic loading and the coseismically induced static stress changes.

4.1. Static stress triggering

From the coseismically induced stress changes of the preceding earthquakes we calculated along the rupture plane of the succeeding earthquake the mean ΔCFS and the maximum ΔCFS value (Table 2). The results are classified according to the following scheme: If the rupture plane of the succeeding earthquake experienced a mean/maximum ΔCFS > 0.1 MPa the earthquake was classified as probably triggered by the static stress changes of the preceding earthquakes, while for a mean/max ΔCFS < 0.01 MPa triggering is unlikely. Given this classification, 8 out of 13 earthquakes show potential triggering due to the maximum ΔCFS values, and 6 out of 13 earthquakes due to mean ΔCFS values. The other earthquakes occur in regions with negative ΔCFS values between -0.03 and -10.51 MPa (Table 2).

4.2. Stress evolution

Evolution of stress along the DSFS is calculated for various times including the effect of tectonic loading and coseismically induced stress changes.

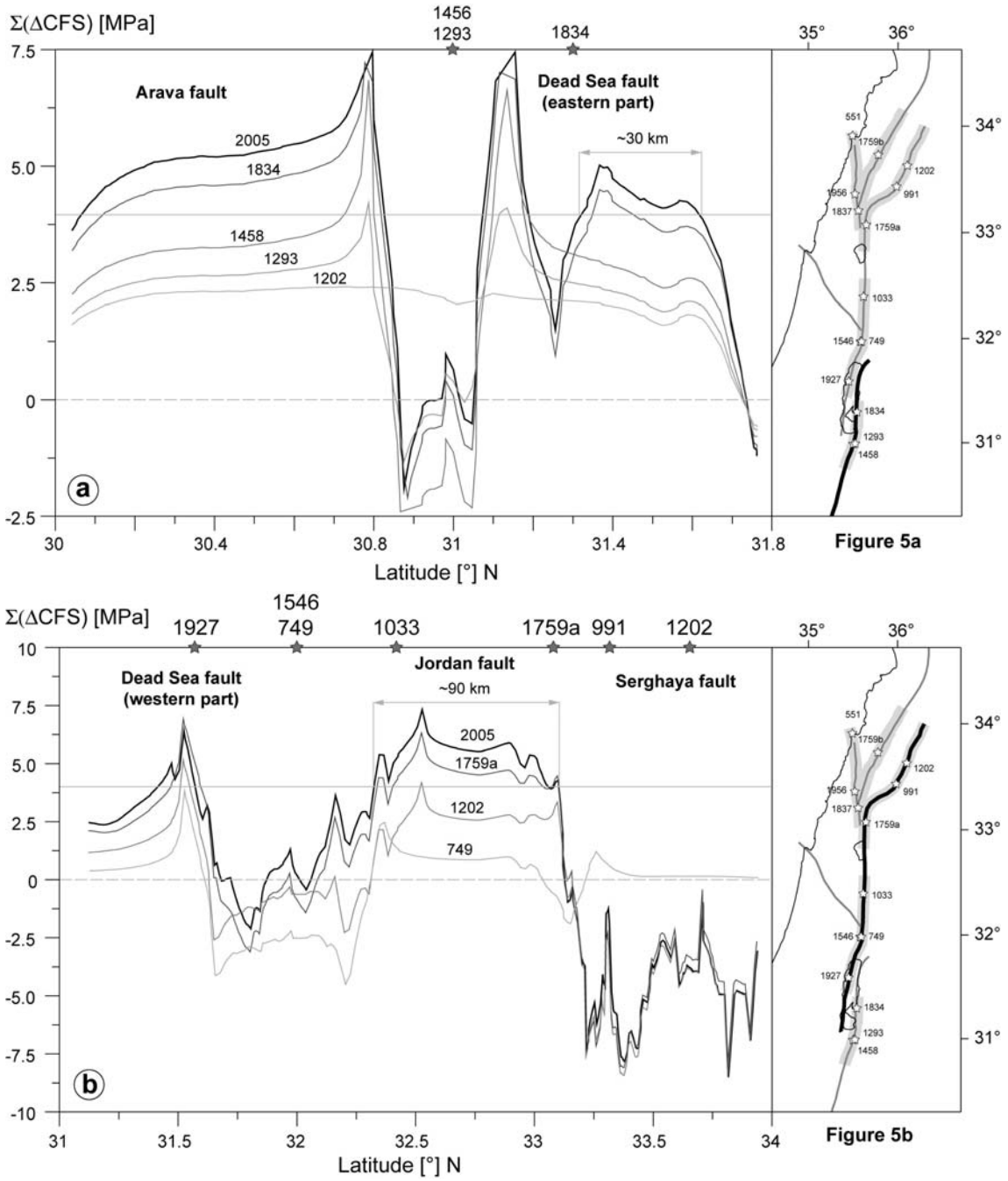

Figure 5. Evolution of ΔCFS for five fault zones along the Dead Sea Fault System (DSFS) from 551 (ΔCFS = 0) to 2005. In order to suppress unrealistic edge effects at the endings of each rupture plane, the five last points are smoothed. Plotted segments are shown on the overview maps as thick black lines. Lines with increasing gray scale represent the stress state of the given year. Stars indicate the position of the earthquake. Dashed lines are the 0 ΔCFS level and the thin grey lines in panels a and b are the 4 MPa ΔCFS level. Note the increased ΔCFS values in year 2005 for a 30-km-long section of the eastern Dead Sea Fault (a) and a 90-km-long section for the Jordan Fault (b) which could according to Eq. (1) produce $\boldsymbol{M_S = 6.8}$ and $\boldsymbol{M_S = 7.4}$ earthquake, respectively.

Fig. 5a-e display the results for the DSFS. The ΔCFS values for the stress evolution are also calculated in steps of 1 km, taking into account the varying orientations of the fault segments.

Fig. 5a shows the results for the Arava Fault and the eastern part of the Dead Sea Fault. The curves display the unloading effect caused by the 1293, 1458 and 1837 earthquake. For the last time step in 2005 the northern part of this segment along the eastern side of the Dead Sea has been loaded with ΔCFS > 4 MPa over a length of ~30 km. According to Eq. (1) this loading could result in a $M_S = 6.8$ earthquake. The high stress level of the Arava Fault south of 30.9°N is probably artificial. Historical earthquakes such as the 1068 earthquake with $M > 6.6$ [52,53], which occurred outside the model boundary, probably unloaded this Arava Fault segment.

Fig. 5b displays the stress evolution for the western part of the Dead Sea Fault, the Jordan Fault and the Serghaya Fault. The curves show the unloading

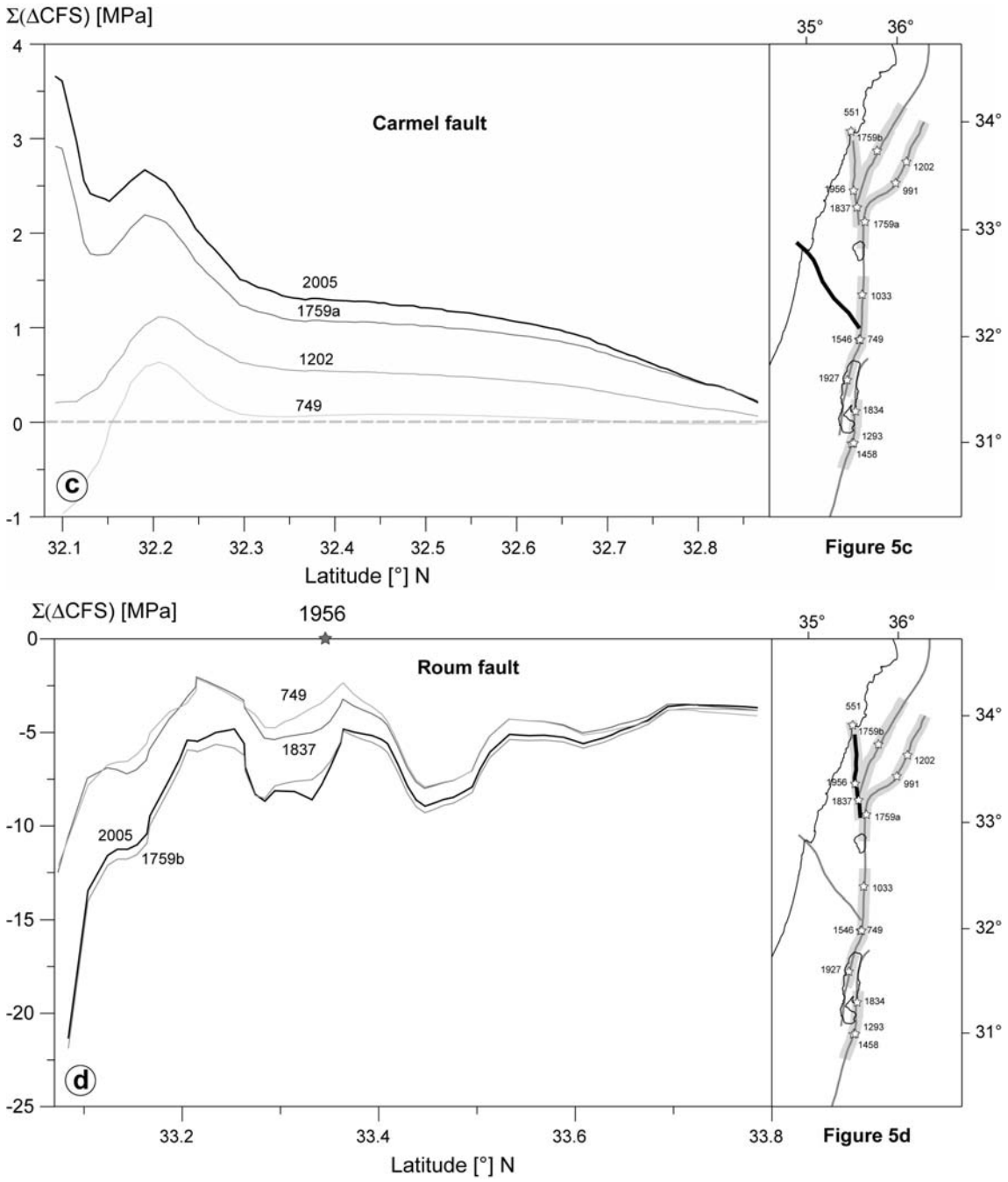

Figure 5. (continued).

effect of the 749 earthquake on the western part of the Dead Sea Fault and the unloading of the Serghaya Fault due to the 1202 earthquake. The final time step of the stress evolution in 2005 indicates that the central segment of the Jordan Fault has accumulated ΔCFS > 4 MPa over a length of ~90 km. Following Eq. (1) this segment might generate a $M_S = 7.4$ earthquake.

Fig. 5c and d give the stress evolution for the Carmel Fault and the Roum Fault, respectively. The Carmel Fault shows small increases in positive ΔCFS values over time with the largest increase near the junction with the Jordan Fault. In contrast to that, the Roum Fault is fully unloaded. Due to the large 551 earthquake and the smaller one in 1956, the ΔCFS < -5 MPa (Fig. 5d).

Fig. 5e represents the stress evolution for the Yammouneh Fault. Here the major unloading effects result from the earthquakes of 1759b and 1837. Thus, the final stage of stress evolution in 2005 reveals an unloaded southern part of the Yammouneh Fault with negative ΔCFS values of ~-2.5 MPa or smaller. North of 34° the ΔCFS values increase to high positive values. However, this is probably an artificial result due to the proximity of the model boundary. The well-documented large historical earthquakes in the 12th century on the Gharb Fault [32,54] are located just north of our study area and

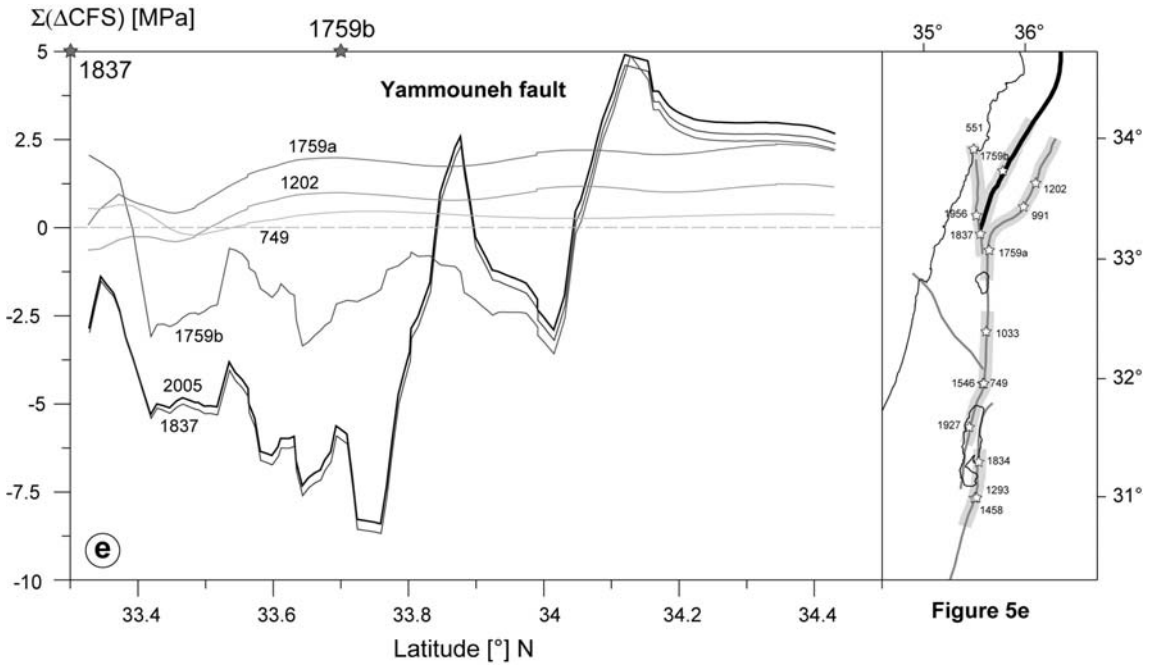

Figure 5. (continued).

probably unloaded the northern segment of the Yammouneh Fault.

The contemporary stress state in 2005 for all segments is summarized in Fig. 6. The areas, which are probably affected by large earthquakes outside our model boundary, were removed from this figure. The map shows that a ~90-km-long segment of the Jordan Fault and a ~30-km-long section of the eastern segment of the Dead Sea Fault have high potential for a future strong earthquake. Fig. 6 emphasizes the close proximity of several large cities to the segments with high ΔCFS values.

5. Discussion

The static stress-triggering hypothesis refers to the causal relationship between two subsequent earthquakes. This hypothesis has been successfully tested for a succession of earthquakes in several continental strike-slip systems such as the North Anatolian Fault, East Anatolian Fault and parts of the San Andreas Fault [3-5,9,13]. *Stein et al.* [5] showed that 9 out of 10 earthquakes from a 20th century sequence of major earthquakes along the North Anatolian Fault are probably triggered by their precursors. In their study, the positive ΔCFS values at the epicentre of the following earthquake were, on average, 0.31 MPa. Furthermore, none of the epicentres showed negative ΔCFS values. In contrast to these findings, our ΔCFS results indicate only limited interaction between the earthquakes due to static stress change. Only 6 (mean ΔCFS values along the rupture plane), or 8 (maximum ΔCFS values on the rupture plane), of the 13 historical earthquakes can be addressed to static stress triggering assuming a threshold value of 0.01 MPa (Table 2). In our model the remaining 7 (mean ΔCFS), respectively 5 (maximum ΔCFS) earthquakes, are located in stress shadows, i.e., in areas where the sum of the coseismic stress changes from the preceding earthquakes is negative. The location of a large earthquake in the stress shadow of the preceding earthquakes has also been detected for the 1911 Morgan Hill earthquake in the San Francisco Bay area [55] and an earthquake doublet from 1997 in Kagoshima, Japan [56]. Furthermore, a recent global analysis of static stress triggering using shallow earthquakes (< 50 km) of the CMT Harvard catalogue from 1976-2001 revealed that strike-slip earthquakes seem less in support of the triggering hypothesis [57]. We are aware that our research is only one possible scenario of stress evolution due to the high uncertainties in location and magnitude of the historical earthquakes, local effects caused by the probably oversimplified fault geometry of the model, and the assumed slip distribution and sense of slip. Thus, in the following we discuss a number of possible ways to explain the deviation from the static stress-triggering hypothesis.

[1] *Large uncertainties in location and magnitude of the historical earthquakes:* This is a severe problem which cannot be addressed until more paleoseismological and archaeological data are available. For instance, very recent findings from paleoseismological investigations along the Serghaya and Yammouneh Fault indicate that the

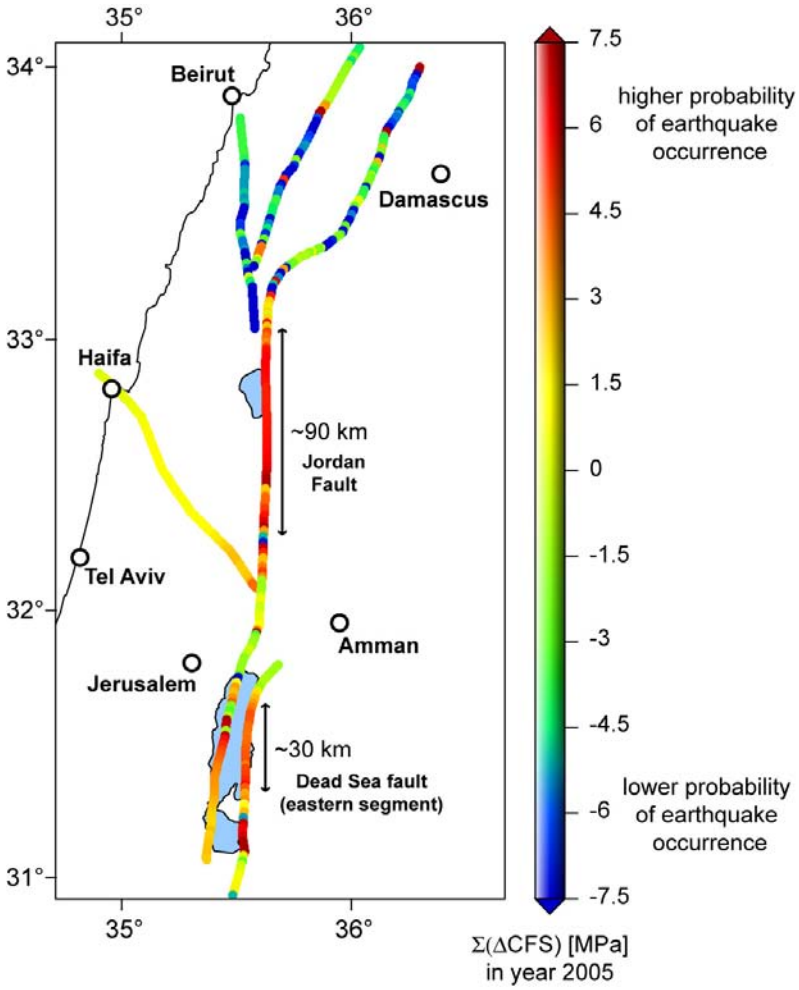

Figure 6. Present-day stress state of the Dead Sea Fault System. Displayed are the cumulative ΔCFS values calculated for the varying orientation of each fault in 1-km steps. The ΔCFS values include the coseismically induced stress changes superimposed by the stress effect from tectonic loading for the period from 551 to 2005. Note the large positive values along the Jordan Fault and the eastern segment of the Dead Sea Fault.

1202 earthquake probably occurred on the Yammouneh Fault and the 1759b earthquake on the Serghaya Fault [58]. We implemented these two earthquakes the other way around in our model following our model assumption to relocate each earthquake to the nearest active fault segment. However, this does not influence the final present stress state since both earthquakes differ only by 0.1 in magnitude and have the same latitude location. Thus, the stress evolution of the Yammouneh Fault and the Serghaya Fault would take a different stress evolution path, but end up in the same final stress state as given in Fig. 5b. Another open question is, whether the 551 earthquake occurred (a) offshore on an undetected thrust Fault which connects the Roum Fault and the Akar Fault [59], (b) on the Roum Fault as assumed in our model [25,27,43], or (c) on the Jordan segment [15]. Future re-locations of historical earthquakes and a re-analysis of their magnitudes could change the results of both, the stress evolution, and thus the present-day stress state, and the assessment of the stress triggering hypothesis along the DSFS.

[2] *Data gaps in the historical earthquake catalogue:* This is relatively unlikely for the study area since it has been always densely populated [14,15]. A strong earthquake would have been described in historical documents and its impact would be reflected in historical buildings such as the impact of the earthquakes 1202, 1759a and 1837 on the crusader castle Vadum Jacob situated on the Jordan Fault [31] or archaeological excavations of the old city of Tiberias located at the Sea of Galilee [30]. However, it cannot be ruled out until a systematic investigation of the paleoseismicity in terms of trenches reveals more details on the historical seismic record along all fault segments.

[3] *The static stress transfer is not the major control for the sequence of earthquakes along the DSFS:* There is either an alternative stress transfer process which causes the earthquake sequence (e.g. visco-elastic relaxation) or there is no coherence between the earthquakes in our study area; that is, the earthquake sequence along the DSFS follows a Poisson distribution. This excites the

question whether the DSFS is different in structure and/or in rheology in comparison to other continental transform faults where the hypothesis of static stress triggering has been tested successfully. Major differences are the neotectonics, the slip rates, and the earthquake recurrence rates. The latter two are approximately five times larger at the North Anatolian Fault [5,60]. However, since our model for the ΔCFS analysis is time-independent, the lower slip rate cannot be responsible for our findings. A major structural difference compared to the North Anatolian Faults, the East Anatolian Faults, and the San Andreas Fault is the neotectonic regime of the DSFS. The tectonic regime changes from a releasing bend where the pull-apart basin of the Dead Sea Fault has been formed to the restraining bend of the Lebanon - Anti-Lebanon mountains. These two features are less than 200 km apart, have major influence on the kinematics, and probably control the unusual seismotectonics of the DSFS.

[4] *Transient stress transfer:* Transient stress changes due to visco-elastic relaxation processes are in the order of 0.1-1.0 MPa in the near field of the rupture plane on time scales varying in dependence of the viscosity of the lower crust and the upper mantle from a few years [61,62] to hundreds of years [63]. *Lorenzo-Martín et al.* [64] applied for their stress evolution model of the North Anatolian Fault due to the 19th century strong earthquakes sequence a visco-elastic rheology with a linear viscosity of 5×10^{19} Pa s for the lower crust and 10^{18} Pa s for the lower crust. The resulting transient contribution to the stress changes e.g. on the Düzce segment was in average 0.2 MPa [64]. However, at the DSFS the contribution from transient processes to the total stress field evolution is probably small since the observed heat flow is in the order of 40 mW m^{-2} indicating a strong lower crust with high viscosities [65]. For large time scales (> 100 years) stresses from tectonic loading and coseismic stress changes are probably predominant. For a fault slip rate of 5 mm/yr, the tectonic loading produces shear stress rates of ~0.003 MPa/yr. The coseismically induced static stress changes are in the order of ~5 MPa in the near-field earthquake rupture plane [5].

6. Conclusions

We tested the static stress triggering hypothesis using a sequence of 14 historical earthquakes along the central part of the DSFS and its stress evolution covering the time period from 551 to 2005. The stress triggering analysis revealed that about half of the earthquakes shows a possible triggering from the stress transfer of all previous earthquakes assuming a threshold value of 0.01 MPa. The present-day stress state indicates that the Jordan segment has the highest potential to fail next. The accumulated ΔCFS stresses are > 4 MPa on a ~90 km segment which could result in a $M_S = 7.4$ earthquake. Since six major cities (Beirut, Damascus, Haifa, Tel Aviv, Amman, and Jerusalem), are in close proximity at distances between 30 and 150 km from the Jordan segment, the seismic risk is probably underestimated. Given that the recurrence rates of devastating earthquakes as well as the magnitudes and locations of historical earthquakes are most important for the seismic hazard assessment in the DSFS, it is crucial to raise more data in order to undertake a more detailed analysis of stress evolution including a quantitative analysis of the uncertainties of the presented stress evolution model. To further constrain such models, and thus the seismic hazard potential, it is absolutely essential to increase the research on contemporary slip rates, e.g. from a dense continuous GPS network, estimation of geological slip rates for the Late Paleocene and Holocene, and paleoseismological research.

Acknowledgements

We especially thank Blanka Sperner, Karl Fuchs and John Reinecker for very constructive comments on an earlier version of this paper. We also thank the reviewer Shimon Wdowinski for constructive comments which improved the paper. The stress field calculation software Poly3D [49] and its graphical user interface Poly3DGUI from Frantz Maerten were provided by David Pollard from Stanford University. Figures were plotted with the Generic Mapping Tools [66]. We also acknowledge the support of the Deutsche Forschungsgemeinschaft (DFG, German Science Foundation) through the Collaborative Research Centre 461 (CRC 461) at the University of Karlsruhe, Germany: “Strong Earthquakes - a Challenge for Geosciences and Civil Engineering”.

References

[1] R.A. Harris, Introduction to special section: stress triggers, stress shadows, and implications for seismic hazard, J. Geophys. Res. 103 (1998) 24347-24358.

[2] S. Steacy, J. Gomberg, M. Cocco, Introduction to special section: stress transfer, earthquake triggering, and time-dependent seismic hazard, J. Geophys. Res. 110 (2005), doi:10.1029/

2005JB003692.
[3] S.S. Nalbant, J. McCloskey, S. Steacy, A.A. Barka, Stress accumulation and increased seismic risk in eastern Turkey, Earth Planet. Sci. Lett. 195 (2002) 291-298.
[4] S.S. Nalbant, A. Hubert, G.C.P. King, Stress coupling between earthquakes in northwest Turkey and the north Aegean Sea, J. Geophys. Res. 103 (1998) 24469-24486.
[5] R.S. Stein, A.A. Barka, J.H. Dietrich, Progressive failure on the North Anatolian fault since 1939 by earthquake stress triggering, Geophys. J. Int. 128 (1997) 594-604.
[6] F. Roth, Modelling of stress patterns along the western part of the Anatolian Fault Zone, Tectonophysics 152 (1988) 215-226.
[7] G. King, A. Hubert, S.S. Nalbant, B. Meyer, R. Armijo, D. Bowman, Coulomb interactions and the 17 August 1999 Izmit, Turkey earthquake, Earth Planet. Sci. Lett. 333 (2001) 557-569.
[8] J. Deng, L.R. Sykes, Evolution of the stress field in southern California and triggering of moderate-size earthquakes: a 200-year perspective, J. Geophys. Res. 102 (1997) 9859-9886.
[9] R.A. Harris, R.W. Simpson, In the shadow of 1857 - the effect of the great Ft. Tejon earthquake on subsequent earthquakes in southern California, Geophys. Res. Lett. 23 (1996) 229-232.
[10] R.A. Harris, R.W. Simpson, P.A. Reasenberg, Influence of static stress changes on earthquake locations in southern California, Nature 375 (1995) 221-224.
[11] T. Parsons, Recalculated probability of $M \geq 7$ earthquakes beneath the Sea of Marmara, Turkey, J. Geophys. Res. 109 (2004), doi:10.1029/2003JB002667.
[12] J.R. Muller, A. Aydin, Using mechanical modeling to constrain fault geometries proposed for the northern Marmara Sea, J. Geophys. Res. 110 (2005), doi:10.1029/2004JB003226.
[13] S. Toda, R.S. Stein, K. Richards-Dinger, S.B. Bozkurt, Forecasting the evolution of seismicity in southern California: animations built on earthquake stress transfer, J. Geophys. Res. 110 (2005), doi:10.1029/2004JB003415.
[14] A. Ben-Menahem, Four thousand years of seismicity along the Dead Sea Rift, J. Geophys. Res. 96 (1991) 20195-20216.
[15] N.N. Ambraseys, C.P. Melville, R.D. Adams, The Seismicity of Egypt, Arabia and the Red Sea, University Press, Cambridge, 1994.
[16] S. Marco, A. Agnon, High-resolution stratigraphy reveals repeated earthquake faulting in the Masada Fault Zone, Dead Sea Transform, Tectonophysics 408 (2005) 101-112.
[17] Z.B. Begin, D.M. Steinberg, G.A. Ichinose, S. Marco, A 40,000 year unchanging seismic regime in the Dead Sea Rift, Geol. Soc. Am. 334 (2005), doi:10.1130/G21115.1.
[18] C. Migowski, A. Agnon, R. Bookman, J.F.W. Negendank, M. Stein, Recurrence pattern of Holocene earthquakes along the Dead Sea Transform revealed by varve-counting and radiocarbon dating of lacustrine sediments, Earth Planet. Sci. Lett. 222 (2004) 301-314.
[19] S. Marco, T.K. Rockwell, A. Agnon, A. Heimann, U. Frieslander, Late Holocene slip of the Dead Sea Transform revealed in 3D paleoseismic trenches on the Jordan Gorge Fault, Earth Planet. Sci. Lett. 234 (2005) 189-2005.
[20] S. Wdowinski, Y. Bock, G. Baer, L. Prawirodirdjo, N. Bechor, S. Naaman, R. Knafo, Y. Forrai, Y. Melzer, GPS measurements of current crustal movement along the Dead Sea Fault, J. Geophys. Res. 109 (2004), doi:10.1029/2003JB002640.
[21] Z. Garfunkel, Internal structure of the Dead Sea leaky transform (rift) in relation to plate kinematics, Tectonophysics 80 (1981) 81-108.
[22] R.W.H. Butler, S. Spencer, H.M. Griffiths, The structural response to evolving plate kinematics during transpression: evolution of the Lebanese restraining bend of the Dead Sea Transform, in: R.E. Holdsworth, R.A. Strachan, J.F. Dewey (Eds.), Continental Transpressional and Transtensional Tectonics, Special Publication, vol. 135, Geological Society, London, 1998, pp. 81-106.
[23] Y. Klinger, J.P. Avouac, N. Abou Karaki, L. Dorbath, D. Bourles, Slip rate on the Dead Sea Transform fault in northern Araba Valley (Jordan), Geophys. J. Int. 142 (2000) 755-768.
[24] N.N. Ambraseys, The earthquake of 1 January 1837 in Southern Lebanon and Northern Israel, Ann. Geofis. 40 (1997) 923-936.
[25] R. Darawcheh, M.R. Sbeinati, C. Margottini, S. Paolini, The 9 July 551 AD Beirut earthquake, Eastern Mediterranean region, J. Earthqu. Eng. 4 (2000) 403-414.
[26] D.H.K. Amiran, E. Arieh, D.L. Turcotte, Earthquakes in Israel and adjacent areas: macroseismic observations since 100 B.C.E., Israel, Explor. 44 (1994) 260-305.
[27] K. Khair, G.F. Karakaisis, E.E. Papadimitriou, Seismic zonation of the Dead Sea Transform fault area, Ann. Geofis. 43 (2000) 61-79.
[28] N.N. Ambraseys, C.P. Melville, An analysis of the eastern Mediterranean earthquake of 20 May 1202, in: H. Meyer, K. Shimazaki, B. Lee (Eds.), Historical Seismograms and Earthquakes of the World, Academic Press, San Diego, California, 1988, pp. 181-200.
[29] N.N. Ambraseys, M. Barazangi, The 1759 earth-

quake in the Bekaa Valley: implications for earthquake hazard assessment in the Eastern Mediterranean Region, J. Geophys. Res. 94 (1989) 4007-4013.
[30] S. Marco, M. Hartal, N. Hazan, L. Lev, M. Stein, Archaeology, history, and geology of the A.D. 749 earthquake, Dead Sea Transform, Geology 8 (2003) 665-668.
[31] R. Ellenblum, S. Marco, A. Agnon, T.K. Rockwell, A. Boas, Crusader castle torn apart by earthquake at dawn, 20 May 1202, Geology 26 (1998) 303-306.
[32] M. Meghraoui, F. Gomez, R. Sbeinati, J. van der Woerd, M. Mouty, A.N. Darkal, Y. Radwan, I. Layyous, H. Al Najjar, R. Darawcheh, F. Hijazi, R. Al-Ghazzi, M. Barazangi, Evidence for 830 years of seismic quiescence from paleoseismology, archaeoseismology and historical seismicity along the Dead Sea Fault in Syria, Tectonophysics 210 (2003) 35-52.
[33] Z. Garfunkel, I. Zak, R. Freund, Active faulting in the Dead Sea Rift, Tectonophysics 80 (1981) 1-26.
[34] Z. Ben-Avraham, Structural framework of the Gulf of Elat Aqaba) - northern Red Sea, J. Geophys. Res. 90 (1985).
[35] R. Freund, I. Zak, Z. Garfunkel, Age and rate of the of the sinistral movement along the Dead Sea Rift, Nature 220 (1968) 253-255.
[36] A.M. Quennell, The structural and geomorphic evolution of the Dead Sea Rift, J. Geol. Soc. Lond. 114 (1958) 1-24.
[37] R. Westaway, Present-day kinematics of the Middle East and eastern Mediterranean, J. Geophys. Res. 99 (1994) 12071-12090.
[38] M. Daëron, L. Benedetti, P. Tapponnier, A. Sursock, R.C. Finkel, Constraints on the post ~25-ka slip rate of the Yammouneh Fault (Lebanon) using in situ cosmogenic ^{36}Cl dating of offset limestone-clast fans, Earth Planet. Sci. Lett. 227 (2004) 105-119.
[39] R.W.H. Butler, S. Spencer, H.M. Griffiths, Transcurrent fault activity on the Dead Sea Transform in Lebanon and its implication for plate tectonics and seismic hazard, J. Geol. Soc. 154 (1997) 757-760.
[40] F. Gomez, M. Meghraoui, A.N. Darkal, R. Sbeinati, R. Darawcheh, C. Tabet, M. Khawlie, M. Charabe, K. Khair, M. Barazangi, Coseismic displacements along the Serghaya Fault: an active branch of the Dead Sea Fault System in Syria and Lebanon, J. Geol. Soc. 158 (2001) 405-408.
[41] C.D. Walley, A braided strike-slip model for the northern continuation of the Dead Sea Fault and its implications for Levantine tectonics, Tectonophysics 145 (1988) 63-72.
[42] H.M. Griffiths, R.A. Clark, K.M. Thorp, S. Spencer, Strain accommodation at the lateral margin of an active transpressive zone: geological and seismological evidence from the Lebanese restraining bend, J. Geol. Soc. 157 (2000) 289-302.
[43] K. Khair, Geomorphology and seismicity of the Roum Fault as one of the active branches of Dead Sea Fault System in Lebanon, J. Geophys. Res. 106 (2001) 4233-4245.
[44] Y. Ben-Gai, Z. Ben-Avraham, Tectonic processes in offshore northern Israel and the evolution of the Carmel Structure, Mar. Pet. Geol. 12 (1995) 533-548.
[45] Z. Ben-Avraham, J.K. Hall, Geophysical survey of Mount Carmel structure and its extension into the eastern Mediterranean, J. Geophys. Res. 82 (1977) 793-802.
[46] N.N. Ambraseys, J.A. Jackson, Faulting associated with historical and recent earthquakes in the Eastern Mediterranean region, Geophys. J. Int. 133 (1998) 390-406.
[47] T. van Eck, A. Hofstetter, Fault geometry and spatial clustering of microearthquakes along the Dead Sea-Jordan Rift fault zone, Tectonophysics 180 (1990) 15-27.
[48] A. Shapira, A. Hofstetter, Source parameters and scaling relationships of earthquakes in Israel, Tectonophysics 217 (1993) 217-226.
[49] A.L. Thomas, Poly3D: a three-dimensional, polygonal element, displacement discontinuity boundary element computer program with applications to fractures, faults, and cavities in the earths crust, MS thesis, Stanford California, 1993.
[50] Z. Ben-Avraham, U. ten Brink, R. Bell, M. Reznikov, Gravity field over the Sea of Galilee: evidence for a composite basin along a transform fault, J. Geophys. Res. 101 (1996) 533-544.
[51] P.A. Reasenberg, R.W. Simpson, Response of regional seismicity to the static stress change produced by the Loma Prieta earthquake, Science 255 (1992) 1687-1690.
[52] E. Zilberman, R. Amit, N. Porat, Y. Enzel, U. Avner, Surface rupture induced by the devastating 1068 AD earthquake in the Arava Valley, Dead Sea Rift, Israel, Tectonophysics 408 (2005) 79-99.
[53] Y. Klinger, J.P. Avouac, L. Dorbath, N. Abou Karaki, N. Tisnerat, Seismic behaviour of the Dead Sea Fault along Araba Valley, Jordan, Geophys. J. Int. 142 (2000) 769-782.
[54] E. Guidoboni, F. Bernardini, A. Cosmastri, The 1138-1139 and 1156-1159 destructive seismic crises in Syria, south-eastern Turkey and northern Lebanon, J. Seismol. 8 (2004) 105-127.
[55] R.A. Harris, R.W. Simpson, Suppression of large earthquakes by stress shadows: a comparison of Coulomb and rate-and-state failure, J. Geo-

phys. Res. 103 (1998) 24439-24451.
[56] H. Horikawa, Earthquake doublet in Kagoshima, Japan: rupture of asperities in a stress shadow, Bull. Seismol. Soc. Am. 91 (2001) 112-127.
[57] Y.G. Wan, Z.L. Wu, G.W. Zhou, Focal mechanism dependence of static stress triggering of earthquakes, Tectonophysics 390 (2004) 235-243.
[58] M. Daëron, Y. Klinger, P. Tapponnier, A. Elias, E. Jacques, A. Sursock, Sources of the large A.D. 1202 and 1759 Near East earthquakes, Geology 33 (2005), doi:10.1130/G21352.1.
[59] A. Elias, P. Tapponnier, G. King, S.K. Singh, A. Sursock, A. Briais, H. Carton, E. Jacques, M. Daëron, R. Jomaa, Fresh submarine seismic breaks due to historical thrust earthquakes offshore Lebanon, Eos, Trans. - Am. Geophys. Union 85 (47) (2004) Abstract T13C-1382.
[60] S. McClusky, S. Balassanian, A. Barka, C. Demir, S. Ergintav, I. Georgiev, O. Gurkan, M. Hamburger, K. Hurst, H. Kahle, K. Kastens, G. Kekelidze, R. King, V. Kotzev, O. Lenk, S. Mahmoud, A. Mishin, M. Nadariya, A. Ouzounis, D. Paradissis, Y. Peter, M. Prilepin, R. Reilinger, I. Sanli, H. Seeger, A. Tealab, M.N. Toksöz, G. Veis, Global positioning system constraints on plate kinematics and dynamics in the eastern Mediterranean and Caucasus, J. Geophys. Res. 105 (2000) 5695-5719.
[61] A.M. Freed, J. Lin, Delayed triggering of the 1999 Hector Mine earthquake by viscoelastic stress transfer, Nature 411 (2001) 180-183.
[62] T. Hergert, O. Heidbach, New insights in the mechanism of postseismic stress relaxation exemplified by the June 23rd 2001 $M_w = 8.4$ earthquake in southern Peru, Geophys. Res. Lett. 33 (2006), doi:10.1029/2005GL024585.
[63] Q. Li, M. Liu, E. Sandvol, Stress evolution following the 1811-1812 large earthquakes in the New Madrid Seismic Zone, Geophys. Res. Lett. 32 (2005), doi:10.1029/2004GL022133.
[64] F. Lorenzo-Martín, F. Roth, R. Wang, Elastic and inelastic triggering of earthquakes in the North Anatolian Fault zone, Tectonophysics 424 (2006) 271-289.
[65] F. Alderson, Z. Ben-Avraham, A. Hofstetter, E. Kissling, T. AlYazjeen, Lower-crustal strength under the Dead Sea basin from local earthquake data and rheological modeling, Earth Planet. Sci. Lett. 214 (2003) 129-142.
[66] P. Wessel, W.H.F. Smith, New, improved version of Generic Mapping Tools released, Eos, Trans. - Am. Geophys. Union 79 (1998) 579.

Originally published as:
GEOPHYSICAL RESEARCH LETTERS, VOL. 33, L02307, doi:10.1029/2005GL024858, 2006

New insights into the mechanism of postseismic stress relaxation exemplified by the 23 June 2001 $M_w = 8.4$ earthquake in southern Peru

Tobias Hergert and Oliver Heidbach

Geophysical Institute, Karlsruhe University, Karlsruhe, Germany

Received 7 October 2005; revised 22 November 2005; accepted 19 December 2005; published 21 January 2006.

[1] The 2001 $M_w = 8.4$ southern Peru subduction earthquake marked the beginning of a transient postseismic surface motion in direction of the coseismic displacement at the permanent GPS station Arequipa. In general this motion is assigned to afterslip. Our hypothesis is that the observed transient signal can be explained by stress relaxation processes in the overriding plate. We use a 2D finite element model incorporating non-linear viscoelastic Maxwell rheology. Our model results indicate that coseismically induced stresses are relieved by viscoelastic stress relaxation in the lower crust. The trenchward directed creep motion is transferred to the upper crust due to elastic coupling leading there to an instantaneous relief of elastic stresses. In contrast to the existing conceptual models for stress relaxation, which incorporate shear stresses, we conclude that tensional elastic stresses throughout the crust and upper mantle are the main driving forces for the transient GPS signal. **Citation:** Hergert, T., and O. Heidbach (2006), New insights into the mechanism of postseismic stress relaxation exemplified by the 23 June 2001 $M_w = 8.4$ earthquake in southern Peru, *Geophys. Res. Lett.*, *33*, L02307, doi:10.1029/2005GL024858.

1. Introduction

[2] During the last decade, high quality time series of permanent GPS stations revealed unexpected transient signals after earthquakes and demanded new concepts of internal deformation processes in the lithosphere. Different driving mechanisms have been proposed to cause these transient surface motions following earthquakes, such as afterslip on the rupture plane or on its downdip extension [e.g., *Ueda et al.*, 2001], aseismic fault creep downdip of the coseismic slip area [e.g., *Melbourne et al.*, 2002; *Montési*, 2004], viscoelastic relaxation of coseismically induced stress changes [e.g., *Hu et al.*, 2004], poroelastic rebound [e.g., *Peltzer et al.*, 1998], and transient silent slip [e.g., *Miyazaki et al.*, 2003] or combinations of these mechanisms [e.g., *Márquez-Azúa et al.*, 2002].

[3] A prominent example is the transient postseismic GPS signal observed after the 23 June 2001 $M_w = 8.4$ thrust earthquake which occurred along the subduction interface of the Nazca Plate and the South America Plate in southern Peru. Figure 1 shows the epicenters of the main shock and the aftershocks with $M > 5$ within two weeks after the main shock including the large $M_w = 7.6$ aftershock. The slip distribution on the rupture plane indicates that the main asperity was located in the southeastern part of the rupture plane [*Kikuchi and Yamanaka*, 2001].

[4] *Melbourne et al.* [2002] ascribed the transient postseismic signal at the GPS station Arequipa to postseismic fault creep downdip of the main shock. *Perfettini et al.* [2005] proposed a semi-analytical model referring the GPS observations to the combined effects of afterslip and ductile flow along the plate interface assuming a Newtonian viscosity. In contrast to this we investigate the hypothesis that the observed transient signal can also be explained by stress relaxation processes in the overriding plate. Our 2D finite element model incorporates nonlinear viscoelastic Maxwell rheology with dislocation creep. We analyze the temporal and spatial evolution of stress and strain after the earthquake and discuss three different conceptual models for stress relaxation and their expected deformation within the crust and the observed signal at the surface. We finally conclude that tensional stresses in the continental plate induced by the earthquake are responsible for the trenchward directed postseismic motion of the GPS station.

2. GPS Data

[5] Figure 2 shows the pre-, co- and postseismic displacements observed at the permanent GPS station of the International GPS Service (IGS) in Arequipa which is located at a distance of 225 km from the Peru-Chile trench. The weekly solutions were provided by the German Geodetic Research Institute (DGFI) (W. Seemüller, personal communication, 2005) according to the procedure described by *Kaniuth et al.* [2002] and *Seemüller et al.* [2002]. Prior to the main shock, a northeast directed motion with a rate of ~1.7 cm/a represents the motion of the GPS station during the interseismic phase of the seismic cycle with the northeast moving Nazca Plate being locked at the plate boundary accumulating elastic deformation. The earthquake displaced the GPS station trenchward by ~51 cm, in the opposite direction of the interseismic motion [*Ruegg et al.*, 2001; *Melbourne and Webb*, 2002]. Two weeks later the $M_w = 7.6$ aftershock produced 4.5 cm of coseismic horizontal displacement.

[6] After the earthquake the GPS station was expected to move in northeastern direction again due to the ongoing tectonic loading along the locked subduction interface. Instead, a rapid motion parallel to the coseismic displacement was observed (Figure 2). During the following 3.5 yrs the rate decreased and ~17 cm of horizontal trenchward displacement was accumulated. The vertical component shows 2.1 cm of coseismic subsidence but no clear postseismic trend is visible.

0094-8276/06/2005GL024858$05.00

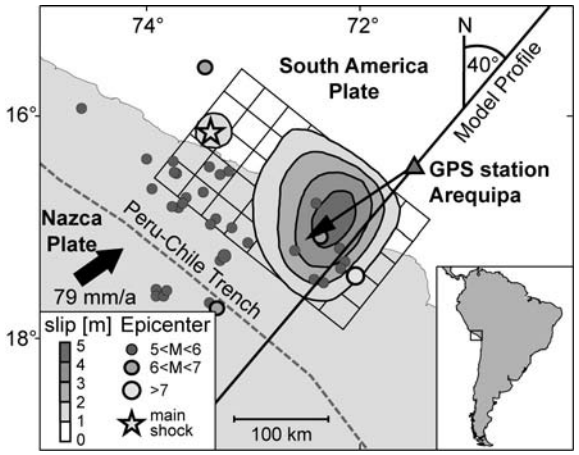

Figure 1. Slip distribution on the rupture plane after *Kikuchi and Yamanaka* [2001] and epicenters of the aftershocks ($M > 5$) within two weeks after the main shock. Thin black arrow indicates the coseismic slip direction, and thick black arrow indicates the motion of the Nazca Plate relative to the South America Plate.

3. Finite Element Model

[7] The profile of our vertical 2D model geometry is oriented perpendicular to the strike of the rupture plane, which is 310° (Harvard CMT catalog, Figure 1). It contains the GPS station Arequipa and is almost parallel to the observed displacements. The model geometry extends 300 km vertically and 600 km horizontally reaching from 100 km southwest of the Peru-Chile Trench to the Andes (Figure 3). The finite element mesh consists of 32,341 linear elements. We implemented three rheological units with different material properties: (1) the oceanic crust of the Nazca Plate with a thickness of 8 km dipping with 18° and below a depth of 60 km with 20° [*Tichelaar and Ruff*, 1991], (2) the continental crust of the South America Plate with a thickness of 45-65 km in the forearc and 65-70 km in the Andes [e.g., *James*, 1971; *Yuan et al.*, 2002], and (3) the upper mantle.

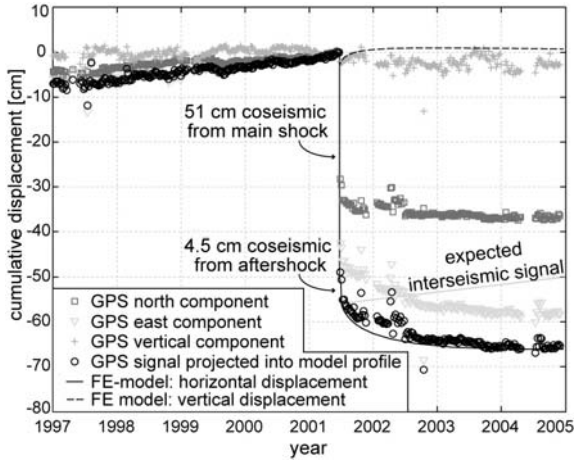

Figure 2. Modeled and observed cumulative displacements at the permanent GPS station in Arequipa (weekly GPS solutions) relative to the position just before the earthquake. Modeled results are best-fit solution of the finite element model. Note the difference between the expected interseismic signal after the earthquake of 1.7 cm/a and the observed postseismic GPS signal.

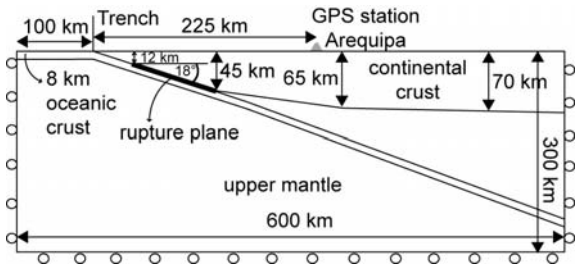

Figure 3. Geometry and boundary conditions of the 2D finite element model. Circles at the model sides indicate that no displacement normal to the boundary is allowed. The upper boundary is a free surface.

[8] The model also contains the rupture plane as contact surfaces, located along the boundary between the continental and oceanic crusts, dipping with 18° (Harvard CMT catalog) and extending from 12 to 45 km depth. At the bottom and the sides of the model only displacements parallel to the model boundaries are allowed. The upper boundary of the model is a free surface. To simulate the coseismic displacement of the earthquake we displaced the nodes along the rupture plane. The slip distribution grows linearly from zero at the upper and lower edges of the rupture plane to a maximum displacement at 32 km depth. We varied the coseismic slip in order to represent the coseismic displacement at the GPS station in Arequipa. The postseismic signal is modeled with non-linear viscoelastic Maxwell rheology using dislocation creep described by

$$d\epsilon/dt = A\sigma^n e^{-Q/RT} \quad (1)$$

where $d\epsilon/dt$ is the strain rate, A a pre-exponent, σ and n the differential stress and the stress exponent, respectively, Q the activation enthalpy, R the gas constant and T the temperature [*Kirby and Kronenberg*, 1987]. According to equation (1) the coseismic stress changes cause the onset of dislocation creep with creep rates depending on the given creep parameters and the temperature distribution. The parameters for the elastic and creep properties of the three rheological units are listed in Table 1 and the needed temperature distribution in the model is adapted from *Springer* [1999]. The numerical problem is solved with the commercial finite element code ABAQUS™, version 6.4-1 (Hibbitt, Karlsson and Sorensen, Inc.).

4. Results

[9] To fit the observed coseismic displacement at the GPS station a maximum slip of 4.87 m along the rupture plane is required in agreement with the findings of *Kikuchi and Yamanaka* [2001]. One fourth of this slip is assigned to the bottom side of the rupture plane and three fourth to the upper side. The modeled postseismic horizontal displacement at the GPS station Arequipa presented in Figure 2 is corrected for the linear effects of the interseismic velocity observed prior to the earthquake and for the coseismic displacement caused by the $M_w = 7.6$ aftershock.

[10] Figure 4 displays the results of the best-fit model

Table 1. Elastic and Creep Parameters Used in the Model

Layer	E, GPa	ν	A, MPa^{-n}s^{-1}	n	Q, kJ mol^{-1}
Continental crust	85 granite	0.27	$3.2 \cdot 10^{-4}$	2.3	154 wet quartzite[a]
Oceanic crust	90 basalt	0.27	$2.0 \cdot 10^{-4}$	3.4	260 diabase[a]
Upper mantle	135 peridotite	0.30	2.0	3.0	433 olivine[b]

[a] *Ranalli* [1995].
[b] *Karato and Wu* [1993].

in terms of the effective strain and stress distribution directly after the earthquake and 3.5 yrs later. Coseismically the effective elastic strain has its maximum at the rupture plane (Figure 4a). After 3.5 yrs a zone of high effective strain with maximum creep strain rates in the order of 10^{-13} s^{-1} in the lowermost part of the continental crust has evolved, whereas effective elastic strain is slightly reduced in the upper part (Figure 4b). The associated effective stress is reduced in the lower crust as can be seen in the shift of the 0.135 MPa isoline towards the rupture plane (Figure 4). In contrast, effective stress is increased in the upper crust, at least in the far field. In the upper mantle the stress magnitudes are slightly reduced after 3.5 yrs.

[11] The associated horizontal displacements in a vertical profile through the continental crust 75 km northeast of the GPS station are presented in Figure 5a. The coseismic displacement decreases with depth whereas the total displacement after 3.5 yrs increases with depth reaching a maximum in approximately 40 km depth. The difference between the two lines gives the postseismic displacement during 3.5 yrs with a maximum in 40-50 km depth.

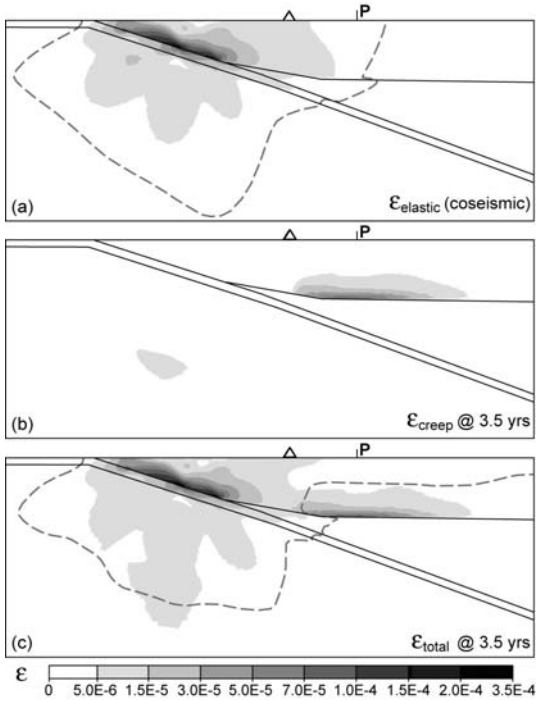

Figure 4. Effective strain (second invariant of the strain tensor). Dashed lines indicate the 0.135 MPa isoline of effective stress. (a) Coseismic. (b) Creep strain. (c) Total strain (sum of elastic and creep strain). Note that Figure 4c is not the sum of Figures 4a and 4b as the elastic strain has changed after 3.5 years. Triangle marks the position of the GPS station, and P marks the location of the vertical profile in Figure 5a.

5. Discussion

[12] During the earthquake the forearc moves trenchward, so that tensional elastic stresses are induced in the crust and upper mantle of the continental plate. In the lower part of the crust a postseismic creep process relaxes these tensional stresses. This results in a concentration of creep strain and a decrease of effective stress in the lower crust (Figure 4) and in a trenchward directed postseismic motion (Figures 2 and 5a). The highest deformation is found in the lower crust because of its lower effective viscosity compared to the colder upper crust and the olivine-rich upper mantle. In response to the creeping lower crust, the tensional stresses in the upper crust are relieved instantaneously due to elastic coupling leading to a concurrent trenchward directed surface motion. This can be deduced from the postseismic decrease of effective elastic strain beneath the GPS station in the upper crust (Figures 4a and 4c) and from the postseismic surface displacement (Figure 5a). A consequence of the trenchward directed surface motion is an increase of tensional stress in greater distances from the rupture plane in the upper crust, i.e. stress diffusion takes place as indicated in the results of Figures 4a and 4c.

[13] This interpretation is in contrast to previous findings and concepts which refer to the relaxation of shear stresses. *Wernicke et al.* [2000] and *Dixon et al.* [2003] proposed an elastic crust imposing a shear traction on a viscous layer beneath. After the earthquake the viscous layer starts flowing and thereby relaxes the shear stress and imparts in turn a traction on the upper layer resulting in a postseismic surface motion. However, the relaxation

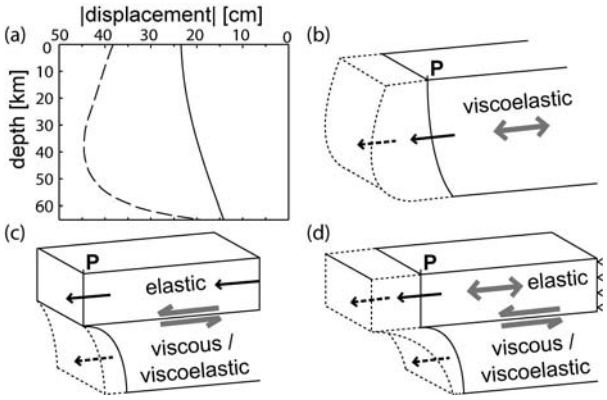

Figure 5. Conceptual models of relaxation processes. Solid lines mark coseismic displacements, and dotted lines mark total displacements. Double arrows indicate the type of stress. (a) Modeled coseismic and postseismic horizontal displacements 3.5 years after the earthquake in a vertical profile 75 km northeast of the GPS station (see Figure 4). (b) Mainly tensional stresses. (c) Shear stresses only. (d) Shear and tensional stresses.

of pure shear stress is not capable of producing further surface motion after the earthquake (Figure 5c).

[14] *Hu et al.* [2004] proposed a coseismic tension in the crust inducing shear stresses in the upper mantle which resist the coseismic motion. They argued that relaxation of the shear stresses allows surface motion as the tensional stresses in the crust concurrently relieve (Figure 5d). This explanation is plausible but not in agreement with our results. If relaxation of shear stresses would predominate, one would not expect the sum of co- and postseismic displacement in the lower part of the crust to be higher than in the upper part (Figure 5a).

[15] Our model results propose that the whole crust and parts of the upper mantle are coseismically stretched rather than sheared as viscoelastic material does not behave viscously but elastically during an earthquake. Thus, we suggest that tensional stresses are the dominant driving forces in the viscoelastic stress relaxation process which controls the postseismic deformation measured by GPS (Figure 5b).

[16] Even though our model can fully explain the postseismic GPS signal with creep processes, we can not rule out that other processes such as afterslip also contribute to the observed surface displacement. An essential requirement for viscoelastic relaxation to be responsible for the observed postseismic motion is a silicate rich continental crust with low viscosity. We determined a minimal effective viscosity in the lower part of the crust of 2.3×10^{16} Pa s in the first six months after the earthquake increasing to 1.1×10^{17} Pa s after 3.5 yrs. *Pollitz* [2003] calculated transient effective viscosities of 7.5×10^{16} Pa s and 1.6×10^{17} Pa s for the lower crust and upper mantle in the Mojave desert after the Hector Mine earthquake in shallower depths. Such low transient effective viscosities are an expression of an unusual silicate rich crust and temperatures of about 1100°C in the lower crust [*Springer*, 1999]. This is supported by *Beck and Zandt* [2002] who found no evidence for *P*-wave velocities higher than 6 km/s even in the lower crust of the central Andes. They interpreted this by a presence of a felsic, quartz-rich crust and suggested a very weak lower crust. Additionally, the v_p/v_s ratio of up to 1.85 beneath the magmatic arc in the central Andes indicates melts and a low viscosity [*Yuan et al.*, 2002].

[17] We conclude that viscoelastic relaxation should be considered as an alternative explanation of the observed postseismic transient signal at the GPS station in Arequipa. Independent of the question to which extent viscoelastic relaxation contributes to the GPS signal we emphasize that according to our numerical modeling results the general mechanism of postseismic stress relaxation predominantly involves tensional stresses.

[18] **Acknowledgment.** We thank Wolfgang Seemüller for the GPS data and Birgit Müller, Blanka Sperner and two anonymous reviewers for very constructive comments.

References

Beck, S., and G. Zandt (2002), The nature of orogenic crust in the central Andes, *J. Geophys. Res.*, *107*; B10, 2230, doi:10.1029/ 2000JB000124.

Dixon, T. H., E. Norabuena, and L. Hotaling (2003), Paleoseismology and GPS: Earthquake-cycle effects and geodetic versus geologic fault slip rates in the Eastern California shear zone, *Geology*, *31* (1), 55–58.

Hu, Y., K. Wang, J. He, J. Klotz, and G. Khazaradze (2004), Three-dimensional viscoelastic finite element model for postseismic deformation of the great 1960 Chile earthquake, *J. Geophys. Res.*, *109*, B12403, doi:10.1029/2004JB003163.

James, D. E. (1971), Andean crustal and upper mantle structure, *J. Geophys. Res.*, *76* (14), 3246–3271.

Kaniuth, K., H. Müller, and W. Seemüller (2002), Displacement of the space geodetic observatory Arequipa due to recent earthquakes, *Z. Vermessungswesen*, *127* (4), 238–243.

Karato, S., and P. Wu (1993), Rheology of the upper mantle: A synthesis, *Science*, *260*, 771–778.

Kikuchi, M., and Y. Yamanaka (2001), Earthquake Information Center seismological note 105, report, Earthquake Res. Inst., Univ. of Tokyo, Tokyo.

Kirby, S. H., and A. K. Kronenberg (1987), Rheology of the lithosphere: Selected topics, *Rev. Geophys.*, *25*, 1219–1244.

Márquez-Azúa, B., C. DeMets, and T. Masterlark (2002), Strong interseismic coupling, fault afterslip, and viscoelastic flow before and after the Oct. 9, 1995 Colima-Jalisco earthquake: Continuous GPS measurements from Colima, Mexico, *Geophys. Res. Lett.*, *29* (8), 1281, doi:10.1029/ 2002GL014702.

Melbourne, T. I., and F. H. Webb (2002), Precursory transient slip during the 2001 $M_w = 8.4$ Peru earthquake sequence from continuous GPS, *Geophys. Res. Lett.*, *29* (21), 2032, doi:10.1029/2002GL015533.

Melbourne, T. I., F. H. Webb, J. M. Stock, and C. Reigber (2002), Rapid postseismic transients in subduction zones from continuous GPS, *J. Geophys. Res.*, *107*; B10, 2241, doi:10.1029/ 2001JB000555.

Miyazaki, S., J. McGuire, and P. Segall (2003), A transient subduction zone slip episode in southwest Japan observed by the nationwide GPS array, *J. Geophys. Res.*, *108*; B2, 2087, doi:10.1029/2001JB000456.

Montési, L. G. J. (2004), Controls of shear zone rheology and tectonic loading on postseismic creep, *J. Geophys. Res.*, *109*, B10404, doi:10.1029/2003JB002925.

Peltzer, G., P. Rosen, F. Rogez, and K. Hudnut (1998), Poroelastic rebound along the Landers 1992 earthquake surface rupture, *J. Geophys. Res.*, *103*; B12, 30,131–30,145.

Perfettini, H., J.-P. Avouac, and J.-C. Ruegg (2005), Geodetic displacements and aftershocks following the 2001 $M_w = 8.4$ Peru earthquake: Implications for the mechanics of the earthquake cycle along subduction zones, *J. Geophys. Res.*, *110*, B09404, doi:10.1029/2004JB003522.

Pollitz, F. F. (2003), Transient rheology of the uppermost mantle beneath the Mojave Desert, California, *Earth Planet. Sci. Lett.*, *215*, 89-104.

Ranalli, G. (1995), Rheology of the Earth, CRC Press, Boca Raton, Fla.

Ruegg, J. C., M. Olcay, and D. Lazo (2001), Co-, post- and pre (?)-seismic displacements associated with the M_w 8.4 Southern Peru Earthquake of 23 June 2001 from continuous GPS measurements, *Seismol. Res. Lett.*, *72* (6), 673–678.

Seemüller, W., K. Kaniuth, and H. Drewes (2002), Velocity estimates of IGS RNAAC SIRGAS stations, in *Vertical Reference Systems, IAG Symp.*, vol. 124, edited by H. Drewes et al., pp. 7-10, Springer, New York.

Springer, M. (1999), Interpretation of heat-flow density in the central Andes, *Tectonophysics*, *306* (3), 377–395.

Tichelaar, B. W., and L. J. Ruff (1991), Seismic coupling along the Chilean subduction zone, *J. Geophys. Res.*, *96*; B7, 11,997-12,022.

Ueda, H., M. Ohtake, and H. Sato (2001), Afterslip on the plate interface following the 1978 Miyagi-Oki, Japan, earthquake, as revealed from geodetic measurement data, *Tectonophysics*, *338*, 45–57.

Wernicke, B., A. M. Friederich, N. A. Nièmi, R. A. Bennett, and J. L. Davis (2000), Dynamics of plate boundary fault systems from Basin and Range Geodetic Network (BARGEN) and Geologic Data, *GSA Today*, *10* (11), 1–7.

Yuan, X., S. V. Sobolev, and R. Kind (2002), Moho topography in the central Andes and its geodynamic implications, *Earth Planet. Sci. Lett.*, *199*, 389–402.

O. Heidbach and T. Hergert, Geophysical Institute, Karlsruhe University, Hertzstr. 16, D-76187, Karlsruhe, Germany. (oliver.heidbach@gpi. uni-karlsruhe.de; tobias.hergert@gpi.uni-karlsruhe.de)

ISSN 1610-0956